THESIS

presented for the partial fulfilment of degree of

Doctor of Philosophy in *Physics*

Nonlinear optical effects of exciton-polaritons in semiconductor microcavities in the near infrared to the ultraviolet range of wavelengths

Mr Anthonin Bruno Raymond Delphan

Under supervision of

Prof. Dmitry Krizanovskii and Dr. Maxim Makhonin

Faculty of Science

School of Mathematical and Physical Sciences

The University of Sheffield

United Kingdom

January 2025

Abstract

Exciton-polaritons (EP) are half-light, half-matter quasiparticles arising from the strong coupling of photons with excitons, the elementary excitations of semi-conductors. In this thesis, we give a literature review on the state-of-the-art of research using exciton-polaritons and give examples of original research. We start by defining exciton-polaritons in a bulk material and show why they cannot be observed directly in such a system. We give examples of systems to confine light in a cavity to overcome this limitation. This allows us to define the weak and strong coupling regimes of light and matter. Some example of research in exciton-polaritons is given, in particular in the materials which we will use later in this thesis.
An overview of the experimental techniques commonly used to study EPs is given. Our original research consists of three chapters covering a wide range of research topics. In the first chapter describing our results, we show the fabrication process of ring resonator structures, which demonstrate polariton lasing in the UV range up to room temperature. In a second chapter, we study, for the first time, exciton-polariton non-linearities in a Cu_2O microcavity, in the visible range of wavelength. We demonstrate Kerr-like nonlinearity arising from the phenomenon of polariton Rydberg blockade. These two chapters have been published in the literature. Supplementary material related to these publications can be found at the end of the thesis in the appendices.
The final chapter describes experimental work still in progress, to realise an analogue black hole using exciton-polaritons in GaAs high quality sample, pumped in the near infrared. We provide motivation and show polariton superfluid-like behaviour appearing after a threshold. We create polariton vortices with very high orbital angular momentum, with the ultimate goal of realising an acoustic analogue black hole system. We conclude with a summary showing the highlights of the different chapters as well as the perspectives for further work offered by our results.

I slowly intoned the famous line. “L’hydre-univers tordant son corps écaillé d’astres.”

I could sense his almost fear-stricken bafflement. He repeated the line softly, savoring each glowing word.

“It’s true,” he stammered, “I could never write a line like that.”

— Jorge Luis Borges, “The Other”

Acknowledgements

Who could have guessed that three years and half worth of work could go by so fast? As the "ultimate hour" draws near, I want to use this page to give heartfelt thanks to colleagues, friends and family without which this work would have been impossible.

I am particularly indebted to Professor Dmitry Krizanovskii, for accepting to supervise this thesis and for his helpful guidance and support throughout my research. I am grateful to Dima for giving me such great opportunities to pursue cutting edge research in such a fascinating field. I also thank the thesis defence committee for their valuable time.

I want to say very special thanks to Doctor Maxim Makhonin for his day-to-day supervision, his patience, his mentoring and his friendliness throughout all our experiments. Max played an invaluable role in this PhD and is a model for supervision.

The other colleagues of the polariton team also deserve great thanks for their help and guidance. I wish to thank in particular Fedor Benimetskiy for the helpful conversations, Tommi Isoniemi for his help with the samples, Paul Walker for his help with the laser and many more things, Maurice Skolnick for his advice, and Seth Lovett for his general guidance.

A special mention goes to Chris Vickers and Thomas Ball for their patience and help with all things cryo-related.

I thank our collaborators for the opportunity to participate on fascinating research projects, with special thanks to Raphaël Butté, Oleksandr Kyriienko, and also Thomas Boulier (as well as his team) for the warm welcome in Toulouse.

I wish to thank all the LDSD team for the friendly conversations and the general atmosphere of the lab, with thanks to Sam, Zara, Oscar, Paul, Alex, Anthony, and many others.

Staying in Sheffield would not have been the same without friends. Among them, I wish to mention Matthew and Oscar, Billy, Seb and John, as well as Yacob, Anthony, Ben, Dave, and countless others from here and further away.

A very big "merci" to Victor, Charlotte, Etienne, Rambo and Charles for their visits and their friendship. Continuez, les gars.

More personal thanks go to Monsieur Bertrand and the other teachers. And in the last, I wish to thank my family for their continuous love and support. Je dédie en particulier cette thèse à Papy Phillipe, repose en paix.

Contents

List of Figures

Figures from the reproduced articles

List of publications

"**Polariton lasing in AlGaN microring with GaN/AlGaN quantum wells**", *Anthonin Delphan*, Maxim N. Makhonin, Tommi Isoniemi, Paul M. Walker, Maurice S. Skolnick, Dmitry N. Krizhanovskii, Dmitry V. Skryabin, Jean-François Carlin, Nicolas Grandjean, and Raphaël Butté; APL Photonics 1 February 2023; 8 (2): 021302. `https://doi.org/10.1063/5.0132170`

"**Nonlinear Rydberg exciton-polaritons in Cu2O microcavities**", Maxim Makhonin, *Anthonin Delphan*, Kok Wee Song, Paul Walker, Tommi Isoniemi, Peter Claronino, Konstantinos Orfanakis, Sai Kiran Rajendran, Hamid Ohadi, Julian Heckötter, Marc Assmann, Manfred Bayer, Alexander Tartakovskii, Maurice Skolnick, Oleksandr Kyriienko and Dmitry Krizhanovskii; Light: Science & Applications volume 13, Article number: 47 (2024) `https://doi.org/10.1038/s41377-024-01382-9`

Presentations

"**Polariton lasing in AlGaN microring with GaN/AlGaN quantum wells**", UK Semiconductors; Sheffield, UK; 6-7 July 2022.

"**Rydberg blockade using exciton-polaritons in Cu2O microcavities**", NANOP2023; Barcelona, Spain; 27-29 November 2023.

Chapter 1

Introduction

Lying at the intersection of optics and solid-state physics, exciton-polaritons are an active topic of research in light-matter interactions with countless practical applications and as a springboard for investigation of other physical phenomena. Exciton-polaritons have a rich history, which begins with a paper by Solomon Pekar [1] that theorised that the interaction between light and excitons (the elementary excitations of semiconductors) would result in "additional waves", travelling through the crystal. This concept was further developed in a paper by John J. Hopefield in 1958 which introduced "exciton-polaritons" [2] to describe such additional waves. In essence, the photons incident to the crystal are absorbed to create excitons, which recombine into photons, creating new excitons... this complex dance within the crystal results in a mixed state, which Hopefield called the exciton-polariton. They are poetically described as "half-light, half-matter" quasiparticules, at the boundaries between two worlds, exhibiting properties of both. In his pioneering paper, Hopefield showed how exciton-polaritons affect the dielectric constant of the crystal, and as such are necessary to understand light-matter interactions in bulk semiconductors.

The motivation to investigate exciton-polaritons is strong. However, in bulk materials, it is difficult to observe them directly. Indeed, in the decades following Hopefield's paper, research about exciton-polaritons dealt mostly with indirect ways of observing them: Raman scattering [3], luminescence [4] or at the surface of crystal [5].

A significant shift took place after 1992, due to the progress of fabrication techniques of cavities to confine light [6] . With this technological breakthrough, C. Weisbuch observed, for the first time, evidence of exciton-polariton with both the light and the exciton confiend in two or fewer dimensions [7]. Confinement of light in a small microcavity, as well as confinement of the exciton using Quantum

Wells, radically changes the interaction mechanisms between light and matter. In particular, microcavities offer a one-to-one mapping between emitted photons and exciton-polaritons, as well as enabling new effects from the increased density of the quasiparticles.

A property of the exicton-polaritons gas that can only be observed when they are confined in a microcavity is their coherence. Exciton-polaritons belong to a category of particles called *bosons*. Their quantum statistics allow them to occupy the same state in energy and momentum; when the occupation number of that state passes a critical threshold, the particles coalesce together in a so-called *Bose-Einstein condensate* (BEC), a macroscopic quantum state, exhibiting long-range order and quantum coherence.

The study of BECs is a fascinating topic in itself. They bring forward important questions about symmetries and symmetry breaking in nature. The phase transition from a thermal state to a coherent one is already highly non-trivial. A BEC is a purely quantum phenomenon, with coherence properties existing at scales much larger than atoms or electrons [8, 9]. Bose-Einstein condensates have been predicted theoretically as early as 1924 [10, 11]; they were realised in clouds of atoms cooled down to the billionth of a degree in 1996 [12, 13]. Today, they remain a topic of research ranging from atomic physics [14] to cosmology [15].

The case of condensates of exciton-polaritons in microcavities is unique in many aspects [16]. First, in that it is an inherently *out-of-equilibrium* phenomenon. Polaritons have finite lifetimes, and they need to be constantly created by the incoming light - called a "pump", and they leak out of cavity. This creates interesting dynamics to study. Exciton-polaritons in microcavities are also not a three dimensional system. This raises interesting questions as to the exact nature of their phase transition [17, 18], and how exactly they match the model of ideal Bose-Einstein condensate in three dimensions. Finally, exciton-polaritons are intrinsically non-linear particles, due to their excitonic nature. As a result of their non-linearity and bosonic nature, many seemingly unrelated physical phenomena are realised in similar polaritonic systems. Exciton-polaritons can display the superfluidity of liquid Helium in one system [19], and they can have the superconducitivty of Cooper pairs in another [20].

The active and persisting interest of the scientific community for exciton-polaritons bears testimony to the richness of their physics. In journals published by the American Physics Society, more than 4000 articles are related to exciton-polaritons, of which more than 3200 were published in the last 12 years.

This thesis aims will focus on the phenomena arising from the coherence properties of exciton-polaritons in microcavities. We will explore different geometries, different materials, and look at different ways in which those coherent properties express themselves.

The first chapter of this thesis will provide the precise background material on exciton-polaritons, introducing the formalism and deriving the fundamental equations of the theory, starting from the fundamental bulk case. The principle of light confinement in microcavities, with an overview of the different microcavities realisations used in this thesis will then be presented. The theory of light-matter coupling in such system will be presented and compared to the bulk case, giving the formalism of cavity polaritons. In the next sections, we will present the semiconductor materials in which we have realised such cavity polaritons, with specific insight and challenged related to the specific materials. With these theoretical tools, we can start to describe the phenomena arising from the non-linear properties of exciton-polaritons. We will also formally discuss Bose-Einstein condensation, we will define coherence, and how polaritons relate to superfluidity and superconductivity.

The second chapter will describe our experimental methods and techniques, showing the flexibility of cavity exciton-polariton optical setups.

The third chapter will describe a particular realisation of mircocavity exciton-polariton: gallium nitrite (GaN) microring resonators with AlGaN quantum wells. We show how the condensation of exciton-polaritons can result in coherent light emission: this is called "polariton lasing". A comparison with "regular lasing" is also provided: several criteria can be used as signatures of polariton lasing as opposed to polariton lasing. In this chapter, we demonstrate polariton lasing in the GaN microring resonators. It is based on a previous publication [21].

In the fourth chapter, we consider a different material. Cuprous oxide (Cu_2O) is known for its excitons with very large radius between the electron and the hole, also known as *Rydberg excitons*. Such excitons can couple to photons and form polaritons. The properties of such Rydberg exciton-polaritons are studied. A phenomenon known as *Rydberg blockade* arises: a Rydberg exciton-polariton with high radius may prevent the formation of another in its vicinity. We demonstrate Rydberg blockade in a Cu_2O microcavity. The lifetime of the non-linear response of polaritons is studied with a pump-probe experiment. We show how different time scales and different mechanisms are involved in the Rydberg blockade. It is also based on a previous publication [22].

In the fifth chapter, we will discuss analogue Physics. The idea of analogue Physics, suggested by Unruh in 1981 [23], is to simulate one physical phenomenon by another. In this case, the dynamics of Black Holes are simulated by a vortex of polariton fluids. We will give a brief overview of analogue physics, describe our experimental setup, objectives and preliminary results.

Finally, we will in conclusion give a summary of our results, and explore some possibilities for further work for the experimental systems we have investigated.

Chapter 2

Background: Exciton-polaritons in microcavities

2.1 Overview

The object of our study are exciton-polaritons. In this chapter, we shall give a formal theory to describe them mathematically, in particular with respect to their coherence and their interactions leading to optical Kerr-like nonlinearity. We shall also give the experimental background needed for the remainder of this thesis.

Exciton-polaritons stand at the border between two worlds: the world of light, described by Maxwell's equations, and the world of matter, described by the physics of electrons and excitons in semiconductors. They are a complex phenomenon, which requires some definitions and groundwork to understand the basic ingredients which together make up an exciton-polariton. We will first treat the case of an exciton-polariton in a bulk material, showing that it is a fundamental concept necessary to understand the interaction between light and matter. The most interesting properties of exciton-polaritons manifest themselves when the dimensionality is reduced and when the light is confined in a microcavity, and when the excitons are confined as well in a structure called a Quantum Well. We will first provide a description of what a microcavity is and how such systems are fabricated.

These elements allow us to provide a description of light-matter coupling in microcavities, starting with the case of so-called weak coupling regime, and then moving on to the strong coupling regime, where the formalism of exciton-polaritons takes a more significant role.

Experimental realisation of cavity exciton-polaritons requires a careful choice of the materials used to fabricate the cavity. The main families of materials used in the course of this thesis will be described in a section outlining their specific properties related to our experiments. We will then list and briefly explain some of the most interesting properties and phenomena that have been observed with exciton-polaritons in such systems in two sections.

The first section will describe the properties of exciton-polaritons as non-linear particles, with effects such as the free motion of solitons [24]. We shall then turn to the main topic of this thesis, which are the non-linear collective properties of excitons-polaritons, including superfluidity [19], superconductivity [25], polariton lasers [26], including at room temperature [27]. In order to accurately describe these fascinating phenomena, we shall also give a description of coherence and in particular of the phenomenon known as *Bose-Einstein condensation*. With this background, we will then describe how Bose-Einstein condensation is realised in microcavity exciton-polaritons, and conclude with an overview of the physics related to the condensation of polaritons.

2.2 Exciton-polaritons in bulk materials

2.2.1 Excitons

Excitons are the elementary excitation of semiconductors. The exposition here shall follow standard textbooks [28, 29], focusing only on the elements needed to draw the polariton picture. Due to the periodic structure, electrons in a crystal are distributed according to their energy E and their wavevector k according to the band structure. The basic band structure of semiconductors shows a valence band, filled with electrons, and an empty conduction band, separated by a small but finite energy gap.

In some materials, the energy minimum of the conduction band and the energy maximum of the valence band do not occur at the same wavevectors. Because the wave vector must be conserved, the interaction process between these two bands needs to be mediated by the creation or absorption of a phonon. Such materials are called indirect gap semiconductors (such as Silicon or Germanium); by contrast, when the bands' extrema coincide, we speak of direct gap semiconductors. For the remainder of this thesis we shall only consider

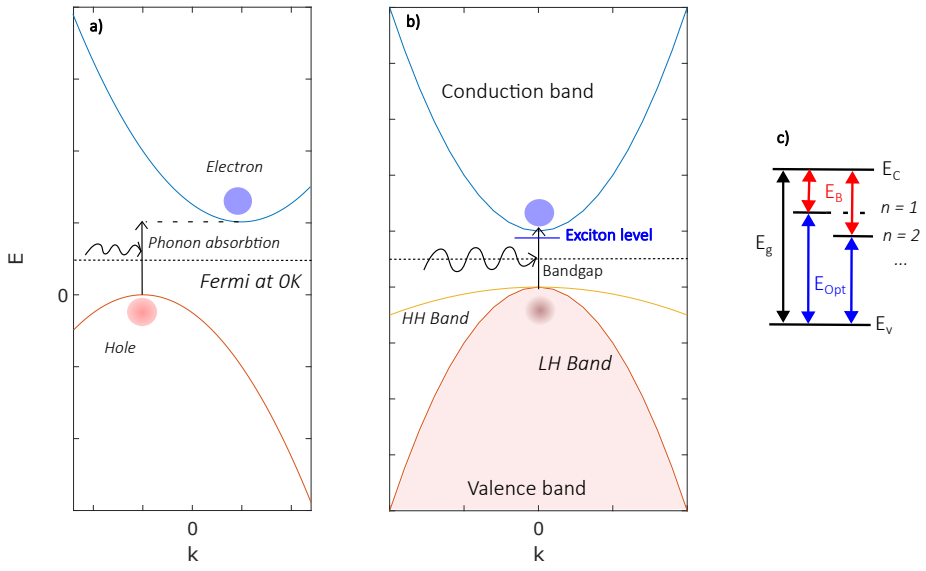

Figure 2.1: Simplified band structure of indirect (a) and direct (b) bandgap semiconductors using an effective mass approximation for the electron and the hole. c) First two energy levels for the excitons, showing bandgap energy E_g, as well as the exciton binding energy E_B and optical gap E_{Opt} for $n = 1$ and $n = 2$.

direct bandgap semiconductors. Figure 2.1 shows a simplified band structure of a semiconductor.

When a direct bandgap semiconductor absorbs energy above its bandgap, the electron in the valence band may be promoted to the conduction band, and leave an empty "*hole*" behind. We shall be interested in this thesis in the promotion of electrons through optical means.

The electron, being negatively charged, and the hole, positively charged, can be bound together by Coulomb interaction, and this forms an exciton. Alternatively, it is possible to pump the semiconductor at an *optical gap* E_{Opt} to directly create an exciton of a given energy level n. The Coloumb-bound electron-hole pair can be compared to an hydrogen-like system, such as positronium (a positron-electron pair). In some cases, such as in Alkali Halides, or near defects, the excitons have a very small radius (compared to the unit cell of the crystal) and are tightly bound. These bound excitons (called *Frenkel excitons*) do not move freely in the crystal: they hop between neighbouring defect sites where the energy potential shows local minima.

By contrast, excitons with a large radius (larger than several unit cells) can freely move around in the crystal, and are called Wannier-Mott excitons. In this case, the hydrogen atom model can be applied. The orbits are quantified, and in particular, the energy is quantified by the principal quantum number n, with the equation:

$$E_n = \frac{\mu}{m_0 \varepsilon_r^2} \frac{\mathrm{Ry}}{n^2} = \frac{R_X}{n^2} \tag{2.1}$$

Where E_g is the bandgap, μ is the reduced effective mass of the exciton (given by $\mu^{-1} = 1/m_e^* + 1/m_h^*$, m_e, m_h being the effective masses electron and the hole respectively), ε_r being the relatively permittivity of the material, and Ry being the Rydberg unit. The "effective mass" of a particle is an approximation of the "mass" the particle modified by the interactions with the crystal periodic potential. In figure 2.1, we see that the exciton may be created with a heavy or a light hole, with different effective mass. In real materials, excitons can have a more complex band structure with different "sub-bands" for the holes. R_X becomes a constant related to the exciton in the crystal.

Excitons have strong non-linear properties, as they are charged particles with Coulomb interactions. They can notably exhibit an electric dipole moment. As they are made of an electron and a hole, their spin is usually a half-integer (typically $\pm 1/2$, but with higher spin in some cases) the components of the excitons are subject to the Pauli exclusion principle. However, the exciton itself has an integer total spin, and is therefore an approximate boson, subject to a different statistic, the Bose-Einstein distribution. The significance of the exciton statistical properties shall be described later in this section.

Excitons are not stable particles and they quickly recombine, with the electron falling back into the valence band. The lifetime of the exciton depends on many factors, such as crystal geometry, purity, temperature, and recombination process.

The recombination process can either be non-radiative, not resulting in the emission of a photon, or radiative, with the emission of a photon. The two main pathways for non-radiative recombination are *Auger recombination* (named after Pierre Victor Auger), in which the recombination results in the promotion of another electron, or defect recombination, where the electron scatters over a defect. As an order of magnitude, the radiative lifetime of an exciton in bulk GaAs at t = 5K is on the order of 1ps [30], whereas in bulk GaN it was measured to be 30ps at the same temperature [31]. Auger recombination lifetimes scale with density and become predominant at higher densities [32]. Additionally, the exciton can dissociate in a free electron and a free hole if the thermal energy in the crystal (given by $k_B T$, with k_B as Boltzmann's constant) is higher than the exciton binding energy. This means that there are temperature cut-offs to observe excitonic effects in given materials; for example, in GaAs the maximum temperature is in the tens of K, whereas in GaN excitons can be observed up

to room temperature, albeit redshifted and broadened in energy.

In this thesis, we are interested in excitons in so far as they are an ingredient to form an exciton-polariton. More specifically, we will study *optically pumped* excitons, in which the promotion to the conduction band happens by the absorption of a photon. We will also work with direct bandgap semiconductors, without phonon mediation, and with a large enough radius to be considered Wannier-Mott excitons. Research into such cases does exist, with Frenkel polaritons [33], but lies outside the scope of this research work.

2.2.2 Polaritons

A "polariton" is a general term to describe a quasi-particle born of the strong coupling of light (a photon) and any elementary excitation in a material. For example, there are phonon-polaritons [34], or plasmon-polaritons for noble metals [35]. In our case, the elementary excitations are excitons in semiconductors, and we speak of "exciton-polaritons". Polaritons are often called "half-light, half-matter" or "hybrid" quasiparticles.

There are a couple of questions raised by this definition. How does the coupling occurs? What is meant by "hybridisation"? How do we quantify the "strength" of the coupling?

The intuitive picture is as follows. A semiconductor is illuminated by photons, creating excitons, which then they recombine radiatively and emit a photon of energy equal to the former exciton energy; this photon is then absorbed, creates an exciton again, and so on and so forth, on a time scale inferior to a picosecond [36]. The process continues as long as more photons are pumped into the system than are lost due to different scattering processes in the crystal. The result is a quantum superposition of a photon and an exciton: this quasiparticle is the exciton-polariton.

Exciton-polaritons can be described either using a semi-classical formalism or with full quantum treatment. The semi-classical theory derives most of the important features of the hybrid particle and answers how the hybridisation occurs, but a full quantum treatment proves to be necessary for the most important applications involving exciton-polaritons, such as quantum information theory [37], quantum computing [37], or their use as "single photon" sources [38], due to photon blockade. In all these cases we must treat light and photons as fully quantum objects.

Semi-classical theory

In the semi-classical formalism, the light component of the exciton-polariton is treated classically, using Maxwell's equations, whereas the matter component (the exciton) is treated quantum mechanically. There cannot be a fully classical picture of the exciton-polariton, as the exciton is fundamentally a quantified excitation of the semiconductor.

The semi-classical theory was first derived by K. Huang [39] in the 1951 in the context of phonon-polaritons, and then transposed to semiconductors by Hopfield in his famous paper [2]. The outlined derivation follows that of the textbook references [40] and [41]. We

In the semi-classical model, exciton-polaritons arise from a constitutive relation between the electric field $\mathbf{E}$ and an excitonic polarisation vector arising as a "response" to the incoming electric field. The polarisation density vector is noted $\mathbf{P}$. This equation follows from classical Maxwell equations, but with terms including quantum mechanical calculations. The constitutive relations are:

$$\frac{1}{\omega_0^2}\ddot{\mathbf{P}} - \frac{\hbar}{M\omega_0}\nabla^2\mathbf{P} + \mathbf{P} = \beta\mathbf{E} \tag{2.2}$$

$$\tag{2.3}$$

...where $\hbar$ is the reduced Planck constant, $M = m_e^* + m_h^*$ is the total effective mass, ω_0 is the frequency associated with the bandgap energy of the excitonic transition ($\hbar\omega_0 = E_g$) and it is associated to a wavevector k_0 by $k_0 = n\omega_0/c$ (with n being the refractive index of the material, c being the speed of light. β is the polarisability of the material, which relates the microscopic polarisation vector to the crystal to the incident electric field. We find the properties of the exciton in the expression of β, which is given by:

$$\beta = \frac{e^2}{m_0\omega_0^2}\frac{f}{V} \tag{2.4}$$

The first fraction contains constants related to the material (ω_0, the mass of the electron m_0, the elementary charge e), whereas the second fraction is the *oscillator strength* f per unit volume of the crystal lattice V. The oscillator strength of a given transition is a dimensionless quantity which characterises the likelihood of such a transition to happen amongst all possible transitions. In the semi-classical approach, it is calculated using "Fermi's Golden Rule", and it shows the quantum character of the excitation. As it scales with the crystal volume, the physically relevant quantity is the oscillator strength per unit volume.

In the equation 2.2, the vectors $\mathbf{E}$ and $\mathbf{P}$ can be expressed by monochromatic

waves, for example, the electric field $\mathbf{E}$ is written as:

$$\mathbf{E} = \mathbf{E_0} \exp\{i(\omega t - \mathbf{kr})\} \tag{2.5}$$

With a similar expression for $\mathbf{P}$. $\mathbf{E}$ and $\mathbf{P}$ are related to one another according to Maxwell's equations in matter [39]. To solve the equation, we must find out what the relationship between ω and k in the $\mathbf{E}$ field (and consequently, in the $\mathbf{P}$ field) must be for equation 2.2 to be true. Physically, this means that the constitutive equation, arising from the interaction between light and matter, only allows waves with a certain energy and wavevector to propagate in the crystal.

This dependency between ω and k is called a dispersion relation. There are two kinds of dispersion relations corresponding to two different modes of propagation inside the crystal. The first are called *transverse modes*, in which the electric field and the polarisation field are perpendicular to the direction of propagation inside the crystal. For transverse modes, the form of a dispersion relation reads as follows:

$$\varepsilon(\omega, \mathbf{k}) = \frac{c^2 k^2}{\omega^2} \tag{2.6}$$

In this equation, $\varepsilon(\omega, \mathbf{k})$ is the dielectric constant of the material. This quantity is a property of the crystal. It relates the fields $\mathbf{E}$ and $\mathbf{P}$ to one another by the well-known equation:

$$\varepsilon(\omega, \mathbf{k})\mathbf{E} = \varepsilon_0 \mathbf{E} + \mathbf{P} \tag{2.7}$$

... in which ε_0 stands for the vacuum permittivity. The final ingredient needed to solve the equation 2.2 is a model for $\varepsilon(\omega, \mathbf{k})$. In the case of a semi-conductor crystal, $\varepsilon(\omega, \mathbf{k})$ can be derived from different energy band models [42]. In our case, the appropriate model is:

$$\varepsilon(\omega, \mathbf{k}) = \varepsilon_\infty + \frac{1}{\varepsilon_0} \frac{\beta \omega_0^2}{\omega_k^2 - \omega^2} \tag{2.8}$$

where ε_∞ is the frequency-independent contribution (arising from all the other electronic resonances in the crystal). The fraction contains the exciton frequency ω_k, which is related to its binding energy. In the effective mass approximation, it is given by:

$$\hbar\omega_k = \hbar\omega_0 + \frac{\hbar^2 k^2}{2M} \tag{2.9}$$

To summarise, we shine on the crystal an electric field $\mathbf{E}$. This induces a polarisation density $\mathbf{P}$. The electric field and the polarisation density are related by the constitutive equation 2.2. For this equation to be verified, there must be a dispersion relation relating the frequency and the wavevector of the fields. In the case of transverse modes, this relation is given by equation 2.6. The last

thing to do to solve the equation is now to put the expression of $\varepsilon(\omega, \mathbf{k})$ given by 2.8 into 2.6. In the end, this gives a relationship between the frequency ω and the wavevector k for the polarisation density vector $\mathbf{P}$ and the electric field $\mathbf{E}$. With this knowledge, we will be able to model how the light propagates within the semi-conductor crystal after it interacts with the excitons.

We find that, for a given wave vector k, the transverse modes admit two solutions: one for higher frequencies (the upper polariton branch, UP), and one for lower frequencies (the lower polariton branch, LP). They are given by the equation:

$$\omega_{1,2}(k) = \frac{\omega_{exciton}(k) + \omega_{photon}(k)}{2} \pm \sqrt{\left(\frac{\omega_{exciton}(k) - \omega_{photon}(k)}{2}\right)^2 + \Omega^2} \tag{2.10}$$

In which $\omega_{photon}(k)$ represents the energy of the photonic mode for a wavevector k, $\omega_{exciton}(k)$ is the same thing for the exciton, and $\omega_{1,2}$ are the two polariton branches resulting from the strong coupling regime. Ω is the so-called "Rabi splitting" between the UP and LP branches where $\omega_{photon}(k)$ and $\omega_{exciton}(k)$ cross. $\omega_{1,2}(k)$ for a bulk semiconductor are plotted in figure 2.2. The study of the transverse dispersion relations in the bulk material reveals some general properties of polaritons. At low k, the LP branch approaches a photonic dispersion with $\omega \sim ck/n$, whereas the UP branch almost becomes degenerate with the exciton, as seen in figure 2.2. At high k, the reverse happens, with the UP branch becoming photonic and the LP branch approaching the transverse exciton mode.

The two branches show anticrossing at the resonance point (ω_0, k_0), where they show behavior that is the furthest away from a photon or an exciton. The splitting in frequency between these two branches is called the Rabi splitting. k_0 It characterises the strength of the polariton coupling, and it is given by:

$$\Omega = \sqrt{\frac{e^2}{4\varepsilon_0 \varepsilon_\infty} \frac{f}{V}} \tag{2.11}$$

The other kind of dispersion relation corresponds to longitudinal modes. In this case, the polarisation "response" to the electric field is not perpendicular to the direct of propagation, but parallel. For these modes, equation 2.8 must be made equal to zero:

$$\varepsilon(\omega, \mathbf{k}) = 0 \tag{2.12}$$

This gives a different relationship between k and ω. "Longitudinal polaritons" in bulk crystals are more difficult to study than transverse polaritons, as they do not result from a direct coupling between light and matter [43]. For the

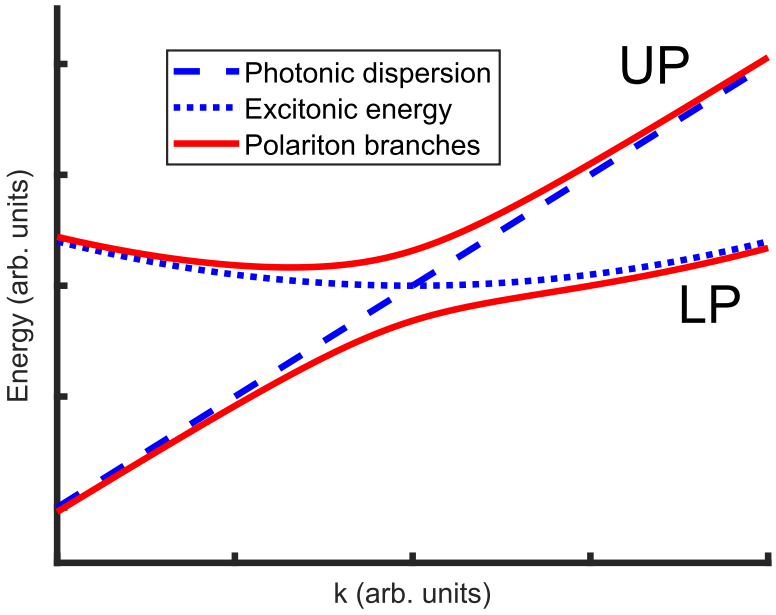

Figure 2.2: Sketch of polariton anticrossing. The regular photonic dispersion is plotted. The "excitonic energy" represents the excitonic dispersion, which are the allowed energy states for an exciton of a wavevector k, which would not couple to light to form a polariton. Due to the free motion of the exciton, the higher momentum states have a higher energy. Due to light-matter coupling, we also have LP and UP branches. Arbitrary units.

rest of this thesis, we will only consider "transverse polaritons" as the study of longitudinal polaritons modes is outside the scope of this thesis.

In a bulk crystal, the transverse exciton direction shows a slight tilt upwards at large wavevectors due to the motion of the exciton itself. A similar tilt is observed in the LP branch, but at a slightly lower frequency. The difference in frequency between the LP branch and the excitonic dispersion varies with k, and by changing the angle of incidence on a bulk semiconductor crystal we can measure this difference. In a 1970 paper [4], experimentalists' were able to model this change of frequency with the angle of incidence with Hopfield's polariton theory, showing that exciton-polaritons were a real physical phenomenon and not a simple mathematical construction.

The anticrossing, and the existence of two branches for a given polarisation, are the most striking features of exciton-polaritons. This "anomalous dispersion" was referenced by Pekar as an 'additional wave': an experimentalist would detect two distinct dispersions in the crystals, an exciton-like wave for the LP branch, and a photon-like wave for the UP branch, as opposed to a single line in a dielectric material. Detection of this additional wave in thin II-IV crystals such as CdSe was used as experimental confirmation of Pekar and Hopfield's theory of exciton-polaritons [44]. However, this effect is much more difficult to observe in thicker or bulk materials.

Thus we have described how exciton-polaritons arise as a result of the coupling between the excitonic field and the electromagnetic wave. The question of characterising the "strength" of such coupling is more complicated. In bulk materials, polaritonic effects are difficult to observe directly. The experimental methods to observe such effects are listed in reference [45], with the main techniques being measurements in reflection [46], by spectroscopy techniques such as Raman scattering [3], Brillouin Scattering [47] or by luminescence when the polariton escapes of the crystal [48, 4], but none of these techniques are able to make an easy one-to-one connection with the detected signal and the exciton-polariton inside the crystal. Only by using thin samples were scientists able to do such a mapping.

A bulk polariton is, essentially, a contribution to the dielectric constant of the semiconductor. In a bulk material, it is always present, but for this contribution to be observable, the coupling needs to remain coherent without a scattering of the polariton by other excitations, including by other polaritons [49] or phonons [50]. Much of the dynamics of the quasi-particle is therefore "lost", inaccessible experimentally and spread out over the bulk of the material. Additionally, it may be difficult to relate the emitted photons to the polaritons in the material. To access the exciton-polaritons directly, it is therefore necessary to confine them in a specifically engineered structure, which is a microcavity. We will now describe such structures.

2.3 Exciton-polaritons in microcavities

2.3.1 Microcavities overview

A cavity is a device designed to confine light of a particular wavelength within a media. The exposition in this section draws from [41]. Optical cavities have also been called "optical resonators", for they are to electromagnetic waves what sound boxes are to acoustic waves.

The dimensions of the cavity restrict what wavelengths are confined, with only wavelengths which are an integer fraction of the cavity length subsiding in the cavity. In the case of optical waves, the cavity dimensions are in the order of a few µm, and such systems are called microcavities. Optimal microcavities have dimensions of exactly half the wavelength of the light they confine, allowing a single mode of light with a very narrow bandwidth.

There are two main ways to confine the light in a microcavity. The first method is to use mirrors, which can be made of high-reflectivity materials, or of stacked pairs of materials with a refractive index difference, forming a Bragg Reflector. An alternative method is to rely on the geometry of the system, using the principles of total internal reflection (TIR).

The particular wavelength of light confined in the cavity, and its associated frequency ω_c and wavevector k_0 forms a cavity "mode". Physically, plane waves with a singular, perfectly defined frequency do not exist, and in a similar way, the linewidth $\delta\omega_c$ of the cavity mode is finite. A cavity is characterised by its reflection spectra: the perfect cavity has a flat reflection of 100 % at all wavelengths expect sharp dips at the cavity modes.

The ratio

$$Q = \frac{\omega_c}{\delta\omega_c} \tag{2.13}$$

... is called the *quality factor* of the cavity. It is related to the lifetime of the photon within the cavity, with a high quality factor resulting in a longer confinement. The cavity may have several modes, and the mode separation is written $\Delta\omega_c$. The ratio

$$F = \frac{\Delta\omega_c}{\delta\omega_c} \tag{2.14}$$

... is called the finesse of the cavity. The finesse describes how well the modes are separated in the reflection spectra. High finesse means sharp and well-defined modes. Physically, it represents the average number of round-trip a *resonant* photon does before leaking out of the cavity. In the context of this thesis, the

media inside microcavities shall be an absorbing or emitting semiconductor. The regime we are interested in is thus one in which the confined light interacts with a thin layer, on the order of magnitude of the wavelength of light, of semiconductor. While the quality factor can be improved by making the cavity larger, high finesse microcavities requires small microcavities with a very high mirror reflectivity.

There is a large panel of different geometries, materials and system to confine light, which opens up for a variety of experiments [51]. This section provides a brief overview of the different realisation of such systems, with an emphasis on two types of microcavities which will be important for the following chapters of this thesis: planar microcavities, and ring resonators.

Planar microcavities

The simplest microcavity geometry consists of two plane mirrors separated by a distance L which is on the order of magnitude of the wavelength of light. The light is thus confined in the direction that is perpendicular to the mirrors. The condition of constructive interference in the cavity means the wave vector is quantified as follows:

$$k_\perp * 2L = 2m\pi \tag{2.15}$$

With m being an integer, and $k_\perp$ is the component of the wavevector that is perpendicular to the cavity. The modes supported by such wave vectors are called Fabry–Pérot modes. which give their name to planar microcavities. The wavevector component $k_\perp$ is quantified, but the other components of the vector (put in a two-dimensional vector $k_\parallel$) are not. Thus there is free in-plane motion of the lightwave.

The free component of the wavevector $k_\parallel$ is related to the angle of illumination θ by the equation:

$$k_\parallel = k_0 \sin\theta \tag{2.16}$$

The dispersion relation as a function of $k_\parallel$ for the mode j of the cavity, for small angles, is given by :

$$\omega(k_\parallel) = \frac{c\pi j}{n_c L} + \frac{c k_\parallel^2 L}{2 n_c \pi j} \tag{2.17}$$

With the n_c being the optical index of the cavity.
Thus the dispersion relation for the photon is parabolic and has a minimum ω_c at $k = k_0$. This is sharp contrast to the linear dispersion relation of a photon in a bulk material, given by $\omega = c * k$. As we shall see, this changes fundamentally

the dispersion relation of exciton-polaritons in a microcavity. We note that according to equation 2.17, if the cavity is designed so that its length L varies smoothly across the plane, then ω_c also varies smoothly. This can be realised by varying the thickness of the cavity media during fabrication. A wedge in the cavity also results in additional losses compared to flat mirrors, but in practice the ability to tune ω_c is highly sought after in experimental realisations.

The plane mirrors which make up the microcavity can be divided in two broad categories. The first one uses metallic mirrors, such as Gold, Aluminium or Silver. The second category uses mirrors made of several alternating pairs of materials with varying reflective indices and thickness, called Distributed Bragg Reflectors.

Metal microcavities are relatively easy to fabricate [52], as one can simply use sputtering machines or evaporators to deposit a metallic surface on the sides of the absorbing media [53]. The quality factor of such cavities is usually on the order of $Q \sim 1000$ as for example in [22]. This is lower than the quality factors which can be achieved with DBRs, with very good field confinement inside the mirrors, as can be seen in figure 2.3. The finesse of microcavities is also an important parameter for efficient mode coupling. In the case of metal mirrors, it is limited by the finite reflectivity.

The basic theory of Bragg mirrors stems from the well-known condition for constructive interference, which was first derived for X-ray difraction in crystal lattices [54]. In the case of visible light, the characteristic lengths are bigger and we can also play with the contrast of optical indices. For layers of optical indices n_a, n_b and of thickness a, b, the constructive interference condition for a wavelength $\overline{\lambda}$ is as follows:

$$n_a a = n_b b = \overline{\lambda} \tag{2.18}$$

The exact theory uses transfer matrices [55] to calculate the effect of the periodic structure on the light wave. It allows for very accurate simulations of the reflectivity spectras of DBR structures [56]. We shall only give the basic equations and final results of such a theory here.

In the case of multiple layer, we model the action of a layer i on the electromagnetic field by a 2x2 transmission matrix $\mathbf{T}_i$, with one collum for the transverse wave and one for the longitudinal wave. Thus the total impact of a periodic structure on the light is modelled by the total transmission matrix:

$$\mathbf{T} = \prod_i \mathbf{T}_i \tag{2.19}$$

This formalism allows a relatively easy calculation of the optical band structure of DBRs. Indeed, it can be shown that the allowed optical bands (in which optical transmission is maximum and reflection, as well as absorption, is minimal)

are given by the equation:

$$\left|\frac{T_{11}+T_{22}}{2}\right| \leq 1 \tag{2.20}$$

And by contrast, the stop-band, in which the transmission is minimal and the optical reflectivity is maximal is given by:

$$\left|\frac{T_{11}+T_{22}}{2}\right| > 1 \tag{2.21}$$

Thus the reflectivity as a function of wavelength of a DBR structure can easily be calculated, as in figure 2.3b. In the case of a planar microcavity with DBR, the absorbing media acts a defect in the periodic structure, resulting in dips in the reflection spectrum, which form the cavity modes we are interested in. These modes can also be factored in the calculation.

Typically, for a DBR which confines light at a wavelength $\bar{\lambda}$ (with by convention $n_b > n_a$), we call the "effective length" of a DBR the following ratio:

$$L_{\mathrm{DBR}} = \frac{n_a n_b}{2(n_b - n_a)}\bar{\lambda} \tag{2.22}$$

The effective length of the DBR is a good figure of merit of its ability to confine light and intervenes explicitly in the theory of light-matter coupling. It is easy to calculate from the properties of the materials used in the cavity. It is approximately equal to the penetration depth of a light field, with a frequency equal to the cavity resonance, inside the mirror. As a result, it should be as close to zero as possible. We can see that for a Bragg mirror with low optical index contrast, the denominator in 2.22 will be small, and conversely the effective length of the DBR will be high. This shows that a good DBR should have a significant optical index contrast.

DBR microcavities can be precisely engineered with extremely high quality factors, as high as 250 000 [57] in materials commonly used in research on light-matter coupling, such as GaAs [58] but also as complex as GaN [59], [60] or ZnO [61]. An infinite quality factor would mean that once the light is trapped in the cavity, it never leaves, which is not possible. An infinite quality factor, according to equation 2.13, would also imply either an infinitely small $\delta\omega_c$, in other words, a perfectly monochromatic field, which is not possible physically, or an infinite frequency, which is also not possible. In reality, there is a compromise between getting a Q sufficiently high to have good light-matter interaction, while accounting for the challenges of fabrication, and also engineering a cavity which works at the frequencies of interest.

The very high reflectivity of the dielectric mirrors also ensure very high *finesse* 2.14. This ensures that the modes are well-separated in energy and we

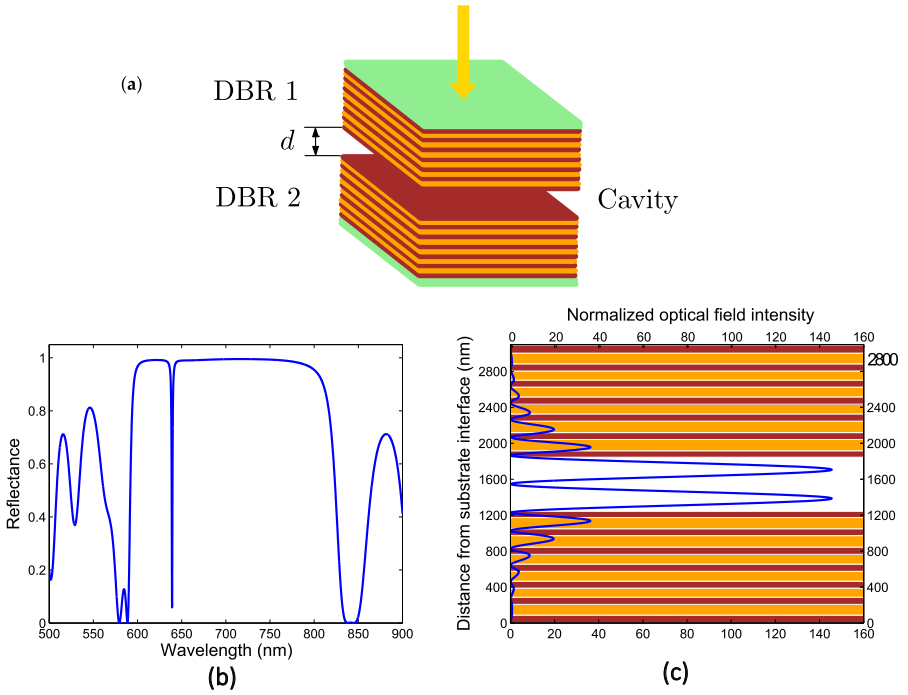

Figure 2.3: (a) A schematic representation of a two DBRs with a cavity of width d between them. (b) Reflectivity spectra of the cavity, with a "stop-band" from 600 nm to 820 nm, and a sharp dip at 640 nm which is the cavity mode. (c) Field structure in the cavity at the resonant frequency. The field is maximum in the cavity and decays inside the mirrors. Taken from [63] CC-BY.

are able to couple to a single mode if necessary. One constraint of using microcavities, as said previously, is that the lattice constant of the DBR materials need to match the cavity media to minimise strain. The increase in quality and the ease of fabrication of such planar microcavities plays a major role in driving applied and fundamental research in all form of light-matter interaction. A recent review on DBR fabrication [62] lists the two main fabrication methods as either chemical vapour deposition or coating of thin films, with each of these methods having its own limits and paths for further improvements. Fabry-Pérot microcavities are among the simplest to realise and work with, and they offer a good basis for experiments with a straightforward geometry. However, some experiments, as well as a number of practical applications, require a different geometry for the best results.

Whispering gallery modes cavities and ring resonators

Whispering Gallery Modes (WGM) were first observed in the St Paul cathedral by Reyleigh in 1910 [64, 65], in which the sound wave propagates without losses along the wall, and forms a standing wave with well-defined nodes and antinodes. The wave can only "survive" if it makes a whole number of bounces along the walls, similarly to the constructive interference condition in 2.15. However in this case, the geometry of the system plays a role. At the interface between the inside of the cavity and the outside of the cavity, the famous Snell-Descartes law $n_{in} \sin\theta_{in} = n_{out} \sin\theta_{out}$ gives a condition for the so-called critical angle of Total Internal Reflection (TIR):

$$\theta_c = \arcsin\left(\frac{n_{in}}{n_{out}}\right) \tag{2.23}$$

By varying the geometry of the interface, the wave can loop back to its starting point after a finite number of TIR bounces, creating a persistent standing wave pattern. In practice, for optical WGM microcavities, the light can be confined in one direction by a Fabry-Pérot planar microcavity, and then a suitable geometry is etched in the cavity so that the in-plane motion of the wave is no longer free, but restricted to particular stationary whispering gallary modes.

WGM microcavities in optics have long been the focus of active research [66], including for their potential as laser sources [67], and as sensors [68].

The basic equation for the wavelength of light λ confined in a WGM microcavity is as follows:

$$m\lambda = Ln_{\text{eff}} \tag{2.24}$$

Where m is the mode number, L is the cavity circumference, and n_{eff} is the effective refractive index of the cavity, which has a similar form to equation 2.15. However, consideration on the TE-TM splitting as well as solving the equations of motions for the electromagnetic wave results in a different picture. In particular, the added degrees of freedom in the geometry of the cavity allows for so-called "dispersion engineering" [69]. Much like DBR microcavities, the properties of such systems can readily be simulated and optimised for different experiments [70] [71].

There are several geometries in which WGMs can be realised. Among these, the most used are spheres [72], microdisks [73], [74], micropillars [75], and most relevant for our experiments, in ring resonators [76], with one example of such geometry being given in figure 2.4.

Microring resonators present a particular interest as they can be coupled to other geometries such as gratings [77], waveguides [78], or even coupled together

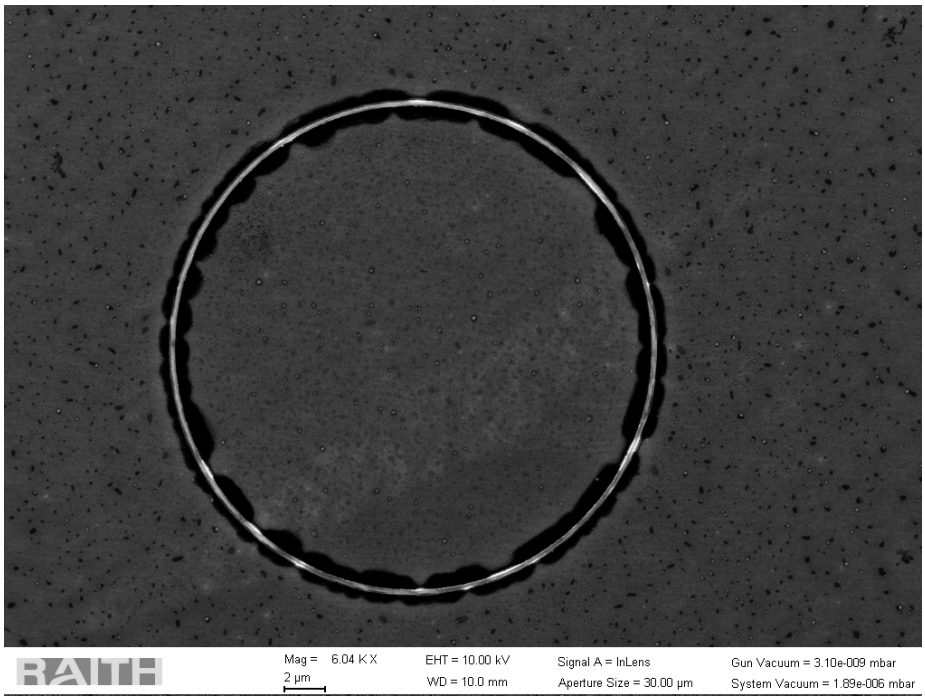

Figure 2.4: SEM Image of a ring resonator with AlGaN quantum wells on a GaN substraste. Courtesy of Tommi Isoniemi

[79] by simply etching a more complicated pattern on the Fabry-Pérot planar microcavity.

A typical microring resonator consists of a planar DBR microcavity, which can be grown by various means such as Molecular Beam Epitaxy. The desired pattern is then written via e-beam lithography or photon lithography [80, 81], before being chemically etched away.

Other cavities geometries

In state of the art photonics, we find sometimes more advanced cavity design. For example, it is possible to very precisely engineer the optical absorption bands of the cavity by creating a *photonic crystal*. While photonic crystals have been proposed as early as 1997 [82], they are still an active field of research as they benefit strongly from progress in realisation techniques [83]. Much like a crystal is a periodic lattice of atoms, a photonic crystal is a periodic lattice of structures with a different dielectric constant. The crystal can be in arbitrary dimensions. In the case of a cavity, the crystal is in two or one dimensions.

The cavity in which the light is confined is a defect in the crystal. A DBR is an example of a basic photonic crystal in one dimension, but more elaborate structures can be engineered.

One such example is the *L3 Cavity*, which consists of an hexagonal pattern with three missing holes in the structure. Such a cavity can be fine tuned by controlling the size of the holes, their spacing, and another parameters. An example of an L3 cavity is shown in figure 2.5.

Microcavities gratings are an example of a one-dimensional photonic crystal, whcih can be used to study topological physics. In this geometry, the cavity is the interface between two gratings with a different periods.

From simple DBRs to more intricate photonic crystals, there is no shortage of design to confine light. The choice of a cavity design is made according to experimental considerations and technical constraints, such as the maximum tolerance for defects, the wanted Q factor, and the physics we want to investigate. In the next section, we shall give an overview of the light-matter coupling physics available in microcavities.

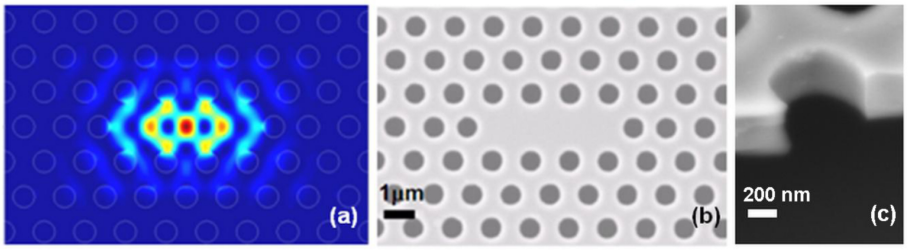

Figure 2.5: (a) Mode structure of the electromagnetic field confined in a L3 Cavity. (b) SEM image of an L3 cavity with the missing holes at the centre. (c) SEM image of the Edge of the L3 microcavity. Taken from [84]

2.3.2 Weak and strong coupling regime

A lot of interesting physics take place when the material embedded in the cavity is an absorbing or emitting semiconductor. All the physics of light-matter interaction that we have described in part I of this chapter, namely, the optical pumping of excitons and the formation of eigenstates of light and matter, exciton-polaritons, also happens within a semiconductor cavity.

In a planar microcavity, the motion of the electrons, holes and excitons in the absorbing semiconductor is typically restricted to the cavity plane by a Quantum Well (QW). A quantum well is an heterostructure in which the difference in bandgap of the semiconductors results in a strong potential energy difference seen by the created exciton, which acts a barrier to its movement [85]. An example of a quantum well is given in figure 2.6 The cavity can also be engineered to create potential walls along waveguides, tubes, rings [21] or other geometries where the motion of the carriers is confined not only in the cavity plane, but also in a particular direction or axis, making a quantum wires. Further restriction on the motion of excitons on both axes of the cavity plane results in a Quantum Dot (QD). Quantum Wells, Quantum Wires and Quantum Dots can also be embedded in non-planar microcavities.

Aside from changing the relation of dispersion of the cavity photons, the confinement of light also changes the exciton-polariton lifetimes. In a bulk conductor, the photon can only be scattered on a defect, or leak out of the material on the surface. By contrast, the lifetime of a photon in the cavity is limited by the number of trips between the cavity mirrors before the light gets absorbed in the mirrors or transmitted. In any real cavity, that number is finite, and the photon will always leak out.

This leads us to rethink the intuitive picture of the exciton-polariton as an particle “hoping” between states of light and matter. What happens if the

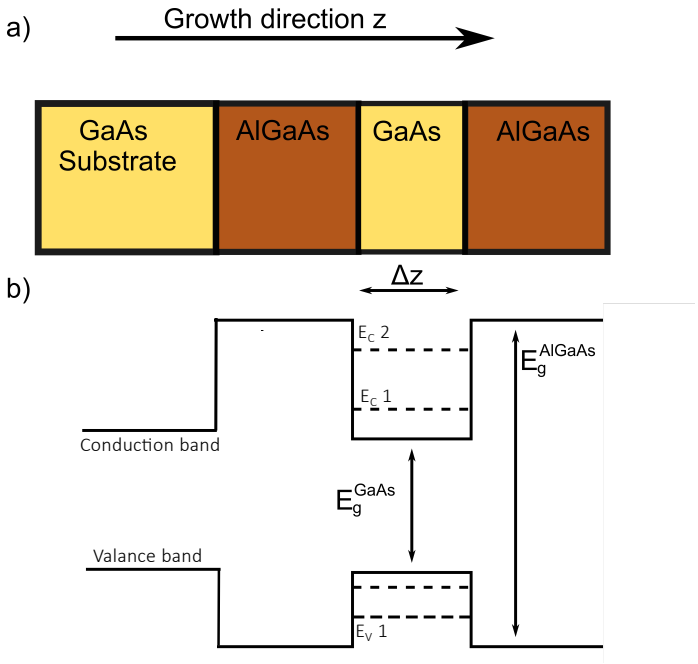

Figure 2.6: An example of an AlGaAa/GaAs heterostructure. a) Quantum Well structure. b) Band structure with the subbands resulting from the QW growth.

photon leaks out of the cavity before such an interaction has occurred? This intuitively distinguishes between two different regimes of light-matter coupling in microcavities: the *weak coupling regime*, in which the lifetime is too short for this "dance" between light and matter to occur, and the *strong coupling regime*, which is the opposite.

In the following sections, we shall briefly outline the theoretical, experimental and practical interest of these two regimes of light-matter coupling, with a strong emphasis on the strong coupling regime, as it is the main object of this thesis.

Weak coupling regime

In the weak coupling regime, the light trapped in the cavity leaks out before it can be reabsorbed. Formally, this means that after the material embedded in the cavity has absorbed the photon, promoting an electron, and then releases it by spontaneous emission, the probability of the emitted photon to leave the cavity is higher than the probability of being re-absorbed [86]. The dynamics of the system are dominated by dissipation [87].

As a result, exciton-polaritons cannot be formed in the weak coupling regime. Nevertheless, it remains a key area for research in light-matter coupling. Indeed, the weak coupling regime was the first example of a scheme to control the spontaneous emission of materials by the means of an external electromagnetic field, with many applications in NMR spectroscopy [88], lasers, and other experimental realisation of Quantum Electrodynamics. It is also a limiting case of the strong coupling regime, which may break down under certain conditions. As such we will briefly describe the basic physics of this system.

The mathematical theory of the weak coupling regime treats the electromagnetic field as a perturbation to the dynamics of the "matter system". This coupling is both irreversible and "inevitable". Let's consider very simple example of a single excited atom in a vacuum. Without coupling to the electromagnetic field, the atom would never relax to the ground state. However, in quantum electrodynamics, the electromagnetic field is always present: even without any quanta of excitation, ie without any photons, the vacuum field interacts with the atomic system, and the resulting perturbation to the dynamics results in spontaneous emission. This is where the "inevitability" of the weak coupling regime comes from. This vacuum field coupling is described by so-called Fermi's golden rule, which gives the probability of emission at frequency ω per unit time Γ_{vac}:

$$\Gamma_{\text{vac}} = 2\pi\Omega_{\text{vac}}^2 \frac{\rho(\omega)}{3} \tag{2.25}$$

Where Ω_{vac}^2 is the vacuum field coupling, and $\rho(\omega)$ is the density of available

modes to relax to. This coupling is also irreversible, as the probability of the spontaneously emitted photon being reabsorbed by the atom is very low. The probability of finding the atom in the excited state as a function of time shows exponential decay.

In a microcavity, the atom is replaced by the absorbing media, and the nature of the coupling can be enhanced or suppressed depending on the dimension of the cavity: if the cavity dimensions are resonant with the wavelength of the transition, the density of available modes increases, and the emission is enhanced, whereas if the cavity length is below the wavelength, it is suppressed.

In this aspect of the weak coupling regime, the electromagnetic field also brings the system into an excited state, and then the cavity enhances spontaneous emission to a selected mode via vacuum field coupling. This enhancement is called the *Purcell effect*, and its figure of merit is the *Purcell factor*, which gives the maximum possible enhancement for an ideal emitter coupled in an ideal way to the cavity:

$$F_{\mathrm{P}} = \frac{3Q(\lambda_c/n)^3}{4\pi^2 V_{\mathrm{eff}}} \tag{2.26}$$

With Q being the quality factor of the cavity, λ_c being the wavelength, n being the refractive index and V_{eff} the effective volume of confinement.

Beyond the regime of spontaneous emission, microcavities can also reach the lasing regime, emitting coherent, monochromatic light. The first example of a laser dates from 1960, using Ruby as an active material [89]. Lasers have since then become an ubiquitous part of daily life, in industry, research, and consumer goods.

The basic physics of a laser can be approximated in a three-levels system, with a ground state 0 of population n_0, a lower energy state 1 of population n_1, and conversely a higher energy state 2 of population n_2. These energy levels 1 and 2 may relax to the ground state with lifetimes τ_1 and τ_2. The lifetime of spontaneous emission for the transition from the state 2 to 1 is written τ_{21}. In addition, the system can undergo stimulated emission from level 2 to level 1, and the associated stimulated absorption (from level 1 to level 2), which are proportional to the radiation field W. Finally, the system is considered pumped out of equilibrium with pump rates R_i for each energy level. The rate equations for this laser read:

$$\frac{\mathrm{d}n_2}{\mathrm{d}t} = R_2 - \frac{n_2}{\tau_2} - n_2 W + n_1 W \tag{2.27}$$

$$\frac{\mathrm{d}n_1}{\mathrm{d}t} = -R_1 - \frac{n_1}{\tau_1} + \frac{n_2}{\tau_{21}} + n_2 W - n_1 W \tag{2.28}$$

The lasing regime appears when the stimulated emission rates $n_i W$ overtake the spontaneous emission rates related to τ_i. This can be achieved by increasing the

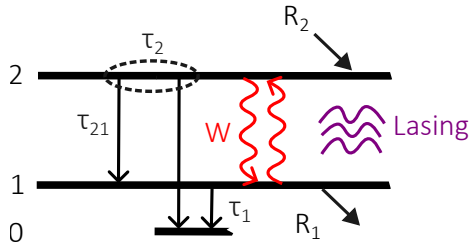

Figure 2.7: Three-levels system which can be used to approximate a laser. The system is lasing when the stimulated emission from the radiation field W overtakes the spontaneous emission given by times τ_i.

"radiation field" W. A schematic for such a three-level system is given in figure 2.7 The basic ingredients for a laser are therefore as follows: a gain medium, a way to drive the gain medium out of equilibrium, and a way to confine the radiation field to avoid losses before the lasing threshold.

Microcavities thus present an ideal environment to realise lasers. In typical applications, the gain medium is not driven out of equilibrium by optical pumping, but by an electrical current at a heterojunction between a p-doped semiconductor and an n-doped semiconductor. With the progress in the growth of microcavities, in particular with the reflectivity of the mirrors, the confinement of the radiation field increased and the current threshold needed to drive the system out of equilibrium decreased tremendously over the years. A smaller microcavity results in better radiation field confinement, but also in lower gain per round-trip between the cavity mirrors, which must be compensated by very high reflectivity and low absorption. The more mature form of weak-coupling cavity lasers are called Vertical-Cavity surface-emitting lasers (VCSELs), with a very narrow angle of emission perpendicular to the cavity, low threshold currents which can operate up to very high temperatures [90]. VCSELs are a very mature and advanced technology, with optically pumped VCSELs reaching the UV range [91, 92]. A schematic of an electrically pumped VCSEL is given in figure 2.8.

Although the radiation field plays a very important role in microcavity lasers, it still only acts as an intermediate between the population levels n_i. The photons in a weak coupling microcavity are never considered beyond the mechanisms of absorption, spontanous emission, or stimulated emission. In particular, there is no consideration of the coupling between an individual photon and an individual excitation of the semiconductor. Their dynamics are coupled, but considered individually.

Beyond the weak coupling regime, in which the light-matter interaction is treated only as a perturbation, we find the strong coupling regime, in which

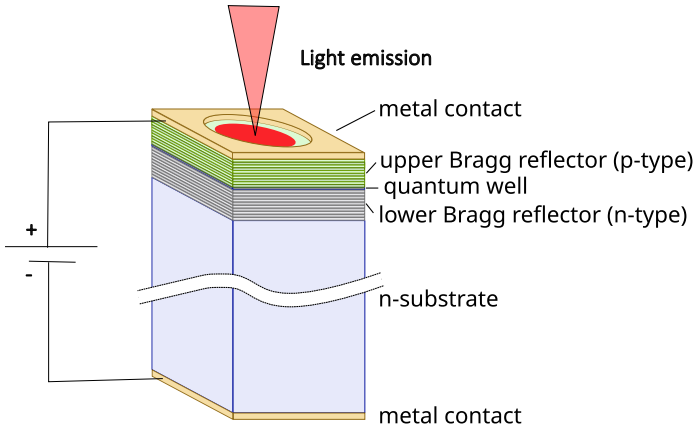

Figure 2.8: Schematic of VCSEL with electrical contact. From Wikimedia

exciton-polaritons appear again.

Strong coupling regime

Unlike in a bulk semiconductor, in which the lifetime of the photon in the microcavity can be considered infinite and the relevance of exciton-polariton is limited by coherence or by the difficulty of detecting them, there is a qualitative difference in microcavities between a perturbative weak coupling regime, which we have described in the previous section, and the strong coupling regime in which the dynamics between light and the excitations of the material predominate over dissipation out of the cavity. This coupling, with absorption and re-emission, is also *reversible* in time, without exponential decay. This means that the discussion in section 2.2.2 can be used to describe light-matter interaction, and the intuitive picture of an exciton-polariton "hoping" between photonic and excitonic state is valid again.

However, there are some changes which must be made to equation 2.10 to account for a microcavity. We account for the exciton dissipation γ and the photon dissipation γ_c. In a Fabry-Pérot microcavity, the photonic dispersion, written $\omega_c(k_\parallel)$ ('c' for cavity) is no longer linear, but parabolic with a well-defined minimal frequency $\omega_c(\mathbf{k_0})$, which corresponds to the cavity frequency at zero incidence. In terms of $k_\parallel$, the minimal frequency is found at $\omega_c(k_\parallel = 0)$. The exciton frequency $\omega_{exciton}(k_\parallel)$ remains parabolic, but since its effective mass is usually much larger than that of the confined photon, it is often approximated as a constant ω_0.

In a good microcavity, the problem reduces itself to finding the eigenvalues of two coupled oscillators with frequency ω_0 and ω_c with coupling strength V. Solving for the eigenfrequencies, we find an anticrossing, similar to the bulk case:

$$\omega_{1,2}(k_\parallel) = \frac{\omega_0 + \omega_c(k_\parallel)}{2} + \frac{i}{2}(\gamma + \gamma_c) \quad (2.29)$$

$$\pm\sqrt{\left(\frac{\omega_0(k_\parallel) - \omega_c(k_\parallel)}{2}\right)^2 + V^2 - \left(\frac{\gamma + \gamma_c}{2}\right)^2 + \frac{i}{2}[\omega_0 - \omega_c(k_\parallel)](\gamma_c - \gamma)} \quad (2.30)$$

In this expression, the imaginary terms are related to lifetimes and dissipation. The difference lies in the form of the cavity photon ω_c. Rather than being linear with respect to the wavevector k, it takes a parabolic form with a well defined minimum for $k = k_0$, which corresponds to incidence normal to the cavity.

Examination of the real part of the square root in equation 2.30 allows us to devise a criterion for the strong coupling regime. For simplification, we will assume that $\omega_c(\mathbf{k_0}) = \omega_0$, in other words, that the cavity resonant is resonant with the excitonic frequency. Then, at $\mathbf{k_0}$, the real part of the squart root reads $V^2 - (\frac{\gamma+\gamma_c}{2})^2$. If the difference is positive, then the two branches are separated in frequency, and we have two branches. However, if it is negative, then the two branches are never separated in frequency, and there is no anti-crossing. It is no

longer valid to use a strong light-matter coupling description if $V^2 < (\frac{\gamma+\gamma_c}{2})^2$. Rather, we are in the weak coupling regime, which has been described briefly in the previous section.

It is not always the case that $\omega_c(\mathbf{k_0}) = \omega_0$. The difference in frequency $\Delta_k = [\omega_0 - \omega_c(\mathbf{k_0})]$ between the cavity resonant frequency at normal incidence and the exciton energy is called the *detuning* of the cavity. At zero detuning, we found that the strong coupling criterion is given by:

$$V > |\frac{\gamma - \gamma_c}{2}| \tag{2.31}$$

In physical terms, the coupling strength must be greater than the dissipative lifetimes. The separation in energy between the two branches at normal incidence is called the *Vaccum Rabi splitting*, written Ω [93]. For a microcavity with quantum wells to confine the exciton, the Rabi splitting is given by [94]:

$$\Omega \approx 2\sqrt{\frac{2\Gamma_0 c N_{\mathrm{qw}}}{n_c L_{\mathrm{DBR}}}} \tag{2.32}$$

In which N_{qw} is the number of quantum wells in the cavity, n_c is the optical index, and important Γ_0 is the "radiative width of the free exciton", which is proportional to its oscillator strength per unit area [95]. This is an approximate expression which is true in the limits of a few Quantum Wells for a small cavity.

Some microcavity designs, for an example a planar Fabry–Pérot microcavity with a wedge, allow for a continuous variation of the detuning. This has in turn some very practical physical applications. The exciton-polariton is a mix of an exciton and a photon, but the mixing of the 'ingredients' is not always a perfect 50/50. Formally, the excitonic and photonic contents of the exciton-polariton at a given wavevector are given by the Hopefield coefficients [41], written $|\mathcal{C}_X|^2$ for the excitonic content, and $|\mathcal{C}_C^2|$ for the cavity photon. These coefficients are given by the equations:

$$|\mathcal{C}_X(k_\parallel)|^2 = \frac{1}{2}\left(1 + \frac{\Delta_k}{\sqrt{\Delta_k^2 + 4\hbar^2\Omega^2}}\right) \tag{2.33}$$

$$|\mathcal{C}_C(k_\parallel)|^2 = \frac{1}{2}\left(1 + \frac{\Delta_k}{\sqrt{\Delta_k^2 + 4\hbar^2\Omega^2}}\right) \tag{2.34}$$

And of course, we have:

$$|\mathcal{C}_X(k_\parallel)|^2 + |\mathcal{C}_C(k_\parallel)|^2 = 1 \tag{2.35}$$

Intuitively, the closer the polariton dispersion is to the photonic branch (for example), the more photonic it is. The same is true for the excitonic fraction.

Some examples of Hopfield coefficients are plotted in figure 2.9. The figure shows that at high $k_{\parallel}$, the polariton dispersions lean closer to the uncoupled photonic dispersion (for the UP branch), or to the excitonic dispersion (for the LP branch). The hybrid nature of the polariton is stronger at low $k_{\parallel}$, in other words, closer to the cavity resonance. For a cavity with zero detuning, at $k_{\parallel} = 0$, the exciton-polariton is exactly half-photonic, and half-excitonic.

Alternatively, pumping the microcavity at an oblique incidence (in other words, a $k_{\parallel} \neq 0$) results in a different cavity frequency ω_c according to equation 2.17. In contrast, ω_0 is a property of the material and remains constant. As a result, we can change the detuning and the Hopefield coefficients. Controlling the photonic and excitonic content of a polariton is very useful in an experimental setting. Typically, a polariton that is more excitonic will have stronger non-linear properties, and a polariton that is more photonic will have a lighter effective mass.

Although the light in the cavity is strongly confined with very high mirror reflectivity, there is no such thing as perfect confinement, and the polaritons will eventually leak out of the cavity. Unlike in the bulk case, however, this process is fast enough for the polaritons to retain their properties without being scattered. As such, there is a one-to-one correspondence between the light emitted by the cavity in the strong coupling regime and the cavity polaritons themselves, which allows to probe the dispersion relation of the polariton very precisely [96]. In particular, it is possible to explicitly resolve their dispersion and anticrossing with angle-resolved spectroscopy [97].

The ease of experimental access to cavity polaritons, in particular the possibility to tune cavities in-situ according to experimental needs, make them much easier to study than bulk polaritons. The confinement of light also results in very strong non-linear properties, which we will describe in a following section.

Beyond the strong coupling regime

Beyond the strong coupling regime, in which the coupling strength V is larger than decay rates, we find the so-called *ultra-strong coupling regime*, in which V becomes comparable to the natural energies of the uncoupled system [98]. Microcavity polaritons present an promising system to study this extreme regime of coupling [99] however for such systems the rotating wave approximation which we have relied on so far is not appropriate.

Even further, when the coupling strength becomes higher than the natural frequency, we reach the *deep coupling regime* [100]. Those new regimes of light-matter couplings are an active field of research, with recent results able to reach it up to room temperature [101]. For the remainder of this thesis, we shall only

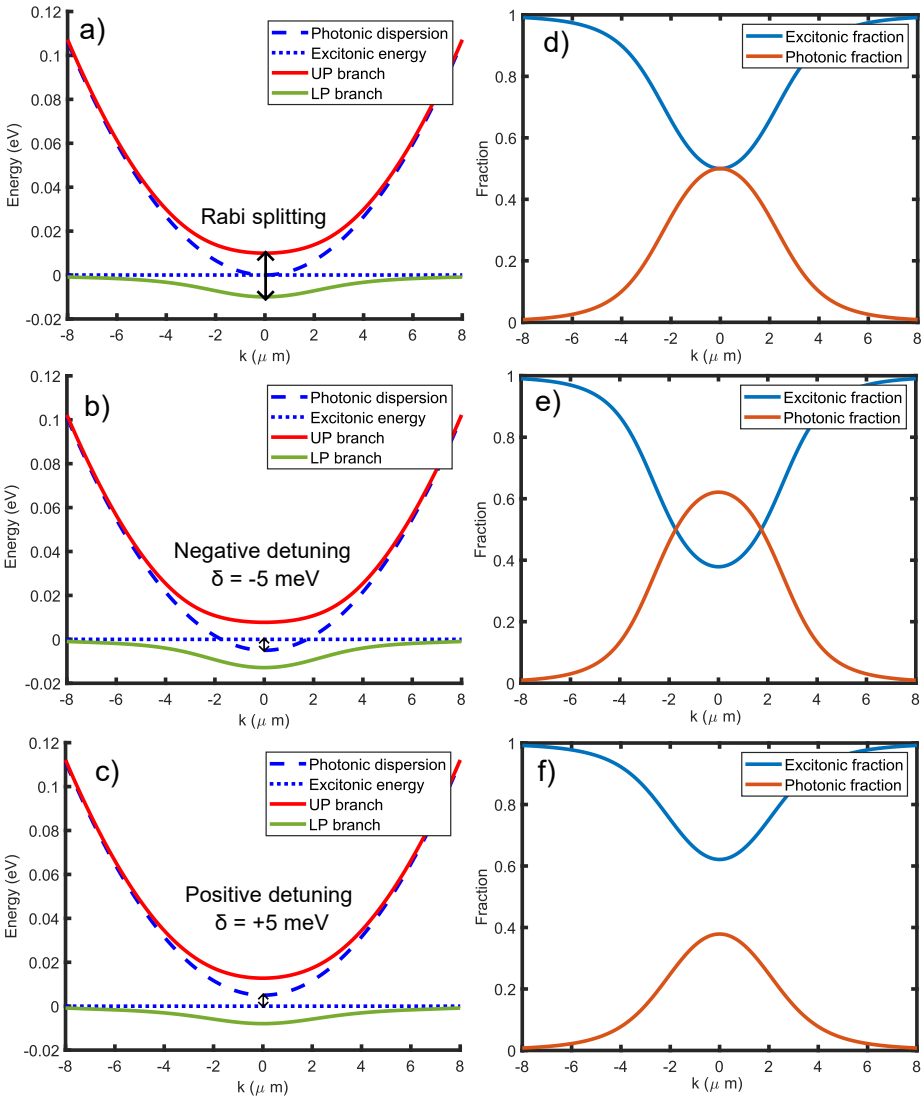

Figure 2.9: Left: polariton branches dispersions at zero (a), negative (b) and positive (c) detuning. The dashed curve represents the purely photonic mode. The dotted curve represents the excitonic energy in the QW. Right: associated Hopfield coefficients as a function of wavevector $k_{\parallel}$.

study cases where V is much lower than the bare frequencies of the system, while still dominating over decay rates.

2.4 Materials for microcavity polaritons

The choice of a material to create the cavity and the absorbing media plays a very important role in the physics of the strong coupling. Some material families bring their own unique challenges in the fabrication process as well as unique opportunities for rich and interesting physics. In this section we will briefly describe three families of materials that have been used in the course of this research: Gallium Nitride-based cavities, Cuprous Oxide cavities, and finally Gallium Arsenide-based cavities. Other materials commonly used in research will be briefly described as well.

2.4.1 **Gallium Nitride** (GaN)

Cavities using GaN as a gain media attract considerable interest due to its large direct bandgap [102]. This bandgap results in a very large exciton binding energy, which allows the exciton to remain bounded even at room temperatures [103]. More generally, the III-N family of materials, including GaN, InN and AlN shows a remarkable flexibility, with AlN having a bandgap in the high UV range with 6 eV, whereas InN is in the infrared range. It is therefore possible to grow QWs with an alloy of $In_xGa_{1-x}N$, and a smooth variation of the alloy parameter x gives a tuning range from infrared to the ultraviolet, which is shown in figure 2.10.

With a large bandgap, the cavities can also be coupled to light with a much higher energy than other materials. In particular, GaN was used to create blue-light emitting diodes [104] and coherent sources of UV light [91] in the weak coupling regime, and have also been used in the strong coupling regime [105].

However, there are considerable challenges to address when working with this family of materials [107]. In particular, its natural crystal structure is hexagonal wurtzite, which is shown in figure 2.11 as opposed to zinc blende crystal structure commonly found in other materials. The symmetry of this structure results in an intrinsic polarisation vector which depends on the lattice parameters. As a result, mismatches in the lattice parameters during the growth process results in strain and defects in the cavity [108], and high-quality cavities must have matching lattice parameters [109]. This limits the options of suitable substrates usable to grow III-N cavities, with the main options being either Sapphire or silicon with a suitable crystal lattice orientation [110].

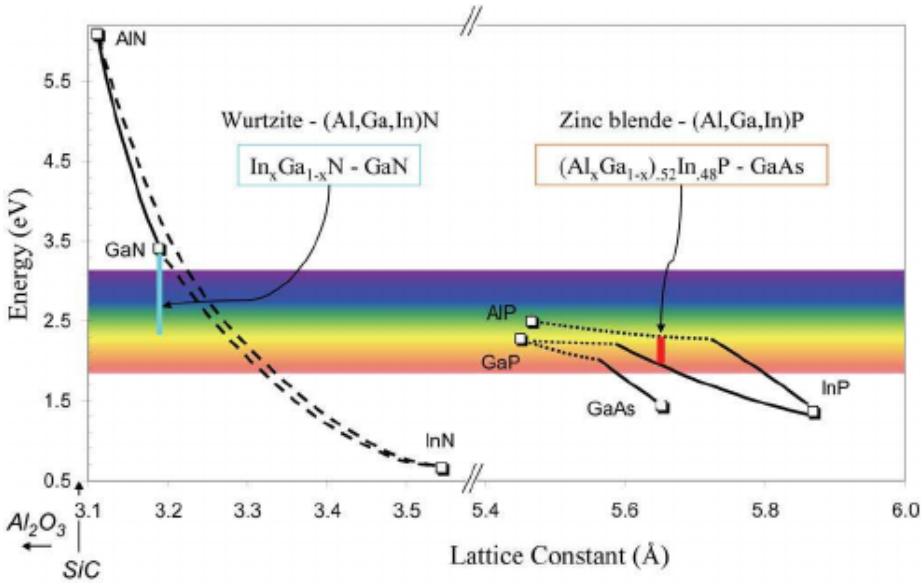

Figure 2.10: Bandgap of III-N semiconducors as a function of lattice constant, with comparison with Zinc Blende structure. Taken from [106]. Copyright © 2007, IEEE (see end of thesis for copyright licence)

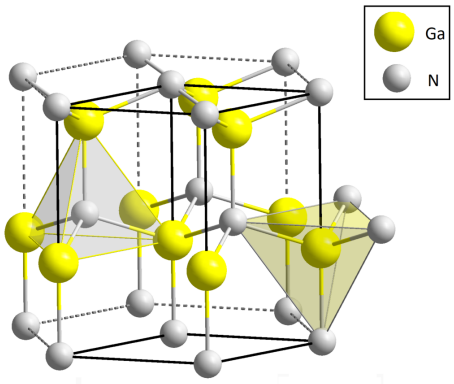

Figure 2.11: Hexagonal wurtzite crystal structure of GaN. Taken from Wikimedia Commons.

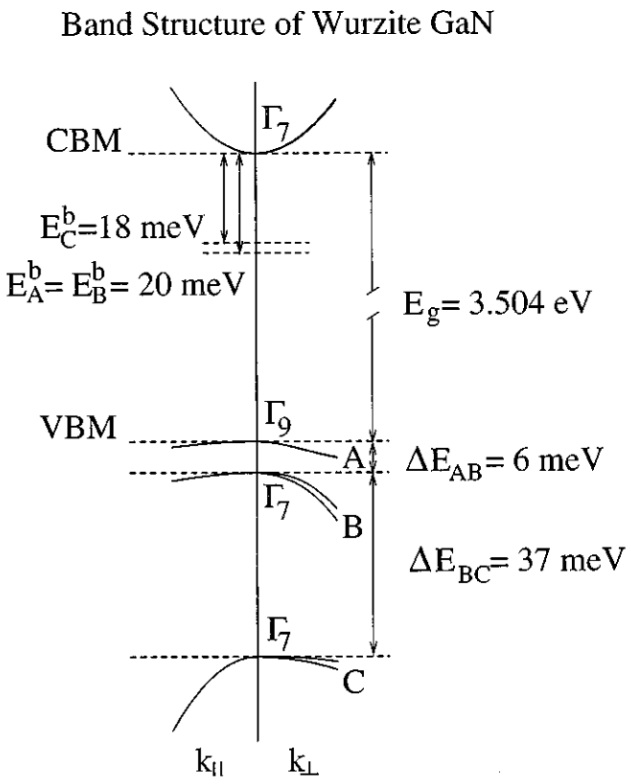

Figure 2.12: Band structure of bulk GaN with A, B, C exciton sub-bands. Taken with licence from [111].

The hexagonal wurtzite structure also results in three subbands for excitons, named the A, B, and C excitons, which are shown in figure 2.12. Excitons from these sub-bands can all couple to light and be visible in PL spectra when investigating light-matter coupling in III − N cavities.

Despite these challenges, GaN based microcavities remain a topic of active and fruitful research in the strong light-matter coupling regime, with so-called "polariton lasing" achieved up to room temperature [112], and at very low threshold [113]. This property make them particularly suited for application as integrated photonic devices [114].

In this thesis, we shall present in chapter 4 an example of polariton lasing in the UV range up to room temperature using a AlGaN ring cavity with a whispering gallery mode geometry.

2.4.2 Cuprous Oxide (Cu_2O)

Cuprous Oxide holds a particular place in the history of condensed matter Physics for being the first material in which excitons were observed [115]. In recent years, there has been renewed research interest in this material as it was reported in a 2014 letter [116] that the excitons with the lowest optical bandgap (the "yellow" series, at 2.1 eV) can be observed with very high principal quantum number n, up to $n = 25$ as shown in figure 2.13.

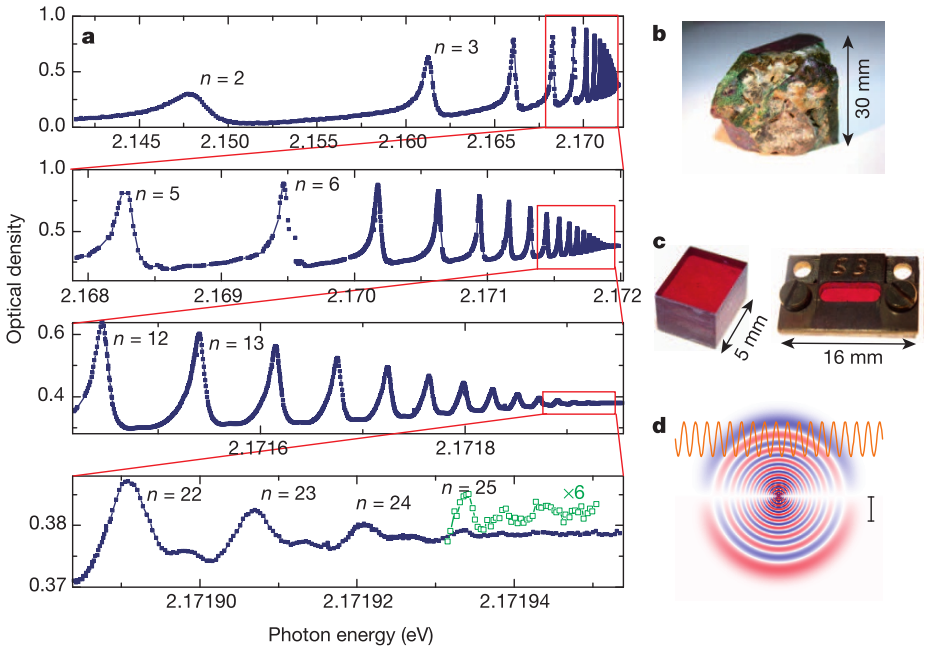

Figure 2.13: a) Spectra in CW single-frequency laser for a simple of thickness 34 µm, cooled down to 1.2 K, showing the full yellow series of excitons. b) Photograph of a natural Cu_2O crystal. c) Experimental setup with the small crystal mounted in a brass holder to minimise strain. d) 2-D slice of the wavefunction of the $n = 25$ exciton. The horizontal bar corresponds to 1000 lattice constants. Taken from [116].

There are other series of excitons in Cu_2O, such as the violet series with a bandgap of 3 eV [117]. However, optically probing such series also results in photoluminescence from the lower energy excitons, which are easier to access experimentally. In particular, the full yellow series is accessible optically, aside from the $n = 1$ state. This comes from the equal parity of the conduction and valence bands in Cu_2O, which forbids excitons with a S-envelope to be observed in one-photon spectroscopy. This includes the $n = 1$ state, which has a 1s

envelope.

As the radius of the exciton scales with n, very large excitons can be observed in Cuprous Oxide. The $n = 25$ exciton has for example a radius of 1.04 µm. This is comparable to the $n = 202$ state of rubibium, which has a radius of 2 µm – which is only one order less than the width of human hair.

The large number of n states accessible allows to study their scaling laws, with interesting behaviour observed at larger n numbers [118, 119], with studies done including the temperature dependency [120].

Rydberg excitons allows physicists to explore phenomena which, in the context of cold atoms physics, would require laser cooling [121]. Rydberg states in cold atom physics have numerous practical and fundamental applications, including in particular for quantum computing [122, 123]. They are also still a topic of active research for their own properties, including for example studies on their coherence time [124].

A challenge unique to Cu_2O is that a particularly high crystal quality is required to observe the higher n states [125]. Artificial growth of Cu_2O crystals is a topic of active research [126, 127], but so far only excitons up to $n = 10$ have been reported in such crystals [128]. Natural Cu_2O crystals are typically harvested in mines, such as the Tsumeb mine in Namibia, Africa, and then cleaved and polished to get thin flakes with lengths of tens of µm. A Cu_2O crystal with smaller thickness would be useful for more scalable applications, single-mode cavities and for example for the study of Rydberg excitons in two-dimensional materials, which has so far only been done in monolayer WSe_2 up to $n = 2$.

One particular phenomenon we expect to see at higher n number is the so-called Rydberg blockade, in which the large spatial extent of the Rydberg state prevents a similar state from being formed in its vicinity [129, 130]. Such a phenomenon has been observed in Rydberg excitons [131], using a thin Cu_2O slap without mirrors. By embedding the Cu_2O in a microcavity, it would be possible to observe Rybderg blockade of the resulting exciton-polaritons [38]. As there is a one-to-one correspondence between the cavity polaritons and the emitted photons, this proposal would create a “blockade of photons”. The mechanism is illustrated in figure 2.14.

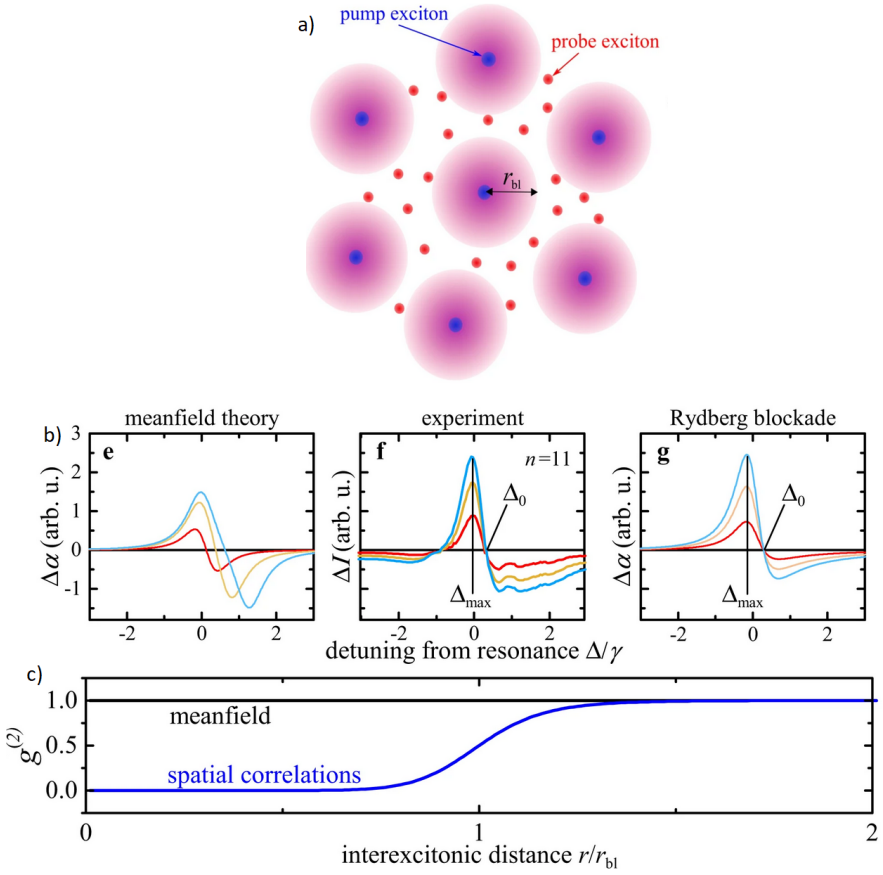

Figure 2.14: a) Illustration of Rydberg blockade: the larger Rydberg excitons block the formation of a higher n exciton in their vicinity. b) Change in absorption $\Delta\alpha$ as a function of energy (normalised to the $n = 11$ excitonic resonance) for different pump powers (red being the lowest power, blue being the highest). Only the Rydberg blockade model explains the features of the experiment, such as a universal maximum at Δ_{max} and minimum at Δ_0. c) The Rydberg blockade model shows spatial correlations as a function of the interexcitonic distance. Taken from [131]

.

Recently, exciton-polaritons in a Cu_2O microcavity were demonstrated [132] up to $n = 6$, paving the way for the realisation of the polariton Rydberg blockade, with these results reproduced in figure 2.15.

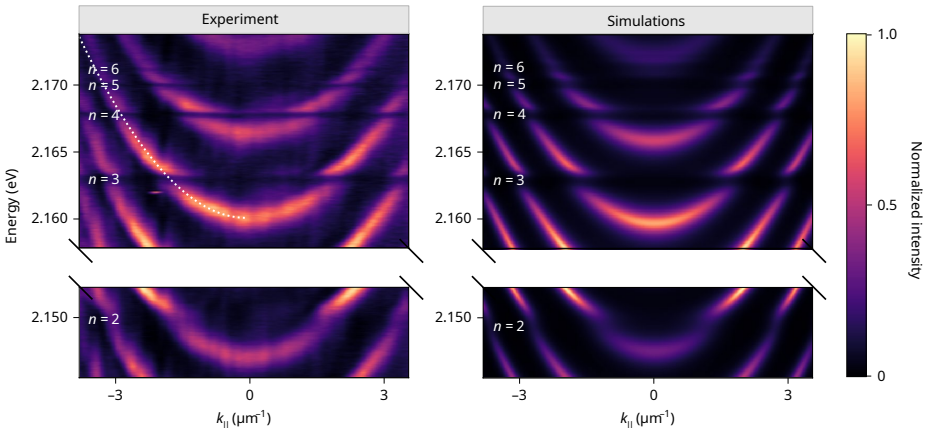

Figure 2.15: k-space imaging of Rydberg exciton-polaritons, in theory and experiments, showing a clear anti-crossing around the excitonic resonances. Taken from [132].

In this thesis, we shall present in chapter 5 our work on Rydberg polaritons in Cu_2O, investigating their non-linear properties and showing scaling laws which are consistent with the Rydberg blockade phenomenon.

2.4.3 **Gallium Arsenide** (GaAs)

Gallium Arsenide (GaAs) is perhaps the most common material used for investigations in the strong coupling regime of light-matter interactions. It was in a GaAs microcavity that the microcavity polaritons were first observed in the seminal paper of reference [7].

GaAs presents a direct bandgap in the near infrared (at 1.426 eV) with a zinc blende crystal structure as shown in figure 2.16.

The Zinc Blende crystal structure provides from an exact, analytical description of semiconductor excitations, with the so-called *Luttinger Hamiltonian* [133]. The valence band is split in light holes and heavy holes with varying effective masses. Below the valence band holes, we find a split-off band (SO) which is seperated in energy. At $k = 0$, in the weak coupling regime, there is a degeneracy in energy between the light holes and heavy holes, with the transition from an heavy holes to an electron being approximately three times higher, and as a consequence it is possible to control the *spin projection* of electrons in GaAs [134].

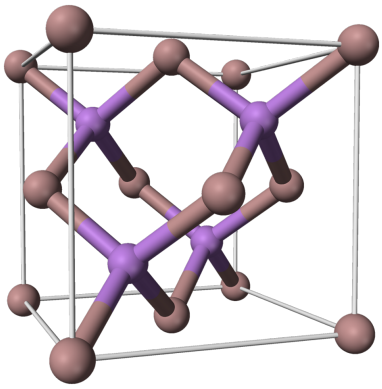

Figure 2.16: GaAs zinc blende crystal structure. From Wikimedia Commons.

Beyond their application for spin and polarisation, GaAs microcavities remain a very safe option for polariton devices, including for superfludity [19], Bose-Einstein condensation [135], and solitons [136], topological physics [137], phase transition in the Bardeen-Cooper-Schrieffer regime [138]. Essentially, if something was done using exciton-polaritons, it was (most likely) done first in a GaAs/AlGaAs cavity – with the notable exception of the first Bose-Einstein condensate being achieved in CdTe [139]. Many of the examples of non-linear polariton physics we shall mention later in this thesis, for examples, were realised using a GaAs system.

This is because the growth and fabrication of GaAs cavities using AlGaAs or InGaAs Bragg Reflectors and Quantum Wells is a well-known and well-studied process [140], and the optical properties of such systems have been reported extensively [141], in part due to the analytical expression of the Hamiltonian of their band structure. When investigating exciton polaritons, GaAs is the default and as such is a useful experimental basis for new experiments or as a baseline for comparison when investigating new materials.

Nevertheless, as with any system or family or materials, there are experimental challenges using GaAs cavities. The main one is that exciton binding energy is very low, on the order of a few meV [142], which requires most experiments to be done at cryogenics temperatures (typically, 10 Kelvins). It is possible to engineer devices so that a GaAs system may work at room temperature [143], but some physics, such as Bose-Einstein condensation, are not accessible. This is not the case for GaN or ZnO systems, where experiments up to room temperature can be performed.

In this thesis, we shall present in chapter 6 an investigation of non-linear properties in a GaAs microcavity, with the goal of studying analogue gravity

effect in polariton fluids of light.

2.5 Non-linear polariton physics

Having described the physics of exciton-polaritons, and having shown some of the experimental realisations in which they are observed, we now turn to some of the most interesting experimental features which arise from exciton-polaritons non-linear properties. This section is by no means an exhaustive list of all the non-linear experiments which can be performed in exciton-polaritons. Rather, it serves as an introduction to the vast realm of Physics accessible with such systems.

In the first subsection, we shall introduce one of most interesting and useful effects arising from polariton non-linearties, which is the blueshift of polariton branches with increasing polariton density. We will then describe one of the first major realisation of non-linearities in the strong coupling regime, which is the stimulated scattering of polaritons. In the last section, we will show how exciton-polaritons are used to realise long-travelling wavepackets, called "solitons".

2.5.1 Polariton blueshift

In an optical experiment involving power dependency, a linear response to power increase simply means that the total collected signal is proportional to the pumping power. Any deviation from this proportional relationship - a non-proportional signal, a change in the emission energy, or phase, or any collective behaviour in the signal - can be called non-linear. The behaviour of photons is derived from Maxwell's equations, which are linear. Photons can only show non-linear behaviour when their interactions are mediated by an another particle. In the case of exciton-polaritons, the interactions are mediated through the matter component of the particle, which is the exciton. As a result, polaritons exhibit polariton-polariton interactions [144], but also interactions with the "exciton reservoir" [145]. These polariton-polariton interactions manifest themselves through a *renormalisation* of the polariton branches, which are shifted to higher energy. The value of the shift corresponds to the interaction strength [146]. Theoretical models sometimes use a "mean field" approach, where the shift in energy is linearly dependant on the density:

$$\Delta E = gn \tag{2.36}$$

... where ΔE is the energy shift, g is a linear slope, and n is the polariton density. This results in a linear shift in energy with increased power, as can be seen in

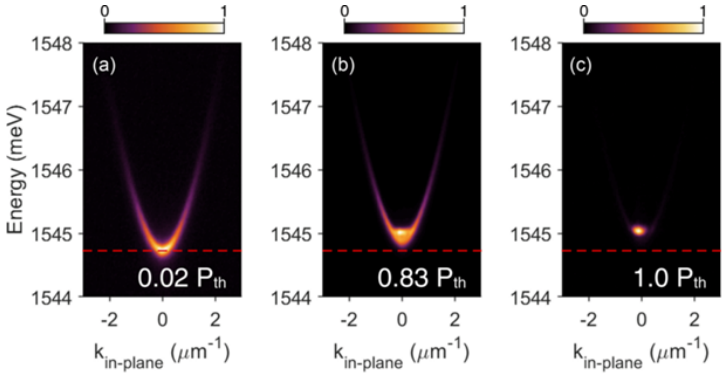

Figure 2.17: Example of a blueshift resulting from increasing pumping power. The exciton-polaritons are pumped non-resonantly, and after a certain power threshold P_{th}, form a condensate. (see section 2.6.4). From [148].

figure 2.17. Models beyond the mean-field approximation can sometimes show surprising results (such as a difference of factor 3 in the interaction strengths [147]), but can be useful to better understand the complex physical phenomena happening inside the cavity.

While this model is useful to understand the basic principle of non-linear blueshift, there are a few challenges when applying it to practical case. The parameter g can be difficult to properly model, but a good approximation is the exciton-exciton interaction strength, given by [146]:

$$g \approx 6E_b a_B^2, \tag{2.37}$$

... where E_b is the exciton binding energy, and a_B is the excitonic Bohr radius. Another difficult challenge in applying 2.36 lies in the estimation of the polariton density n, which can be hard to properly estimate. A common method, as shown for example in the methods section of [149], consists of calculating the total injected number of photons by the pump, and to multiply it by the photonic Hopefield coefficient. However, this approach neglects some effects, such as Auger recombination.

At the microscopic level, blueshift occurs because polaritons, due to repulsive interactions arising from their excitonic fraction, cannot occupy the same physical space in the sample. This, in turn, means they do not occupy the same spot in "phase space", and shift to different energy. As the density is increased, more and more of phase space is filled, resulting in a stronger blueshift. However, unlike electrons (which are Fermionic particles), polartions *can*, under the right experimental parameters, occcupy the same energy state. This in turn results in other non-linear behaviour. We will show one such behaviour in the following section.

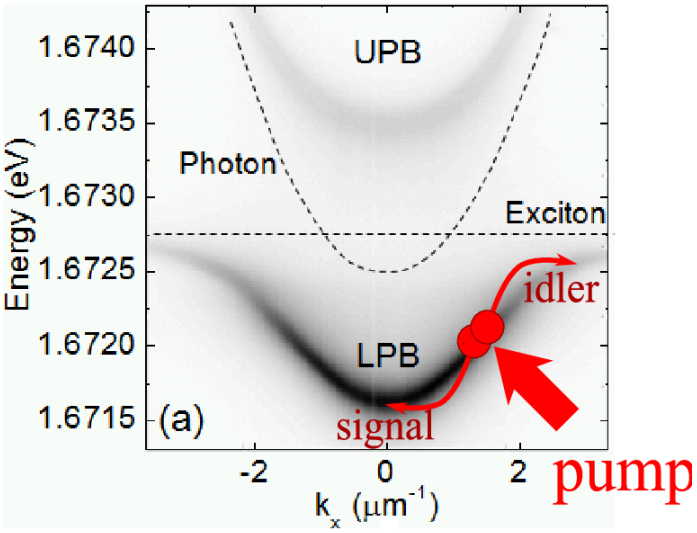

Figure 2.18: OPO process with pumping at the "magic angle", near the bottom of the LPB, in a AlAs cavity with GaAs quantum wells. Taken from [152]

2.5.2 OPO regime: stimulated scattering

The *optical parametric oscillator (*OPO) regime of exciton-polaritons, also called *parametric* or *simulated scattering*, was first discovered in 2000 by Savvidis & al [150] and developed in a later paper [151].

When pumped near-resonantly, at a particular wavevector k_0 (the "pump"), the exciton-polaritons undergo a parametric scattering with preferential occupation of two states, $k = 0$ (signal) and $k = 2 * k_0$ (and idler). The scattering process can be schematically represented by the equation 2.38 and is represented in figure 2.18.

$$(k, k) \rightarrow (0, 2 * k), \text{subject to the conservation of total energy} \tag{2.38}$$

At a so-called "magic angle" [153] of incidence, k, the scattering process is resonantly amplified, and after a certain pumping threshold, the occupation of the final states scales non-linearly with pumping power, with gains over 10 000%. The dynamics of such scattering process can be observed with time-resolved, pulsed pump-probe experiments as in [150], or more recently [154]. Such a process is called *parametric* as it conserves both energy and momentum (it can also be called "elastic").

The polariton OPO regime is a signature of their bosonic nature, as fermions would not be able to show macroscopic occupancy of the same state. As a result of scattering processes between the signal and the idler, these states become macroscopically occupied. The scattering becomes stimulated by the final occupancy number, resulting in very large gains. It is also a feature unique to polaritons [155]: photons would not able to scatter off one another, and while such a feature has been observed in excitons [156], it requires much lower temperatures (down to 50mK) and the strength of scattering is lower.

The very high non-linearity of the OPO regime comes from the excitonic nature of the exciton-polaritons. The signal from $k = 0$ and $2k$ can be separated in angle-resolved spectroscopy. The signal from $k = 0$ also turns out to be *coherent*, with both first and second order correlation functions being equal to one [157]. A discussion on those correlation function is given in section 2.6. Some experiments have demonstrated pulsed coherent control of the OPO signals [155], which is why these modes are sometimes called "OPO condensates", by analogy with Bose-Einstein condensates which will be described in a further section. However, it is important to note that, unlike in a Bose-Einstein Condensate, there are two states with macroscopic occupation of population. Additionally, a Bose-Einstein Condensate requires thermalisation of the macroscopically occupied state. This is not the case for the OP regime.

In CW excitation, a microcavity polariton system presents a smaller alternative to bulkier equivalent systems for lasers, in which the scattering process is different and takes the form of a down-conversion [158], with a given pump frequency 2ω and a small parameter ε showing scattering of the pump photon in two different photons:

$$(2\omega, \varnothing) \rightarrow (\omega + \varepsilon, \omega - \varepsilon) \tag{2.39}$$

The OPO regime of stimulated scattering was a first major realisation for the study of exciton-polaritons. Today, it is still the basis for the analysis of most resonant pumping experiments, and some analysis of the bistability effects when varying pump power are still being performed [159]. It was a major step in investigating the non-linear properties of exciton-polaritons, in particular the ones owning to its bosonic nature.

2.5.3 Solitons

The non-linear properties of polaritons make them particularly suitable to reproduce in an easily controllable manner other physical phenomena, such as

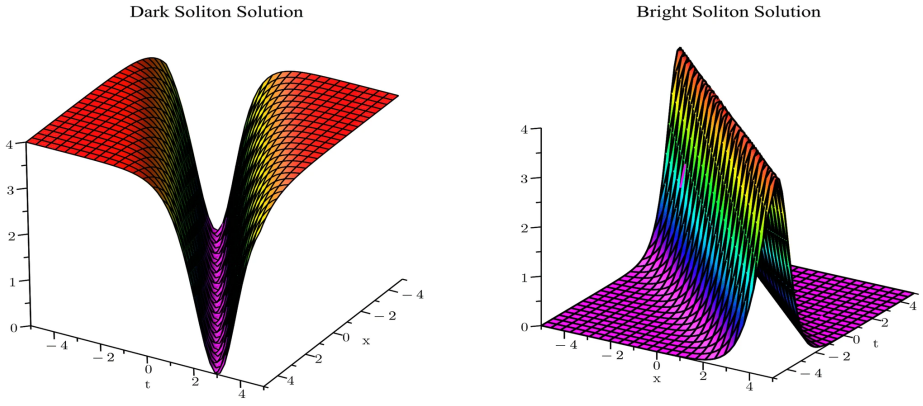

Figure 2.19: Bright (left) and dark (right) soliton in one dimension with time dependency. Taken from [164].

"solitons" or solitary waves. Waves typically spread out in space while travelling, eventually decaying, or when they collide. This is not the case for solitons [160]. Qualitatively speaking, a soliton is a stable, travelling wave, which keeps its form over long distances.

Historically, solitons were first discovered in 1834 when Scottish engineer John Scott Russell observed that, in a still water canal, the waves in the wake of a boat which had suddenly stopped would continue travelling without losing their form for miles on end [161]. The modern approach to solitons mainly deals with non-spreading electromagnetic waves in fiber optics. For electromagnetic waves, the non-spreading nature of the soliton is explained by a competition between the non-linear properties of the wavepacket and the dispersive effects of the media.

Research on fibre optics solitons has been a topic of active interest for decades [162], and is still a topic of research due to its applications in communication technologies [163]. The current research distinguishes between two types of solitons. The first are called *temporal solitons*, which are generated using pulsed lasers. The pulse dispersion enters in competition with the non-linearity of the propagating media. On the other hand, *spatial solitons* are caused by a competition between beam diffraction and the non-linearity of the propagating media.

The soliton can further be called "dark" or "bright". A bright soliton is a regular propagating wave, whereas a dark soliton would be a propagating dip or hole in a continuous background. An example is given in figure 2.19.

The mathematical formalism of solitons lends itself to a wide variety of fields,

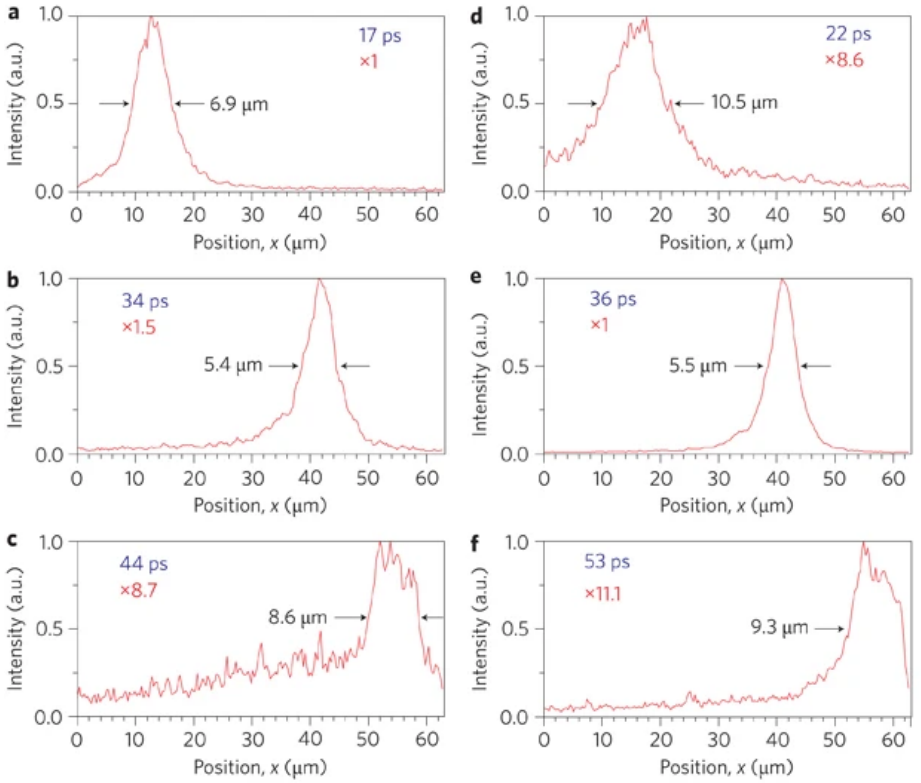

Figure 2.20: Polariton soliton propagation for a beam of diameter of 5 µm (a, b, c) or 15 µm (d, e, f).
The observed lifetimes (tens of picoseconds) are one order of magnitude higher than the polariton lifetime in the GaAs cavity (5 ps). Taken from [24].

including oceanography [165] or more surprisingly, the De Brooglie matter wave of a cold atom Bose-Einstein condensate [166].

As a highly non-linear system, exciton-polaritons are a promising ground for the generation of solitons without the constraints of optical fibres or cold atom physics. Such solitons are very large, up to the µm scale [24] (see fig 2.20) (on the picosecond scale), and with higher non-linearities. The exciton-polaritons also create a soliton faster (on the picosecond scale) than equivalent systems in cold atom physics. Both dark and bright solitons have been realised using cavity polaritons, and in particular exciton-polaritons offer possibilities not accessible to optical fibres experiments [167] [168], including at very low pumping power [136].

The non-linear properties of the polaritons necessary to get a soliton can be

tuned easily by changing the experimental parameters, for example by pumping at an angle to modify the effective mass, including a negative effective mass. However, unlike cold atoms matter waves, the polaritonic solitons are an intrinsically out of equilibrium system, which requires the cavity losses to be compensated with additional pumping. An example of a model for such a system must treat the exciton ψ and the photonic mode amplitude A independently, is given in [136], is as follows:

$$\frac{2i\beta_e}{v_g}\left(v_g\frac{\partial}{\partial z}+\frac{\partial}{\partial t}+\gamma_p\right)A+\frac{\partial^2 A}{\partial x^2}=-k_e^2\psi \tag{2.40}$$

$$-2i\left(\frac{\partial}{\partial t}+\gamma_e\right)\psi=gA-\chi|\psi|^2\psi \tag{2.41}$$

In this coordinate system, the soliton propagates along the direction z, and across the direction x. β_e is a propagation constant for the photonic mode at the exciton resonance, γ_p and γ_e are the losses for the photonic and the excitonic mode, respectively, k_e is the wavevector for the exciton and finally, g is the rate of light-matter coupling and χ is the exciton non-linear parameter. We see, importantly, that the group velocity v_g plays an important role in the equation, showing a competition between a group velocity dispersion and the non-linearities of the system. Such an equation can be approximately resolved if the losses are neglected. It results in dark or bright solitons depending on the signs of the non-linearity and the sign of the effective mass.

The experimental richness of polariton solitons has taken them to very exotic experiments, including in topological physics [169]. A striking result from such research is that a soliton which scatters on a topological defect can be described as a *magnetic monopole* [170], an elusive physical concept which, while not strictly forbidden by the laws of nature [171], has nevertheless not been observed in any of the fundamental particles.

2.6 Coherence and Bose-Einstein condensation

Among all the non-linear properties of exciton-polaritons, some of which we have outlined in the previous section, we shall be particularly interested in this thesis in their statistical and coherence properties. The notion of coherence is very important for modern physics, and in fact we have been alluding to it, for example in the description of light emission in the OPO regime of section 2.5.2. Now comes the time to give a brief overview of the Physics involved for a description of coherence applicable to exciton-polaritons.

A classical thermal light source, such as the Sun, or a light appliance, does not have a perfectly defined wavelength, amplitude or phase, as a monochromatic plane wave would have, but is closer to a statistical average of many

waves, with a finite spread in wavelength, amplitude and phase. We call such an average a wavepacket. The accessible data is therefore a statistical average of the properties of the wavepacket. A statistical treatment for the light is also necessary when taking into account the temperature, as it is itself the result of treating the media in which the light evolves in a statistical manner.

The coherence of a light wave measures how well these statistical properties evolve over time and space. The theory of coherence is, similarly to statistical physics, closely related to information theory. In this analogy, the statistical properties of light, which is called a "signal", are thought of as information. The coherence of the signal measures how this information evolves.

Coherence properties of exciton-polaritons are at the heart of this research work. They underpin the three experimental chapters which constitute the remainder of the thesis.

In this section, we shall first describe how the coherence properties of light can be treated classically, which gives a good overview of the physics involved. As we shall see, the purely classical formalism is not suited to fully describe exciton-polaritons, and a quantum description of coherence shall be needed. We will then describe a particularly important feature of quantum statistics of exciton-polaritons, which is their ability to undergo a Bose-Einstein condensation. We will describe in details the physics involved, with in particular the specifics of exciton-polaritons. Finally, we will give an overview of the rich physics made accessible by polariton condensates. The exposition in this section draws from references [41, 172] and [173].

2.6.1 A classical description of coherence

In practice, the coherence of a light source can be measured by how well it is possible to interfere it at remote locations. If the information of the signal changes too much over time, then interference shall not be possible. The loss of coherence is called decoherence.

The main decoherence mechanism is that the phase and amplitude of the wavepacket change over time. For example, if the wave in the wavepacket follow a Gaussian distribution, the width of that distribution will grow larger over time. The *coherence time* of a wavefront with central wavelength λ and spectral width $\Delta\lambda$ is given by the relation [41]:

$$\tau_c = \frac{\lambda^2}{c\Delta\lambda} \tag{2.42}$$

... from which we can reduce the *coherence length* by the equation $l_c = c\tau_c$. One way to measure the statistical properties of a given signal over time is to look at its Fourier transform, which will give its frequency spread. For example, a perfect monochromatic wavefront would have a single well-defined frequency, but implies an infinite lifetime (see figure 2.21). A more realistic wavefront with a lifetime given by $1/\gamma$, where γ is the linewidth of the source, would have a finite spread in the frequency domain. Typical coherence lengths can vary from a few centimeters for thermal sources, to several kilometers for lasers. Quantum emitters, such as Quantum Dots, are characterised by a very narrow linewidth γ and as such have very long lifetimes and a well-defined amplitude, in contrast to classical light sources.

In the language of information theory, the coherence between two signals is also called a correlation, which measures how much the information carried in one relates to the information carried in the other. In the case of a single light source, we may speak of self- or *autocorrelation*.

If we consider a fully coherent field E, then the information in the signal does not change between two measurements $E(t)$ and $E(t')$. By contrast, if the signal is fully incoherent, then there is no relationship between the two measurements. As a result, the coherence of the signal can be characterised by looking at the product $E(t)E(t')$. To account for the amplitude and any arbitrary property of the signal, it is compared to the product $E(t)^2$.

In a real signal, a single measurement will be subject to uncertainty due to the statistical properties of the field. These statistical properties can be taken into account by averaging over many measurements. Finally, we take the complex conjugate $E^*(t')$ for mathematical properties. We find the coherence

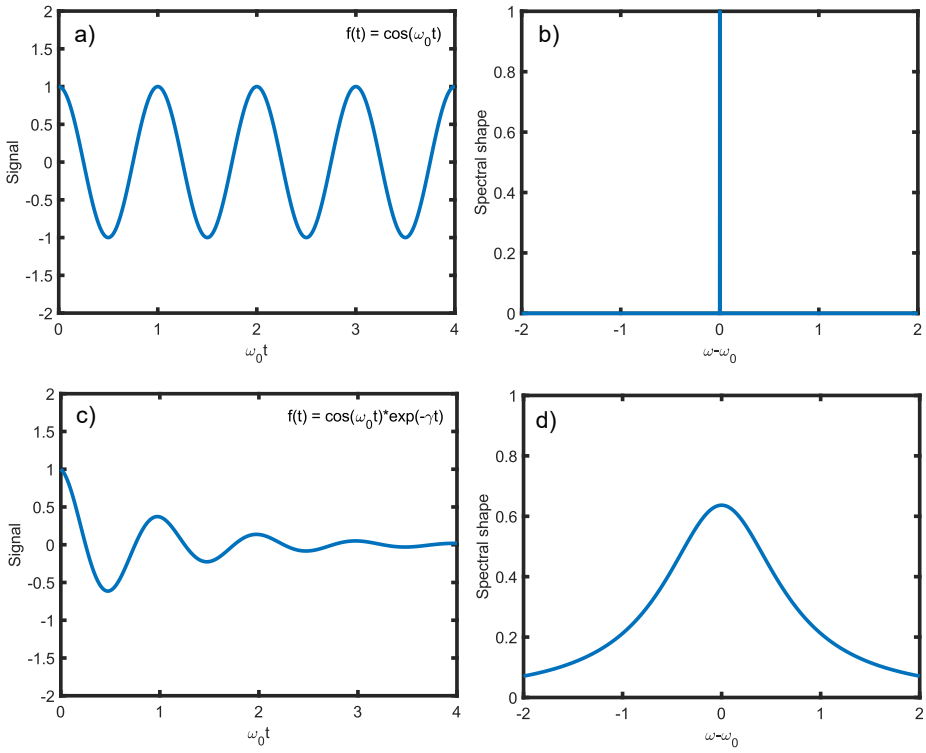

Figure 2.21: Simple plot of the signals (a, b) and spectral shapes (c, d) for a perfect monochromatic source (top), and a source with a finite lifetime γ (bottom) which shows a Lorentzian broadening.

to be:

$$g^{(1)}(\tau, t) = \frac{\langle E^*(t)E(t+\tau)\rangle}{\langle |E(t)^2| \rangle} \tag{2.43}$$

In this expression, we have subtracted the t, t' notation for one explicitly including the delay τ. The superscript (1) comes from the fact that the function $g^{(1)}$ is called the first-order coherence, as opposed to higher orders, which shall be described later. This expression can also be generalised to include spatial coherence by making the field E dependent on the position.

In the case of a steady-state system, only the delay τ is taken into account, and the expression then reads:

$$g^{(1)}(\tau) = \lim_{t\to\infty} \frac{\langle E^*(t)E(t+\tau)\rangle}{\langle |E(t)^2| \rangle} \tag{2.44}$$

$g^{(1)}(\tau)$ is a complex number in general, which is symmetrical with $g^{(1)}(\tau) = g^{(1)}(-\tau)^*$ and $|g^{(1)}|(0) = 1$.

The function $g^{(1)}(\tau)$ can be related to the emission process of the source of light by the Wiener-Khinchin theorem [174]. For a coherent source, like a laser, we would have $|g^{(1)}|(\tau) = 1$ for all τ. By contrast, incoherent sources show exponential decay (for Doppler-broadened light) or a Lorentzian shape (for emitters with a finite lifetime). A plot of such $g^{(1)}(\tau)$ is given in figure 2.22.

We have measured so far the correlation in the amplitude of the signal. It is possible to extend this analysis to other quantities. In particular, we can measure the correlation in *intensities* of the signal, with $I(t) = E(t)E^*(t)$. The field intensity I is directly related to the detection of photons, and as such the *second order coherence*, which is given by:

$$g^{(2)}(\tau, t) = \frac{\langle E^*(t)E^*(t+\tau)E(t+\tau)E(t)\rangle}{\langle E^*(t)E(t)\rangle^2} \tag{2.45}$$

... can be interpreted as the probability that, after having detected a photon at time t, a photon from the same source is detected at time $t+\tau$, which will be noted as $g^2(\tau)$ in the steady state. The experimental method to measure $g^{(2)}(\tau)$ necessarily involves two synchronised detectors with a variable detection delay, and in particular with simultaneous detection to measure $g^{(2)}(0)$. This illustrates the difference between $g^{(1)}(\tau)$, which splits a signal and then imposes a delay, and $g^{(2)}(\tau)$, which takes two different signals from the same source.

A particularly interesting result regarding $g^{(2)}(\tau)$ was obtained by Robert Hanbury Brown and Richard Twiss in their 1956 paper [175], where they investigated the light emitted from distant stars and found that it had a $|g^{(2)}(0)|$ greater than 1 and decreasing with τ. This meant that stars emitted photons

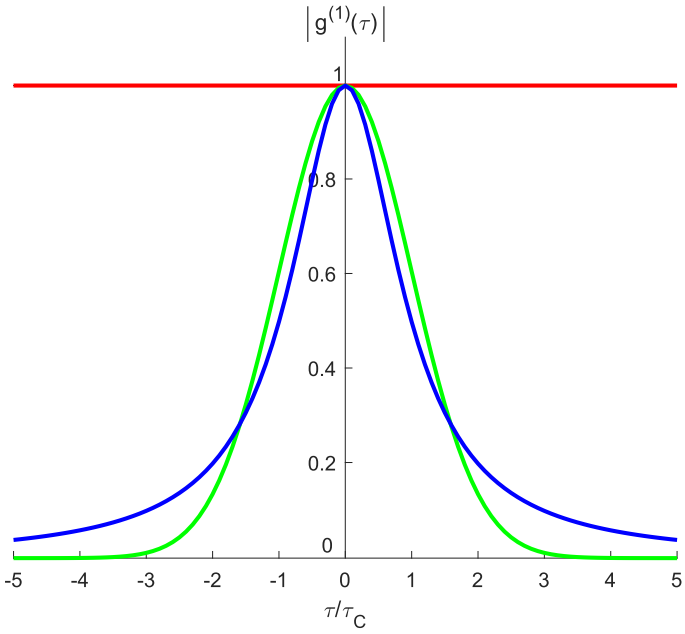

Figure 2.22: First-order correlation function for coherent light (red), Doppler-broadened Gaussian light (green), and collision-broadened light with a Lorentz distribution (blue). τ_C is a characteristic time of emission. Figure inspired by Wikimedia Commons.

in a bunched manner, with bursts of photons followed by lower probability of emission. This property was found to be common to all incoherent and thermal light sources, such as incandescent lamps and LEDs. While it can be described classically in terms of intensity coherence, it requires a full quantum treatment to be properly explained.

By contrast, coherent sources have a $|g^{(2)}(0)| = 1$ and then $|g^{(2)}(\tau)| = 1$ for all τ. In particular, the classical interpretation of $|g^{(2)}|(\tau)$ as being related to a probability of two-time coincidence imposes $|g^{(2)}|(\tau) \geq 1$ for all τ.

2.6.2 A quantum description of coherence

In a full quantum treatment, light is no longer described as a vector field E but rather via creation and annihilation operators $a^\dagger$ and a as we have described in section **??**. With this formalism, the first and second order coherence functions can be written as:

$$g^{(1)}(\tau, t) = \frac{\langle a^\dagger(t)a(t+\tau)\rangle}{\langle a^\dagger(t)a(t)\rangle} \tag{2.46}$$

$$g^{(2)}(\tau, t) = \frac{\langle a^\dagger(t)a^\dagger(t+\tau)a(t+\tau)a(t)\rangle}{\langle a^\dagger(t)a(t)\rangle^2} \tag{2.47}$$

It is possible to define higher order coherence functions, but they find little experimental applications. A state is said to be *perfectly coherent* when it is coherent in all order in the quantum mechanical formalism.

We shall introduce more precisely how the statistical properties of coherence can be expressed in quantum states $|\psi\rangle$. The basic "building block" of those quantum states is the pure state with a fixed number of photons n, written $|n\rangle$. Such states are called *Fock states*. Fock states have no statistical uncertainty, and are the states for which $a^\dagger$ and a act as ladder operators.

Fock states can be used as a basis to write *coherent states*, written $|\alpha\rangle$, with α being a complex number. They are given by the equation:

$$|\alpha\rangle = \exp(-|\alpha|^2/2) \sum_{n=0}^{\infty} \frac{\alpha^n}{\sqrt{n!}} |n\rangle \tag{2.48}$$

Coherent states have statistical uncertainty, being a superposition of an infinite sum of Fock states. However, it can be shown that they minimise the quantum uncertainty, in other words that they satisfy the relation:

$$\Delta X \Delta P = \frac{\hbar}{2} \tag{2.49}$$

With X being the position operator and P being the momentum operator. Coherent states are "quasi-classical", they are the most classical states it is possible to construct while respecting the postulates of quantum mechanics. The complex number α has the physical meaning of being the well-defined (complex) "phase" of the state, with the real part being the X variable and the imaginary part being the P variable. By contrast, the phase of a Fock state is not defined. It can also be shown that the coherent states are eigenstates of the annihilation operator a, with the relationship:

$$a\,|\alpha\rangle = \alpha\,|\alpha\rangle \tag{2.50}$$

Coherent states are used to describe the light emitted by a coherent source such as a laser.

Finally, to describe the light emitted by incoherent sources, such as by light bulbs or stars, we use a general incoherent or "thermal" state. The formalism to describe such a state is called the density matrix. A full definition of the density matrix can be read in [172], but in this work we shall describe it as a matrix on a "continuous basis" of coherent states. In other words, incoherent light is the sum of many uncorrelated coherent light sources with a well-defined "phase" α. The formal definition is as follows:

$$\rho(t) = \int P(\alpha, \alpha^*, t)\,|\alpha\rangle\,\langle\alpha|\,\mathrm{d}^2\alpha \tag{2.51}$$

In this integral, $P(\alpha, \alpha^*, t)$ is the "density distribution" of the coherent states which make up the density matrix. This description is due to physicists Glauber and Sudershan. Glauber can be considered the "father" of the theory of quantum coherence, a theory for which he recieved a Nobel Prize in 2005. In Glauber's formalism, a coherent state $|\alpha_0\rangle$ for example would have a density distribution of $\delta(\alpha - \alpha_0)$. An incoherent state is simply defined as a state whose density distribution is Gaussian with a well-defined average number of particles . Its probability distribution is independent of time, and reads:

$$P(\alpha, \alpha^*) = \frac{1}{\pi\tilde{n}}\exp(-|\alpha|^2/\tilde{n}) \tag{2.52}$$

The density distribution for a Fock state on the basis of coherent states is more complex. The formalism of the density matrix can also be adapted to use the Fock states as a basis, in which case the integral becomes a sum and the density matrix can be represented with integer indexes row and columns.

In this case, the diagonal elements of the density matrix represents the statistical uncertainty, whereas the off-diagonal elements represent quantum correlations.

In the basis of coherent states, it is also possible to describe a "mixed state" which is the superposition of a coherent source and an incoherent source by taking the convolution product of the density distributions P of the two sources.

The density matrix representation is a powerful tool to represent both the quantum and statistical properties of a state in a single mathematical object, with freedom in the choice of basis. It can also be mathematically related to the Hamiltonian of a system and ultimately, to the dynamics of the ladder operators $a^\dagger$ and a. The main result is that the quantity:

$$g^{(2)}(0) = \frac{\langle (a^\dagger)^2 a^2 \rangle}{\langle a^\dagger a \rangle^2} \tag{2.53}$$

... can be evaluated explicitly for all states. We find it to be $g^{(2)}(0) = 2$ for a thermal state, and and decreasing as τ becomes higher, confirming that incoherent light is *bunched*. The shape of the decay is exponential for Doppler-broadened light, and Lorentzian for a collision broadened light.

For a coherent state, we find, as the classical case, $g^{(2)}(0) = 1$ and more generally $g^{(2)}(\tau) = 1$ for all τ. This means, interestingly, that the probability of observing a second photon after the first one remains constant over time. In other words, photons are emitted independently, but with a fixed mean rate, according to a Poisson distribution. This is a standard result for lasers.

Finally, for a Fock state $|n\rangle$, we find that $g^{(2)}(0) = 1 - 1/n$. In particular the single-photon state has $g^{(2)}(0) = 0$, which can intuitively be understood as having a zero probability of emitting a second photon after the first one. This contradicts the classical rule $g^{(2)}(0) > 1$, which shows that Fock states are a purely quantum phmenon, unlike thermal and coherent states which have classical analogues. This comes from the fact that a single photon source needs to be a single isolated emitter, whereas classical light sources are made of a very high number of uncorrelated emitters, resulting in decoherence. An illustration of the emission dynamics is given in figure 2.23, and a plot of $g^{(2)}(\tau)$ functions for all the main cases is given in figure 2.24.

The emission of photons "one at a time" is known as photon *antibunching*. [176] On-demand single photon sources are used extensively in quantum information processing and quantum computing applications [177] as well as quantum metrology and biology, or even to test the foundations of quantum physics [178]. The possibility of investigating the dynamics arising from the interaction of a defined number of photons allows to reduce, for example, the biological processes of vision down to the most fundamental level [179], by testing whether or not the human eye can detect a single photon.

Experimental realisation of single photon sources is a very rich and active research fields, with microcavities playing a key role in recent developments [180, 181] with in particular quantum dots or quantum well embedded in microcavites as "artificial atoms" [182], sometimes up to room temperature [183], see fig 2.25. In the strong coupling regime, antibunched light can be generated from so-called Rydberg blockade of exciton-polaritons [38]. In Chapter 5 of this thesis, we show

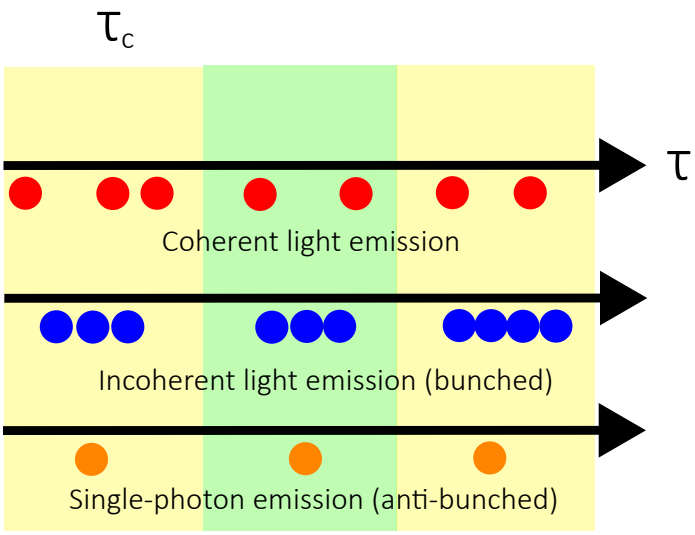

Figure 2.23: Illustration of the photon emission dynamics as a function of time for the coherent, bunched light, and anti-bunched light cases. Figure inspired by Wikimedia Commons.

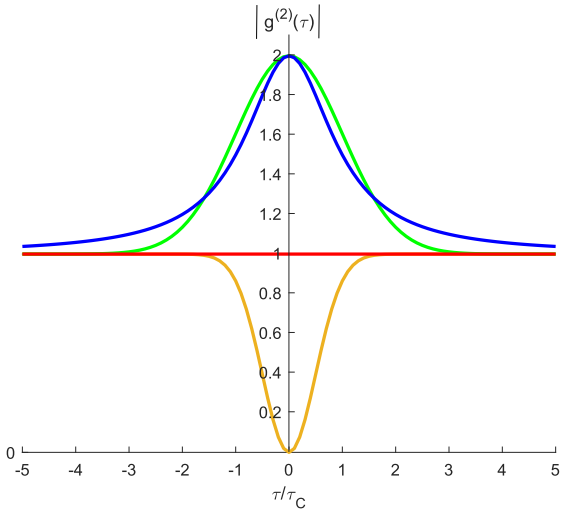

Figure 2.24: Second-order correlation function for coherent light sources (red), bunched light with Gaussian (green) and Lorentzian (blue) broadening, as well as anti-bunched light with $g^{(2)}(0) = 0$.

an experimental realisation of such Rydberg blockade.

The definition of coherence in terms of a coherent quantum state applies not only to light, but also more generally to any system of bosons. The emergence of a coherent state can happen from stimulated emission after an inversion of population, which is the case in weak-coupling microcavities after their lasing thereshold. However, in such a case, the emitted photons do not interact with one another. Exciton-polaritons on the other hand have non-linear properties and do interact with one another, leading to the emergence of another type of coherent state, known as a Bose-Einstein condensate. The properties of such a state, notably its long-range order and spatial coherence, will be described in the following sections.

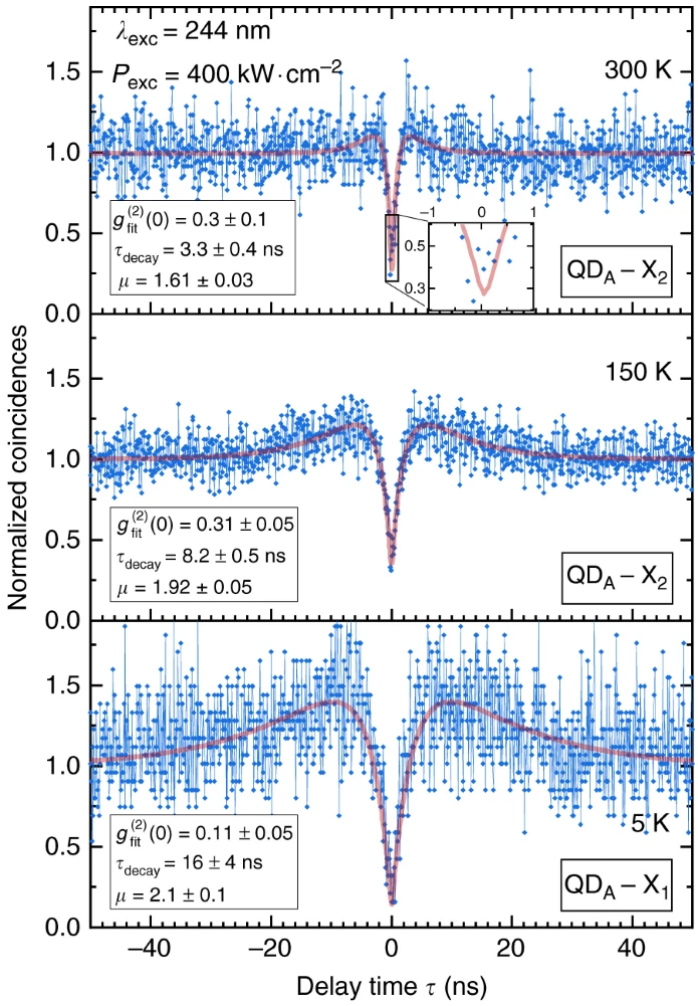

Figure 2.25: $g^{(2)}(\tau)$ measurements in GaN/AlGaN Quantum Dots, optically excited at wavelength λ_{exc} and power P_{exc}, at different temperatures, from two optical transitions (X_1 and X_2). It shows anti-bunching up to $T = 300$K. Taken from [183].

2.6.3 Bose-Einstein condensation

General theory

Before we consider the physics of Bose-Einstein condensation and the particular role played by polaritons, we shall describe more precisely how the bosonic nature of a particle relate to their statistical properties.

In classical physics, a particle can be well-identified by its position and momentum, including when it is considered statistically in a gas of many particles. In quantum mechanics, the position and momentum of a particle are no longer well-defined as a consequence of the uncertainty principle. As a result, when the particles are considered statistically, quantum mechanical particles are *indistinguishable*. We can write the quantum state Ψ of a system of N particles as:

$$\Psi = \Psi(r_1, ..., r_N, ...) \tag{2.54}$$

Where the r_i identify the dynamical variables of each particle in the system. From the indistinguishably of particles, there are specific symmetry conditions on this quantum state Ψ. For particles known as *fermions*, the state Ψ is anti-symmetric with respect to the dynamical variables, and changes sign when two particles are swapped, whereas for *bosons*, the sign remains the same.

From these symmetry considerations, it is impossible for fermions to occupy the same state, as the wavefunction Ψ would be zero, whereas for bosons, occupancy of the same state is not forbidden.

This observation lead Albert Einstein to predict [11] a quantum state in which a macroscopic number of particles would all occupy the same ground state energy level. In an open system with temperature T and chemical potential μ, and with ground state energy $E_0 = 0$ the total number of particles is given by:

$$N(T, \mu) = \frac{1}{\exp\left(\frac{-\mu}{k_B T}\right) - 1} + \sum_{k, k \neq 0} f_B(k, T, \mu) \tag{2.55}$$

In this expression, the first term on the right-hand side is the number of the particles in the ground state ($k = 0$), whereas the second term is the number of particles in higher energy states. The index k represents the wavevector, which can be mapped to the energy. k_B is Boltzmann's constant, and f_B is Bose-Einstein's distribution. At $\mu = 0$, there is a divergence, with an "infinite" number of particles in the ground state.

In a real system, we take the so-called "thermodynamic limit" in which the size R of the system and the number of particle N are taken to go to

infinity, but the density n, which is the relevant physical value, remains finite. Mathematically, this means that we replace $N(T, \mu)$ in equation 2.55 with the density n, bearing in mind the change of units.

Einstein calculated that there is a critical density $n_c(T, \mu)$ of particles which can be accommodated by the Bose-Einstein distribution. If the density n is higher than n_c, then the chemical potential of the system decreases to accommodate the new density. However, the value of μ is bounded by the energy of the ground state E_0, which in our case is set to 0. Once the chemical potential in the system reaches 0, $n_c(T)$ becomes a hard limit. The total density reads:

$$n(T) = n_0(T) + n_c(T) \tag{2.56}$$

At this threshold, any further changes in the system, for example by increasing the total density $n(T)$ or by changing the temperature so that $n_c(T)$ becomes smaller means that the particles "fall" into the ground state. The density of the ground state n_0 becomes macroscopic and comparable to the total density n, forming a Bose-Einstein condensate (BEC). In essence, there is a maximum number of excited states in the system: everything past that numbers falls into the ground state, which shows macroscopic occupancy. This is in sharp contrast to the state before the threshold, where the Bose-Einstein distribution accommodates particles over a large range of energies and no state is macroscopically populated.

This phase transition is the phenomenon of Bose-Einstein condensation. It is particularly interesting as it is a purely statistical property: no consideration other than the bosonic nature of the particles is necessary to derive it. A perfect gas of non-interacting bosons can undergo a Bose-Einstein condensation. At the same time, the system needs to be thermalised, with a well-defined temperature. Therefore photons, for example, cannot undergo a Bose-Einstein condensation on their own, as they lack a way to thermalise. We also note that this transition is unlike a classical phase transition from liquid to gas, which is a sharp discontinuous change in the properties of the system involving a latent heat. The BEC transition consists of a continuous change of the chemical potential μ until it reaches the critical value 0 with a drastic change in the properties of the system, and does not involve latent heat. The BEC transition belongs to the class of *second-order phase transitions*, with μ being its *order parameter*.

The critical density for BEC, $n_c(T)$, is given by the integral:

$$n_c(T) = \lim_{\mu \to 0} \frac{1}{(2\pi)^d} \int_0^\infty f_{\mathrm{B}}(\mathbf{k}, T) \mathrm{d}\mathbf{k} \tag{2.57}$$

Where d is the dimension of the system, and the discrete sum of $\mathbf{k}$ is approximated by an integral. This integral can be evaluated explicitly if the energy dispersion $E(\mathrm{k})$ of the bosons is parabolic, which is approximately the case of

exciton-polaritons in microcavities. At the same time, it diverges for a system with $d < 3$, meaning that a two-dimensional system can theoretically accommodate an infinite number of bosons. This is related to the the absence of long-range order in two-dimensional systems [17]. However, this theoretical limitation can be discussed and overcome, as discussion in the next sections will show.

The theoretical prediction of Bose-Einstein condensation was initially met with some criticism, however the discovery of superfluid ^{4}He helped to convince the scientific community of its validity. ^{4}He becomes superfluid at $T_c = 2.17$K, as opposed to a superfluid temperature for ^{3}He of only 0.0025K. A direct application of Einstein's ideal Bose gas theory predicts a critical temperature very close to the T_c observed, showing that the bosonic nature of ^{4}He plays a major role in the superfluid transition. At the same time, superfluid Helium is in a dense liquid phase, with particle interactions playing a major role, and is not an ideal Bose Gas.

An experimental realisation of a BEC requires to either increase the density of particles n to go over n_C, or alternatively to cool down the system to decrease n_C. There are a number of experimental challenges involving such a process. In particular, the particles need to be weakly interacting so that they can thermalise, but at the same time, they cannot coalesce to form a liquid or solid phase. The first experimental attempts involved gases of atomic Hydrogen, separated in polarisation to prevent them from becoming H_2 molecules [184]. These early attempts were not immediately successful, due to extremely low temperatures required, but paved the way for a better understanding of the dynamics of cold atomic gases. The discovery of laser cooling processes such as Doppler cooling allowed to reach ultra-low temperature of sub K to observe in 1996 the Bose-Einstein condensation first of heavy atoms [13, 185] and then of atomic Hydrogen [186].

The experimental observation of atomic BECs gives a microscopic meaning to the abstract statistical derivation of the condensate. It is a well-known postulate of Quantum Mechanics that any particle, and not only light, exhibits a wave-particle duality with a "thermal wavelength" characterising the scale at which a wave-like behaviour can be observed. The thermal wavelength, also known as the De Broglie wavelength, of a gas with particles of mass m at temperature T is given by:

$$\lambda_{\mathrm{th}} = \sqrt{\frac{\hbar^2 2\pi}{m k_{\mathrm{B}} T}} \tag{2.58}$$

In the condensate phase of cold atoms, the temperature T is so low that this thermal wavelength λ_{th} becomes comparable to the inter-particle spacing of the gas. As the wavefunctions of individual atoms overlap, they can no longer be distinguished, resulting in a single wavefunction whose length λ_c is much larger

than the thermal wavelength λ_{th}. The realisation of BEC is therefore intimely linked with the wave-like nature of atoms, and can be considered an exprimental proof of their wave-particle duality.

The research in atomic Physics which ultimately resulted in the condensation of heavy atoms took the path of reducing the temperature to decrease the critical density in order to increase the thermal wavelength. Such an approach gives a very dilute, almost perfect Bose gas that is very close to the original thought experiment of Albert Einstein. But the temperature required to achieve such a condensate are extremely low. By contrast, photons already display a wave particle duality, but cannot condensate due to the lack of interactions.

This observation lead to research in an another path to BEC, which started from photons and looked into ways to get them to thermalise and interact. Such an approach must go further than the ideal Bose gas case by having the interactions between particles at the heart of the theory.

Condensation of a weakly interacting Bose gas

The only way for photons to interact with one another is when coupled to matter. We note that the linear dispersion of photons in a bulk material does not admit a minimum and as such cannot show BEC. By contrast, the dispersion of photons in a microcavities is parabolic and has a well-defined minimum. Microcavities are therefore a natural tool to study light-based BEC.

The case of a pure "BEC of photons" can be realised in an organic microcavity with dye as the absorbing media [187, 188]. The photons are absorbed and remitted by the dye molecules until they thermalise, while the process needs to be fast enough to not have the photons absorbed the cavity walls. This results in a coherent light source which can operate in the UV range, at room temperature, and that, importantly, is not a laser.

The BEC of photons in a microcavity is an example of a BEC with a weakly interacting Bose gas, in which the photons gain a small effective mass thanks to the cavity.

Another type of light-induced BEC in a microcavity can be realised with excitons. While their effective mass is higher than confined photons, it is small enough to be a good BEC candidate. A specific issue with excitons is that they are not "pure" bosons, but are composed of two fermionic particles. Their canonical commutation relation read:

$$[a, a^\dagger] = 1 - O(na_{\text{B}}^2) \tag{2.59}$$

Where $a, a^\dagger$ are the ladder operators for an exciton in a given band at a given

energy, n is the density of excitons and a_B is their Bohr radius. We find that excitons behave as "approximate bosons" in the low density, low temperature limit. At higher densities, Coloumb interactions between the particles and the Fermi exclusion principle become prevalent. In particular, when the density becomes too high, the scattering potential created by other charge carriers becomes stronger than the interaction between the electron and the hole. The gas of excitons becomes a plasma of free electrons and holes and the semiconductor becomes a metal. This effect is known as the Mott transition, and it signals a transition from the strong coupling regime to the weak coupling. At high temperature, the excitons may also lose their bosonic feature as the thermal interactions become stronger than the binding energy.

In the quest to observe BEC, "dark excitons", which are not directly coupled to light, have been an important research area [189, 190]. Dark excitons can be created optically (for example, by non-resonant pumping), and their band structure forbid radiative recombination. As a result, such excitons have therefore a very long lifetime, which can go as high as a microsecond in monolayer structures [191]. Recent advances have allowed very accurate probing of such states [192, 193] and as such they remain an active topic of research. Yet there has not been, to this day, a conclusive signature of a dark exciton condensation. Despite the advances in probing techniques, measuring optical properties of a dark exciton remains very difficult [194]. Imperfections inherent to semiconductor structures can also lead to the excitons being trapped in local minimas of the disorder potential, even in monoloyers structures [195], which limits their ability to interact with one another, thermalise and form a coherent condensate.

As a result, it may be suitable to study instead "bright" excitons, directly coupled to light. As we have shown in previous sections, the coupling between light and excitons in such cases result in exciton-polaritons. The effective mass of exciton-polaritons make them very good candidates for BEC. From their photonic component, it is up four order of magnitudes lower than that of an exciton [196], and much lower than a cold atom. According to equation 2.58, this reduces the critical density needed and raises the critical temperature, making an experimental realisation of a BEC of exciton-polaritons easier. In some materials, the polariton BEC can even happen at room temperature. Additionally, microcavities present a favourable environment to tune experimental parameters according to the effects we wish to observe. In practice however, there are several additional challenges and unique properties of a polariton BEC, which we will describe in the following section.

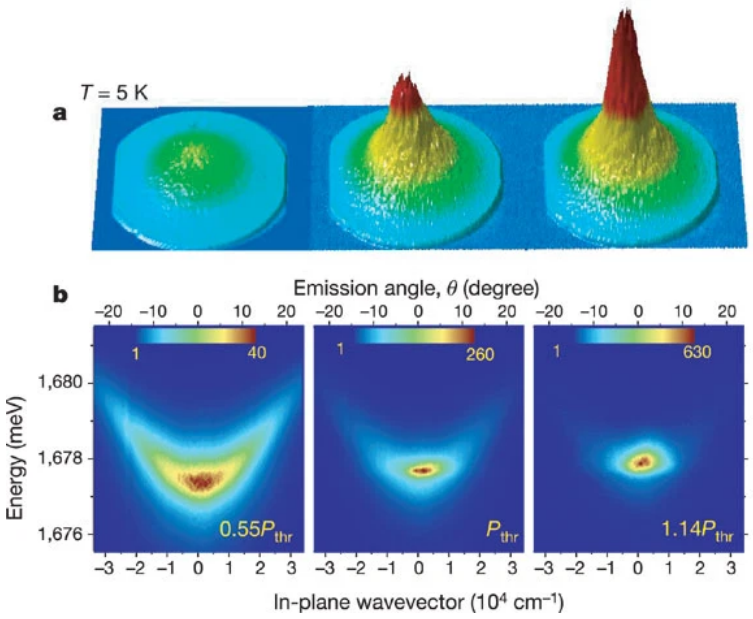

Figure 2.26: Top: Pseudo-3D imaging of the polariton condensate emission, below, at, and above condensation threshold, showing the strong increase in emission intensity. Bottom: LPB dispersion below, at and above threshold, showing the macroscopic occupation of the $k = 0$ state at the bottom of the branch. Taken from [139].

2.6.4 Condensation of exciton-polaritons

Experimental realisation

The first unambiguous claim of BEC using exciton-polaritons was given in 2006 by Kasprzak & al. [139] in a CdTe microcavity cooled down to 5K, non-resonantly pumped, shown in figure 2.26.

The non-resonant pumping scheme is necessary to populate all the states of the LPB, which then scatter to $k = 0$ as the critical density for BEC is reached. More details about resonant and non-resonant pumping are given in chapter 3. This is the main difference from the OPO regime of section 2.5.2, which is pumped near resonantly, and in which not one, but three states show macroscopic occupation of population (pump, signal, and idler).

As there is a one-to-one correspondence between the emitted photons and the microcavity polaritons, a clear signature of a BEC of polaritons can be

found in the emission of coherent light after a threshold, a so-called "polariton laser" [26] resulting not only from inversion of population of the excited free carriers in the semiconductors (also known as stimulated emission), but rather from *stimulated scattering* of the pumped exciton-polaritons, relaxing to the ground state, which becomes macroscopically populated. The finite lifetimes of the microcavity polaritons result in light emission, and the coherence of the condensate results in coherence of the emitted light. Kasprzak's experiment sparked a lot of interest in the topic of polariton BECs, and in the following years, several major reviews were publish to show the interest of the scientific community in the subject [197, 16].

Unlike in the OPO case of the previous section, the condensate is characterised by the macroscopic occupency of a *single* state at $k = 0$. Polariton condensates are also typically realised with off-resonant pumping, and with coherence building up from the condensation process, rather than the near-resonant pumping of OPOs.

Yet coherent emission alone is not a sufficient proof to claim condensation. Indeed, a cavity in the weak coupling regime does emit coherent light with a regular laser mechanism. Unlike a laser in the weak coupling regime, a polariton laser can have a very low operating threshold, which makes it highly suitable for practical applications. For example, room temperature lasing can be observed at a power density of 4.5 W/cm^2 in a GaN substrate [198], which is to 2.5 times less than the predicted density for collapse of the strong coupling regime. Thanks to continous advances in microcavity design technologies, there has been multiple realisation of ultra-low threshold polariton condensation and lasing in a multitude of different geometries and materials [199], including monolayers [200].

One way to ensure the coherent light emission from the cavity results indeed from a polariton condensate is to run a power dependency that exhibits both behaviour, starting at powers low enough to observe both the BEC condensation, the crossover from weak to strong coupling regime, and finally the inversion of population. Such a power dependency would have two characteristic thresholds [201]. Experimental realisations of this proposal have been published [202, 203], showing unambiguously a transition from strong to weak coupling regime with two different lasing thresholds for the two mechanisms. However, in practice, there can be experimental constraints to this approach, such as a low damage threshold to the sample preventing higher powers to be reached, or a photonic lasing threshold too high to be reached in the same experimental pumping scheme as polariton lasing.

The non-linear properties of polariton condensates may be an indicator to claim BEC. However, some of them are very similar to that of photonic laser. Both BECs and photonic lasers exhibit linewidth narrowing after their threshold, described in the ideal case by the Schalow-Tones equation [204], with ad-

ditional linewidth broadening arising from temperature or cavity imperfections. In a similar fashion, both polariton and photonic lasers are expected to blueshift as a function of power, but with very different underlying physical mechanisms. A photonic laser exists in a semiconductor with a plasma of electrons and holes, which may screen the electromagnetic field, ie the light emitted by the cavity. This feature cannot happen in the strong coupling regime, as it is only observed above the Mott transition [103]. By contrast, blueshift of the polariton laser is driven by polariton-polariton interactions [205], and renormalisation of the LPB [206] which are stronger for polaritons with a stronger excitonic content. As those mechanisms are different, it is possible in principle to distinguish between polariton blueshift and other kinds of blueshift. In practice, it is preferable to look for other signature of polariton lasing.

One such signature can be the emergence of a strong polarisation after threshold, from an unpolarised pump. This feature was used as a signature of lasing in [139], and described as "spontanous polarisation" in reference [207]. This can be interpreted as a form of *spontaneous symmetry breaking* arising as a consequence from condensation. Below threshold, the light emitted is unpolarised. Formally, we say there is a *symmetry* with respect to the polarisation in the sense that a mathematical operation changing the polarisation leaves the system unchanged. The interaction of mathematical group theory with symmetries of physical systems is a key element to the modern understanding of the quantum theory of phase transitions and quantum systems. A review of the mathematical formalism can be found in [208]. Above threshold, the symmetry is broken, and the system "selects" an arbitrary polarisation among all other possibilities. In a similar way, at the condensate level, there's a spontaneous symmetry breaking with respect to the phase. Below threshold, the phase of the system can be arbitrarily changed, but after threshold, a specific phase is selected across the entire condensate. However, such a phenomenon is also observed in weak coupling lasers [209], and can be described in the same formalism of spontaneous symmetry breaking.

Thus there are common elements to the two kinds of lasers. In order to distinguish between a polariton laser and a photonic one, we must look at the specific unique properties of a BEC [210]. A direct measurement of the spatial and temporal coherence of the condensate stands among the best tests to demonstrate its existence and probe its properties [211, 212], see also chapter 3. Such tests have been performed for exciton-polaritons [213], but they require very precise interference measurements, and, as we shall see, the fact that cavity polaritons are a two-dimensional and inherently out of equilibrium system presents additional challenges.

Besides the spontaneous polarisation, Kasprzak [139] used the dispersion properties of the polaritons to claim condensation. The parabolic dispersion is expected to blueshift, and after threshold the emission is main near the $k = 0$ point of the dispersion rather than coming from all k values. This is an

experimental manifestation of a macroscopic occupency of the $k = 0$ state.

However, in the case of a cavity supporting several modes close to one another in energy, it may be difficult to resolve the polariton dispersion accurately. In this case, it is the *free spectral range* (FSR), the separation between the modes, which can be used to distinguish between polariton lasing and photonic lasing. In the weak coupling regime, the FSR can be easily calculated from the properties of the cavity, and is linked to the cavity finesse. In the strong coupling regime, the FSR curves as a function of the excitonic fraction of the polariton mode. The weak and strong coupling regime have thus very different Free Spectral Ranges. In the case of a multimode cavity, the FSR can be used to distinguish between polariton lasing and regular "photonic" lasing. However, this test can only be applied for very large cavities in which the FSR is small enough to be resolved. This is usually the case of WGM cavities with very long propagating lengths, but it is not the case for DBR cavities, which are too small and in which the FSR is too large.

After Kasprzak milestone paper, many other examples polariton condensation were claimed in different materials, such as ZnO [214], GaN [112, 21], Cu_2O [132], which showed other interesting aspects of BEC physics in exciton-polaritons systems. In order to better describe those phenomena, a more modern description of the BEC theory is necessary.

Modern BEC theory and long-range order

The initial Einstein proposal of BEC showed a lot of insight in the hidden properties of an ideal quantum Bose gas and describes well the statistical process of BEC. Nevertheless, it was formulated in the (glorious) early days of Quantum Mechanics and several theoretical developments were made to make the formalism adaptable to non-ideal cases. In particular, the theory of Spontaneous Symmetry Breaking and how it is realised in various systems gives insights on their nature, linking together long-range order phenomena (such as ferromagnetism) with BEC [215]. Einstein's theory also only considered an ideal gas, with the phase transition happening only due to statistical properties. In practice, the role of interactions is fundamental to understand the formation of the condensate and emergence of coherence [216, 217]. Finally, Einstein's theory is not written in the modern formalism of density matrices, which has been our basis so far to describe coherent states.

These considerations lead to the definition of a new criterion for Bose-Einstein condensation. Rather than simply considering the number of particles in the ground state, we consider an "average wavefunction" $\langle\psi(\mathbf{r})\rangle$, together with its phase θ. It is defined by taking the average wavefunction of all particles

in the ground state at a point $\mathbf{r}$ [218]:

$$\langle\psi(\mathbf{r})\rangle = \sqrt{n(\mathbf{r})}e^{i\theta(\mathbf{r})} \tag{2.60}$$

In this expression, $n(\mathbf{r})$ can be interpreted as the density of the condensate wavefunction. Below threshold, the Hamiltonian system must be invariant under an arbitrary change of $\theta(r)$, which is a symmetry known as a **gauge invariance**. This means that all particles in the ground state have a random phase. The mathematical group of operations under which the Hamiltonian is invariant is the gauge group of the system. When the transition happens, that symmetry is broken, and a specific phase is randomly selected throughout the entire condensate, and we have:

$$\theta(\mathbf{r}) = \theta_0 \tag{2.61}$$

... for all position vectors $\mathbf{r}$. All particles in the condensate now share the same phase. The phase θ_0 is arbitrary, but constant across the entire condensate, which in theory may extent infinitely in space. This theoretical peculiarity explains why the idea of BEC was initially met with skepticism. Penrose and Onsager solved this problem by taking the following limit as a criterion for long-range order:

$$\langle\psi^\dagger(\mathbf{r})\psi(\mathbf{r'})\rangle \xrightarrow{|\mathrm{r}-\mathrm{r}'|\to\infty} \langle\psi(\mathbf{r'})\rangle^* \langle\psi(\mathbf{r})\rangle \tag{2.62}$$

Where the average is taken over many different position of $\mathbf{r}$ and $\mathbf{r'}$. This definition can be related to the density matrix of of the state, and in the coordinate basis, the off-diagonal elements, which measure the coherence of a state at different points, are non-zero. This is known as *off-diagonal long range order* (ODLRO) [219]. Such a formalism was originally developed to describe the superfluid phase of liquid Helium, but is well-suited for any interacting Bose gas, such as a gas of exciton-polaritons with a low density.

The nature of the BEC transition in exciton-polaritons

The two "extremes" of a polariton gas in a microcavity are, on the low density side, a weakly interacting Bose-gas below condensation and, on the high density side, a weak coupling microcavity above the Mott transition. In the intermediate regime, the polaritons may overlap strongly and thermalise without breaking down into an electron-hole plasma. This intermediate regime is given by the condition:

$$\frac{m^*}{\mu}\frac{\Omega_R}{\mathrm{Ry}} \ll n a_\mathrm{B}^2 \ll 1 \tag{2.63}$$

... where μ is the reduced mass and Ry is the Rydberg binding energy of an *exciton*. By contrast, the other terms in the equation relate to polaritons: m^* is

the reduced mass and Ω_R is the binding energy (the Rabi splitting) of *polaritons*. As in equation 2.59, n is the two-dimensional density and a_B the Bohr radius of the exciton. In the intermediate regime, the exciton-polaritons are a coherent condensed state. Such a condensate must be thermalised. At the same time, the polariton BEC is an out of equilibrium phenomenon with constant pumping and escape through the cavity mirror. As a result, there are two relevant time scales for the thermalisation mechanisms: an ultrafast (on the picosecond sale) polariton-polariton scattering which thermalises the polariton gas "with itself" [220, 146], and a slower polariton-phonon scattering [221] which thermalises the polariton gas with the crystal. The crystal thermilisation time scale is usually longer than the lifetime of polaritons, which makes them an out-of-equilibirum phenomenon.

In the condensed phase, as a gas of identical bosons, with the pump and dissipation taken into account, the dynamic of the ground state ψ is given by the Gross-Pitaevskii equation, also known as the "non-linear Schrödinger equation". It reads:

$$i\partial_t\psi = \left(-\frac{\nabla^2}{2m^*} + V(r) + U|\psi|^2 + i[\gamma - \kappa - \Gamma|\psi|^2]\right) \tag{2.64}$$

On the right-hand side of the equation, the real parts are related to the "steady-state" dynamics, whereas the imaginary parts are related to the losses and gains from the pump and dissipation. The first real term is merely the kinetic energy, with ∇ being the gradient operator and m^* being the reduced mass of the polariton. The second term is the potential energy $V(r)$. The third term is characteristic of the Gross-Pitaevskii equation and describes the non-linearities of the state ψ with the non-linear coefficient U. On the imaginary part, γ is the pumping rate of the system, κ is the photon decay, and finally Γ describes the non-linear losses.

We have mentioned that "true" long-range order cannot happen in a two-dimensional system [17], as an infinite number of bosons can theoretically be accommodated by an infinite two-dimensional system. This is known as the Mermin-Wagner theorem. With this result, a BEC of polaritons in a microcavity should not be possible, as the microcavity is a two-dimensional system. This problem can be solved by considering a system of finite size, which would only accommodate a finite number of bosons. However, in such a system, the definition 2.62 no longer makes sense. As a result, for systems of interacting bosons confined in two dimensions, the BEC transition is replaced by the so-called Berezinskii–Kosterlitz–Thouless transition (BKT). The BKT transition traces its origin to the study of 2D phases of condensed matter described by so called XY model, [18, 222], which has been used to describe ferromagnetism [223], superfluid Helium [224] and superconductivity [225], among others. Qualitatively speaking, the BKT transition involves the creation of bound vortex-antivortex pairs (see fig. 2.27) as opposed to featureless bosons.

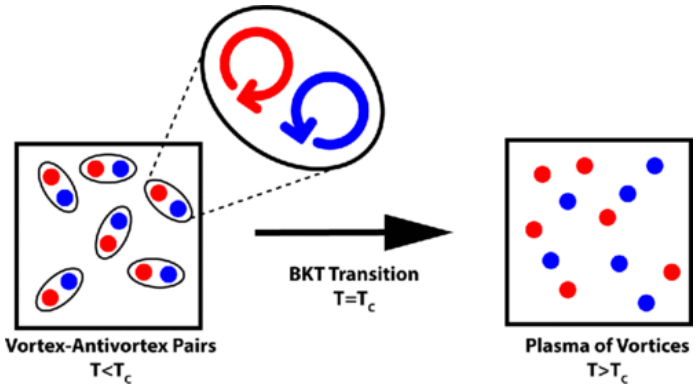

Figure 2.27: An illustration of the BKT transition with ordered bound vortex-antivortex pairs. Taken from [226].

The BKT transition does not exhibit strict "infinite" long-range order, but has correlation decreasing as a power function, as opposed to an exponential decay in a thermal phase. Comparison between the BEC and the BKT transitions has shown that the BEC case coincides with the BKT case in the limit of vanishing interactions [227]. Exciton-polaritons in microcavities have highly tunable interaction strengths depending on the density, materials used, cavity design, and detuning between the exciton and photonic energies. As a result they form a useful system to study the BKT transition [228, 229].

In practice, however, the Marmin-Wagner theorem which forbids the existence of two-dimensional long-range order predicts that fluctuations in the coherence diverge logarithmically [230], which is slow enough to still consider the system in a coherent state from an experimental point of view. In the limit of finite-size two dimensional system, with low interactions, it is therefore permissible to speak of a Bose-Einstein condensate. As of the writing of this thesis, there is no convention against claiming BEC in two dimensional microcavities [187] or even in one dimensional [231]. Theoretical studies on BEC in arbitrary dimensions [232] have discussed the subtleties of the apparently simple definition of "long-range order". For the reminder of this thesis, we will take the view that the condensation of exciton-polaritons can be classified as BEC.

With this more generous definition, the phenomenon of BEC, and its interacting case of BKT, can be linked to a plethora of well-known and impressive physical phenomena. With their high condensation temperature and their experimental tunability, exciton-polaritons offer a particularly rich ground to study such phenomena.

2.6.5 Polariton BEC effects

The most common signature of polariton condensation is the coherent light emission, named "polariton lasing", which we have described in the previous section. It is only one among the many physical phenomenons made accessible by polariton condensation. We shall see that the polariton condensate may crossover to different regimes, depending on the density of polaritons.

The BCS transition, superconductivity, and high density phases

In the middle of the spectrum of polariton density, whose extremes are the dilute non-condensed polariton phase on the low density end, and a plasma of electrons and holes on the high density end, we find the BEC condensation. Beyond the density required for condensation, but before the plasma phase, at density below but comparable to Mott density, however, there is another phase. This is called the "Bardeen–Cooper–Schrieffer" phase transition, also called the *BCS* phase [233]. It shares its name with the theory used for the correlated Cooper pairs of superconductivity.

Superconductivity was first observed in 1911, when it was found that sufficiently cooled down Mercury showed a sharp drop in resistivity, close to zero, at cryogenic temperatures [234]. In 1957, Brardeen, Cooper and Schrieffer provided a microscopic theory of superconductivity for metals at cryogenic temperatures [235], which also provided an explanation for related phenomenons such as the magnetic levitation of superconducting materials, known as the Meissner effect. In the BCS theory, electrons in the metal couple to lattice vibrations to form correlated pairs of fermions (known as Cooper pairs) which, as bosons, are able to occupy the same quantum state, which changes the mechanism of charge transport. Cooper pairs are typically pairs of electrons, but an electron-hole pair can also form a Cooper pair – which is the case for cavity semiconductors when they undergo the BCS transition.

Research in the superconductivity is one of the most widely reported and discussed by the general public in Physics. After the initial experiments in Mercury at cryogenic temperatures, there was a renewed interest in the topic after the discovery of higher-temperature superconductors (up to 30K) by Betram Batlogg in 1988 [236]. It would, however, prove difficult to cross the line up to room temperature superconductivity. The highest unambiguous temperature recorded for superconductivity, without extreme pressures, at the time of writing this thesis, is only 133**K** [236]. However, for such materials, the BCS theory may no longer be sufficient.

Claims, counter-claims, accusations (and proofs) of fraud are sadly common

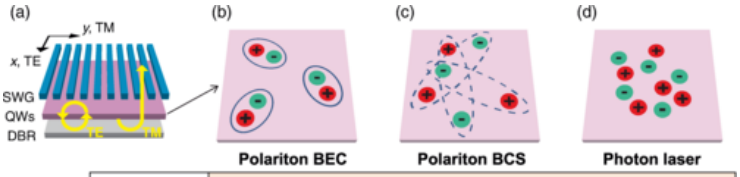

Order Parameter	Measured by occupancy and coherence of $q_{\parallel}$= 0 emission.		
Carrier density	$n \ll n_{\mathrm{Mott}}$	$n \geq n_{\mathrm{Mott}}$	$n \gg n_{\mathrm{Mott}}$
Electron, hole distribution	no inversion	small inversion	strong inversion
Gain type	bosonic	fermionic	fermionic
Emission frequency	below cavity	below cavity	close to cavity
Constituent quasiparticle	exciton-polariton with bound exciton	*e-h* polariton with bound *e-h* pair	*e-h* plasma, unbound
Spectral gap	gap by exciton binding & photon coupling	BCS-like gap by *e-h* pairing & photon coupling	gap possible (light-induced spectral hole)

Figure 2.28: a) Schematic of the experimental setup, with a subwavelength grating to allow access to the electronic properties of the systems. b, c) Comparative table of the three states existing in the cavity, with differences between BEC and BCS highlighted in green, whereas the differences between BCS and photonic lasing are highlighted in blue. Taken from [138].

in the superconductivity community. The latest claim of room-temperature, ambient pressure superconductivity, in a novel material called LK99 [237], made world headlines without convincing the wider scientific community, showing the very difficult challenges faced by researchers in this topic. In this context, as microcavity exciton-polaritons are predicted to undergo a BCS transition [233], there is a strong motivation to investigate the properties of this high density phase in detail.

Experimental access to the BCS phase of polaritons proves to be very challenging [138], as there is little difference in the light emission spectra between the two regimes as shown in figure 2.28. The BCS case can be excluded by ensuring the system is below the Mott transition, as was done in the analysis of [21].

The ability of excitons and exciton-polaritons to undergo a BCS transition can cause some challenges in precisely identifying the dynamics of the polariton gas inside the microcavity, with only measurements of excitonic density needed to rule it out, and an elaborate setup to access the BCS phase. However, it has also sprung several proposals to engineer a device that would use polaritons to create a superconducting phase, which we will detail in the next section.

Superconducting polaritons

There has been several attempts and theoretical proposals to realise superconductivity in polaritons, with an early proposal dating from 1979 [238].

In a more recent project paper [25], the authors show that an "exciton-polariton mediated superconductivity" could be possible. In this paper, the authors want to replace the phonon and lattice vibrations which play a major role in the theory of superconductivity by BEC of exciton-polaritons. In such a proposal, the ability of exciton-polaritons to condense at a higher temperature - up to room temperature in GaN systems - would be very useful, and could lead to much higher superconductivity temperature. This hybrid approach of a "Bose gas" of exciton-polaritons on one hand, and a "Fermi gas" of electrons which becomes superconducting on the other, in a multi-layered structure, such as the one in figure 2.29. Theoretical reviews on the possibility to realise these two coexisting phases [239] puts a strong emphasis on the technical challenges to realise such a structure, but at the same time, also note how exciton-polaritons offer a lot of experimental freedom.

An experimental realisation of this proposal was done in a two-dimensional structure coupling a two-dimensional electron gas with a polariton BEC [240], but still at cryogenic temperatures.

Research still continue on these hybrid Bose-Fermi systems [241], such as for example the one in figure 2.29. Many other exotic physical phenomena are made accessible in these systems, such as the study of exotic quasiparticles known as "rotons" [242].

Superconducting phases are a very promising aspect of research in exciton-polaritons, with many exotic proposals that rely on their condensation properties. Research focuses on two-dimensional materials, such as, for example, h-BN [243].

"Quantum fluids of light": superfluid polaritons

Superfluidity is another fascinating condensed matter phenomena which has been observed in microcavity exciton-polaritons.

The original observation of superfluidity dates back from 1937, where it was discovered independantly by Pyotr Kapitsa [244] and by Allen and Messmer [245]. The original superfluid behaviour was observed in the isotope ^{4}He of Helium, cooled down below the so-called λ point of 2.17K.

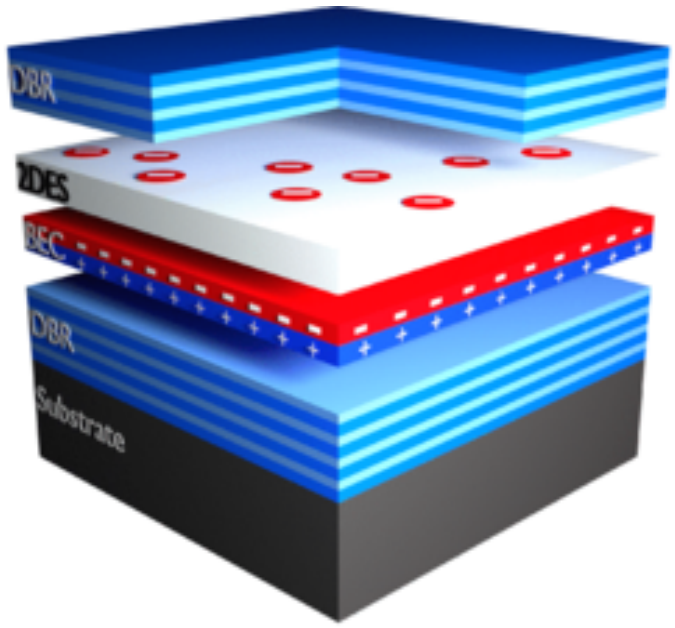

Figure 2.29: Fabry–Pérot microcavity with an heterostructure supporting a BEC of exciton-polaritons (on the bottom) and a Fermi gas which can transition into a superconducting phase. Taken from [240]

.

Experimentally, superfluidity manifests itself most strikingly by the ability of the liquid to creep up horizontally over containers, or to flow without friction in tubes.

The superfluid transition of liquid Helium was closely linked with the theory of BEC as the λ point proved to be very close to the theoretical critical temperature for a BEC with the ^{4}He particles considered as bosons.

A proper microscopic theory of superfluid Helium was given by Lev Landau in 1941 [246] and earned him the Nobel Prize in 1962. The Landau theory of superfludity splits the Helium in two phases, the so-called Helium-II phase, in the superfluid state, which is able to flow without friction, and a normal fluid phase (Helium-I). The ratio between the two phases changes with temperature, with a total superfluid phase at the limit of zero Kelvins. This can be directly compared to a Bose-Einstein condensate, which consists of a condensed phase in the ground state with density n_0, and an uncondensed phase at higher energies with density $n_k = n - n_0$. The total density n remains constant during the transition, while the condensed phase density n_0 increased.

The main difference, as we have said, is the role of interactions in a superfluid phase. Liquid Helium cannot be directly compared to a Bose gas, even weakly interacting, as it is in a liquid phase with strong Van Der Walls interactions.

Landau devised an experimentally verifiable criterion for superfluid behaviour [247]. A liquid is said to be in the superfluid state inside a capillary when the *relative velocity* between the fluid and capillary in which it travels is below a certain critical value. The criterion reads as:

$$v_{\text{fluid}} < v_c, \text{ where } v_c = \min_p \frac{E(p)}{p} \tag{2.65}$$

... where p is the momentum of the particles in the fluid, and $E(p)$ is the energy of the particles according to Bose-Einstein statistics. It can be shown that when this criterion is verified, any perturbation (hence, losses of energy) in the system is less energetically favourable than frictionless flow. The velocity v_c can also be called a "speed of sound" in the liquid Helium fluid. In other words, if the fluid travels below the speed of sound, it is a superfluid. This theory allows to consider superfluidity as a property of any system of interacting bosons. Indeed, a form of superfluid flow was observed in a BEC of cold atoms [248]. If polaritons are able to condensate as well [139], then a path to superfluid effects in polaritons is possible, and was predicted [249].

A first realisation of superfluidity in polaritons [250] showed frictionless flow, but was not able to verify the Landau criterion. Soon after [19], this was also achieved in a AlGaAs microcavity with InGaAs QWs.

The superfluidity of polaritons has earned them the rather poetic name of

"quantum fluids of light" [197]. While the superfluid polaritons are closely related to BEC of polaritons, the experimental scheme is different. Rather than being pumped off-resonantly at a higher energy, populating the entirety of the polariton dispersions, the cavity is pumped near-resonantly in superfluid experiments, at a small detuning and angle of incidence k_p, and only states with $-k_p < k < k_p$, including $k = 0$, are populated. As the pumping power increases, non-linear processes such as the ones described in section 2.5.1 cause the LPB dispersion to blueshift, until the bottom of the polariton branch meets the pumping energy. Then, the polaritons injected to the cavity are in the minimal energy state, without a Bose-Einstein condensation taking place. When enough polaritons are in the minimal energy state, a transition to the superfluid state takes place.

Pumping at a non-zero angle of incidence k_p gives the polariton fluid a non-zero momentum. If the excitation spot is placed on top of a defect in the structure, the transition to the superfluid regime then manifests itself when the polariton fluid flows around the defect without scattering, as shown in figure 2.30. The superfluid regime also manifests itself in strong changes to the shape of the polariton dispersion, which is expected to become linear as a result of the collective behaviour of polaritons in the ground state.

To check if the Landau criterion is satisfied, we must first find an explicit equation for the speed of sound in the polariton fluid, which can be related to experimental parameters as opposed to the formal definition of equation 2.65. In ref. [19], it is derived as:

$$v_c = \sqrt{\frac{\hbar g|\psi|^2}{m}} \tag{2.66}$$

... where g is the polariton-polariton interaction strength, $|\psi|^2$ is the density of polaritons, and m is the effective mass of the LPB. This speed of sound is compared to the speed of the polariton fluid itself, which is:

$$v_p = \frac{\hbar k_p}{m} \tag{2.67}$$

... where m is effective mass of the polariton, and k_p is the polariton momentum.

If the parameters of the experiments are chosen so that $v_c < v_p$, then the Landau criterion is satisfied and the polariton is superfluid. Superfluid polaritons have a key advantage compared to liquid Helium experiments, as many of the parameters can be tuned experimentally. For example, the density $|\psi|^2$ depends on the pumping power of the incident laser, and the polariton velocity is directly dependent on the momentum k_p, which is itself given by the angle of incidence. The polariton coupling strength g can also be tuned by changing the excitonic content of the polaritons.

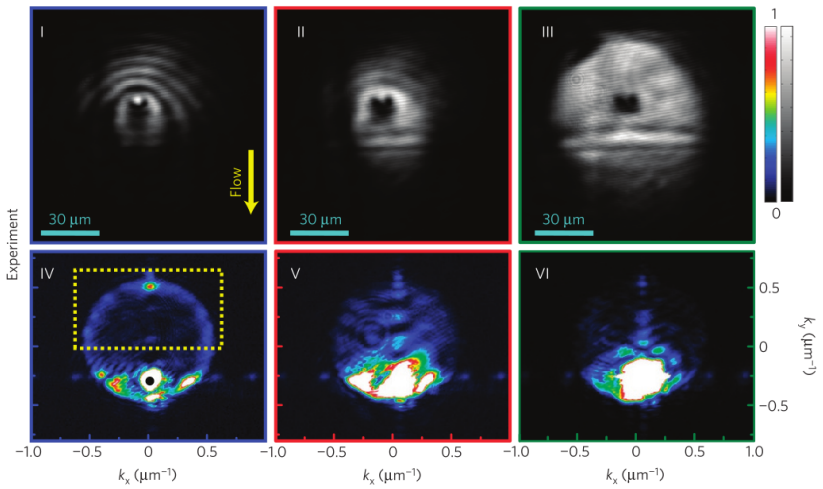

Figure 2.30: Top: experimental data, in near-field imaging, of a polariton fluid around a photonic defect, below (I), near (II) and above (III) superfluid threshold. Above the threshold, in the superfluid regime, the polariton fluid flows around the defect without scattering.
Bottom: experimental data, in far-field imaging (k space), of a polariton fluid around a photonic defect, below (IV), near (V) and above (VI) threshold. The elastic scattering ring in (IV) disappears after threshold in (VI). Taken from [19].

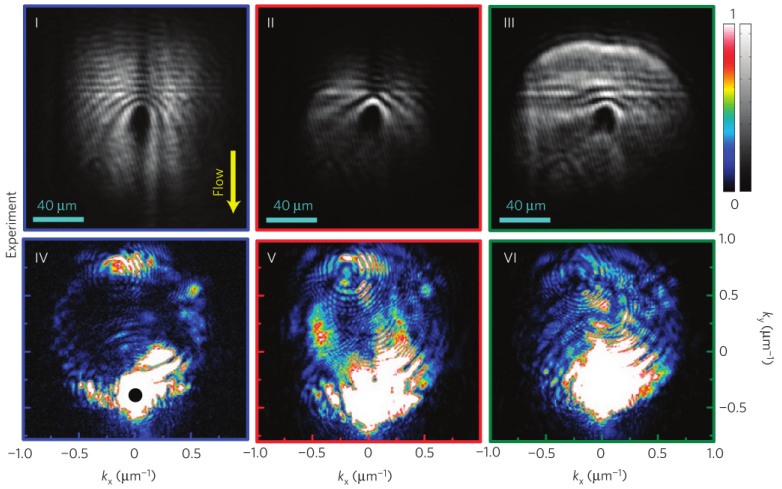

Figure 2.31: Top: experimental data, in near-field imaging, of a polariton fluid around a photonic defect, below (I), near (II) and above (III) threshold in the supersonic fluid of light regime. Above the threshold, the parabolic wavefront take a characteristic linear shape.
Bottom: experimental data, in far-field imaging (k space), of a polariton fluid around a photonic defect, below (IV), near (V) and above (VI) threshold. The far-field image is much complicated than for the pure superfluid case. Taken from [19].

In particular, it is possible to excite the polariton fluid at a higher angle k_p, increasing the fluid velocity so that the Landau criterion is no longer fulfilled, while remaining close to a BEC phase. The polariton fluid now scatters around the defect producing so-called "Bogoliubov excitations" [251, 252]. As the polariton fluid velocity v_p is higher than the speed of sound in that fluid v_c, the polariton enters a supersonic or so called "Čerenkov" regime [253], which is shown in figure 2.31.

After the original breakthrough of superfluid polaritons at cryogenic temperatures, recent research has been able to observe signatures of superfluid behaviour up to room temperature [254, 255]. Superfluid polaritons remain an active area of research, with potential applications in Quantum computing [256], or, as we shall see in chapter 6 of this thesis, in analogue physics.

2.7 Conclusion

Exciton-polaritons are a fundamental excitation of light in semiconductors. The theory shows how a normal mode splitting with two distinct branches arises from the interaction of the photon and the exciton in the crystal. A quantum description gives the picture of a truly mixed state, half-light and half-matter, showing properties from both worlds.

Yet the most interesting properties of this curious state of matter need specific structures to be observed. There has been considerable interest in the study and fabrication of such microcavities needed to confine light, and we have described the most relevant geometries for our research. The science of microcavities is a vast topic with considerable applications, many of them lying beyond the scope of just exciton-polaritons. They are, however, a key ingredient in the conception of experiments related to exciton-polaritons.

Such experiments show the wealth and breadth of the physics accessible with polaritons. We have listed the most striking ones, but we could not be fully exhaustive. The question of the actual nature of the BKT transition, the out-of-equilibrium nature of polariton condensates, are topic of fundamental interest which are still not fully resolved. Their nature as a fundamental component of light-matter interaction in semiconductors, as well as the importance of light confinement for such interaction, explains such versatility and richness of the physics. Exciton-polaritons also show how some deep concepts of Physics such as Bose-Einstein condensation and coherence have a "universal" nature: they are at the root of phenomena as diverse as superfluidity, superconductivity, or lasing.

We have given in this an introduction to all the concepts needed to understand exciton-polaritons in their context. In the following chapters, we will look at experiments involving exciton-polaritons in microcavities and showing how the general theoretical framework applies to specific experiments.

Chapter 3

Experimental methods

3.1 Overview

We have stressed in the previous chapter how cavity exciton-polaritons map easily with the emission from the cavity itself. Our experiments are based mostly on this property. The incident light on the cavity is the key experimental parameter. The first question is the wavelength of light used to pump the system, which can either be near-resonant with the bottom of the LP branch, or non-resonant, at higher energies.

The non-resonant case involves complex relaxation phenomena to populate the LP branch. At higher pumping powers, the UP branch of higher energy may also be populated, although with less density, as the higher energy states have a lower probability of relaxation. These complex relaxation dynamics are not studied in this thesis, but are a topic of active research [257]. One advantage of populating the full polariton dispersion is that the non-linear effects affecting it are easier to observe when varying pumping power, temperature, or applying external fields. In the case of a planar microcavity, if the sample has a wedge, it is also possible to measure the detunning by moving across the sample. Pumping at higher energy than the cavity modes can also excite several modes at once. By contrast, resonant or near-resonant pumping only populates part of the dispersion, and often a single cavity mode. The case of quasi-resonant pumping has its own special physics, as populating the so-called "bottleneck" region of the dispersion results at the exact wavevector, so called "magic angle" which we have described in section 2.5.2. Finally, pumping directly at the resonant energy creates polaritons at the bottom of the dispersion, without any relaxation dynamics. When using a pump with energy levels close to the

polariton dispersion, the pumping bandwidth in energy is also a key parameter, with a broadband pumping able to also populate several cavity modes. By convention, we only speak of resonant pumping when a single mode is populated.

Aside from pumping frequency, pumping power is a key parameter in light-matter interactions. Pumping power directly controls the density of excitons, which can then couple to light to form exciton-polaritons. Even in the simple case of resonant pumping, it can be difficult to relate the exciton-polariton density to pumping power. The non-resonant case add additional relaxation processes which further complicate the estimation. The density of polaritons is usually measured on the emission power spectrum rather then calculated from the pump.

In the case of non-resonant pumping, the coherence and time dynamics of the pump are usually lost during the relaxation processes, which is why such pumping is also called incoherent. In particular, ultrafast pulsed lasers, with pulse duration lower than the polariton lifetime, combined with a time-resolved streak camera, can be used to study the dynamics of the polariton system.

Data in our experiments comes from transmission, reflection, or photoluminescence. The signal from the sample can either be imaged directly on a camera (in our experiments, a Thorlabs CMOS Camera), or sent through a slit and then resolved in energy with a spectrometer. The size of the slit gives the spectrometer's resolution in energy, with a smaller slit able to resolve smaller energies. For these experiments, we have used a Spectrometer from Princeton instruments, with the model number "Action Spectra PRO SP-2500". The spectrometer uses a grating to spectrally resolve the wavelength of the signal, with some gratings offering a better resolution for a given wavelength.

The spectrometer CCD uses a Peltier system to cool itself down to $-60°C$ in order to minimise any thermal noise in the system. However, there are two main limitations when measuring data from a spectrometer. The first limitation is the maximum available signal power that the CCD is able to resolve without saturation effects. When the CCD is saturated, the signal bleeds over nearby pixels and the data is less useful. This can be mitigated by the use of neutral density filters optics to reduce the signal, but the optics themselves may provide additional challenges, such as extra reflections, inhomogeneous attenuation or defects. The second limitation comes from random spikes in the signal with a far greater intensity than the collected data. Such spikes may come from cosmic ray radiation. There are several ways to deal with this unwanted signal, including their removal in post-processing as outliers, the reduction of the acquisition time to minimise the chance of picking up such a spike, or alternatively, taking many times the same data to select the ones without parasitic spikes.

Given a particular sample, the basic experimental scheme consists therefore of selecting an input light suitable for the physics we wish to create, shine it onto

a sample, and then collecting the signal to send it on a CCD or a spectrometer. To control the conditions of pressure and temperature, the sample is typically placed in continuous flow Liquid Helium cryostat, which cools it down to 4K. The cryostat has a heater built into it so that the temperature may be raised to reach intermediate temperatures. An example of an experimental scheme, in the reflection geometry, is given in figure 3.1.

This experimental scheme also involves the selection of the right optics in the illumination and the collection path to minimize losses, and the important task of correctly aligning and focusing the illumination path. For example, when working with UV light sources, we select mirrors made of Aluminum as they have better reflection at these wavelengths. Alignment and focus control key experimental parameters such as power density, angle of incidence, and the precise spot of illumination, which control the exciton-photon detuning in wedged samples.

3.2 Pulse shaping

There are also more involved ways to shape the illumination beam. In the case of pulsed lasers, it may be necessary to "shape" the pulse by narrowing it spectrally to achieve a more resonant excitation. This can be done using a pulse-shaper system.

Pulse-shapers work in a similar way to a spectrometer, using a slit and a lens to get a divergent beam, which illuminates a grating, spectrally separating the wavelengths that make up the incoming beam. The spot is then spectrally cut using a slop. As the incoming light is diffracted, the original pulse gets chopped into several smaller pulses. To recombine those chopped pulses, a second grating is necessary. In some geometries, it is possible to reflect the pulse back on the same grating.

An example of a pulse-shaper using these principles is given in figure 3.2.

The quality of the pulse-shaper is characterised by how narrowly it can compressed the incoming pulse of light. This is referred to as the *resolution* of the pulse-shaper. This resolution depends on how efficiently the grating is illuminated, with a fully illuminated grating separating the wavelengths more effectively. Additionally, the focal lengths of the lenses used to create a divergent beam which is then cut help improve the resolution. Specifically, a longer focal length results in a greater spectral separation of wavelengths.

In practice, pulse-shapers are also limited by the power losses. The signal suffers some losses when the pulse hits the grating and some orders of diffrac-

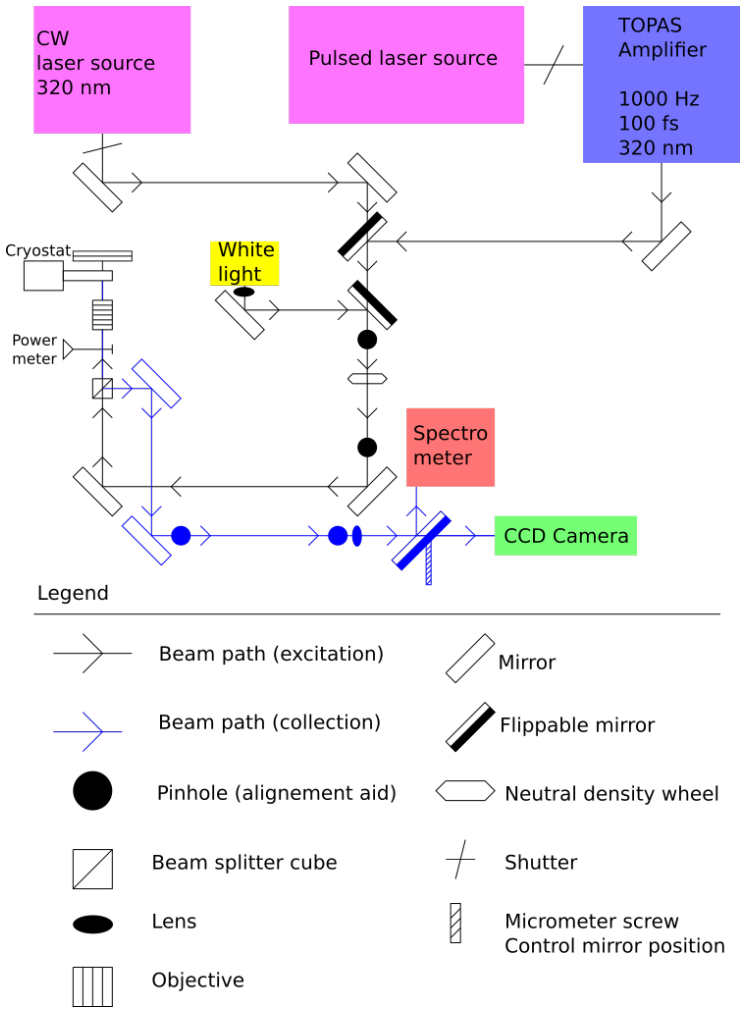

Figure 3.1: Experimental scheme in the reflection geometry, showing the ability to select between three different light soruces (CW laser, pulsed laser, white light) and two different collection processes. This scheme was used for the data collection in chapter 4.

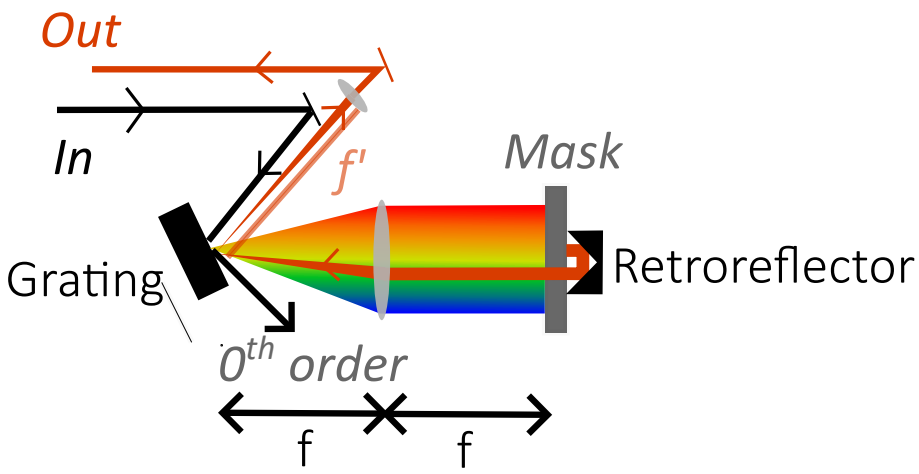

Figure 3.2: An example of a single-grating, two-lenses pulse shaper. The incoming light is diffracted by a grating. The first order of diffraction is collimated by a lens of focal length f. A mask cuts to the desired wavelength. The cut wavelength is reflected on the grating to recombine it into a single pulse. Finally, a second length of length f' collimates the output light.

tion are lost. Similar losses occur when the pulse is truncated to the desired wavelength. The losses result in lower average power. The pulse will also be longer, owning to the well-known inequality $\Delta\omega\Delta\tau \geq 1/2$. In practice, it is sometimes necessary to compromise between optimal resolution and optimal power. Pre-assembled spectrometers can make particularly efficient and stable pulse-shapers. However, another option is to build a spectrometer from scratch, selecting the most efficient grating and focal lengths for the desired pulse resolution.

3.3 Polarisation

In the following discussion, the electric and magnetic field can be used interchangeably. We will consider the electric field as a convention.

3.3.1 Linear polarisers and half-wave plates

The polarisation of the incident light is another degree of freedom for optical experiments. Most sources of light, such as natural sunlight, or light emitted by LEDs, are said to be *unpolarised*.

The direction of the electric field component of the electromagnetic wave has an arbitrary direction on the plane perpendicular to the direction of propagation, changing arbitrarily in time. By contrast, if the direction of the electric field is well-defined, we speak of a linearly polarised light. In a linearly polarised light, the direction of the electric field is constant, but its magnitude changes over time, in accordance with the magnetic field, with the total magnitude $|E|^2 + |B|^2$ remaining constant.

Unpolarised light can be thought of a superposition of several polarised wavefronts, averaged to create a wavefront without any defined polarisation.

An arbitrary polarisation can be imposed to any incident beam in a straightforward manner by the use of *polarisers* and $\lambda/2$-*wave plate* (or half-wave plate).

First, we must transform unpolarised or mixed-polarised light into light with a well-defined polarisation, we use a *polariser*. A polariser has a well-defined axis of transmission, given by an angle θ from the horizontal. Only wavefronts with a polarisation matching θ are transmitted through the polariser. Other polarisations are either absorbed (an effect called dichroism), or reflected at an angle (for example, in polariser beam-splitters). Several materials for absorbing polarisers exists, with the most modern ones using gold or silver nanoparticles embedded in glass plates [258]. In practice, we often use reflective polarisers in experiments. Thin-films or wire-grid polarisers are inexpensive optics suitable for low-power applications, but get damaged at high powers. By contrast, designs such as Glan-Taylor prisms or polariser beam-splitters are needed for high-power applications.

Once the light is linearly polarised, the direction of polarisation can be changed with a half-wave plate. A wave plate is composed of a *birefringent* material, with an optical index varying with the polarisation of light. Such materials are usually specific dielectrics such as quartz, glass or plastics. The optical index changes the *phase velocity* of the wavefront travelling through the glass. One polarisation axis experiences minimum delay (the fast axis), whereas the other experiences maximum delay (the slow axis). After going through the sample, the incident light see its polarisation changed. By changing which axis the incident light goes through, we are able to control how the incident polarisation changes.

In experimental practice, commercially sold half-wave plates have their fast axis indicated on a mount, which can be rotated easily. The range of wavelengths affected by birefringence depends on the material used to make the wave-plate, its thickness, its polish quality, and other aspects of the fabrication process. Experimentally, we select a suitable half-wave plate design depending on the experiment. Unlike polarisers, half-wave plates have very high damage thresholds.

3.3.2 Jones Calculus

In this section, we will give a more mathematical and abstract treatment of polarisation. The polarisation state of the incident beamn will be modelled by a vector, and the different components acting on it can be represented as matrices.

Typically, we speak of *horizontal polarisation* when the electric field is fixed on the x axis of the plane perpendicular to the direction of propagation, and of *vertical polarisation* for the y axis.

The more general polarisation state is a vector on the unit circle of the plane perpendicular to the direction of polarisation, called the Jones vector $\left(e^{i\varphi_x(t)}, e^{i\varphi_y(t)}\right)$. For example, horizontal polarisation has a Jones Vector $(1, 0)$ and vertical polarisation has a Jones vector $(0, 1)$. Unpolarised light is made of several arbitrary Jones vectors.

Optical components acting on the polarisation state are represented by matrices acting on the vector, called Jones matrices. For example, in the case of a half-wave plate with a fast axis having an angle θ to the vertical axis, the Jones matrix reads:

$$e^{-\frac{i\pi}{2}} \begin{pmatrix} \cos^2\theta - \sin^2\theta & 2\cos\theta\sin\theta \\ 2\cos\theta\sin\theta & \sin^2\theta - \cos^2\theta \end{pmatrix} \tag{3.1}$$

The half-wave plate thus changes the polarisation by a controllable angle θ. In the case of unpolarised light, it acts on all the components of the unpolarised states, which means it leaves it unpolarised.

$$\begin{pmatrix} \cos^2\theta & \cos\theta\sin\theta \\ \cos\theta\sin\theta & \sin^2\theta \end{pmatrix} \tag{3.2}$$

By contrast, an horizontal polariser with an axis of transmission along the x axis would read:

$$\begin{pmatrix} 1 & 0 \\ 0 & 0 \end{pmatrix} \tag{3.3}$$

Such a matrix would cut off all non-horizontally polarised components from the incident light. Jones calculus using matrices and vectors is useful to model complex optical setups, as subsequent optical components can all be represented by matrices and the total effect of the components is represented by multiplying the matrices together.

Polarised light is useful experimentally when the studied sample presents polarisation-dependant effects, such as birefringence, or so-called TE-TM splitting, in which case the optical response of the sample changes depending on

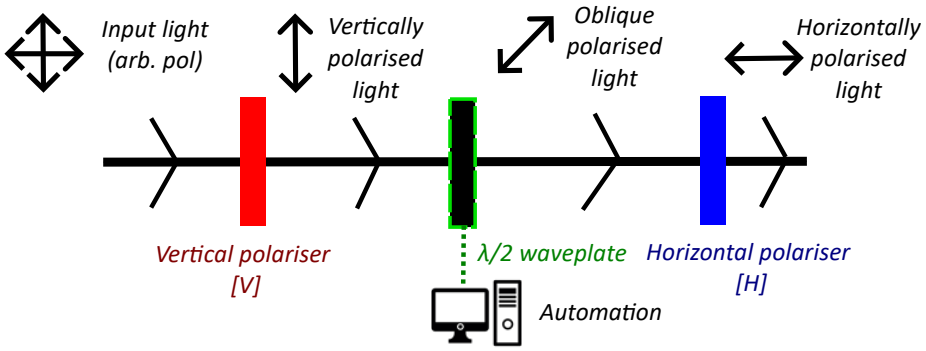

Figure 3.3: Automated polarisation setup for power dependency.

whether or Electric or the Magnetic field is transverse to the sample. In such experiments, it is very useful to precisely control how the electric and magnetic fields are positioned in the plane perpendicular to the direction of propagation.

3.3.3 Power attenuation

There are also more practical uses to polarisation-controlling optical components. For example, they can be used as a way to precisely control the incident power of an excitation laser on the sample. The process is described in figure 3.3. It consists of taking a vertically polarised light, making it pass through a wave-plate with an arbitrary angle, and then pass through a polarised with a fixed angle, which by convention we will considered to be horizontally polarised. If the half-wave plate is also horizontally polarised, then the polariser is at maximum transmission and lets all the light through. By contrast, if the half-wave plate is vertically polarised (at a $\phi = \pi/2$ angle with the polarised), then the polariser would not let any light in transmission at all. In practice, the polariser has finite minimum transmission, and also incurs small losses at maximum transmission. The ration between the maximum and minimum transmission is called the *extinction ratio* of the polariser, and commercial Glan-Taylor polarisers claim ratios as high as 10^5.

The attenuation scheme with polarisers has several advantages compared to the use of neutral density filters. In particular, it is homogeneous across the full beam waist, which is not the case for the commercially sold neutral density filter wheels with continuously varying attenuation across the glass, making them unsuitable for larger beam waist. The main advantage, however, is that the attenuation process can be automated by placing the half-wave plate on a motorised mount, which can be remotely controlled by a software. A digital power meter can be added to the system, and the software can rotate the half-

wave plate, record the resulting power. A power dependence experiment can be fully automated in that fashion, and by going from 0 to π, a continuous ramp-up and ramp-down of the incident power is achieved, which can be useful to investigate hysteresis effects. A more elaborate software program can use the power meter readings as feedback to find out the precise fast-axis angle for a selected power. However, typical laser fluctuations are on a very fast time scale, whereas the response time of a motorised mount is on the order of a few seconds. As a result, such a setup cannot correct fluctuations in the laser power. Electro-optic modulators [259] can be used in such cases, but have their own limitations, such as not being suitable for pulsed lasers.

Automation can also easily measured the polarisation of a given wave, by measuring transmitted power against the fast axis orientation of a polariser, which results in an angular plot. Unpolarised light will have the same transmitted power regardless of polariser orientation, and the pattern will be circular, whereas strongly polariser light will stronger transmission for a particular orientation of the fast axis.

3.3.4 Elliptical polarisation

In addition to the linear polarisation of light, in which the direction of the electric field is constant, and the unpolarised case, in which it varies randomly over time, the light be *elliptically polarised*, and the electric field vector varies continuously in direction and magnitude (with the magnetic field vector varying according to keep a constant magnitude), tracing an ellipse in the $(\mathbf{E}, \mathbf{B})$ plane. In the limiting case, when the magnitude of E remains constant, we speak of *circularly polarised light*.

To change the ellipticity of a given wave, we use a *quarter wave-plate*. Circular polarisers, which select only a given degree of ellipticity, can be constructed by using a quarter wave-plates and a linear polariser as shown in figure 3.4.

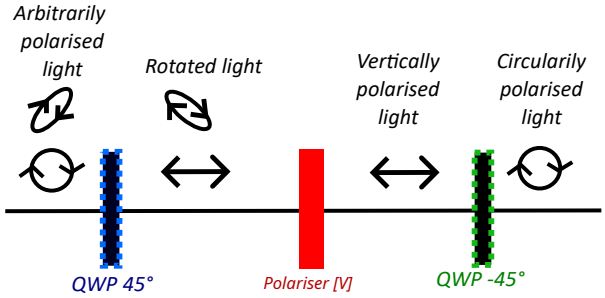

Figure 3.4: A circular polariser consisting of two quarter wave-plates and a linear polariser. The input is light with arbitrary polarisation. The first quarter wave-plate (QWP) rotates the light so that the desired circular polarisation becomes a vertical linear polarisation. The linear polariser filters all but the vertical linear polarisation, which is then rotated back to the desired circular polarisation.

3.4 Time-resolved spectroscopy and pump-probe experiments

Exciton-polaritons are an out-of-equilibrium phenomenon with continuous dissipation as the particles leak through the cavity mirrors and are replenished with a pumping laser. When the pumping laser is pulsed, the dynamics of the system become accessible.

The most direct way to obtain time-resolved data involves using a Streak camera apparatus. This device can be mounted on some spectrometers to access the time evolution of a signal in a very precise manner, with time resolution as fine as 0.2fs.

However, the high cost of Streak cameras can be a barrier to their use in routine experiments. They also require relatively weak signals to resolve the time-data effectively, as they can saturate at higher power levels. In this section, we present an alternative method to access time-resolved data on longer time scales, with higher output power, but at the cost of less accurate time resolution.

The experimental setup consists of using a pump-probe setup with a variable delay between the high power pump and the low power probe. In practice, the high-power pump populates the exciton-polaritons in the microcavity, and the low-power probe measures their non-linear properties in the transmission spectrum. By measuring the transmission spectra as a function of the delay between pump and probe, we can access the non-linear dynamics of the exciton-polaritons, and in particular the time scales associated with such dynamics. As

the non-linearity scales with the exciton-polariton density, this method also allows for the determination of exciton-polariton lifetimes.

This scheme requires the use of a synchronised pulsed laser for the pump and the probe so that the delay can be precisely determined and adjusted. In practice, we can use a single laser source that is divided in two optical paths: one for the probe and one for the pump. The probe path can then be attenuated and delayed using a precise motorised stage with a retroreflector. The delay stage varies the position of the retroreflector, thereby changing the beam path length, and as a result the delay between the two optical paths. In practice, the motorised stage is controlled using a software so that the measurement can be automated with measurements taken at multiple delays in a single run. The delay stage however needs to be calibrated for the $\tau = 0$ delay which corresponds to to two beam paths of identical lengths.

Without a Streak camera, the measured signal is averaged at time scales usually much greater than the relevant time scales for the experiments, typically on a millisecond time scale. This much greater than the experimental time scales of nanoseconds.

As a result, the signal for the pump is also collected. To solve this problem, the pump signal is *filtered in polarisation*. An arbitrary linear polarisation (for example, vertical) is imposed to the pump signal, and an orthogonal polarisation (in this case, horizontal) is imposed to the probe signal. The collected signal after the sample is filtered by the use of a polariser which only lets through horizontally polarised light, rejecting the signal resulting from the pump while transmitting the signal from the probe.

For this technique to work, the extinction ratio of the polariser must be greater than the ratio between the pump and the probe. For example, if the extinction ratio is 10^6, and the ratio between the pump and the probe is 10^3, then after the polariser the probe signal will be $10^6/10^3 = 10^3$ times stronger than the pump signal. Such an experimental scheme is shown in figure 3.5.

In addition to measuring the transmitted signal as a function of time delay with fixed pump power, the experiment can also be conducted with fixed time delay and variable pump power. Combining the two techniques, we get a two-dimensional map of the probe signal in transmission, as a function of pump power and time delay.

The pump-probe experimental setup is relatively straightforward to setup, can be automated, and allows for investigation of longer-scale dynamics. However, it requires the non-linear response to be polarisation-independent, as the pump and probe always have orthogonal polarisations, and that it assumes the sample does not alter the polarisation of transmitted light. In the case of polariton lasing, for example [139], this assumption does not hold, as spontaneous

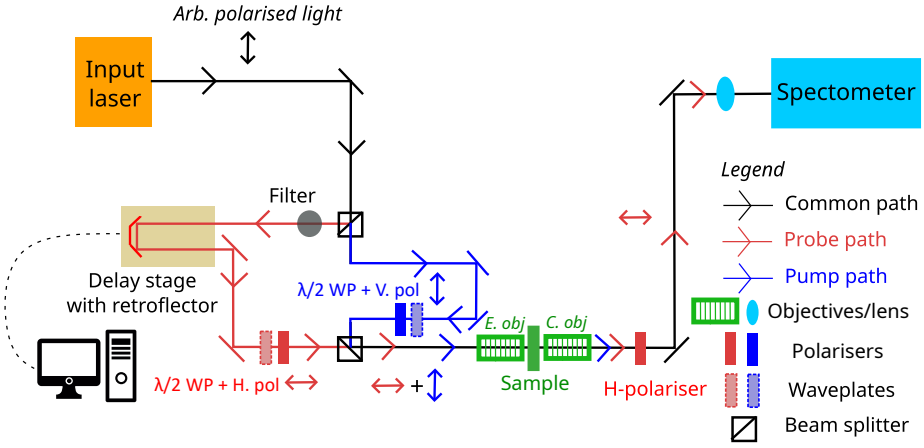

Figure 3.5: Experimental pump-probe scheme filtered in polarisation. The pump and probe are separated by a beam splitter, a controllable delay is added to the probe path, and they are given orthogonal polarisations with a half-wave plate ($\lambda/2$ WP) and a polariser (H. pol and V.pol). After they illuminate the sample, the pump signal is filtered by a polariser. This scheme was used for the data collection in chapter 5.

polarisation occurs.

3.5 Interferometry

The transmitted signal from the sample provides information about the amplitude of exciton-polariton signal. However, in many experiments, we are interested in how the phase of the exciton-polaritons varies across the sample. A phase measurement is only meaningful as a relative phase compared to a chosen reference. The best way to access to the phase difference is to build an interferometer between a signal beam and a reference beam.

Interferometry is typically used to measure the coherence of a beam by the use of Mach–Zehnder or Michelson interferometer, in which a beam is separated using a beam splitter, and an arbitrary delay τ is imposed on one arm of the interferometer. When the two beams met, they produce an interference pattern with a visibility $\mathcal{V}$, defined by:

$$\mathcal{V} = \frac{I_{\max} - I_{\min}}{I_{\max} + I_{\min}} \tag{3.4}$$

Where $I_{\min}$ and $I_{\min}$ are the maximum and minimum intensity of the interfered signal. The visibility of an interfered signal with delay τ can then be related to the first order coherence $g^{(1)}(\tau)$ by the formula:

$$\mathcal{V} = |g^{(1)}(\tau)| \tag{3.5}$$

In the specific case of measuring the phase, we fix $\tau = 0$. As $g^{(1)}(0) = 1$ for all signals, the visibility is maximised, yielding $\mathcal{V} = 1$. The measured data is no longer the contrast of the interference pattern, but rather the pattern itself. We have the two beams undergo different optical optical paths, one of them being a signal beam, and another acting as a reference beam.

In practice, we can choose between two types of reference beams. The first method is to split the input beam before it illuminates the sample, and then have one arm illuminate the sample, while the other does not. The two arms of the interferometer then meet at a beam splitter resulting in an interference pattern which is imaged on a CCD Camera. For the interference pattern to be optimal, the reference and signal beam need to be of equal intensity and synchronised, with an equal travel time on both arms. This requirement translates to having equal travel distances. The delay stage can be used on the reference arm of the interferometer to precisely control its length, in a similar way to pump-probe experiments, but in this case calibrated to ensure zero delay. In optimal conditions, if the phase difference is equal to π, the interference is destructive and the interference pattern will show no signal, and if the phase difference is equal to 0, then the interference is constructive and the interference pattern will show a maximum signal.

This experimental scheme allows to measure any change on the phase imparted by interaction with the sample. Another technique consists of using the

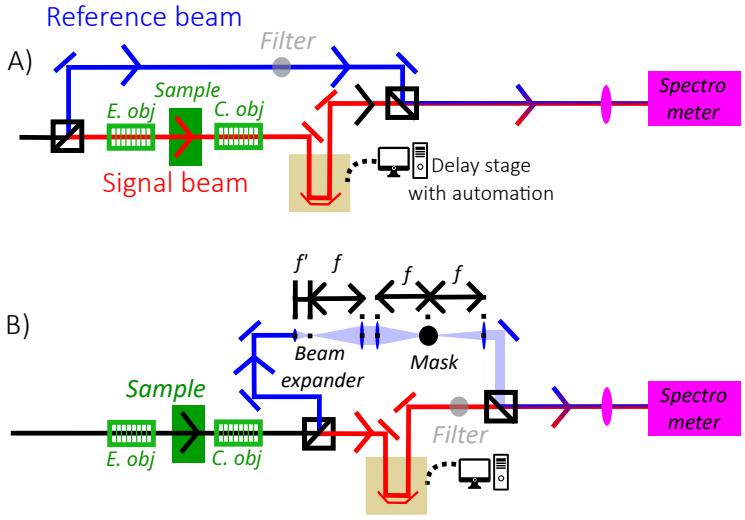

Figure 3.6: Comparison of the two interferometry setups. In A), the reference beam is split off before hitting the sample and the excitation (E. obj) and collection (C. obj) objectives. It needs to be attenuated to get equivalent powers on both arms of the interferometer. This is the common Mach–Zehnder geometry. In B), the reference beam is split off after the sample. It is expanded and imaged into a mask. The cut-off image is then interfered with the signal beam. The signal beam needs to be attenuated with a filter to get equivalent powers.

signal from a small region of the sample as a reference. Experimentally, the signal from the sample is split, and in the reference beam arm of the resulting interferometer, it is imaged on a slit and then cut to a narrow region, and then expanded using a telescope made of lenses. The phase across this small region of the emitted beam is assumed to be constant, but this is not the case in practice. The process of slicing the reference image and then expanding it results in a loss of power, and the process is also limited by the physical size of the optical slit. An alternative technique consists of using an expanding telescope on the reference image without cutting it, so that the beam size of the region of interest matches the beam size of the full signal beam. This experimental scheme gives access to the phase difference across the sample, in particular whether or not the phase is homogeneous. A comparison of these two experimental setups is given in figure 3.6.

A limit inherent to interference measurements is the coherence of the signal and the reference beam being interfered. A meaningful interference can only occur if the length of the interferometer's arms is smaller than the coherence length of the sources. In practice, for laboratory-grade lasers, the coherence length is in the order of tens of meters and as such is long enough. However, a long interferometer may suffer from instabilities inherent to the system (vibrations,

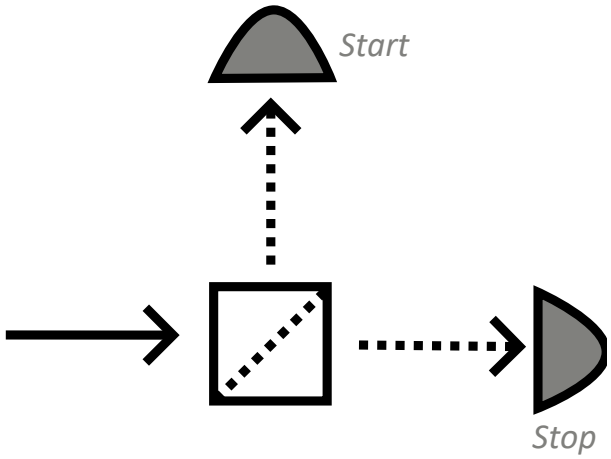

Figure 3.7: Simplified setup of the experiment used in [175]. The beam is split in two paths, with two detectors 'START' and 'STOP'. When a photon is detected on the 'START' path, a clock is triggered. The clock stops when a photon is detected on the 'STOP' path. The coincidence counts are recorded by measuring the value of the 'STOP' detector with fixed time delays. Figure inspired by [260].

laser variations) and it is preferable to keep it as short as possible.

The measurement of second-order correlation functions is more complex as it requires two synchronised high-precision single-photon detectors, as was described in [175]. A simplified version of the setup is given in figure 3.7.

3.6 k-space measurements

The experimental setups we have described thus far, for example, in figure 3.1, all measure the "real space" or the direct space of the sample, probed by the transmitted or reflected beams. In white light, for example, it is possible to observe the surface of the sample, with its defects and features. This direct observation of the sample can also be done in the CCD of the spectrometer in the so-called zero order.

In many cases, the real space data is the main data of interest, for shifts in energy emission, intensity, or for scattering of the polariton superfluid. However, there are also key information contained in the so-called reciprocal space, also called k-space. Most importantly, the full polariton dispersion can be resolved in k-space, including its anti-crossing, if both the lower polariton branch and

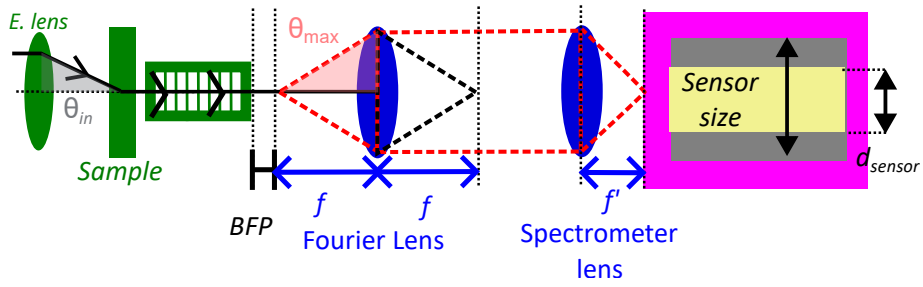

Figure 3.8: Example of a basic Fourier imaging setup, with a non-zero angle of incidence θ_{in}. The Fourier lens images the back focal plane (BFP) of the collection objective. The Fourier image path is in red, and the real space image path is in black. With the Fourier lens, only the k-space image (red) is collected, with a maximum angle θ_{max}. The real space image (black) is defocused. The Fourier lens can be mounted on a flip mount to switch between real space and k-space.

the upper polariton branch are populated.

The blueshift in energy of the polariton branch and the strong emission from its bottom point at $k_{\|} = 0$ in the case of polariton lasing are among the experimental features only visible in k-space. And conversely, many experimental parameters of polariton experiments can be controlled by measurements in k-space. The most significant one is the so-called "magic angle" of incidence that is required to pump a microcavity in the OPO regime, as was discussed in section 2.5.2. Another example is how a large dispersion in momentum is required to create a polariton soliton, as was discussed in section 2.5.3. And finally, the superfluid regime depends on the polariton group velocity, which is controlled by pumping the sample at a given momentum. This momentum is directly related to the pumping angle and the pumping wavevector.

Measurements in k-space can be done in a relatively straightforward manner, with a spectrometer and a lens. The Fourier lens is placed to collect light on the back focal plane of the collection objective. Such lenses are usually mounted on flip mount which can be raised or lowered if a real space or k-space measurements needs to be done.

Control over the pumping wavevector can also be readily achieved. A beam that passes through the centre of the excitation lens will pump the sample with a $k_{\|} = 0$ wavevector. The wavevector can be controlled by shifting the beam to the left or to the right of the excitation lens. This can be done with a micrometer stage. An example of a setup with k-space measurement and control over the incident wavevector is given in figure 3.8.

The raw data measured by the spectrometer is an image on the CCD of x by y pixels. In must be calibrated in energy and wavevectors. The pixels on the x axis represent the energy, and the calibration can be done by the spectrometer software, accounting for the grating, and its resolution is limited by the entry slit.

The pixels on the y axis represent the wavevectors. The calibration of this axis involves the following calculations.

The Fourier space lens is characterised by its numerical aperture NA. It will focus a collimated beam with an opening angle $\theta_{\max}$ given by the equation $NA = n \sin \theta_{\max}$, where n is the refractive index in which the lens is working. On the detection side, we will get an image of Δy pixels. We can first find out the total angular dispersion is able to resolve by inverting the equation for NA:

$$\theta_{\max} = \arcsin \frac{NA}{n} \tag{3.6}$$

Thus the calibration of the angular dispersion is given by $\Delta y = 2 * \theta_{\max}$. The angular resolution is then given by:

$$1\text{px} = \delta\theta = \frac{2 * \theta_{\max}}{\Delta y} \tag{3.7}$$

The calibration in wavevectors is then a simple conversion process using equation 2.16, assuming a sinusoidal dispersion, which is valid for small angles. k_0 is calculated by measuring the bare cavity mode energy $\hbar\omega_0$ and then using the dispersion relation 2.17. Alternatively, it can be read directly on the energy axis of the spectrometer, with the relation:

$$k_0 = \frac{2\pi}{\lambda_0} \tag{3.8}$$

Where λ_0 is the wavelength at the bottom of the lower polariton branch.

Experimentally, there is a compromise between access to the full polariton dispersion (which requires a high $\theta_{\max}$), and angular resolution, which is limited by the number of pixels.

The total opening angle is related to the numerical aperture, which itself is related to the lens focal length f by:

$$NA = n \frac{D}{2f} \tag{3.9}$$

Where D is the lens entrance pupil, effectively, its diameter. With a fixed pixel count Δy, lens with a large focal length will have a lower NA, thus a lower maximal range $\theta_{\max}$, but a lower $\delta\theta$ and a better resolution. Conversely, a lens with a smaller focal length will see more angles, but with less precision.

The size of the image Δy is another parameter. Physically, it is given by the spot size of the CCD sensor d_{sensor}, and depends on the spot size in Fourier space d_{Fourier}. d_{Fourier} depends on the optics of the systems, such as the excitation objective, and the back focal length of the collection objection. On the collection path, the image in Fourier space can be changed, for example with telescopes or masks.

In the simplest case of figure 3.8, we have Fourier lens of focal length f and a lens focusing on the slit of the spectrometer of focal length f'. The size of the image d_{sensor} is given by:

$$d_{\text{sensor}} = d_{\text{Fourier}} \frac{f}{f'} \tag{3.10}$$

Thus the size of the image can be controlled by selecting the right f'. In particular, an image size larger than the CCD sensor must be avoided, as it is not possible to calibrate. In practice, f' is typically selected so that the image is equal to three-fourths of the CCD sensor, leaving the number of pixels Δy unambiguous and thus resulting in easy calibration.

3.7 Conclusion

There are many experimental techniques to create exciton-polaritons with very precisely defined parameters such as energy, wavevector, and in the case of pulsed lasers, pulse duration and pulse width, using optical components on a tabletop. This freedom of experiment design enables a lot of flexibility in pumping schemes and collection schemes, including pump-probe experiments or interferometry.

This experimental freedom, however, usually involves making several compromises between desired experimental parameters. A common example is the compromise between peak pulse power and the narrowness of pulse widths when using a pulse-shaper.

Overall, the experimental techniques involving exciton-polaritons are varied and allow for many different experimental schemes with control over many different parameters at the same time, while using straightforward transmission or reflection geometries. This wealth of experimental techniques plays a major role in polariton research, as it enables scientists to probe many different phenomena.

Chapter 4

Polariton lasing in III-N microring geometry

In this article, we have realised a polariton laser in a AlGaN cavity with a microring geometry, confining the light using total internal reflection. The excitons are confined using GaN/AlGaN quantum wells. The laser is operating up to room temperature, which is an expected an important properties of III-N systems as we have described in section 2.4.1.

An important challenge is when claiming polariton lasing is to rule out the possibility of "regular" weak coupling lasing, which we have described in section 2.3.2. As we are using ring resonators rather than a Fabry-Perot cavity, we do not have access to the full polariton dispersion to resolve this ambiguity. Instead, we use several of the techniques outlined in section 2.6.4, for example, the reduction of the Free Spectral Range and a sharp threshold when lasing occurs. The non-linearities of the polariton system are described and analysed, showing blueshift as power increases, until a saturation and a thermal redshift at very high laser powers. Interestingly, when studying the non-linearities (such as in figure 4), we can see that the higher energy polariton modes – which are more excitonic – blueshift more than the lower energy ones.

One challenge of this experiment is that many cavity modes hybridise with the excitons to create multiple polariton modes in the cavity. This is the regime of "coexisting condensates". The resulting mode competition reduces the non-linearity. In the ring resonator geometry, the polariton condensate propagates across the ring, and it is possible to collect it from the opposite of the excitation side. At higher temperature, the lasing signal is much stronger, which is an interesting feature clearly visible in figure 3.f.

We have also noted that the emission intensity is very highly dependant on the precise illumination spot and collection window. Further work on these samples could involve a study of their threshold power and threshold intensity as a function of temperature. Given the similarity between 4 K and 200 K, and the sharp difference between 200 K and 300 K, we expect a non-linear trend. A more thorough study of the threshold dependence to temperature was not possible for the lack of time.

My contribution, as an author to this paper, was experimental. I have run the experiment, collected and processed the data for all the figures of the main paper, as well as several in the supplementary material. I wrote much of the main text, in particular, the section which analyse the figures and use them to justify our claim at polariton lasing. Over exchanges with co-authors, we have also performed additional measurements of the width of the non-polariton exciton modes to rule out a system above the Mott transition. I have also wrote the main draft of the article and was involved in the response to referees over the peer review process.

This article plays into the topic of non-linear effects in exciton-polaritons by displaying spontaneous coherence build-up, in the form of Bose-Einstein condensate, at room temperature, and several key features of this phenomenon are identified.

After publication, this paper was cited as a reference and as comparison by other realisations of polariton lasing in different materials and geometries.

Polariton lasing in AlGaN microring with GaN/AlGaN quantum wells

Cite as: APL Photon. 8, 021 302 (2023); doi: 1 0.1 063/5.01 321 70
Submitted: 27 October 2022 • Accepted: 9 January 2023 •
Published Online: 2 February 2023

Anthonin Delphan,[1] Maxim N. Makhonin,[1] Tommi Isoniemi,[1] Paul M. Walker,[1] Maurice S. Skolnick,[1] Dmitry N. Krizhanovskii,[1] Dmitry V. Skryabin,[2] Jean-François Carlin,[3] Nicolas Grandjean,[3] and Raphaël Butté[3,a)]

AFFILIATIONS

[1] Department of Physics and Astronomy, University of Sheffield, Sheffield S3 7RH, United Kingdom
[2] Department of Physics, University of Bath, Claverton Down, Bath BA2 7AY, United Kingdom
[3] Institute of Physics, École Polytechnique Fédérale de Lausanne (EPFL), CH-1015 Lausanne, Switzerland

[a)] Author to whom correspondence should be addressed: raphael.butte@epfl.ch

ABSTRACT

Microcavity polaritons are strongly interacting hybrid light–matter quasiparticles, which are promising for the development of novel light sources and active photonic devices. Here, we report polariton lasing in the UV spectral range in microring resonators based on GaN/AlGaN slab waveguides, with experiments carried out from 4 K up to room temperature. Stimulated polariton relaxation into multiple ring resonator modes is observed, which exhibit threshold-like dependence of the emission intensity with pulse energy. The strong exciton-photon coupling regime is confirmed by the significant reduction of the free spectral range with energy and the blueshift of the exciton–like modes with increasing pulse energy. Importantly, the exciton emission shows no broadening with power, further confirming that lasing is observed at electron–hole densities well below the Mott transition. Overall, our work paves the way toward the development of novel UV devices based on the high-speed slab waveguide polariton geometry operating up to room temperature with the potential to be integrated into complex photonic circuits.

Microcavity polaritons are hybrid light–matter quasiparticles, arising from strong exciton–photon coupling in semiconductor photonic structures. They have attracted significant attention in the last 15 years with a number of fundamental effects observed such as polariton condensation[1] and lasing,[2] superfluidity,[3] solitons,[4] polariton blockade,[5] and single polariton nonlinearity,[6] to name just a few, which are enabled by giant polariton interactions. Interacting polaritons are highly promising for the development of novel quantum light sources, photonic nonlinear simulators,[7] logic gates, and quantum optical signal processing.[8]

Polariton lasing, the coherent light emission from polariton condensates, provides several advantages over standard photonic lasing, including operation without population inversion with a threshold lower than that in conventional semiconductor lasers.[9] It has been demonstrated via optical[2,10] and electrical pumping.[11] Room temperature (RT) operation has been reported in structures based on wide bandgap semiconductors[10,12,13] enabled by their large exciton binding energy. Polariton lasing has been mainly studied in planar semiconductor microcavities (MCs) made of two Bragg mirrors, which are challenging to fabricate. On the other hand, polaritons have also been investigated in the slab waveguide (WG) geometry,[14,15] where photonic confinement in the vertical direction arises from total internal reflection (TIR). The main advantages of the WG geometry over MCs are low disorder due to thinner and simpler structures and the high polariton speed, enabling long propagation distances up to several hundreds of μm, which makes this system favorable for the development of integrated polariton circuits. A number of nonlinear effects arising from giant optical Kerr-like polariton nonlinearity, such as dark and bright solitons,[16,17] continuum generation,[18] and ultrafast pulse modulation,[19] have been reported in the WG polariton platform.

III-nitride based polaritons are of particular interest since they enable coherent emission and low threshold ultrafast nonlinear

optical modulation in the UV spectral range and can operate at RT[19] with many potential applications including studies of chemical reactions, coherent Raman spectroscopy, and manipulation of trapped ions. UV polariton lasing in III-nitride WG devices has been reported only recently in GaN ridge resonators up to 150 K, likely limited by the smaller exciton binding energy in bulk GaN[20] compared to that in quantum heterostructures.

In this paper, we report polariton lasing in microring resonators fabricated from GaN/AlGaN quantum well (QW) slab WGs with operation in a wide temperature range from 4 to 300 K enabled by the large exciton binding energy in the GaN QWs (~48 meV) and a lower surface state recombination velocity than their III-arsenide counterparts.[21] Polariton lasing from the multiple ring resonator modes is revealed by the threshold-like dependence of the emission intensity with increasing pump pulse energy. The free spectral range (FSR) between the modes reduces as the polariton energy approaches that of the exciton due to the strong dependence of the polariton group velocity on the photonic fraction of the polaritons, a clear signature of strong exciton–photon coupling. Furthermore, a strong blueshift of the lower polariton exciton-like states with increasing pulse energy is observed due to polariton interactions.

Apart from the development of coherent UV polariton sources, our demonstration of microring polariton resonators also paves the way toward further applications in integrated polariton circuits (e.g., filtering and directional coupling) and studies of low threshold generation of frequency combs and Kerr solitons.

Our microring resonators are formed by etching an AlGaN planar slab WG containing multiple GaN QWs,[15] which was grown by metal–organic vapor phase epitaxy on *c*-plane free-standing GaN substrate. Propagating polaritons have been demonstrated in similar unetched planar WGs with a Rabi-splitting of ~60 meV.[15] The confinement induced by the ring geometry is expected to lead to discrete clockwise and counterclockwise ring polariton modes. The samples are fabricated by means of e-beam lithography and reactive ion etching.

After etching, the total height of the structures amounts to ~315 nm [Fig. 1(a)]. Rings of different radii (R) and widths (t) have been etched on the sample. The radius is measured from the center to the mid-point of the ring. Here we studied microrings with R = 3, 4, 6, and 8 μm and t = 2 μm. A scanning electron microscopy (SEM) image of a typical microring (R = 3 μm and t = 1 μm) is shown in Fig. 1(b) (see also Fig. S1 in the supplementary material).

We study polariton lasing over a wide range of temperatures (T = 4–300 K) by using a continuous flow liquid helium cryostat. A standard microphotoluminescence (μ-PL) setup allows us to excite and collect light emission at different spots on the sample in a backscattering configuration [see Fig. 1(b)]. Pulsed laser excitation is performed with a frequency-quadrupled optical parametric amplifier (TOPAS) pumped by a Ti:sapphire regenerative amplifier. The excitation pulses were centered around 320 nm and had a duration of 100 fs and a repetition rate of 1 kHz. The PL signal collected by a microscope objective (NA = 0.39) is sent to a spectrometer with a resolution of 0.16 nm while being integrated over the entire rectangular entrance slit of the monochromator.

The optical resonances in the ring structures occur when the circumference of the ring is an integer multiple (m) of the polariton wavelength. This condition can be written as $k(E)2\pi r_{\text{eff}} = 2\pi m$, where $k(E)$ is the polariton wavenumber at energy E and r_{eff} is

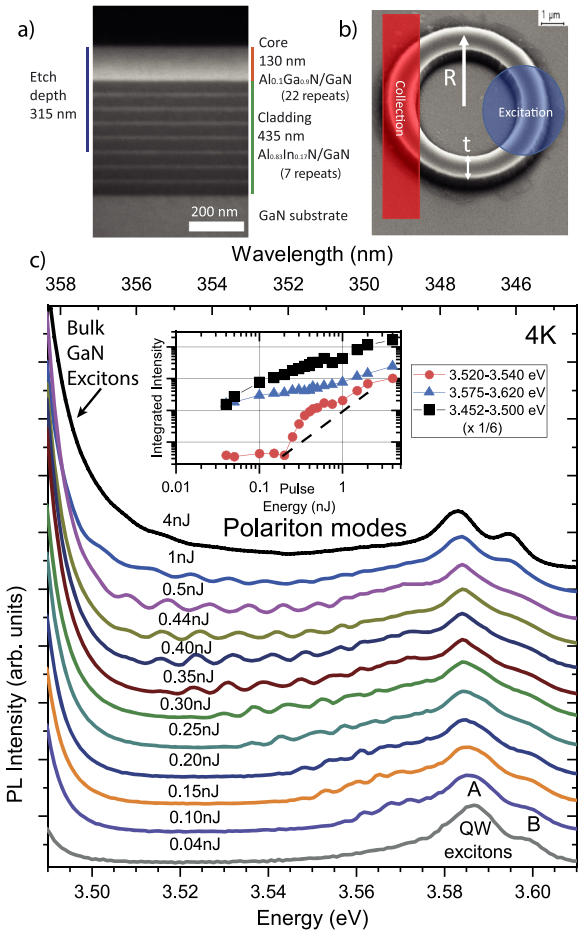

FIG. 1. (a) Cross-section scanning electron microscopy (SEM) image of the waveguide structure with relevant geometric parameters. (b) SEM image of a ring resonator at a tilted angle of 30° from the surface normal, R = 3 μm and t = 1 μm, with overlaid excitation and collection areas. (c) PL spectra (linear scale) of an AlGaN resonator with t = 2 μm and R = 4 μm collected at T = 4 K for pulse energies ranging from 0.04 to 4 nJ. The PL intensity is normalized to the intensity of the QW A exciton: the signal obtained from the exciton is divided by a different factor for each power so that it is equal to unity for all powers. The spectra are then shifted for clarity by half-unity. See also supplementary material Sec. 2. Inset: Integrated intensities (log–log scale) for the region with modes on which background contribution is negligible (red), the region corresponding to the QW exciton (blue), and the region corresponding to the bulk GaN exciton (black). The black dashed line represents a quadratic increase.

the effective radius at which the mode propagates. In addition, the finite thickness of the ring may give rise to quantization of polariton waves along the radial direction and formation of transverse modes characterized by the integer quantum number n. We calculated the optical modes of the circular waveguides using the Lumerical MODE finite difference eigenmode (FDE) solver (see supplementary material discussion 4).

To demonstrate polariton lasing, we carried out a PL pulse energy dependence study on the R = 4 μm and t = 2 μm resonator with pulse energies varying from 0.04 to 4 nJ. The emission spectra

for this entire excitation range at $T = 4$ K are shown in Fig. 1(c). At low pulse energies, the spectra consist of excitonic peaks at ~3.587 and ~3.598 eV associated with QW A and B excitons, as previously reported in studies led on similar wafer samples.[15] Even though the detection and excitation regions are spatially separated, exciton emission in the detection region may arise from the propagation of high velocity upper polaritons away from the excitation spot with their subsequent relaxation into the lower energy low momenta exciton states. Upon increasing pulse energy, narrow full width at half maximum (FWHM) ~3 meV modes start to appear abruptly at energies below the QW exciton peaks, first closer to the QW exciton emission, and then at lower energies down to 3.501 eV between the QW excitonic peaks and the bulk GaN exciton emission (centered at ~3.46 eV) originating from the substrate.

As we argue below, the appearance of these modes with increasing pulse energy is associated with stimulated polariton scattering into the optical ring resonator states, which are in the strong coupling regime with the QW excitons. The bulk GaN excitons are isolated from the ring structure by the cladding layers and thus are only weakly coupled to the resonator modes. Importantly, our polariton system is nonequilibrium: the multiple modes (co-existing condensates) become macroscopically occupied due to the dynamical equilibrium between gain and dissipation channels.[22,23] At 4 K, relaxation to the polariton states occurs mainly through exciton–exciton and exciton–polariton scattering, since at low temperature phonon-assisted scattering is inefficient.[24] Initially, at pulse energies just above the threshold, scattering to the exciton-like polariton states whose energy is close to the QW exciton level is more efficient. With further increase in pulse energy scattering to more photon-like states increases[25] leading to polariton lasing from the lower energy ring states [see Fig. 1(c)]. The macroscopical occupation of the polariton modes is confirmed by the superlinear (threshold-like) increase of the mode emission intensity (integrated in the energy interval where the background from GaN and QW excitons is negligible) with pulse energy, whose dependence is much faster than quadratic, as shown in the inset of Fig. 1(c). If the filling factor of the polariton modes was less than unity, it is expected that enhanced relaxation due to interparticle scattering would lead only to a quadratic dependence. For comparison, we also show in the inset of Fig. 1(c) that the integrated emission intensity exhibits a linear or slightly superlinear power dependence in the energy range where QW and GaN backgrounds dominate, respectively.

We note that in our case the modes are confined in the vertical direction due to TIR and the emission is likely observed due to Rayleigh scattering on fabrication imperfections of the ring resonators.

Below the threshold, the polariton emission from the ring resonator modes is too weak to be detected because the latter is guided in the microring resonator plane. It is only above the threshold that the scattered light from the lasing modes becomes sufficiently strong and comparable to the excitonic background to be coupled to our microscope objective.

The FSR of the ring resonator modes is given by the following equation:

$$\mathrm{FSR} = \frac{\hbar v_G(E)}{r_{\mathrm{eff}}}, \tag{1}$$

where $\hbar$ is the reduced Planck's constant and $v_G(E)$ is the (energy dependent) group velocity of planar slab WG polariton modes at energy E, and r_{eff} is the radius around which the lasing modes propagate. In the strong coupling regime $v_G(E)$ and hence the FSR is expected to decrease strongly with increasing E as the lower polariton dispersion curves strongly toward the exciton level (see supplementary material discussion 5). We investigated the stimulated emission from ring resonators of different radii at 4 K over the wavelength range 346–354 nm, with the raw data shown in Fig. 2(a). The FSR vs energy is summarized in Fig. 2(b). The FSR increases with decreasing ring radius R, as expected from Eq. (1). The FSR also decreases with increasing energy. For $R = 3$ and 4 μm, the FSR decreases drastically by a factor of 2–3 as the energy approaches the exciton level, which is a strong confirmation that the observed modes are in the strong coupling regime. Some trend of decreasing FSR with energy is also visible for $R = 6$ and 8 μm, although the dependence is more noisy for $R = 8$ μm since the FSR becomes comparable to the spectral resolution. The theoretical FSR for purely photonic modes was calculated using FDE as described above and the FSR for polaritons was calculated using the photonic values and a standard coupled oscillator model (see supplementary material Sec. 5). The solid lines in Fig. 2(b) show the theoretical polariton FSR and their curvature is in good agreement with the experiment. The purely photonic FSR theory curves (dashed lines) also show decreasing FSR with energy, which occurs mainly due to the energy dependence of the material refractive indices. However, this curvature is much shallower than that seen in the experiment. In summary, the strong curvature of the FSR vs energy cannot be explained without invoking a strong coupling picture, thus confirming that the system remains strongly coupled while in the lasing regime. Further detail is given in the supplementary material Sec. 5.

Furthermore, we perform measurements on an $R = 8$ μm microring over a wider temperature range up to 300 K. The PL spectra for different pulse energies are displayed in Figs. 3(a)–3(c) for $T = 4$, 200 and 300 K, respectively. At all temperatures, the bunch of narrow ring resonator modes associated with polariton lasing appear below the QW A exciton energy level with increasing pulse energy. As in the case of $R = 4$ μm, the emission intensities integrated in the energy range where modes are the most visible demonstrate a clear threshold-like behavior with a faster than quadratic dependence in Figs. 3(d)–3(f) at all temperatures, indicating macroscopic occupation and lasing of several modes. By contrast, the bulk GaN and QW excitonic peaks behave linearly (see supplementary material Sec. 7). As the data taken at 200 and 300 K sits on a strong incoherent PL background originating from the bulk GaN and the QW exciton emission peaks, this background has been subtracted. The resulting PL spectra are available in the supplementary material (Sec. 6). In the supplementary material (Sec. 5), we plot FSR measurements at 300 K and compare them with the theoretical simulations, which support the strong exciton–photon coupling at room temperature.

While with increasing temperature both the exciton and the polariton emission shift to lower energy due to bandgap reduction, it is also observed that the onset of lasing occurs in more photon-like polariton states at higher T. This occurs because (a) the losses of the exciton-like states with energies closer to the exciton level increase due to phonon scattering, and (b) at elevated temperature, the polaritons can relax to more photon-like states by exciton–phonon

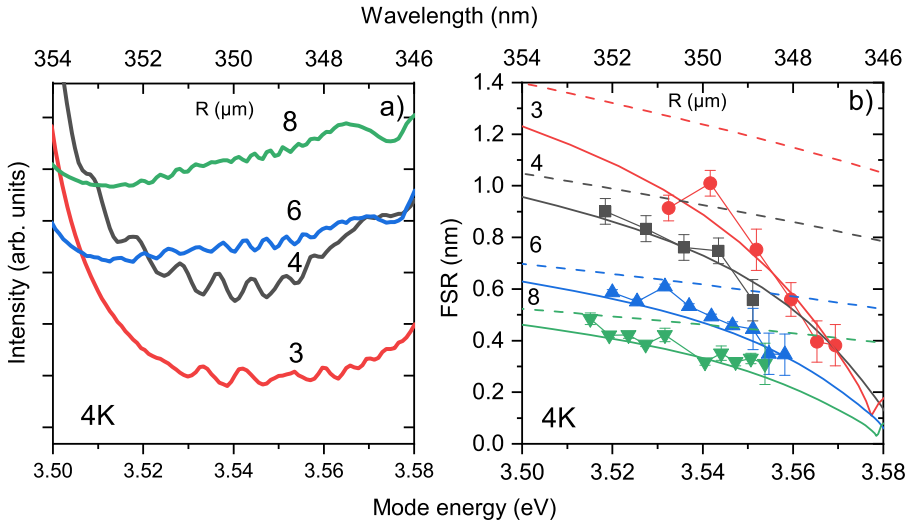

FIG. 2. (a) PL spectra in a linear scale of microring resonators measured for different radii (3, 4, 6, and 8 μm), with a 2 μm width, at pulse energy above threshold (0.4 nJ) taken at 4 K. (b) Free spectral range of the same rings. The solid lines are a fit according to Eq. (1) accounting for the excitonic content of the guided modes. The dashed lines show the results of a purely photonic model. Simulation details and FSR data recorded at 300 K are shown in the supplementary material (Secs. 4 and 5).

as well as exciton–exciton and exciton–polariton scattering.[24–26] The non-radiative processes and polariton losses increasing with temperature also lead to the increase of the lasing threshold from 0.25 nJ at 4 K to 0.35 nJ and ~1.8 nJ at 200 and 300 K, respectively. Interestingly, however, this overall increase in the polariton lasing threshold with temperature remains within a factor of about seven. Such a variation is far smaller than that reported recently for ridge waveguide polariton lasers made from bulk GaN, where the drastic increase in the lasing threshold by more than two orders of magnitude from 70 to 220 K was incompatible with a polaritonic picture that could hold from cryogenic to room temperature.[20] This reduced sensitivity for our sample is again most likely stemming from the quantum heterostructure nature of our polariton gain medium, which leads to stabler excitons. We are also able to explore a significant range of pumping conditions above the threshold with pulse energy values nearly up to an order of magnitude larger than those at the threshold at 4 K for the 8 μm ring resonator [Figs. 3(d)–3(f)] and even beyond one order of magnitude for the 4 μm ring resonator [Fig. 1(c) and corresponding inset].

The excitonic component of the polariton wavefunction leads to strong polariton–polariton interactions responsible for the blueshift of polariton resonances with increasing density. In

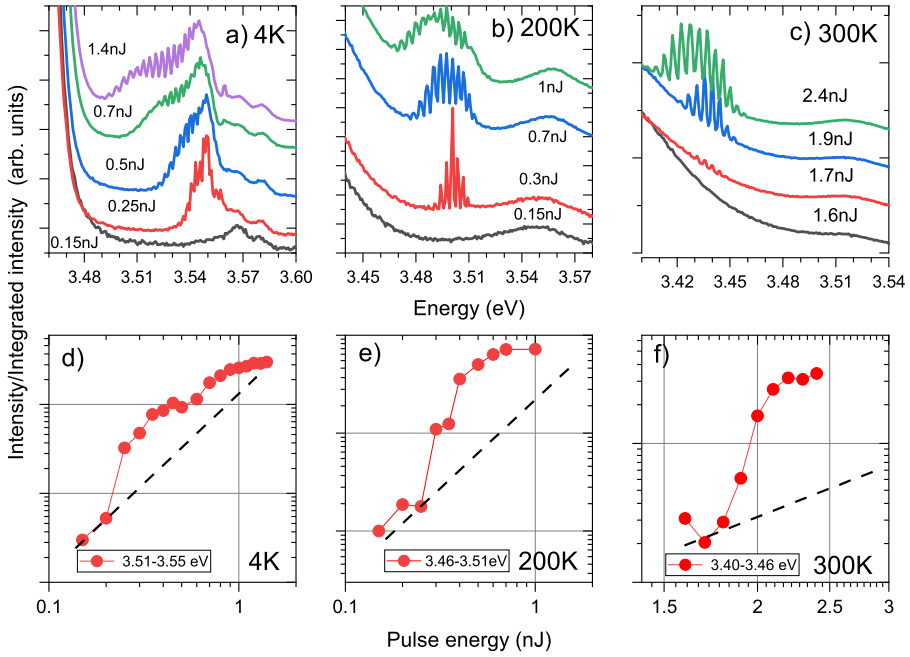

FIG. 3. (a)–(c) PL spectra for the 8 μm radius, 2 μm wide ring at different pulse energies (in nJ) labeled in the figures for T = 4, 200, and 300 K, respectively. Each spectrum is normalized to the QW A exciton (3.566 eV at 4 K, 3.547 eV at 200 K, and 3.511 eV at 300 K) and then shifted for clarity. Non-shifted values and an alternative presentation are given in supplementary material Sec. 2. (d)–(f) Integrated intensity of the modes within given energy boundaries plotted in log–log scale for T = 4, 200, and 300 K, respectively. The black dashed line represents a quadratic increase.

Figs. 4(a)–4(c), we plot expanded spectra for different pulse energies, tracing the peak position of each of the lasing modes. The extracted peak positions of the polariton modes are plotted in Figs. 4(d)–4(f), respectively. As expected, the higher energy exciton-like states exhibit a stronger blueshift with pulse energy than the lower energy photon-like polaritons. At 4 and 200 K, an energy blueshift up to 6–7 meV is observed for exciton-like modes, with the excitonic fraction ranging from 0.91 to 0.24 for 4 K and from 0.57 to 0.21 at 200 K, whereas at 300 K the observed shifts are much less, ~1 – 2 meV, due to the decreased excitonic content of the lasing modes, ranging this time from 0.20 to 0.08, and increased thermal effects, which may lead to a polariton redshift counterbalancing the effect of interactions. Note that only inter- and intra-mode polariton–polariton interactions are responsible for the polariton blueshifts, whereas the interaction with the higher energy exciton reservoir does not play a role since its density is expected to be pinned above the polariton lasing threshold.[27] The evolution of the peak intensity of the modes with pulse energy is finally given in Figs. 4(g)–4(i). The peak intensity is given by the maximum intensity of the mode minus the intensity at the base of the peak. We can see that the modes examined here have a different threshold-like increase at a given pulse energy, and then stagnate or decrease as

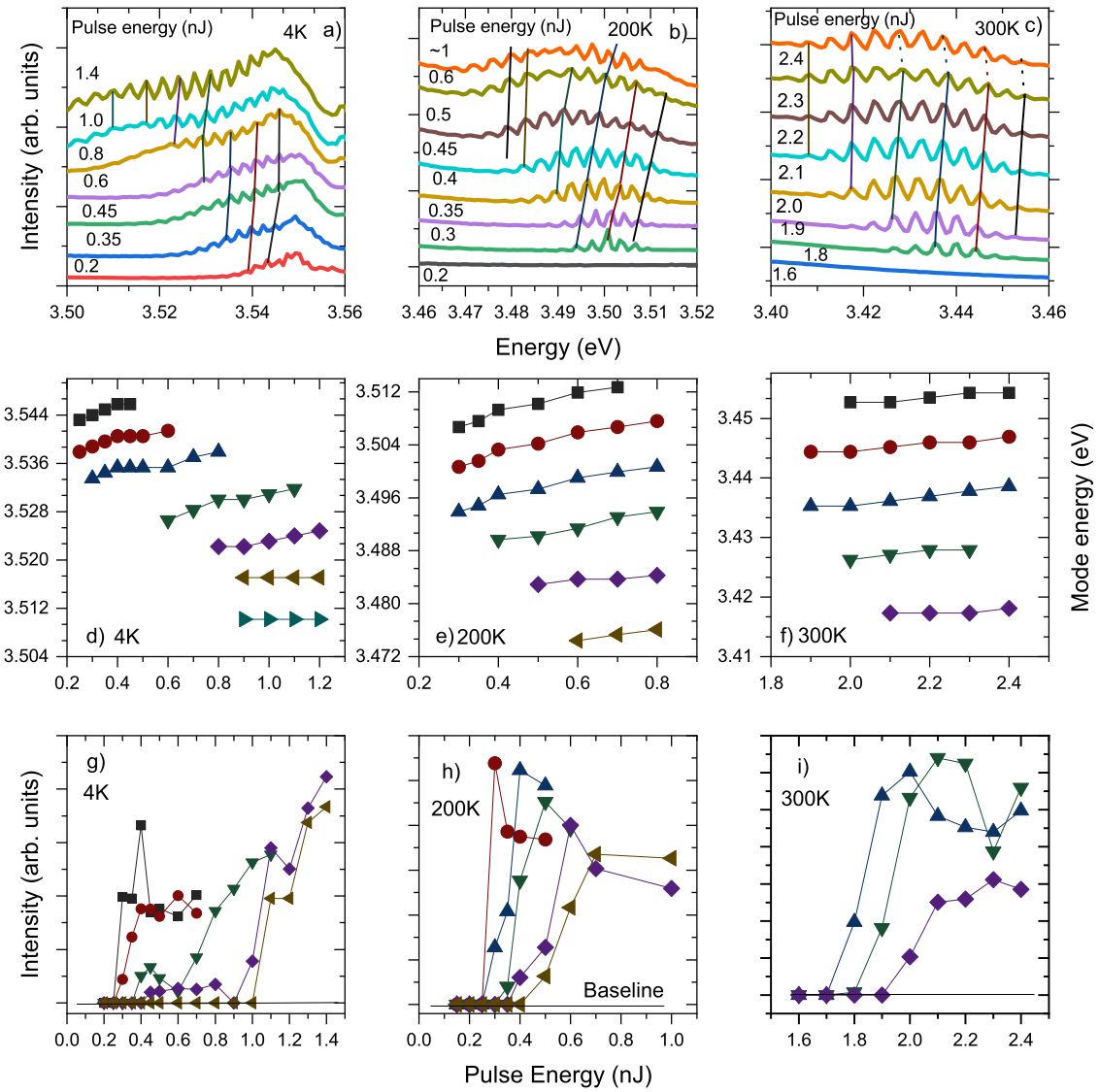

FIG. 4. (a)–(c) PL spectra of the 8 μm ring resonator taken at T = 4, 200, and 300 K, respectively. The solid lines act as guides for the eye to indicate the shift of selected modes with pulse energy. The dashed lines represent points where the shift is less visible. Data are obtained from Fig. 3. (d)–(f) Mode energy vs pulse energy of selected modes, identified by the line color, at 4, 200, and 300 K, respectively. (g)–(i) The peak mode intensity vs pulse energy of selected polariton modes, identified by their line color, at 4, 200, and 300 K, respectively.

more modes, and hence mode competition, come into play. Similar strong blueshifts are seen in the 4 μm ring at 4 K (see supplementary material Sec. 8). Finally, we note that interparticle interactions and mode competition may determine the linewidth (FWHM ~ 2–3 meV) of the lasing modes above threshold (see supplementary material Sec. 3).

Importantly, the fact that the exciton emission line, detected either in the area of the pump spot or on the opposite side of the ring (Figs. 1 and 3), does *not* broaden with pulse energy and shows no or small energy blueshift (~10 meV) confirms that there is a limited screening of the built-in electric field and that the created electron–hole density in each QW is well below the Mott density ($\sim 10^{12}$ cm^{-2}).[28] Indeed, above the Mott density, the emission is expected to originate from an electron–hole plasma with a high energy emission tail extending by 50–60 meV from the exciton peak maxima.[28] This observation is another confirmation that the nonlinear emission is associated with polariton lasing.

In conclusion, we report UV polariton lasing from multiple modes in microring resonators fabricated from AlGaN planar waveguides with embedded GaN quantum wells at temperatures up to 300 K. The micro-structured polariton system we present has the potential to be used to study modelocking of polaritons into a sequence of short pulses, generation of UV soliton trains, and frequency combs supported by giant polariton Kerr nonlinearity. Polariton modelocking was demonstrated numerically for resonantly pumped microring resonators.[29] Beyond this, a non-resonant pump like the one used in this work and a combination of both resonant and non-resonant pumping offer several avenues for further research into the complex interplay between turbulence and modelocking.[30] Additional opportunities should arise from the coupling between two and more rings, which includes combining space topology and modelocking,[31] an aspect not easily within reach with the linear WG geometry. Overall, our work has the potential to be a significant step forward for the development of compact active nonlinear polariton devices operating at RT.

See supplemental document for supplementary material concerning experimental methods and simulation models for polariton dispersion.

We acknowledge the UK EPSRC Grant Nos. EP/V026496/1, EP/S030751/1, and EP/R007977/1. Anthonin Delphan would like to thank Christopher Vickers and Thomas Ball for their help with the cryogenics setup.

AUTHOR DECLARATIONS

Conflict of Interest

The authors have no conflicts to disclose.

Author Contributions

Anthonin Delphan: Conceptualization (equal); Data curation (equal); Formal analysis (equal); Investigation (equal); Methodology (equal); Software (equal); Validation (equal); Visualization (equal); Writing – original draft (equal). **Maxim N. Makhonin**: Conceptualization (equal); Data curation (equal); Formal analysis (lead); Investigation (equal); Methodology (equal); Software (lead); Supervision (equal); Validation (equal); Visualization (equal); Writing – original draft (lead). **Tommi Isoniemi**: Investigation (equal); Methodology (equal); Resources (equal); Writing – review & editing (supporting). **Paul M. Walker**: Conceptualization (equal); Data curation (equal); Formal analysis (equal); Methodology (equal); Software (equal); Visualization (equal); Writing – review & editing (lead). **Maurice S. Skolnick**: Conceptualization (equal); Methodology (equal); Writing – review & editing (supporting). **Dmitry N. Krizhanovskii**: Conceptualization (equal); Funding acquisition (lead); Methodology (equal); Project administration (lead); Supervision (equal); Writing – review & editing (lead). **Dmitry V. Skryabin**: Methodology (equal); Writing – review & editing (supporting). **Jean-François Carlin**: Methodology (equal); Resources (equal); Writing – review & editing (supporting). **Nicolas Grandjean**: Methodology (equal); Resources (equal); Writing – review & editing (supporting). **Raphaël Butté**: Conceptualization (equal); Methodology (equal); Project administration (equal); Supervision (equal); Writing – review & editing (lead).

DATA AVAILABILITY

The data that support the findings of this study are available from the corresponding author upon reasonable request.

REFERENCES

[1] J. Kasprzak, M. Richard, S. Kundermann, A. Baas, P. Jeambrun, J. M. J. Keeling, F. M. Marchetti, M. H. Szymańska, R. André, J. L. Staehli, V. Savona, P. B. Littlewood, B. Deveaud, and L. S. Dang, Nature **443**, 409 (2006).
[2] D. Bajoni, P. Senellart, E. Wertz, I. Sagnes, A. Miard, A. Lemaître, and J. Bloch, Phys. Rev. Lett. **100**, 047401 (2008).
[3] A. Amo, J. Lefrère, S. Pigeon, C. Adrados, C. Ciuti, I. Carusotto, R. Houdré, E. Giacobino, and A. Bramati, Nat. Phys. **5**, 805 (2009).
[4] M. Sich, D. V. Skryabin, and D. N. Krizhanovskii, C. R. Phys. **17**, 908 (2016).
[5] A. Delteil, T. Fink, A. Schade, S. Höfling, C. Schneider, and A. İmamoğlu, Nat. Mater. **18**, 219 (2019).
[6] T. Kuriakose, P. M. Walker, T. Dowling, O. Kyriienko, I. A. Shelykh, P. St-Jean, N. C. Zambon, A. Lemaître, I. Sagnes, L. Legratiet, A. Harouri, S. Ravets, M. S. Skolnick, A. Amo, J. Bloch, and D. N. Krizhanovskii, Nat. Photonics **16**, 566 (2022).
[7] A. Amo and J. Bloch, C. R. Phys. **17**, 934 (2016).
[8] S. Ghosh and T. C. H. Liew, npj Quantum Inf. **6**, 16 (2020).
[9] A. Imamoğlu, R. J. Ram, S. Pau, and Y. Yamamoto, Phys. Rev. A **53**, 4250 (1996).
[10] S. Christopoulos, G. B. H. von Högersthal, A. J. D. Grundy, P. G. Lagoudakis, A. V. Kavokin, J. J. Baumberg, G. Christmann, R. Butté, E. Feltin, J.-F. Carlin, and N. Grandjean, Phys. Rev. Lett. **98**, 126405 (2007).
[11] C. Schneider, A. Rahimi-Iman, N. Y. Kim, J. Fischer, I. G. Savenko, M. Amthor, M. Lermer, A. Wolf, L. Worschech, V. D. Kulakovskii, I. A. Shelykh, M. Kamp, S. Reitzenstein, A. Forchel, Y. Yamamoto, and S. Höfling, Nature **497**, 348 (2013).
[12] F. Li, L. Orosz, O. Kamoun, S. Bouchoule, C. Brimont, P. Disseix, T. Guillet, X. Lafosse, M. Leroux, J. Leymarie, G. Malpuech, M. Mexis, M. Mihailovic, G. Patriarche, F. Réveret, D. Solnyshkov, and J. Zuniga-Perez, Appl. Phys. Lett. **102**, 051102 (2013).
[13] G. Christmann, R. Butté, E. Feltin, J.-F. Carlin, and N. Grandjean, Appl. Phys. Lett. **93**, 051102 (2008).
[14] P. M. Walker, L. Tinkler, M. Durska, D. M. Whittaker, I. J. Luxmoore, B. Royall, D. N. Krizhanovskii, M. S. Skolnick, I. Farrer, and D. A. Ritchie, Appl. Phys. Lett. **102**, 012109 (2013).

[15]J. Ciers, J. Roch, J.-F. Carlin, G. Jacopin, R. Butté, and N. Grandjean, Phys. Rev. Appl. **7**, 034019 (2017).
[16]P. M. Walker, L. Tinkler, D. V. Skryabin, A. Yulin, B. Royall, I. Farrer, D. A. Ritchie, M. S. Skolnick, and D. N. Krizhanovskii, Nat. Commun. **6**, 8317 (2015).
[17]P. Walker, L. Tinkler, B. Royall, D. Skryabin, I. Farrer, D. Ritchie, M. Skolnick, and D. Krizhanovskii, Phys. Rev. Lett. **119**, 097403 (2017).
[18]P. M. Walker, C. E. Whittaker, D. V. Skryabin, E. Cancellieri, B. Royall, M. Sich, I. Farrer, D. A. Ritchie, M. S. Skolnick, and D. N. Krizhanovskii, Light: Sci. Appl. **8**, 6 (2019).
[19]D. M. Di Paola, P. M. Walker, R. P. A. Emmanuele, A. V. Yulin, J. Ciers, Z. Zaidi, J.-F. Carlin, N. Grandjean, I. Shelykh, M. S. Skolnick, R. Butté, and D. N. Krizhanovskii, Nat. Commun. **12**, 3504 (2021).
[20]H. Souissi, M. Gromovyi, T. Gueye, C. Brimont, L. Doyennette, D. Solnyshkov, G. Malpuech, E. Cambril, S. Bouchoule, B. Alloing, S. Rennesson, F. Semond, J. Zúñiga-Pérez, and T. Guillet, Phys. Rev. Appl. **18**, 044029 (2022).
[21]M. Boroditsky, I. Gontijo, M. Jackson, R. Vrijen, E. Yablonovitch, T. Krauss, C.-C. Cheng, A. Scherer, R. Bhat, and M. Krames, J. Appl. Phys. **87**, 3497 (2000).
[22]J. Kasprzak, D. D. Solnyshkov, R. André, L. S. Dang, and G. Malpuech, Phys. Rev. Lett. **101**, 146404 (2008).
[23]D. N. Krizhanovskii, K. G. Lagoudakis, M. Wouters, B. Pietka, R. A. Bradley, K. Guda, D. M. Whittaker, M. S. Skolnick, B. Deveaud-Plédran, M. Richard, R. André, and L. S. Dang, Phys. Rev. B **80**, 045317 (2009).
[24]J. Ciers, D. D. Solnyshkov, G. Callsen, Y. Kuang, J.-F. Carlin, G. Malpuech, R. Butté, and N. Grandjean, Phys. Rev. B **102**, 155304 (2020).
[25]A. I. Tartakovskii, M. Emam-Ismail, R. M. Stevenson, M. S. Skolnick, V. N. Astratov, D. M. Whittaker, J. J. Baumberg, and J. S. Roberts, Phys. Rev. B **62**, R2283 (2000).
[26]P. G. Savvidis, J. J. Baumberg, D. Porras, D. M. Whittaker, M. S. Skolnick, and J. S. Roberts, Phys. Rev. B **65**, 073309 (2002).
[27]M. Wouters and I. Carusotto, Phys. Rev. Lett. **99**, 140402 (2007).
[28]G. Rossbach, J. Levrat, G. Jacopin, M. Shahmohammadi, J.-F. Carlin, J.-D. Ganière, R. Butté, B. Deveaud, and N. Grandjean, Phys. Rev. B **90**, 201308(R) (2014).
[29]O. A. Egorov and D. V. Skryabin, Opt. Express **26**, 24003 (2018).
[30]M. Piccardo, B. Schwarz, D. Kazakov, M. Beiser, N. Opačak, Y. Wang, S. Jha, J. Hillbrand, M. Tamagnone, W. T. Chen, A. Y. Zhu, L. L. Columbo, A. Belyanin, and F. Capasso, Nature **582**, 360 (2020).
[31]Z. Yang, E. Lustig, G. Harari, Y. Plotnik, Y. Lumer, M. A. Bandres, and M. Segev, Phys. Rev. X **10**, 011059 (2020).

Chapter 5

Rydberg blockade: exciton-polaritons in Cu_2O microcavities

In this paper, we have investigated the nonlinearities in a Cu_2O microcavity. The properties of Cu_2O have been described in section 2.4.2. Unlike the previous article, we use here a "bulk microcavity", without any quantum wells. Without Quantum Wells, the excitons are not constrained in a particular region of the microcavity. We start the experiment with a broadband excitation using a Supercontinuum source to probe the polariton modes in the sample, before exciting the modes individually using a different, narrow-band excitation laser with higher peak power.

The main result of this paper can be seen is that we find, for the exciton-polaritons with principal quantum number n between 4 and 7, an intermediate regime, between Rydberg blockade and Pauli blockade. The higher the quantum number associated with an exciton polariton, the faster a blockade effect These two regimes are described and compared. The corresponding non-linear indices are plotted and discussed. The non-linear indices β are also used to characterise the Kerr-like nonlinearity of materials, in accordance with previous works on that subject [261].

Finally, lifetime measurements show that the non-linear response has two characteristic time scales, including one that is too short to resolve in a pump-probe setup. We assimilate this short time scale to the p-series exciton-polaritons. By contrast, we find a longer time scale, on the order of a few hundreds ps. This longer time scale is assimilated to the plasma and 1s states, called in the paper

"para-exciton", which means that the electron and holes making up the exciton have opposite spins.

These lifetimes are currently a subject of investigation [125]. Another interesting question raised by this paper is the large discrepancy between the non-linear indices that we report and the ones under CW excitation for a bare Cu_2O flake [262], suggesting that a major influence of the long-lived 1s exciton reservoir in the non-linear dynamics of the system. Further investigations are ongoing at the time of writing to explain these differences.

In this paper, I ran the experiment, collected the data necessary to make the figures, and participated in the data analysis. In particular, it was after several iterations that a two-oscillator model with only the coupling strength as a free parameter was chosen. With the addition of the pulse-shaper envelope, it fits the data remarkably well and was used as a baseline for the theoretical analysis.

I have helped to design the experimental scheme that allowed for the automation of the pump-probe experimental, giving time-resolved data which was then used for figure 5, in particular by writing the code necessary for the automation, and participated in the discussion for the analysis. I have also wrote a large part of the main text and elements in the supplementary material referring to the experimental details.

This article is related to the main topic of this thesis, non-linear effects in exciton-polaritons, as it displays a very strong repulsive interaction between polaritons in the form of Rydberg blockade. The ultimate goal of Rydberg blockade is the emission of anti-bunched light, using spatial anti-correlation which results from the Rydberg blockade phenomenon. This paper is a step forward in that direction, helping to characterise the non-linearities of the Cu_2O system.

Official journal of the CIOMP 2047-7538
www.nature.com/lsa

ARTICLE Open Access

Nonlinear Rydberg exciton-polaritons in Cu_2O microcavities

Maxim Makhonin[1]✉, Anthonin Delphan[1], Kok Wee Song[2], Paul Walker[1], Tommi Isoniemi[1], Peter Claronino[1], Konstantinos Orfanakis[3], Sai Kiran Rajendran[3], Hamid Ohadi[3], Julian Heckötter[4], Marc Assmann[4], Manfred Bayer[4], Alexander Tartakovskii[1], Maurice Skolnick[1], Oleksandr Kyriienko[2] and Dmitry Krizhanovskii[1]

Abstract

Rydberg excitons (analogues of Rydberg atoms in condensed matter systems) are highly excited bound electron-hole states with large Bohr radii. The interaction between them as well as exciton coupling to light may lead to strong optical nonlinearity, with applications in sensing and quantum information processing. Here, we achieve strong effective photon–photon interactions (Kerr-like optical nonlinearity) via the Rydberg blockade phenomenon and the hybridisation of excitons and photons forming polaritons in a Cu2O-filled microresonator. Under pulsed resonant excitation polariton resonance frequencies are renormalised due to the reduction of the photon-exciton coupling with increasing exciton density. Theoretical analysis shows that the Rydberg blockade plays a major role in the experimentally observed scaling of the polariton nonlinearity coefficient as $\propto n^{4.4\pm1.8}$ for principal quantum numbers up to $n = 7$. Such high principal quantum numbers studied in a polariton system for the first time are essential for realisation of high Rydberg optical nonlinearities, which paves the way towards quantum optical applications and fundamental studies of strongly correlated photonic (polaritonic) states in a solid state system.

Introduction

Prior to the study of Rydberg excitons in solids, significant efforts have been devoted to the research of Rydberg atoms—giant atomic states with valence electrons occupying orbits of high energy excited states (with sizes up to tens of micrometres). Rydberg states have been at the focus of fundamental and applied science in areas of metrology[1], sensing[2,3], quantum information and simulation[4–6]. Their strong long-range dipole–dipole interactions lead to the Rydberg blockade phenomenon[7–9], where the presence of one excited atom prevents the excitation of another in its vicinity, at the same frequency. This effect forms the basis for quantum information processing (QIP) with Rydberg atoms[10–13]. Furthermore, coupling light to Rydberg atoms[14,15] enables strong effective photon–photon interactions down to the single particle level paving the way towards the development of various quantum optical devices (single-photon switches, phase shifters, transistors etc.[16]).

Recently, Rydberg excitons (the analogue of Rydberg atoms in condensed matter systems) were observed in a number of materials including transition metal dichalcogenides (TMDCs)[17], perovskites[18], and Cu_2O[19–22], where the Rydberg exciton radius reaches a few microns in states with principal quantum numbers as high as $n = 30$[23] and ultra-high nonlinearities have been reported in CW regime[21,24]. Rydberg exciton blockade was demonstrated experimentally[25]. On the other hand, there is a strong interest in the study of hybridised excitons and photons in microcavities and waveguides, which lead to the realisation of giant Kerr-like optical (polaritonic) nonlinearities[26,27]. These nonlinearities can be exploited for

Correspondence: Maxim Makhonin (m.makhonin@sheffield.ac.uk)
[1]Department of Physics and Astronomy, University of Sheffield, Sheffield S3 7RH, UK
[2]Department of Physics and Astronomy, University of Exeter, Stocker Road, Exeter EX4 4PY, UK
Full list of author information is available at the end of the article

the development of highly nonlinear and scalable optical devices on a chip with possible applications in QIP[28]. Polariton nonlinear phenomena, such as superfluidity, solitons, photon blockade[29,30] and single-photon phase shifts[28], to name a few, were investigated mostly for 1 s Wannier-Mott excitons. Nonlinear energy shifts have been reported for Rydberg exciton-polaritons in TMDCs[17,31,32] and perovskites[18], but these studies are limited to the first two excited exciton states. By contrast, large principal numbers n are available in Cu_2O and very recently strong exciton-photon coupling was observed in a microcavity with embedded Cu_2O[33], where only the linear optical response of Rydberg exciton-polaritons was addressed.

Here, we study yellow series Rydberg exciton-polaritons in a planar FabryPerot microcavity with embedded Cu_2O thin crystal. We report a strong and ultra-fast nonlinear optical response for these states and demonstrate the highly superlinear scaling of the nonlinearity with the principal quantum number up to $n = 7$. This scaling opens up the potential for ultra-high nonlinearity at the highest numbers ($n = 30$) observed so far in bare Cu_2O crystals. The nonlinearities are found to be comparable or even exceeding (for $n \geq 5$) the giant optical Kerr-like nonlinearities observed in other polariton platforms, such as GaAs or hybrid perovskites[34]. Nonlinear indices n_2 are found to be in the range from 10^{-17} m^2/W to 4×10^{-15} m^2/W, for $n = 3$ to $n = 7$. In a single pulse experiment, the response time of nonlinearity must be given by the polariton lifetime comparable to the duration of the pulse ~1 ps. Additional pump-probe measurements reveal that the nonlinearities at $n = 4$ are found to respond within a picosecond rise time and fall within the ~40 ps range. This ultra-fast response is followed by additional nonlinear dynamics rising and falling on density-dependent timescales of order 100 ps to 2 ns. This demonstrates that multiple processes contribute to the nonlinear response. Crucially, our pulsed resonant excitation method significantly reduces the interactions with long-lived ground state excitations and electron-hole plasma and enables us to access the pure, ultra-fast, Rydberg nonlinearity. To complete our study we provide a theoretical model that takes into account contributions from Rydberg and Pauli blockade and semi-quantitatively explains the observed experimental behaviour at high excitation densities.

Single pulse experiment

Experiment

We study a microcavity system formed by two silver mirrors with an embedded thin flake of Cu_2O material deposited on top of SiO_2 substrate with an intermediate PMMA layer (see Fig. 1a, b). Multiple cavity modes with a free spectral range of 9 meV form (see SI, Fig. S1) due to the thickness of Cu_2O slab of approximately 26 μm. We reveal the strong coupling between the cavity modes and Rydberg excitons in the angular-resolved transmission spectra of a super-continuum laser source (see Fig. 1c), similar to recently published results[33]. The transmission spectra recorded for different in-plane k-vectors show anti-crossings between the cavity modes and Rydberg exciton resonances in Fig. 1c with clear doublets corresponding to the upper (UP) and lower (LP) exciton-polariton states. To highlight the strong coupling in Fig. 1d we also plot the dispersion of Rydberg exciton-polaritons for $n = 3$, 4 and 5. The formation of polaritons for $n = 6$ and 7 excitons is not resolved for this position on the sample, since the cavity mode is in resonance at higher wavevectors and the high-frequency spectral noise leads to weak signal-to-noise ratio and in k-space prevents observation of the anticrossing. The signal-to-noise ratio is higher for detection in real space (i.e Fourier transform of k-space) and the polariton doublets for $n = 6$ and 7 are clearly observed in transmission for a different spot on the sample with a slightly different Cu_2O thickness, when the energy of the cavity mode at $k = 0$ is tuned into resonance with these excitons by changing position on the sample (SI, Sec. 4).

To probe Rydberg exciton-polariton nonlinearities we record the transmission spectra in real space at different energies of the laser pulse (with full width at half maxima FWHM 1.75 meV), directed at normal incidence to the sample and tuned in resonance with the polariton states arising from excitons with different n. In Fig. 2 we show the power dependencies of the transmission spectra of these states. At small powers, the doublet of LP and UP states is clearly visible for quantum states from $n = 3$ to $n = 7$. There is a minor asymmetry between the intensities of the lower and upper polariton branches observed for $n = 4$ and 6 states, which is attributed to a small detuning between the laser peak energy and the centre between polariton resonances (this detuning is set manually by the diffraction grating in the pulse shaper and cannot be very precise) so that one resonance is pumped slightly more efficiently than the other.

As power increases the separation between the polariton resonances becomes smaller, which we attribute to the decrease in coupling strength, and eventually a collapse of strong coupling. The resulting transmission spectra profiles become a singlet (here, limited by the pulse spectral width). We note the sharp contrast in power threshold needed to reach a singlet between the $n = 3$ case (of the order 100 nW or 500 $\mu J/cm^2$) and the $n = 7$ case (of the order of 1 nW or 5 $\mu J/cm^2$). We exclude excitation-induced thermal effects as no redshifts of the exciton resonances were detected in the experiments (for details see SI, Sec. 3).

The fitting of the spectra at each power is performed using a coupled oscillators model previously used for Rydberg exciton-polaritons[33], taking into account the

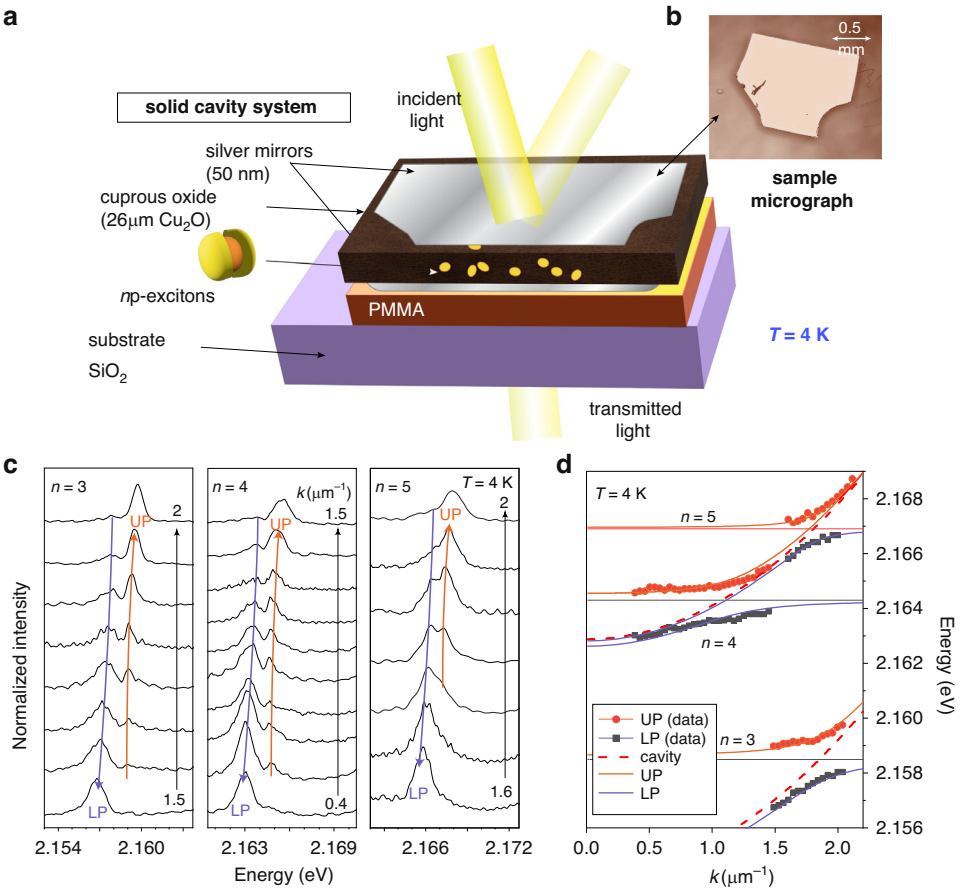

Fig. 1 Sketch of the Cu_2O microcavity sample and its dispersion. a A schematic of the solid cavity used for the transmission experiment. **b** Microscopy image of the natural Cu_2O sample of thickness approximately 26 μm with silver mirrors (recoloured). **c** Waterfall spectra plots taken with super-continuum laser in transmission for different wavevectors near $n = 3$, $n = 4$ and $n = 5$ excitons. Upper and lower polaritons are visible as a doublet at resonant conditions. **d** Polariton peak positions as a function of wavevector extracted from (**c**). Lines show cavity, exciton and polariton dispersions (for higher principal quantum numbers, see SI, Sec. 4)

spectral profile of the pulse and with the coupling strength being the main fitting parameter (see Methods and SI, Sec. 1). The model fits the experimental data well, in particular at low powers. From these fits we can extract the Rabi splitting Ω as a function of exciton density ρ, which is plotted in Fig. 3 (see Methods for the equation to deduce ρ and SI, Sec. 5 for its derivation). We stress that ρ being the excitonic fraction of resonantly pumped polaritons is an important parameter that defines the absolute value of nonlinear energy shifts. At low pump power, the overall Rabi splitting drops with quantum number n, since larger exciton size leads to smaller oscillator strength[35]. The Rabi splitting is also observed to decrease strongly with ρ or pumping power, showing a fast initial drop and overall nonlinear scaling with density at larger occupations. We also note that deducing this drop becomes difficult at larger n as the absolute value of the linear light-matter coupling decreases, while the cavity decay rate remains the same.

The exciton-polariton Kerr-like nonlinearity due to the reduction of Rabi splitting Ω with density ρ is usually characterised by the coefficient $\beta = d\Omega/d\rho$[36–38]. Classically, the Rabi splitting arises because the excitonic oscillators in the Cu_2O active region add a frequency-dependent contribution to the refractive index which modifies the cavity resonance condition[39]. The magnitude of this refractive index component, as well as the Rabi splitting, decreases as ρ grows. Thus we can directly relate the nonlinear refractive index of Cu_2O to β (see refs. [36,40] and references therein, and SI).

Here we focus on the nonlinear response at lower densities when the polariton doublets are still resolved and Ω behaves nearly linearly with ρ. The deduced β factors are plotted in Fig. 3b as a function of the principal quantum number n of polaritonic states (black dots, labelled as β_{exp}). We observe rapid increase of nonlinearity as a function of n (note the log-linear scale), and the fitting provides scaling $\beta_{exp} \sim n^{4.4\pm1.8}$ (red solid curve

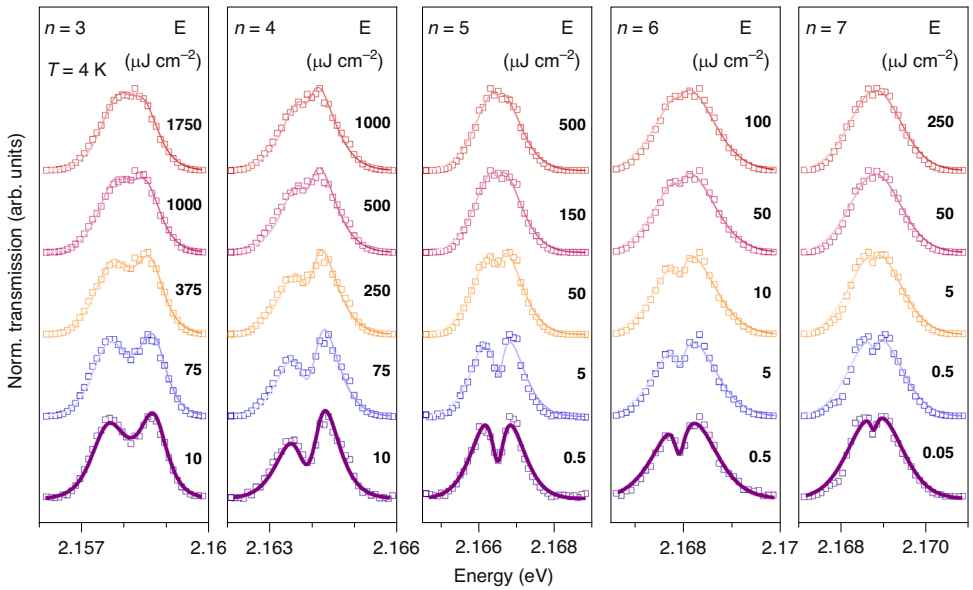

Fig. 2 Normalised transmission spectra with increasing pump power. We plot the transmission of the Cu_2O microcavity from narrowband (1.75 meV) excitation (see Methods) for different principal quantum numbers n, taken at different pump fluence $E = P_{avg}/(fA)$ (P_{avg} is pump incident average power, f is the repetition rate of the laser, A is the effective excitation area). The spectra are normalised to unity and shifted by 1 for clarity. The solid curves represent a fit with a coupled oscillator model

in Fig. 3b) (see SI, Sec. 7.1). The β-values are found to be between 0.01 μeV μm^3 for $n = 3$, to 0.4 μeV μm^3 for $n = 7$ (note, here we use volume units as natural for bulk crystal in a cavity). Already for $n = 5$ this nonlinearity exceeds that in other highly interacting polariton platforms, such as microcavities with GaAs-based quantum wells, if one takes into account excitonic spatial confinement (see SI, Sec. 6). Below we use the experimentally obtained β values and scaling to analyse main potential contributions and compare with our theoretical model.

Theoretical analysis

To explain the experimental results we develop a theory for describing the effective decrease of light-matter coupling. Specifically, we take into account dipole–dipole interactions between Rydberg states of p-wave excitons, which are known to reduce Cu_2O absorption with increasing exciton density in the cavity-free case[20]. This phenomenon may be explained as the formation of a blockade region in the vicinity of spatially extended exciton. In this region, light can no longer create new excitons due to the strong dipole–dipole interaction shifting the exciton energy out-of-resonance. Consequently, the optically active region in a sample decreases with the increase of exciton density.

We model this blockade effect and plot the β_{Rydberg} dependence using the theoretically predicted values of dipole–dipole interactions[41] (solid purple curve in Fig. 3b). We observe that β_{Rydberg} scales as $\sim n^{5.5}$ (SI, Sec. 7.2). In this theoretical plot, a full blockade is assumed where the blockade region is defined sharply by a step-like boundary at the Rydberg blockade radius (r_C). In reality, the blockade effect is coming from the exciton's density-density correlations such that the transition between blockaded and non-blockaded regions is smooth[25], meaning that the creation of additional exciton within r_C is not strictly forbidden. Therefore, the full blockade result gives approximately the upper bound which is likely to overestimate the nonlinearity. Furthermore, since the dipole–dipole interaction constants are generally difficult to calculate exactly and may be also overestimated[20,41]. To compare, we plot a scaled line (by a factor of 1/5) for the strength of dipole–dipole interaction, which matches the overall trend for experimental nonlinearity and provides a good fit (dashed purple curve in Fig. 3b).

Another possible origin of the reduction of Rabi splitting with increasing density is a nonlinear phase-space filling (NPSF) in polaritonic systems, as commonly observed with ground state s-excitons[36,38]. Nonlinear phase-space filling, also known as nonlinear saturation, is the statistical effect that emerges from the non-bosonic behaviour of excitons at large occupations. As excitons are composite quasiparticles, the Pauli blockade prevents the excitation of certain excitonic configurations if they are already occupied. This nonlinear decrease in the density of states leads to the effective reduction of light-matter coupling. Similarly to the Rydberg-induced case, the nonlinearity also grows with the exciton size, as a

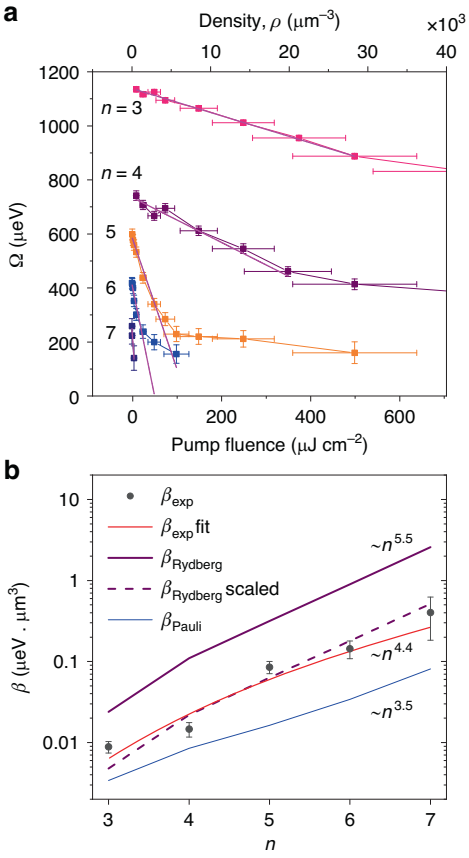

Fig. 3 Nonlinear Rabi splitting decrease and its scaling. a Rabi splitting vs exciton density ρ and/or pump fluence is shown for different principal quantum numbers n, and reveals an n-dependent nonlinear coefficient. Data are extracted from spectra in Fig. 2. The lines show the linear trend seen at low density. **b** Linear-log plot of nonlinear coefficients (β-factors) vs principal quantum number n. Filled dots correspond to the experimental β-factor extracted from Fig. 3a, which can be fitted with an $n^{4.4\pm1.8}$ dependence (solid red curve, error for 90% confidence level). The dashed purple and solid blue curves show the calculated β-factors for Rydberg and Pauli blockade, respectively. The solid purple curve depicts Rydberg saturation scaling for the full blockade ($C_6 \approx 10^{-15}\ n^{11}$ meV μm^6). (All calculated error bars are for standard error)

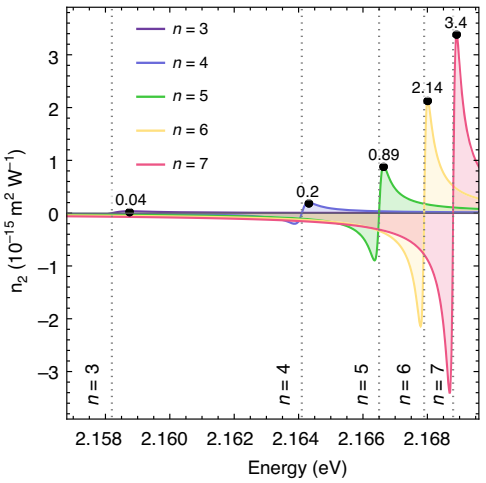

Fig. 4 Nonlinear refractive index n_2. Coloured curves show contributions from each excitonic mode with $n = 3,\ldots,7$. Here we use $\beta = 1.41 \times 10^{-5} n^{5.5}$ μeV μm^3 corresponding to the dashed purple curve in Fig. 3

smaller number of excitons can be created (per volume or area) until the medium becomes effectively transparent. The blue curve in Fig. 3b shows the scaling of Pauli-induced nonlinearity for the experimentally deduced Bohr radius $a_0 = 0.83$ nm (for $n = 1$, see SI, Sec. 7.2). The β factor associated with the Pauli blockade (β_{Pauli}) has an asymptotic $\sim n^{2.5}$ scaling, while at low n it is described by a $\sim n^{3.5}$ dependence (SI, Sec. 7.2). The Pauli blockade curve, which has no fitting parameters, is well below the experimental values. To at least partially fit the experimental values using only the Pauli blockade, the Bohr radius must be set to $a_0 \approx 2$ nm. This greatly exceeds the exciton radius estimates from the measured low-density absorption (SI, Sec. 7). Therefore, we conclude that the Pauli blockade alone cannot explain the observed nonlinearity and that the Rydberg-induced blockade plays a dominant role. The contribution of the Rydberg blockade to exciton-polariton nonlinearity is an order of magnitude stronger (see Fig. 3b).

Nonlinear n_2 parameter

From the nonlinear optics perspective, the polariton nonlinearity can be also characterised by the nonlinear refractive index n_2 of the active medium in a microcavity (Cu_2O in our case)[36]. This nonlinear parameter appears in the total refractive index as a frequency- and intensity-dependent term, $n_T(\omega) = n_0(\omega) + n_2(\omega)I$. The n_2 parameter from blockade effects may be estimated by using Eq. (1) (see SI, Sec 7.3):

$$n_2(\omega) \approx -\frac{h_n \beta_n}{2cn_0^2\omega} \frac{G_n^{(0)}(\omega - \omega_n)}{(\omega - \omega_n)^2 + \frac{1}{4}\gamma_n^2} \tag{1}$$

where $G_n^{(0)}$ is the light-matter coupling constant, ω_n is the Rydberg resonance frequency, γ_n is the excitonic linewidth, n_0 is the background refractive index of Cu_2O, c is the speed of light in vacuum and h_n is a constant of proportionality (determined from the measured Rabi splitting using Eq. (S25), see SI, Sec. 7.3). Using the β-factors in Fig. 3b, we derive the energy dependencies of n_2 for each individual excitonic mode in Fig. 4. Black dots show the upper bounds of n_2 obtained using the theoretical estimates of β, with values ranging from 10^{-17} to 10^{-15} m^2/W, for $n = 3$ to $n = 7$. Using the experimentally measured β-factors we deduce peak n_2 values ranging from 10^{-17} m^2/W to 4×10^{-15} m^2/W, for

$n = 3$ to $n = 7$. The peak values measured for $n = 7$ exciton resonance are comparable to n_2 in GaAs polariton waveguides[40].

These values of n_2 are 8 orders of magnitudes lower than those measured on bulk Cu_2O in ref. [21], where CW excitation was used in resonance with Rydberg excitons. However, we note that studies of polariton nonlinearity in GaAs-based photonic systems showed that CW excitation usually results in observed effective n_2 values one to two orders of magnitude bigger than in the case of picosecond pulsed pumping. Such a discrepancy was explained by a population of long-lived (up to 100 ps) excitons by the CW beam, the interaction with which leads to enhanced nonlinear energy shift[42]. In the case of Cu_2O, the CW excitation in the vicinity of Rydberg exciton resonances and the subsequent relaxation of the photoexcited carriers to the ground 1 s level is expected to lead to high population of long-lived (with a lifetime of 13 μs[43]) dark 1 s paraexcitons. Lifetimes up to several hundred microseconds were also reported, which was attributed to long-lived excitons trapped at defects or unknown metallic impurities[44]. At sufficiently high density long-lived 1 s excitons or excitons trapped to defects may further recombine through Auger recombination creating plasma. The exact density of 1 s excitons and plasma in this case may depend on the particular sample and the number of defects at which 1 s excitons may accumulate.

A possible explanation for the very high values of n_2 observed in ref. [21] is therefore an interplay between resonantly pumped Rydberg excitons and plasma. Free carriers may increase the strength of the Rydberg blockade through screening, which increases the size of the Rydberg excitons leading to enhancement of the dipole–dipole interactions[24]. At the same time, the screening may reduce the oscillator strength of the excitons resulting in a density-dependent change in their contribution to the refractive index. In support of this suggestion, we note that Heckötter et al.[45] characterised the influence of free carriers, showing that absorption for $n = 10$ Rydberg excitons reduces by a factor of ~3 at free carrier density as low as ~0.5 μm^{-3}. In the following section, we use time-resolved measurements to shed some light on the regimes where the polariton nonlinearity is dominated by ultra-fast processes, such as Rydberg blockade, and where it may be complicated by slower processes such as Auger-mediated generation of plasma.

Pump-probe experiment

Importantly, in the single pulse experiment presented above the polariton nonlinearity that we measured must be ultra-fast since it develops within the picosecond timescales of the probe pulse (which is also the pump pulse in that case) and the polariton lifetime. However, some of the resonantly excited exciton-polaritons can be absorbed, with the resultant formation of lower energy excitons, and then plasma through the Auger exciton recombination. Therefore the Rabi splitting may remain quenched for some time after the pump pulse is gone due to interaction with this long-lived plasma. To reveal this effect we further perform pump-probe measurement of Rabi splitting for the $n = 4$ resonance. The $n = 4$ polaritons were excited with a strong pump and the transmission of the sample was measured using a much weaker probe pulse delayed by some time from the pump. The linear polarisation of the probe is chosen to be perpendicular to the pump and the transmitted pump beam was rejected by a linear polariser. The $n = 4$ state was chosen because it provides a good signal-to-noise ratio for small probe powers.

We plot the results of the pump-probe experiment in Fig. 5. In Fig. 5a, b we show the transmission spectra for selected delays between pump and probe pulses for pump fluences of 100 μJ cm^{-2} and 450 μJ cm^{-2}, respectively. The probe fluence was 50 μJ cm^{-2}. The transmission spectra are then fitted to extract the Rabi splittings as a function of the time delay. In this fitting procedure, we omit those time delays between −29 and 37 ps (apart from zero delay), for which the interference between the residual pump and probe prevents reliable fitting (the residual pump intensity in the polarisation of the probe is about 30 times less than that of the probe for pump fluence 450 μJ cm^{-2} and can not be suppressed completely by the linear polariser, see SI, Sec. 9).

At pump fluence of 100 μJ cm^{-2} the Rabi splitting is reduced at $t = 0$ as expected for the instantaneous Rydberg exciton-polariton blockade mechanism and by $t \approx 40$ ps has recovered almost back to its value prior to the pump arrival (Fig. 5c, bottom panel). At longer delay times $t > 40$ ps the Rabi splitting reduces and then increases again on a timescale of 200–300 ps. We attribute this behaviour to the 1 s exciton and plasma dynamics created by the pump pulse, which is expected to occur on a nanosecond timescale at exciton densities 10^3–10^4 μm^{-3} given the Auger recombination rate of 1 s excitons of the order of 10^{-4} $\mu m^3/ns$[46]. At higher pump fluences of 450 μJ cm^{-2} and 1000 μJ cm^{-2}, shown in the middle and upper panels of Fig. 5c, the creation of plasma after the pump pulse is expected to occur on a shorter timescale and indeed we observe the Rabi splitting is rapidly quenched and then recovers monotonically on timescales of 1.2 and 1.8 ns, respectively. The exact explanation of the observed temporal dynamics requires complex modelling of the exciton-plasma conversion and decay using the corresponding rate equations[46] and is beyond the scope of this manuscript.

Finally, we also study Rydberg exciton-polariton transmission spectra under non-resonant CW excitation well above the band gap of the Cu_2O. In this case, we find that

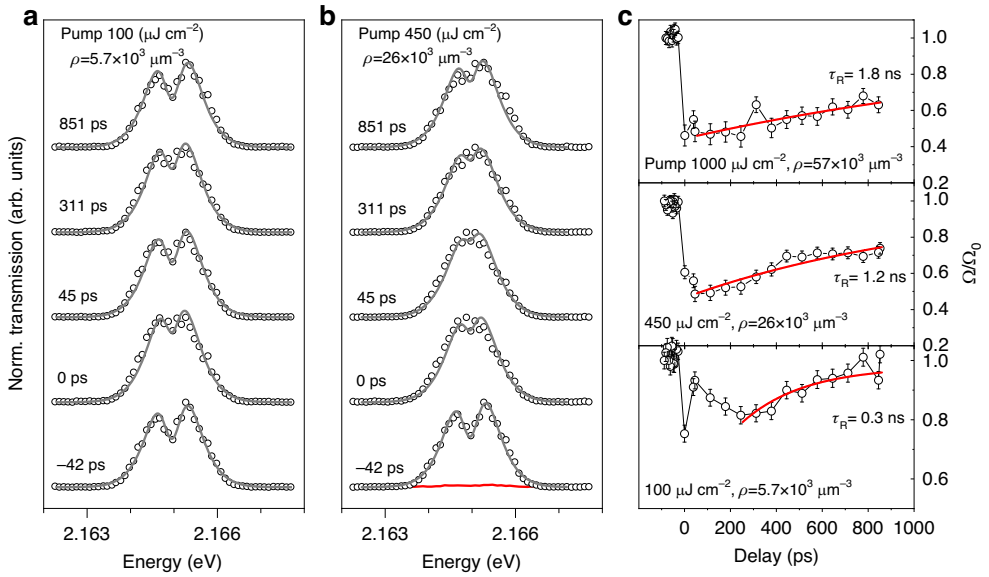

Fig. 5 Pump-probe of the Rabi splitting at $n = 4$. a Normalised transmission spectra at different delay times between pump and probe pulses at fixed pump(probe) fluence 100 μJ cm^{-2} (50 μJ cm^{-2}). Solid grey lines correspond to fits. **b** Normalised transmission spectra at different delay times between pump and probe pulses at fixed pump(probe) fluence 450 μJ cm^{-2} (50 μJ cm^{-2}). The red line corresponds to pump only transmission signal (≈30 times smaller than the probe after polarisation rejection). Solid grey lines correspond to fits. **c** Rabi splitting normalised by Rabi splitting at negative time delays (Ω/Ω_0) extracted from the spectra and plotted as a function of delay time between pump and probe at three pump fluences (100, 450 and 1000 μJ cm^{-2}). Solid red lines are single exponent fits

the collapse of the Rabi-splitting is observed at photon densities about 6 orders of magnitude less than in the pulsed excitation regime (see SI, Sec. 8). This experiment further confirms the important role of long-lived 1 s states and plasma, the density of which can be significantly higher in CW than pulsed excitation.

Conclusion

In conclusion, for the first time, we investigated the nonlinear behaviour of a polaritonic system based on Cu_2O in the ultra-fast pulsed regime. The polariton system allows us to probe the collapse of the Rabi splitting for Rydberg exciton-polaritons and we observed that the associated polariton nonlinearity increases as $\sim n^{4.4\pm1.8}$ with principal quantum number n due to stronger dipolar exciton–exciton interactions. The experimental values of polariton nonlinearity coefficient β are in good agreement (within a factor of 5) with our microscopical model, which takes into account both the Rydberg dipole–dipole interactions and Pauli blockade without fitting parameters. Furthermore, our pump-probe data suggests that there are several contributions to the nonlinearity in Cu2O-based systems, which act on several different timescales. As well as the ultra-fast response there are contributions which can persist significantly longer than pulse duration and polariton lifetime. The timescales for these are consistent with the population of long-lived states and the creation of plasma. In the CW excitation regime, these can be even more pronounced resulting in greatly enhanced nonlinearity. In order to investigate the effect of plasma on Rydberg exciton or exciton-polariton blockade in more detail, and to fully explain the drastic differences observed in nonlinearities for pulsed and CW excitation, we suggest further studies using for example pulsed excitation with varying pulse duration and repetition rate.

We note that higher exciton-polariton nonlinearities are possible to achieve by modification of several factors: (i) use higher quality crystals and observe higher n states, (ii) use higher quality microcavities to increase strong coupling with high n states, (iii) reduce the thickness of Cu_2O to the quantum well level to decrease absorption losses in the cavity and enhance exciton–exciton interactions, and (iv) exploit electromagnetically induced transparency for the reduction of losses due to phonons[47]. Our work demonstrates that Rydberg polaritons in Cu_2O are a suitable platform for quantum polaritonics with nonlinearities that scale sufficiently strongly with Rydberg exciton quantum number to reach the single polariton nonlinearity.

Methods

Sample and setup

Our cavity containing a natural Cu_2O sample is cooled down to 4 K in a continuous flow liquid Helium cryostat. Natural Cu_2O crystals are employed here since these are of higher quality than artificially grown samples[19,48]. To prepare the microcavity sample, the Cu_2O flake was first

cleaned in xylene with 1 min of delicate sonication and rinsed in isopropanol. Producing the mirror layers was done by initially securing the Cu_2O flakes onto a substrate with a 45 mg/ml solution of PMMA and toluene. The sample with the Cu_2O flake was then loaded into an ˚Angstrom Engineering thermal evaporator. Silver was then evaporated onto the Cu_2O using a resistive source at a rate of $0.2\,\mathrm{nm}\,s^{-1}$. The final thickness of the silver mirror was 50 nm. The sample was then unloaded and the Cu_2O flake was removed and carefully rotated to expose the opposite side that has no silver deposited. The PMMA solution was then used to secure this to a new substrate and the deposition was repeated with the same thickness. To attach the resulting structure on the final substrate, PMMA 495 resist in 8% anisole was spun at 4000 rpm on a glass slide resulting in a 600 nm thick layer. The flake was transferred onto the resist and then baked for 5 min at 180 °C.

The Fourier space imaging spectra in Fig. 1 have been obtained with a 1 ns super-continuum laser with a repetition rate of 23 kHz and a spectral width after filtering of 50 nm. In order to achieve narrowband resonant excitation in Fig. 2, we used 100 fs pulses at 1 kHz repetition rate obtained from the frequency-doubled output of a TOPAS optical parametric amplifier and then filtered by a 4f configuration pulse shaper with a 1200 g/mm grating and a slit slightly displaced from the focal plane to obtain a Gaussian shape spectrum with FWHM 1.75 meV.

Fitting procedure and extraction of β factors

The transmission spectra resulting from resonant excitation consist of a doublet centred around the excitonic resonance. In order to extract the coupling strength of the Rydberg polariton from the transmission spectra, we fit the data according to the model used in[33] taking also into account the small spectral width (FWHM = 1.75 meV) of the excitation pulse [see SI, Sec. 1, Eq. (S1)]. Cavity and excitons linewidths in the fit were fixed for all powers and obtained in separate measurements for each n (see SI, Sec. 2). Two fitting parameters were allowed to vary with power: the amplitude and the coupling strength. Thus we extract the coupling strength dependence on average power. To extract β we plot the Rabi splitting as a function of resonantly excited exciton density estimated from the transmitted power through the cavity in resonant conditions and fit it with the linear function. The slope provides an average estimate for β.

The density of excitons ρ per volume is calculated from the incident average excitation power P_{avg} by using the following equation:

$$\rho = \frac{T P_{\mathrm{avg}} \tau' |X|^2}{f \tau_p L A \hbar\omega |C|^2} \qquad (2)$$

where $T = 1/180$ is the fraction of incident power that is transmitted, $\tau' = 14$ ps is the inverse of the tunnelling rate of photons out of the cavity, through the silver mirror and towards the detector, $f = 1$ kHz is the laser repetition rate, $\tau_{\mathrm{p}} \approx 1.57$ ps is the effective laser pulse width, $A \approx 20\,\mu\mathrm{m}^2$ is the effective area for the interaction[28], $L = 26\,\mu$m is the cavity length, $\hbar\omega$ is the single-photon energy and $|C|^2 = 0.5$ and $|X|^2 = 0.5$ are photonic and excitonic fractions of the polaritons respectively (see SI, Sec. 5 for more details).

Acknowledgements

We acknowledge UK EPSRC grants EP/V026496/1, EP/S014403/1 and EP/S030751/1. OK and KWS acknowledge UK EPSRC grants EP/V00171X/1 and EP/X017222/1, and NATO SPS project MYP.G5860. HO acknowledges The Leverhulme Trust (Agreement No. RPG-2022-188).

Author details

[1]Department of Physics and Astronomy, University of Sheffield, Sheffield S3 7RH, UK. [2]Department of Physics and Astronomy, University of Exeter, Stocker Road, Exeter EX4 4PY, UK. [3]SUPA, School of Physics and Astronomy, University of St Andrews, St Andrews KY16 9SS, UK. [4]Fakultät Physik, TU Dortmund, August-Schmidt-Straße 4, 44227 Dortmund, Germany

Author contributions

M.M., A.D., K.O., S.K.R. designed and conducted the experiments. J.H., T.I., P.C. contributed to the sample fabrication. O.K., K.W.S. provided theoretical support. M.M., A.D., O.K., K.W.S., P.W., H.O. and D.K. wrote the manuscript. All authors contributed to the analysis and interpretation of the results and critical reading of the paper.

Data availability

The data supporting these findings are freely available from the corresponding author upon reasonable request.

Code availability

The code used for analysis is freely available from the corresponding author upon reasonable request.

Conflict of interest

The authors declare no competing interests.

Supplementary information The online version contains supplementary material available at https://doi.org/10.1038/s41377-024-01382-9.

Received: 25 August 2023 Revised: 10 January 2024 Accepted: 11 January 2024
Published online: 06 February 2024

References

1. Ding, D. S. et al. Enhanced metrology at the critical point of a many-body Rydberg atomic system. *Nat. Phys.* **18**, 1447–1452, https://doi.org/10.1038/s41567-022-01777-8 (2022).
2. Fancher, C. T. et al. Rydberg atom electric field sensors for communications and sensing. *IEEE Trans. Quant. Eng.* **2**, 1–13, https://doi.org/10.1109/tqe.2021.3065227 (2021).
3. Fancher, C. T. et al. A self-locking Rydberg atom electric field sensor. *Appl. Phys. Lett.* **122**, 094001, https://doi.org/10.1063/5.0137127 (2023).
4. Gallagher, T. F. *Rydberg Atoms* (Cambridge University Press, 2005).
5. Graham, T. M. et al. Rydberg-mediated entanglement in a two-dimensional neutral atom qubit array. *Phys. Rev. Lett.* **123**, 230501, https://doi.org/10.1103/PhysRevLett.123.230501 (2019).
6. Tiarks, D. et al. A photon–photon quantum gate based on Rydberg interactions. *Nat. Phys.* **15**, 124–126, https://doi.org/10.1038/s41567-018-0313-7 (2019).

7. Lukin, M. D. et al. Dipole blockade and quantum information processing in mesoscopic atomic ensembles. *Phys. Rev. Lett.* **87**, 037901, https://doi.org/10.1103/PhysRevLett.87.037901 (2001).
8. Urban, E. et al. Observation of Rydberg blockade between two atoms. *Nat. Phys.* **5**, 110–114, https://doi.org/10.1038/nphys1178 (2009).
9. Gaëtan, A. et al. Observation of collective excitation of two individual atoms in the Rydberg blockade regime. *Nat. Phys.* **5**, 115–118, https://doi.org/10.1038/nphys1183 (2009).
10. Saffman, M., Walker, T. G. & Mølmer, K. Quantum information with Rydberg atoms. *Rev. Mod. Phys.* **82**, 2313–2363, https://doi.org/10.1103/RevModPhys.82.2313 (2010).
11. Wu, X. L. et al. A concise review of Rydberg atom based quantum computation and quantum simulation. *Chin. Phys.B* **30**, 020305, https://doi.org/10.1088/1674-1056/abd76f (2021).
12. Morgado, M. & Whitlock, S. Quantum simulation and computing with Rydberg-interacting qubits. *AVS Quant. Sci.* **3**, 023501, https://doi.org/10.1116/5.0036562 (2021).
13. Shi, X. F. Quantum logic and entanglement by neutral Rydberg atoms: methods and fidelity. *Quant. Sci. Technol.* **7**, 023002, https://doi.org/10.1088/2058-9565/ac18b8 (2022).
14. Murray, C. & Pohl, T. Chapter seven—quantum and nonlinear optics in strongly interacting atomic ensembles. *Adv. Atom. Mol. Opt. Phys.* **65**, 321–372, https://doi.org/10.1016/bs.aamop.2016.04.005 (2016).
15. Fleischhauer, M., Imamoglu, A. & Marangos, J. P. Electromagnetically induced transparency: optics in coherent media. *Rev. Mod. Phys.* **77**, 633–673, https://doi.org/10.1103/RevModPhys.77.633 (2005).
16. Firstenberg, O., Adams, C. S. & Hofferberth, S. Nonlinear quantum optics mediated by Rydberg interactions. *J. Phys. B Atom. Mol. Opt. Phys.* **49**, 152003, https://doi.org/10.1088/0953-4075/49/15/152003 (2016).
17. Gu, J. et al. Enhanced nonlinear interaction of polaritons via excitonic Rydberg states in monolayer WSe_2. *Nat. Commun.* **12**, 2269, https://doi.org/10.1038/s41467-021-22537-x (2021).
18. Bao, W. et al. Observation of Rydberg exciton polaritons and their condensate in a perovskite cavity. *Proc. Natl Acad. Sci. USA* **116**, 20274–20279, https://doi.org/10.1073/pnas.1909948116 (2019).
19. Kazimierczuk, T. et al. Giant Rydberg excitons in the copper oxide Cu_2O. *Nature* **514**, 343–347, https://doi.org/10.1038/nature13832 (2014).
20. Aßmann, M. & Bayer, M. Semiconductor Rydberg physics. *Adv. Quant. Technol.* **3**, 1900134, https://doi.org/10.1002/qute.201900134 (2020).
21. Morin, C. et al. Self-Kerr effect across the yellow Rydberg series of excitons in Cu_2O. *Phys. Rev. Lett.* **129**, 137401, https://doi.org/10.1103/physrevlett.129.137401 (2022).
22. Steinhauer, S. et al. Rydberg excitons in Cu_2O microcrystals grown on a silicon platform. *Commun. Mater.* **1**, 11, https://doi.org/10.1038/s43246-020-0013-6 (2020).
23. Versteegh, M. A. M. et al. Giant Rydberg excitons in Cu_2O probed by photoluminescence excitation spectroscopy. *Phys. Rev. B* **104**, 245206, https://doi.org/10.1103/PhysRevB.104.245206 (2021).
24. Walther, V. & Pohl, T. Plasma-enhanced interaction and optical nonlinearities of Cu_2O Rydberg excitons. *Phys. Rev. Lett.* **125**, 097401, https://doi.org/10.1103/PhysRevLett.125.097401 (2020).
25. Heckötter, J. et al. Asymmetric Rydberg blockade of giant excitons in cuprous oxide. *Nat. Commun.* **12**, 3556, https://doi.org/10.1038/s41467-021-23852-z (2021).
26. Carusotto, I. & Ciuti, C. Quantum fluids of light. *Rev. Mod. Phys.* **85**, 299–366, https://doi.org/10.1103/RevModPhys.85.299 (2013).
27. Byrnes, T., Kim, N. Y. & Yamamoto, Y. Exciton–polariton condensates. *Nat. Phys.* **10**, 803–813, https://doi.org/10.1038/nphys3143 (2014).
28. Kuriakose, T. et al. Few-photon all-optical phase rotation in a quantum-well micropillar cavity. *Nat. Photon.* **16**, 566–569, https://doi.org/10.1038/s41566-022-01019-6 (2022).
29. Delteil, A. et al. Towards polariton blockade of confined exciton–polaritons. *Nat. Mater.* **18**, 219–222, https://doi.org/10.1038/s41563-019-0282-y (2019).
30. Muñoz-Matutano, G. et al. Emergence of quantum correlations from interacting fibre-cavity polaritons. *Nat. Mater.* **18**, 213–218, https://doi.org/10.1038/s41563-019-0281-z (2019).
31. Chernikov, A. et al. Exciton binding energy and nonhydrogenic Rydberg series in monolayer WS_2. *Phys. Rev. Lett.* **113**, 076802, https://doi.org/10.1103/PhysRevLett.113.076802 (2014).
32. Coriolano, A. et al. Rydberg polaritons in ReS_2 crystals. *Sci. Adv.* **8**, eadd8857, https://doi.org/10.1126/sciadv.add8857 (2022).
33. Orfanakis, K. et al. Rydberg exciton–polaritons in a Cu_2O microcavity. *Nat. Mater.* **21**, 767–772, https://doi.org/10.1038/s41563-022-01230-4 (2022).
34. Fieramosca, A. et al. Two-dimensional hybrid perovskites sustaining strong polariton interactions at room temperature. *Sci. Adv.* **5**, eaav9967, https://doi.org/10.1126/sciadv.aav9967 (2019).
35. Heckötter, J. et al. Scaling laws of Rydberg excitons. *Phys. Rev. B* **96**, 125142, https://doi.org/10.1103/PhysRevB.96.125142 (2017).
36. Emmanuele, R. P. A. et al. Highly nonlinear trion-polaritons in a monolayer semiconductor. *Nat. Commun.* **11**, 3589, https://doi.org/10.1038/s41467-020-17340-z (2020).
37. Brichkin, A. S. et al. Effect of coulomb interaction on exciton-polariton condensates in GaAs pillar microcavities. *Phys. Rev. B* **84**, 195301, https://doi.org/10.1103/PhysRevB.84.195301 (2011).
38. Zhang, L. D. et al. Photon-photon interactions in Rydberg-atom arrays. *Quantum* **6**, 674, https://doi.org/10.22331/q-2022-03-30-674 (2022).
39. Khitrova, G. et al. Nonlinear optics of normal-mode-coupling semiconductor microcavities. *Rev. Mod. Phys.* **71**, 1591–1639, https://doi.org/10.1103/RevModPhys.71.1591 (1999).
40. Walker, P. M. et al. Ultra-low-power hybrid light–matter solitons. *Nat. Commun.* **6**, 8317, https://doi.org/10.1038/ncomms9317 (2015).
41. Walther, V. et al. Interactions between Rydberg excitons in Cu_2O. *Phys. Rev. B* **98**, 165201, https://doi.org/10.1103/PhysRevB.98.165201 (2018).
42. Walker, P. M. et al. Dark solitons in high velocity waveguide polariton fluids. *Phys. Rev. Lett.* **119**, 097403, https://doi.org/10.1103/PhysRevLett.119.097403 (2017).
43. Mysyrowicz, A., Hulin, D. & Antonetti, A. Long exciton lifetime in Cu_2O. *Phys. Rev. Lett.* **43**, 1123–1126, https://doi.org/10.1103/PhysRevLett.43.1123 (1979).
44. Rogers, J. P. et al. High-resolution nanosecond spectroscopy of even-parity Rydberg excitons in Cu_2O. *Phys. Rev. B* **105**, 115206, https://doi.org/10.1103/PhysRevB.105.115206 (2022).
45. Heckötter, J. et al. Rydberg excitons in the presence of an ultralow-density electron-hole plasma. *Phys. Rev. Lett.* **121**, 097401, https://doi.org/10.1103/PhysRevLett.121.097401 (2018).
46. Stolz, H. et al. Scrutinizing the Debye plasma model: Rydberg excitons unravel the properties of low-density plasmas in semiconductors. *Phys. Rev. B* **105**, 075204, https://doi.org/10.1103/PhysRevB.105.075204 (2022).
47. Walther, V., Johne, R. & Pohl, T. Giant optical nonlinearities from Rydberg excitons in semiconductor microcavities. *Nat. Commun.* **9**, 1309, https://doi.org/10.1038/s41467-018-03742-7 (2018).
48. Lynch, S. A. et al. Rydberg excitons in synthetic cuprous oxide Cu_2O. *Phys. Rev. Mater.* **5**, 084602, https://doi.org/10.1103/PhysRevMaterials.5.084602 (2021).

Chapter 6

Optical vortices in polariton fluids: towards analogue black holes

6.1 Overview

"Un affreux Soleil noir d'où rayonne la nuit."
(A terrible black Sun from which night radiates.)
— Victor Hugo, Les Comtemplations

In this section, we shall present how exciton-polaritons in microcavities can be used to study a seemingly entirely unrelated phenomenon: black holes. This new and promising area of research, known as "Analogue Physics", offers a novel approach to exploring phenomena which cannot be observed directly. In the first section, we shall give a short introduction to black holes, to give motivations for our study. The second section will present a brief overview of the existing analogue physics techniques. Using exciton-polaritons to study black holes is one such technique, and in the third section we shall present our experimental objectives and results. Finally, the fourth section discusses further possible work in this intriguing area of study.

This chapter serves as illustration of the possible application of superfluid-like non-linear exciton-polaritons for fundamental research. It also explores the properties of the superfluid phase of polaritons, which is another expression of their bosonic nature.

6.2 Black holes

Few things in Physics have inspired the imagination so much as black holes, strange singularities in space time whose mass is so strong, not even light can escape from their gravitational pull. Formally speaking, black holes are stable solutions of Einstein's field equations in general relativity, and have been conceptually predicted as early as the eighteenth century [263], but it was only after Einstein's theory had been established that Karl Schwarzchild found the first solution for the field equation around a massive, immobile spherical object of radius R [264]. In general relativity, the geometry of space-time is governed by a mathematical object known as a *metric*. The *Schwarzschild metric* describes how space-time is deformed by a spherically symmetric immobile massive object.

Schwarzchild found that his solution had "singularities" at two points, $r = 0$ (where r is the radius from the object's centre) and at a certain radius $r = r_S$, called the Schwarzchild radius. According to general relativity, the escape velocity, which is the velocity required for an object to escape the gravitational pull, becomes greater than the speed of light at this singularity. For bodies in which $R > r_S$ (such as planets and stars) for example, this is of no consequence. However, for bodies which $R < r_S$, known as Schwarzschild black holes, no light can be seen from within said radius. Conventional assumptions about time and space fall apart inside the radius, known as the *event horizon* of the black hole. The events in the black hole cannot affect an observer outside its event horizon. An external observer, for example, would perceive an object falling toward the event horizon as approaching it asymptotically — never quite reaching it, falling forever. From the perspective of the falling object, however, the horizon has already been crossed, as David Finkelstein explained in 1958 [265].

By the 50's, several predictions of General Relativity had been confirmed with a remarkable degree of accuracy, and black holes were becoming a subject of active theoretical and experimental research. Roy Kerr discovered solution to the Einstein equations for rotating objects [266], now known as "Kerr black holes". It also emerged, mathematically, that within the framework of general relativity, a black hole can fully be described by only three parameters: its mass, angular momentum, and electric charge [267].

Nevertheless, the idea that black holes could be a physical reality caused controversy, and their space-time altering properties were sometimes thought to be mathematical artifacts. However, observational evidence began to support their existence, and in 1975, the first evidence for a black hole was reported [268], in a stellar object known as Cygnus X-1.

Since then, black holes have continued to fascinate physicists and laymen alike, and more and more of their properties have emerged, including their role

in the detection of gravitational waves [269], or the phenomenon of black hole evaporation [270], also known as Hawking radiation. Hawking's theory predicts that black holes eventually disappear. This opened up one of the most fundamental questions in Physics, known as the "black hole information paradox": the information that comes out of black hole should be thermal, with seemingly no relation to the bodies that enter them [271].

The fascination that black holes create, however, is only matched by the very difficult challenges involved in their study. The theory of black hole evaporation involves a semi-classical approach, combining elements of quantum theory and general relativity. A full treatment of quantum gravity could help to better understand the phenomenon. However, a unified theory of general relativity and quantum mechanics, a long-standing goal in the foundations of physics, has not been developed yet, as the axioms in general relativity are not compatible with that of quantum mechanics.

On the experimental side, black holes are situated thousands of light years away from us [272]. Direct experimental data from black holes is difficult to acquire, and these observations require very elaborate and expensive equipment. Finally, for the phenomenon of Hawking radiation, the time scales associated with black hole evaporation are so immeasurably large that it would be practically impossible to observe it in a meaningful way except for very small black holes. To meaningfully observe black hole evaporation, a more "down-to-earth" approach proves to be necessary.

6.3 A review of Analogue Physics techniques

William George Unruh published in 1981 a paper with a title ending in a question mark, "Experimental Black Hole Evaporation?" [23], in which he offered to study black hole phenomena directly in the laboratory, using nothing more than a tabletop setup. In Unruh's proposal, the black hole is replaced by a irrotational fluid optical vortex. Unruh showed that the equation of motion for the fluid in this system are equivalent to a Schwarschild's black hole metric. In particular, if the fluid velocity at a radius r_S exceeds the speed of sound waves within the fluid, the singularity of the Schwarzschild's metric is recreated.

Such systems are called "accoustic black holes", or "dumb holes" – here, "dumb" has the meaning of "deaf". In a real black holes, *photons* are unable to escape the event horizon as the required escape velocity is greater than the *speed of light*. In an acoustic black hole, *phonons* are unable to escape the sonic event horizon. The speed of the phonons is the speed of sound in the fluid, and the required escape velocity is equal to the fluid velocity. This means that an event horizon is created if the fluid velocity is greater than the *speed of sound*.

Unruh also demonstrated, mathematically, that if the phonons were treated quantum mechanically, then they would also display "thermal evaporation" – sound waves would be emitted beyond the sonic event horizon, with a thermal distribution, unrelated to the sound waves within the event horizon.

Unruh's model can be realised experimentally and uses well-established theoretical concepts. However, he also acknowledged several limitations of his model. Namely, the assumptions of fluid mechanics break down near the optical vortex. This is also true for General Relativity, which cannot describe the singularity at the very centre of the black hole. More importantly, the evaporation temperatures predicted by Unruh were extremely small, on the order of a µK, which were thought to be undetectable in any real fluid, where turbulence and other phenomena would drown out such low signal.

Nevertheless, the quest to create "Artificial Black Holes" [273] was started, and analogue physics was born. Many reviews have listed and discussed the experimental projects to realise Unruh's proposal [274, 275]. The simplest example of an "artificial black hole" is a purely classical phenomenon. It consists of a surface water waves in a shallow basin with a controlled depth h. An obstacle is placed at the bottom of the channel, which reduces the velocity of the surface waves while increasing the velocity of the flow [276], which creates the desired sonic event horizon. As research progressed, more evidence and properties of the "sonic event horizon" were probed, for example so-called "backreaction", in which the flow of water waves changes the properties of the event horizon [277].

It is certain that such a setup has many limitations. As water is a classical fluid, none of the assumptions of quantum mechanics necessary to predict Hawkings radiation hold, and the turbulence effects cannot be neglected. Additionally, the scale of temperature for Hawking radiation is vastly different from the room temperature at which the water flows. Nevertheless, a classical limit of the phenomenon was reported, with results still under discussion [278].

To counteract this limitation, researchers have used Bose-Einstein condensates as analogue physics models, which exist at temperatures comparable with the black hole evaporation temperatures. This was made possible with the advent of laser cooling and the realisation of the first Bose-Einstein condensate of cold atoms [13], 15 years after Unruh's proposal. A sonic event horizon was achieved in a cloud of ^{87}Rb atoms [279] in 2010, and a few years later Hawking radiation was reported [280], although the exact interpretation of the result remains controversial (see e.g [281] arguing against the Hawkings radiation interpretation, and the author response [282]).

Other experimental setups to create "artificial black holes" or study analogue gravity include superfluid Helium [283, 284, 285], and exciton-polaritons: the so-called "quantum fluids of light" [286, 287].

6.4 Analogue Exciton-Polaritons

Exciton-polaritons offer several advantages compared to other models of analogue gravity. Unlike water waves, they are a quantum phenomena in which turbulence, decoherence, and other classical effects masking relevant properties of the system can be minimised. In comparison to cold atoms, such a system is much easier to create and has more freedom in the experimental parameters. Exciton-polaritons analogue black holes have been realised in one [288] or two dimensions [287]. Unlike cold atoms, analogue exciton-polaritons black holes are directly coherently injected, rather than forming spontaneous coherence after Bose-Einstein condensation.

Beyond black hole evaporation, another phenomenon available for study in analogue physics is the so-called *Penrose process*, which is a form of energy emission by rotating black holes [289]. It is believed to be responsible for the "relativistic jets" commonly seen around black holes. A "jet" is a flow of ionised matter emitted on the axis of rotation.

A proposal to observe the Penrose effect in exciton-polariton analogue black holes was given in ref. [290]. It involves the creation of a bound vortex/anti-vortex pair, which is predicted to split at the event horizon of the black hole. The optical vortex is expected to scatter outside of the event horizon, and the anti-vortex to be absorbed by the acoustic black hole. This theoretical process is described in figure 6.1.

While it is possible to observe semi-classical analogues of the Hawking radiation in classical fluids, the Penrose process cannot be simulated in water tank experiments, as the angular momentum of the vortex/anti-vortex needs to be quantised. In a classical fluid, the turbulent effect would dominate over the scattering. The experimental flexibility afforded by exciton-polaritons also gives them an advantage over an experiment involving cold atoms or liquid Helium. Finally, the dynamics of polariton vortices have been studied [291], which gives a strong theoretical basis.

The Starobinskii-Unruh effect is related to black hole evaporation and is sometimes called the "spontaneous Penrose effect" [292], which arises from vacuum instability. The prevalence of the Starobinskii-Unruh effect is related to the size of the "ergosphere" of the black hole, which lies outside of its event horizon.

In analogue physics systems, the size of the ergosphere can be easily controlled by the velocity of the fluid in which the acoustic black hole is created. This makes exciton-polaritons a system particularly suited for the study of this effect, once again owing to their experimental flexibility.

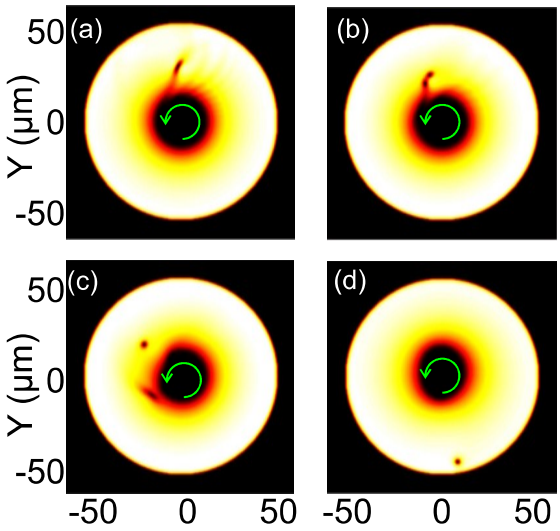

Figure 6.1: Simulation images of an analogue black made of an exciton-polariton BEC. The bright part of the images correspond to high polariton density, and the dark parts to low polariton density. The green arrow corresponds to the rotation direction.
In (a), a defect is introduced to the black hole. That density "dip" then undergoes a Penrose process. In (b) the defect scatters into a vortex/anti-vortex pair. In (c), one of the vortices gets annihalted by the black hole, and in (d) another escapes outside of the event horizon. Taken from [290].

6.4.1 Experimental realisations

To create an analogue gravity system using micro-cavity exciton-polaritons, two things are necessary: the exciton-polaritons must be in a fluid-like phase, and this phase must display a sonic event horizon [293].

To meet this condition, the polaritons can be brought into the superfluid regime, which was described in section 2.6.5. According to the Landau criterion, the speed of the polariton quantum fluid of light would be below the speed of sound in the superfluid regime.

If the velocity follows a gradient, the event horizon is created at the point where the Landau criterion is no longer fulfilled.

More precisely, the region of space where the polariton is in the superfluid regime – hence subsonic – would be *outside the event horizon*, and the region of space where the polariton is no longer in the superfluid regime – hence at supersonic speeds – would lie *inside* of it.

There have been many realisations of polariton superfluids [19, 197]. This has been used for the realisation of one-dimensional analogue black holes, with a single oblique excitation spot resulting in a flowing polariton superfluid [288]. As the fluid propagates, losses result in a lower polariton density. When the density reaches a threshold, the polariton is no longer in a condensed phase, loses its superfluid properties, and as a result becomes necessarily *supersonic*. An horizon is created. This scheme is presented in figure 6.2.

This scheme results in a one-dimensional, non-rotating black hole with an "open" event horizon. This is a relatively simple approximation which cannot reproduce all phenomena associated with black holes. In particular it cannot reproduce the Penrose process, which is predicted to occur in rotating black holes.

To create a rotating black hole, we create a ring-shaped two-dimensional polariton superfluid with a well-defined angular momentum. There are several ways to generate such a polariton superfluid. If the cavity is pumped near-resonance, as is often the case for a polariton superfluid, any angular momentum and pattern in the optical pump will be carried to the exciton-polariton. The goal is then to impart a well-defined momentum to the excitation beam; this is easily done for a single Gaussian spot, as shining the beam at a given angle will give it the desired linear momentum.

The process is more complicated for a ring-shaped beam. The desired pattern, with well-defined angular momentum number l, is the Fourier transform of a Laguerre-Gaussian beam [294]. Having a ring-shaped beam in Fourier space

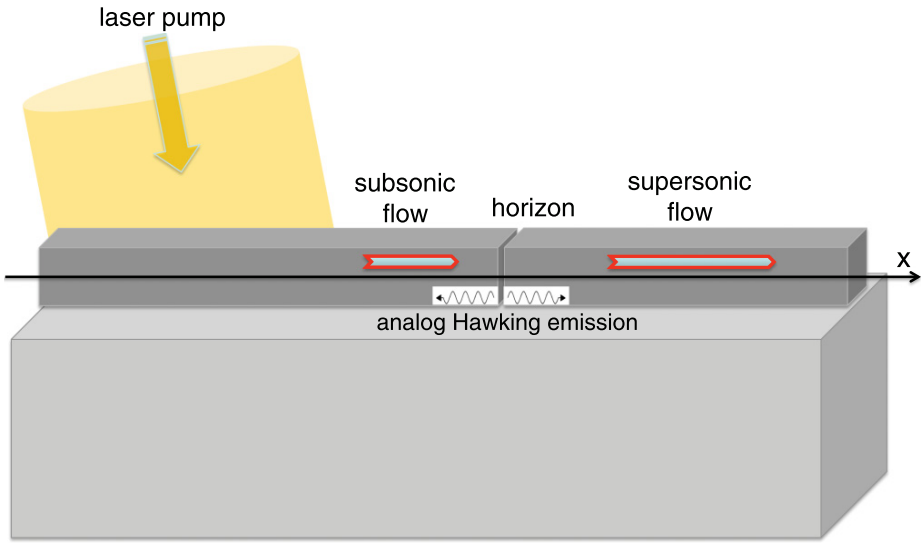

Figure 6.2: "Polariton wire" device used in [288]. The cavity exciton-polariton are pumped with a non-zero angular momentum and flow in the wire, and eventually an event horizon.

allows us to shine a ring-shaped beam in real space on the sample.

The phase along the edge of the optical vortex varies continuously, with a total variation equal to $2*\pi l$, and in the ideal case the intensity on the edge of the ring remains constant. Those doughnut-shaped rings are called *"perfect vortex beams"*, and there are many techniques to generate such beams. In recent years, a remarkable degree of control over the beam profile, diameter, beam width [295] and the topological charge l was achieved [296], as can be seen in figure 6.3

For our experiment, we used a programmable phase plate, known as a *spatial light modulator* (SLM) from the company HoloEye. This phase plate consists of a programmable screen of 1920 x 1080 pixels on a 15.36 x 8.64 mm screen. Any arbitrary image can be projected on the screen. When the light hits the screen, a delay on reflection is imposed depending on the colour of the pixel, with maximum delay for a black pixel – corresponding to a phase shift of 2π – and no delay for a white pixel. This gives very good flexibility to impart a deterministic phase map to an incoming Gaussian beam, which can be changed on the fly depending on the need of the experiment. To create a vortex with angular momentum number l, a spiral with l segments going linearly from black to white is projected on the SLM. However, with only a spiral, all orders of diffraction are reflected by the SLM at the same angle. To separate between them, the image of a fork-like grating is superimposed on the spiral. An interferometer is then built to image the phase pattern on the ring. This system is shown in

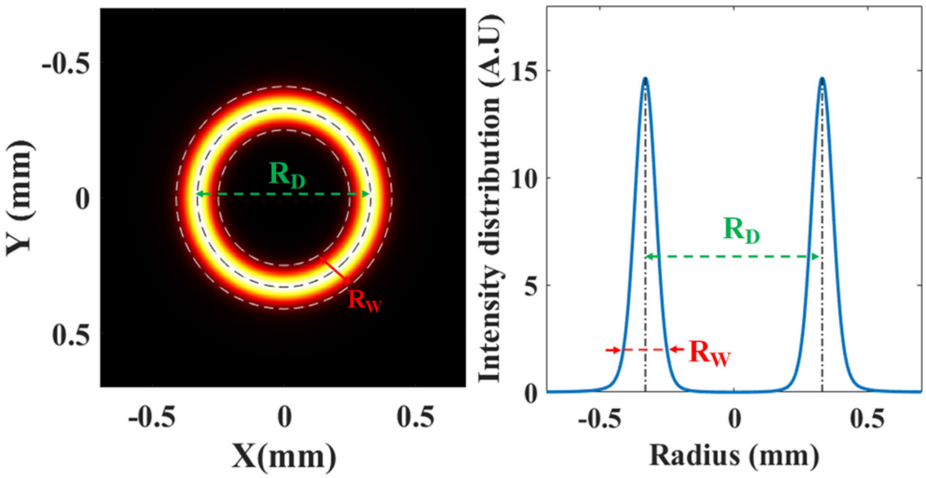

Figure 6.3: Example of a perfect optical vortex, with a very small vortex thickness, constant intensity in the ring, and a sharp Gaussian profile. Generated via Fourier transform of a Laguerre-Gaussian beam. Taken from [296].

figure 6.4.

The SLM offers a very large degree of flexibility and allows switching between different l numbers on the fly with very little re-alignment required. However, one limit is that the Laguerre-Gaussian beams it generates are very difficult to collimate and diverge over large distances. The size of the ring, which is dependent on the l number, as well as its energy of the laser, are critical experimental parameters. We must find a point in the parameter space where, at a given laser energy, the size of the ring in k-space is equal to the spacing of the LPB dispersion at the same energy, so that there is an **overlap** between the polariton dispersion and the ring. This can be quite challenging to achieve in practice. We call this procedure "matching" the ring to the edges of the dispersion.

To ensure that the optical vortex has the correct experimental parameters, the LPB is populated by the use of an off-resonant red laser at 633 nm, illuminating the sample in the reflection geometry, while the vortex shines through the sample in the transmission geometry. A Fourier lens is used to image the LPB and the optical vortex in k-space. The idea is then to use experimental parameters to make the vortex match the dispersion. This geometry is given in figure 6.5.

The size of the ring reflected by the SLM is related to its size in k-space. As a result, it is possible to use a telescope to increase or decrease the size of the ring to meet the edges of the LPB. However, a bigger ring results in a lower power density, and as a result, an increased threshold for BEC, which can be harder

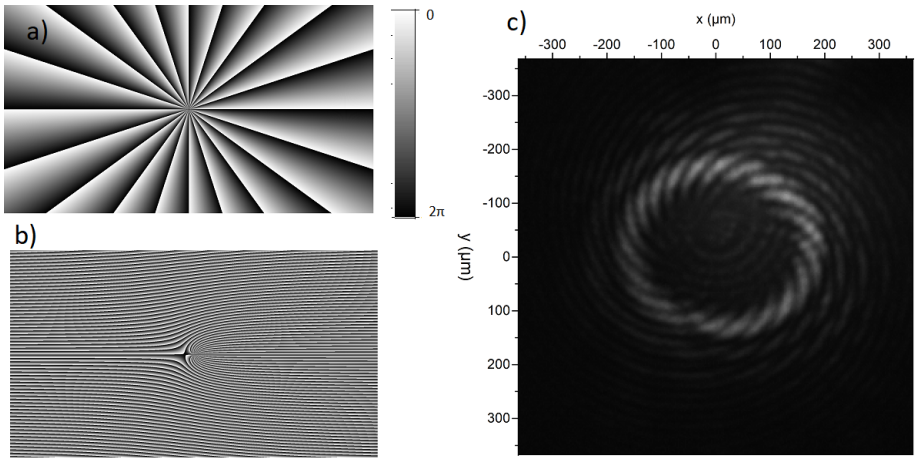

Figure 6.4: Optical vortex generation using a spatial light modulator. a) Image of the phase pattern used to generate a $n = 20$ vortex. b) Image of the $n = 20$ vortex-generating phase pattern multiplied by a grating to separate the different diffraction orders. c) Interference pattern arising from the interference $n = 20$ vortex beam transmitted through the sample with a reference beam.

to provide experimentally, as the maximum available power density is limited by the damage threshold of the SLM. An optimum must be found between the desired topological charge l, the ring size in k-space, and the maximum power density. The size of the optical vortex and the topological charge l also give the polariton vortex angular velocity, which is a key parameter for the superfluid regime and the event horizon. Finally, as it gets focused from a large ring in free space into a µm-sized ring on the sample, the ring acquires some radial velocity, since it is not focused through the centre of the lens. This radial velocity can be an unwanted parameter in the experiment.

Once the ring has been shaped to the desired size, it must be resonant in energy with the LPB. This can be done either by tuning the incident laser (a Ti-Sapphire oscillator which can be tuned simply using a dial) in energy, or by leveraging the exciton-cavity detuning in a wedged sample to tune the LPB in resonance with the ring.

Tuning the laser is simple in theory. In practice, we excite the sample with a pulsed Tsunami laser, whose wavelength can be tuned very precisely, and with a laser linewidth of ~ 10 µeV, which is small enough to excite the LPB resonantly. The laser has a pulse duration of 100-200 ps at a repetition rate of 80 MHz.

The experiment consists of a three way compromise between pulse duration, laser stability, and wavelength. Some parameters can result in a short enough

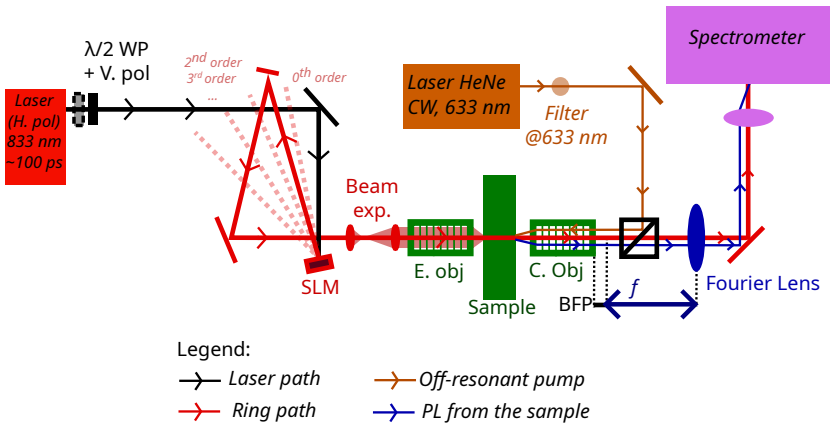

Figure 6.5: Experimental setup to create an exciton-polariton optical vortex with controllable parameters. On the excitation side, the main pump laser is controlled in power by a polariser and a half wave-plate. The laser is redirected onto the SLM, where the first order of diffraction is collected. A beam expander is used to control the size of the optical vortex in k-space, and the ring is projected onto the sample in the transmission geometry.
On the collection side, a non-resonant HeNe laser is used to measure the LPB dispersion in photoluminsence in the reflection geometry. The two measurements can be done at the same time as they use different geometry. The beam paths of on the collection side are shifted for clarity, but hit the sample at $k = 0$ incidence.

pulse duration to get high peak power, and a pulse with a stable enough configuration that the system remains at the set wavelength and doesn't need to be tuned in the middle of a measurement. However, optimising these parameters change the emitted wavelength of the laser.

Achieving a good compromise between these tree parameters is particularly challenging at wavelengths in the 832-833 nm region, where contaminants in the laser system such as water or oxygen may be absorbed and make the laser less stable. Unfortunately, this is also the region of interest for our experiment.

By contrast, if the laser is set in a stable configuration with a fixed wavelength, tuning the cavity to the desired wavelength is easier experimentally. In a wedged cavity, it consists of simple moving the sample using micrometer screw to the desired region. However, it may be more difficult to get the desired excitonic and photonic fractions for the polaritons.

6.4.2 Polariton optical vortexes in the superfluid regime

Non-linear behaviour of the ring

The sample we use for this experiment consists of a cavity with GaAs/AlGaAs DBRs, with GaAs/$In_{0.04}Ga_{0.96}As$ QWs in the cavity. It is selected for its good sample quality at a wavelength that can easily be reached with the Ti-Saphirre laser. The exciton resonance is approximately 1.4968 eV at 4 K. The sample is described in figure 6.6. The cavity is wedged, which allows for a controlled exciton-photon detuning and control of the Hopfield coefficients.

We can demonstrate the strong coupling in this system by showing an anti-crossing of the lower and upper polariton branch, as was done in figure 6.7.

In figure 6.7, it is necessary to completely saturate the LPB to see the UPB. For the remainder of this experiment, we were unable to systematically probe both branches. As a result, it is only possible to give an approximate value of the coupling strength over the sample, and as such the precise values of the excitonic and photonic fractions cannot be given all the time. In the case of figure 6.7, we estimate the Rabi splitting to be 4.45 meV. As a result, we can say, depending on the position of the bottom of the LPB, if the polaritons created at a particular point in the sample are more excitonic (if the LPB is closer to the exciton resonance, ie, at a lower wavelength) or more photonic (if the LPB is at a higher wavelength), and estimate the photonic fraction using this approximate Rabi splitting.

Our first objective is to show a non-linear behaviour of the ring-shaped

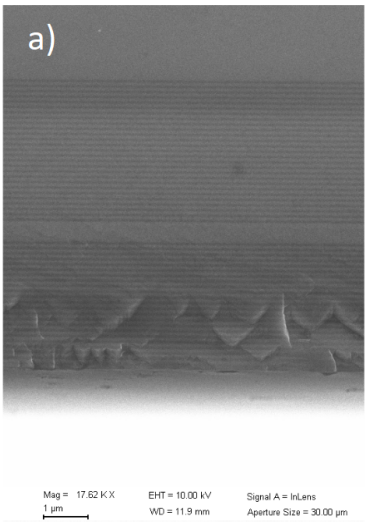

b)

Repeats	Thickness	Thickness tolerance	Material
23	58.27 nm		GaAs
23	69.16 nm		$Al_{(0.85)}Ga_{(0.15)}As$
1	111.55 nm		GaAs
1	10.0 nm		$In_{(0.04)}Ga_{(0.96)}As$
1	106.55 nm		GaAs
1	10.0 nm		$In_{(0.04)}Ga_{(0.96)}As$
1	106.55 nm		GaAs
1	10.0 nm		$In_{(0.04)}Ga_{(0.96)}As$
1	111.55 nm		GaAs
26	69.16 nm		$Al_{(0.85)}Ga_{(0.15)}As$
26	58.27 nm		GaAs
1	69.16 nm		$Al_{(0.85)}Ga_{(0.15)}As$

Figure 6.6: a) SEM imaging of the sample, showing the growth substrate on the top, the DBR pairs, then the cavity in the middle, and the second layer of DBR at the bottom. b) Growth specifications of the sample with the materials. Courtesy of Tommi Isoniemi.

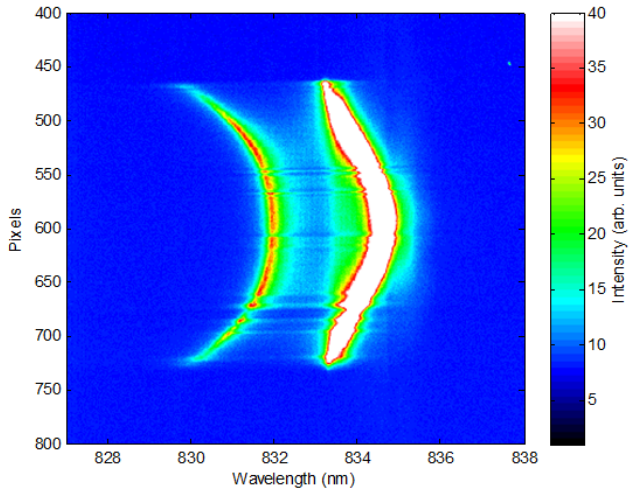

Figure 6.7: Polariton emission in a k-space as a function of wavelength and angle of emission, resulting from a non-resonant pumping of the sample. It shows anti-crossing of the upper polariton branch and the lower polariton branch. Courtesy of Tommi Isoniemi. For this run, the k axis was not calibrated.

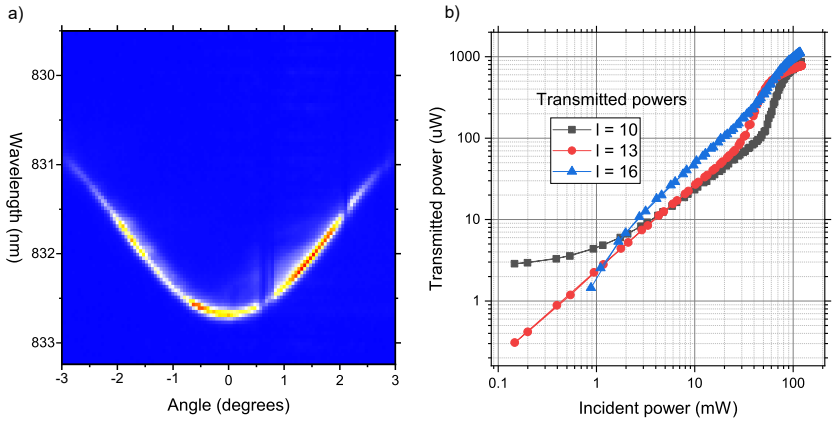

Figure 6.8: a) LPB dispersion for testing the non-linear behaviour of the ring. b) Power dependency of rings with different l numbers.

pattern, in this case a non-linear shift of the polariton dispersion. If we pump the sample slightly above the bottom of the LPB, the transmission through the sample is initially low, but will get much stronger after the LPB shifts enough in energy to be in resonance with the pump. We must demonstrate that the sample does indeed show non-linear shift of the LPB. Showing that the sample exhibits non-linear behaviour is a first step on the road for the realisation of superfluidity and an event horizon. We stress that this behaviour is different from the non-linear threshold of polariton condensation, as the polaritons are coherently injected directly in the system, as opposed to the "spontaneous" coherence which builds up from non-resonant pumping for polariton BECs.

To demonstrate this non-linearity, we measure the total transmitted power as a function of the incident power, for different ring sizes, for the polariton dispersion plotted in figure 6.8.a, with a ring laser resonant with the bottom of the LPB.

In figure 6.8.b, we show the transmitted power, measured after the sample, as a function of the incident power carried by the ring, measured before the sample. The larger optical vortex ($l = 16$) shows a purely linear dependency, with no threshold, whereas the $l = 10$ vortex shows a sharp threshold. The $l = 13$ case is intermediate, showing a less pronounced "kink" but at lower powers. This can be attributed to the polariton density, with scales with the size of the optical vortex. The size of the optical vortex is in turn given by the l numbers. In other words, the bigger the l number, the larger the optical vortex; the larger the l vortex, the lower the polariton density; and for low polariton densities, no non-linear behaviour is expected to occur.

In conclusion, for a given optical vortex size, a non-linear behaviour consis-

tent with polariton superfluid transition can occur for ring-shaped beams with a relatively high l number. At even higher l numbers, only a linear behaviour in power is observed, and no polariton superfluidity occurs. This rules out these very high l numbers for the experiment.

In theory, this limitation could be overcome with a telescope to expand or shrink the beam, however an angular momentum close to $l = 10$ is considered suitable for analogue physics experiment.

Influence of the Hopfield coefficients and ring filtering

The previous section has demonstrated evidence of exciton-polariton non-linear behaviour for vortices of a large l quantum number when pumped near-resonance. However, to realise a superfluid polariton, it is necessary to pump the cavity with a certain detuning in energy from the bottom of the lower polariton branch. Indeed, the transition to the superfluid regime depends on the Landau criterion, which is dependant on the polariton fluid velocity. This velocity is directly dependant on the initial momentum of the injected polariton, as given by equation 2.67, and in particular, if we inject polaritons resonant with the bottom of the LPB, then their velocity will be zero.

At the same time, the beam must be shaped so that its size in k-space is equal to the spacing of the LPB at the same energy, "meeting the edges" of the polariton dispersion. For example, if the injected polaritons are resonant in energy with the bottom of the LPB, but with a high wavevector, then no non-linear behaviour will occur.

One challenge of this experiment is that there is a very large parameter space to cover. We will analyse the non-linear behaviour of the ring at three points in the wedge cavity: one with a more excitonic fraction (fig 6.9.a, b, c), with a LPB wavelength of 831.17 nm, one with a more photonic fraction, with a LPB wavelength of 832.80 nm (fig 6.9.d, e, f), and finally one with a more "balanced" fraction (fig 6.9.g, h, i), with a LPB wavelength of 832.24 nm. This gives excitonic fractions $|C_X|^2$ of approximately 0.33 for the more excitonic case, 0.25 for the "balanced" case, and finally 0.20 for the photonic case.

The results show that a more excitonic polariton makes a poor realisation of the ring-shaped vortex beam, which does not display a sizeable change in the ring shape as power is increased. This can be attributed to the large effective mass of exciton-like polaritons in the cavity, as opposed to photon-like polaritons. Indeed, in [19] the author explicitly attributes the fluid-like behaviour of exciton-polaritons to their photonic fraction.

A very photonic ring does display a sizeable change in the ring after thresh-

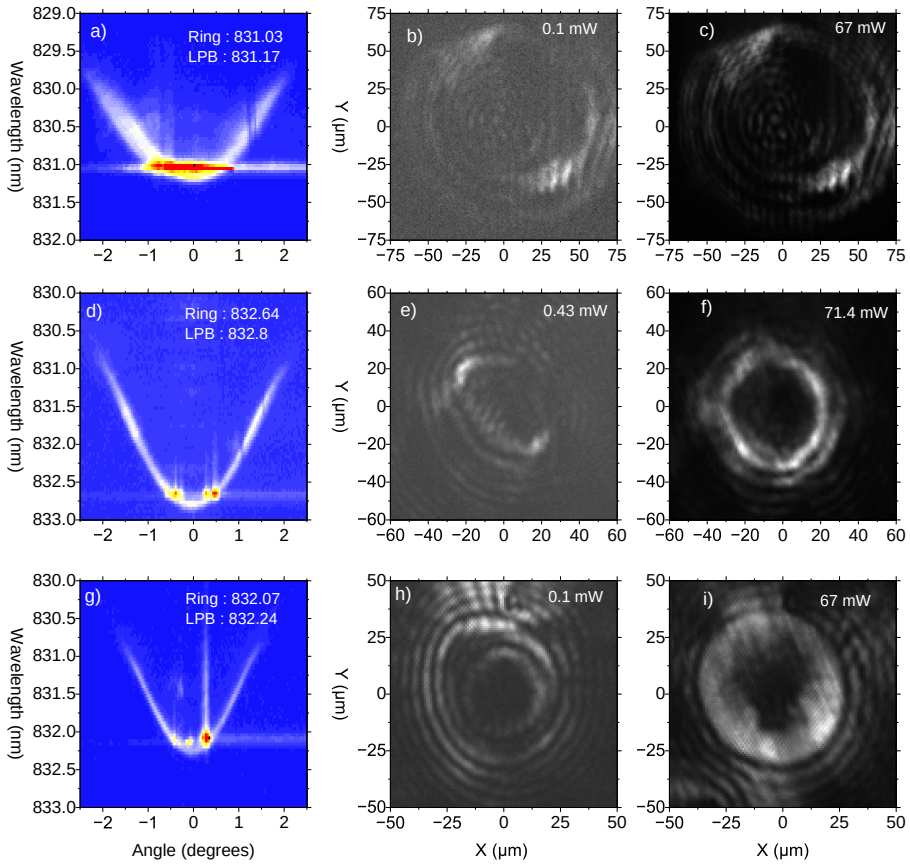

Figure 6.9: Non-linear behaviour of the optical vortex for excitonic polaritons (a, b, c), photonic polaritons (d, e, f), and balanced polaritons (g, h, i). The colour scale for (a, d, g) is logarithmic, with warmer colours indicating a greater signal. The colour scale is greyscale for the ring images, with brighter pixels indicating a stronger signal.
On the first column, the dispersion and the vortex are plotted in k-space imaging, with a slight vortex-LPB detuning in energy. On the second column, the *real-space* image of the vortex is plotted at low powers, and on the third column, the ring is plotted at high powers.
Axis: for the dispersion, the x-axis is the dispersion angle in degree, and the y-axis is the wavelength in nm. For the optical vortexes, the x and y axis are distances from the centre of the ring in µm. The axis titles are not repeated to save space.

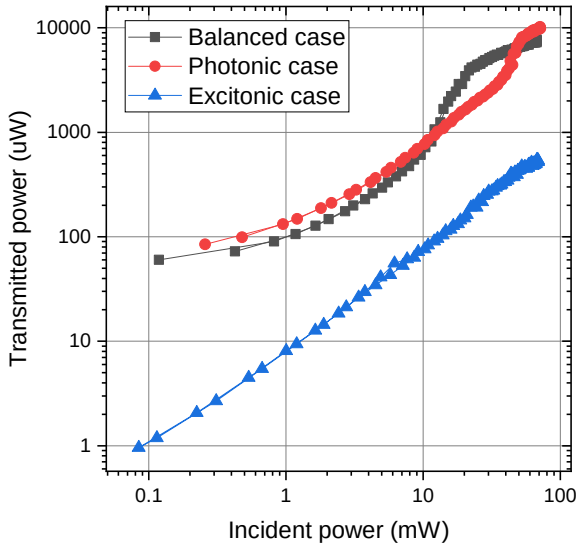

Figure 6.10: Transmitted power of the ring as a function of incident power for the pumping detuning of figure 6.9. The balanced case is for $|C_X|^2 = 0.25$, the photonic case for $|C_X|^2 = 0.20$, and the excitonic case for $|C_X|^2 = 0.33$.

old, which can be seen in the second line of figure 6.9. However, the change of the ring is less pronounced than the balanced case. and we note that the ring shows a distortion at low power.

The balanced exciton-polariton, on the third line, results in a very sharp non-linear threshold and a sizeable change in the ring shape. This procedure helps to rule out very excitonic and very photonic polaritons and reduces the parameter space.

A similar conclusion can be drawn from the study of the transmitted power of the rings through the sample, as a function of incident power, as seen in figure 6.10. The very excitonic rings do not display any threshold-like behaviour, and the more photonic rings have a high threshold. By contrast, the "balanced" case shows a sharp threshold at lower power.

An interesting result of this preliminary experiment relates to the shaping of the optical vortex beam. We find that, if the ring size in k-space does not match the LPB dispersion, then the ring shrinks or expands in k-space to match the edges of the dispersion. This is because polariton states at a given energy resides on a ring in k-space which is given by the polariton dispersion. This is

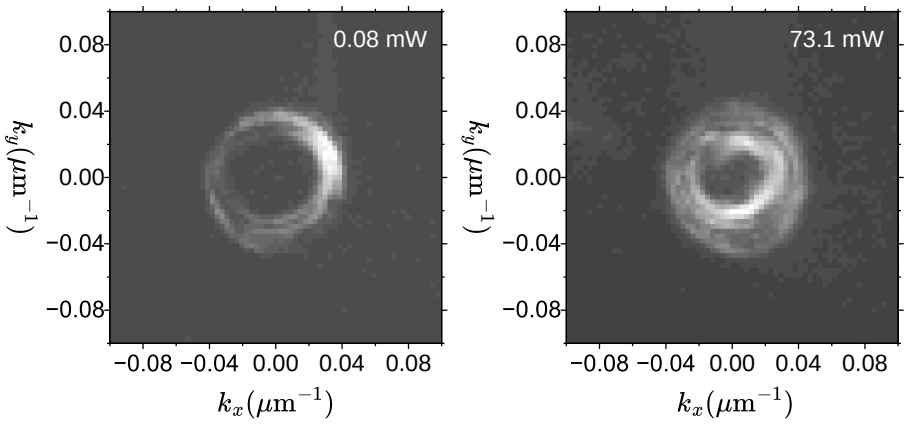

Figure 6.11: k-space imaging of an $l = 10$ ring, before (left) and after (right) non-linear threshold. For this ring, the LPB was at 832.305 nm, and the ring was at 832.210 nm, giving a detuning in energy $\delta_{\mathrm{Laser-LPB}} = 170$ µeV. The data is plotted in logarithmic greyscale, with brighter pixels meaning higher signal.

known as *cavity filtering*: the optical vortex shrinks or expands to match the allowed polariton momenta space. The shrinking of the ring in k-space results in a distortion of the transmitted optical vortex in real space, which can be seen for example on the photonic case of figure 6.9 at low powers. Interesting, the transmitted optical vortex becomes less distorted after threshold. We attribute this to a shift of the LPB which results in less cavity filtering and less distortion of the ring.

A direct measurement of the LPB dispersion under highly resonant pump power is difficult, as the injected polaritons are close to the resonance, and do not populate the full dispersion. However, it is possible to image the ring in k-space, as seen in figure 6.11. As we increase the power, the cavity filtering can be seen as the ring in k-space changes size and becomes thicker. This can be tentatively interpreted as the injected polaritons populating lower energy states of the dispersion, and shrinking their size in k-space to accommodate for the lower k-space "size" of the polariton dispersion at these energies. This implies a shift of the polariton dispersion, which would be consistent with a superfluid transition as described in [19].

Evidence of superfluid behaviour

We can now perform a direct test of the superfluid behaviour of the exciton-polaritons. To demonstrate superfluid behaviour, we create the ring-shaped beam on a region of the sample with a prominent surface defect.

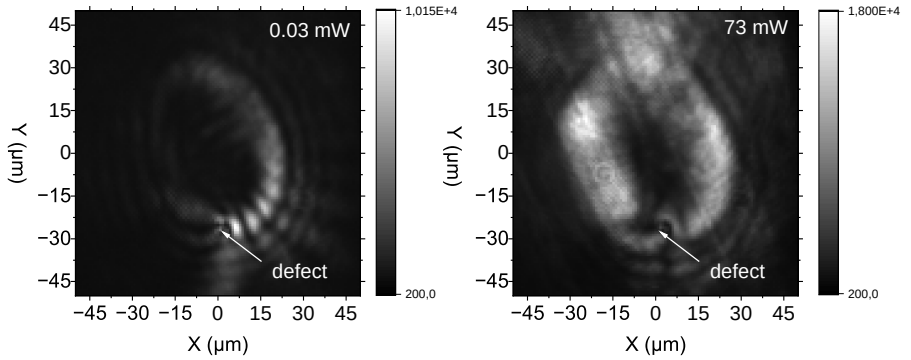

Figure 6.12: Real-space images in transmission of an $l = 8$ before (left) and after (right) non-linear threshold, showing superfluid behaviour. The ring rotates clockwise, and below threshold some ripples due to the interference of the scattered light with the incoming light are observed. Those ripples dissapear in the superfluid regime, and the light flows freely around the defect.
This plot uses a linear greyscale colour scheme, with brighter pixels having more signal.

We find that the fluid of exciton-polaritons shows ripples around the defect below threshold, but such ripples vanish above threshold, as seen in figure 6.12. The best results are obtained for a ring with a higher polariton density, and as such with a lower l number. The LPB is at 832.509 nm, and the ring is pumped at 832.4331 nm, resulting in detuning in energy $\delta_{\mathrm{Laser-LPB}} = 135$ µeV.

These ripples come from the back-scattering of the polariton fluid across the defect. As the polariton moves in a circular fashion, it hits the defects and some gets scattered in the opposite direction. On the detection side, this creates a phase interference pattern, resulting in the formation of fringes and ripples. However, after the threshold and once the polariton is in the superfluid regime, this back-scattering no longer occurs, and the fringes dissapear.

It is easy to reverse the direction of the angular momentum by flipping the image (fig 6.4.b) used to create the polariton vortex. Once the flow is reversed, the ripples flow in the other direction. After the threshold is reached, the light flows around the defect without scattering. This confirms that the optical vortex acts as a fluid of light with a clockwise or anti-clockwise flow which can be easily controlled with the SLM, and that above a certain threshold, it acts as a superfluid. This is shown in figure 6.13.

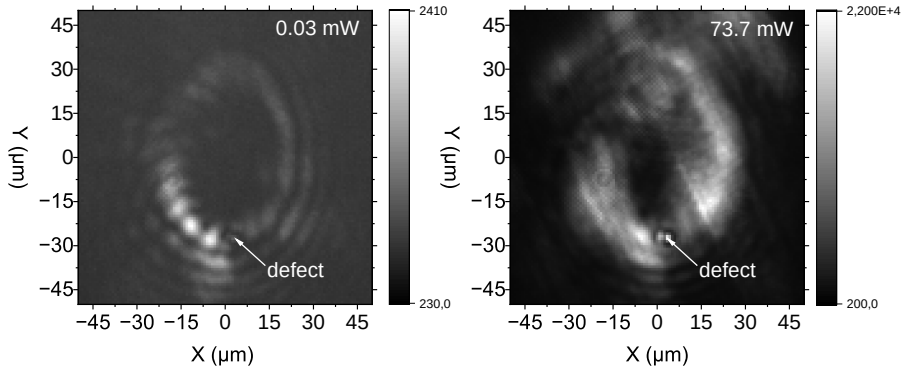

Figure 6.13: Real-space images in transmission of an $l = 8$ before (left) and after (right) non-linear threshold, showing superfluid behaviour. The ring is illuminated on the same defect as in figure 6.12, but with the direction of propagation reversed.
This plot uses a linear greyscale colour scheme, with brighter pixels having more signal.

Discussion

Our sample shows behaviour consistent with polariton superfluidity. However, a challenge remains as we need to display a clear, unambiguous event horizon for analogue physics experiments. The event horizon for an exciton-polariton analogue black hole is characterised by a transition from the superfluid to the Cerenkov regime. This can be characterised by sliding the optical vortex left and right across the defect. Where the optical vortex has a high density of polaritons, we should see a superfluid-like frictionless flow, whereas where the vortex has a lower density of polaritons, we should see a Cerenkov-like scattering, as in figure 2.31, with small straight ripples very close to the defect, as opposed to curved ones.

It is difficult to unambiguously claim this in our experiments. Indeed, our vortex-shaped beam shows a very sharp decrease in intensity on the edges, as seen in figure 6.14. Therefore, it is difficult to project the ring in such a way that the polariton density is high enough to observe the Cerenkov-like behaviour, but low enough that it does not reach the superfluid regime.

Additionally, our rudimentary study has shown behaviour consistent with the superfluid regime but failed to clearly identify a superfluid critical velocity. A more systematic study would have allowed us to identify the key experimental parameters needed to reach the Cerenkov regime.

Unfortunately, this study proved to be difficult as getting the pump laser to

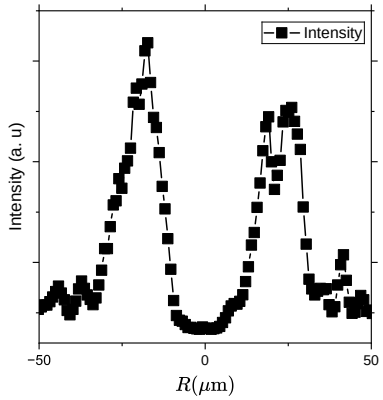

Figure 6.14: Intensity profile along the x axis for a $l = 10$ ring, above threshold.

consistently emit at the same wavelength with the same pulse duration was not possible, as our pump laser was quite unstable. This was a persistent experimental challenge during our investigation of exciton-polariton analogue black holes. Other challenges include the very large parameter space of different l numbers, and the size of the ring in k-space which needs to match the dispersion to avoid too much distortion due to cavity filtering.

6.5 Further work

Our experiment has shown some evidence of superfluid behaviour for different l numbers and a very large experimental flexibility to tune the parameters of the experiment. However, this also comes with experimental difficulties due to the very large parameter space. Further work on this experiment will focus on ways to claim the creation of an event horizon and the study of the angular velocity and phase properties of the exciton-polariton analogue black hole.

6.5.1 Aharonov-Bohm effect

An interesting signature of analogue physics is the so-called Aharonov-Bohm effect. In quantum electrodynamics, the Aharonov-Bohm effect is observed when a charge is affected by an electromagnetic field even in a region where the intensity of the field should be zero [297]. This effect is purely quantum, and comes from the coupling of the charge's complex phase to the potential from which the electro-magnetic field derives.

A gravitational analogue of the effect is expected to happen for gravitational fields [298]. Analogue physics experiments were proposed to investigate this phenomenon [299], with ultimately some results in a cold atoms condensate [300].

The electromagnetic Aharonov-Bohm effect is typically measured using interference patterns, as the phase of the particles affected by the potential are phase-shifted according to the potential's angular momentum. Observing a phase-shift due to the Aharonov-Bohm effect would be a proof that we have realised an analogue black hole without the need to check for an event horizon.

6.5.2 Phase measurements

To observe the Aharonov-Bohm effect, we build an interferometer to measure the phase across the ring to quantify the angular momentum l and verify that the imprinted optical vortex retains the angular momentum. The geometry of the interferometer is given by figure 3.6.B. In this case, the pump beam is sent an angle compared to the reference beam. This allows us to recreate the phase-pattern of the 6.4, and an algorithm [301] used a Fourier transform to extract the phase data from such measurements.

While this approach is suitable for $l = 1$, as shown in figure 6.15.b, it proves to be more challenging for higher l numbers, as seen in figure 6.15.d. As the time of writing this thesis, experimental efforts focus on finding the best available ways to find a phase map for the extraction.

6.5.3 Filtering in intensity

The geometry to realise the Aharonov-Bohm effect is quite complex. One possible geometry requires a two-beam experiment. One beam is used to realise the analogue black hole using the geometry we have described in figure 6.5. The other beam would be used to probe the phase shift resulting from the analogue gravity, and would be sent at a small angle, on the edges of the optical vortex. The two beams need to be separated in energy.

On the collection side, it is necessary to filter the pump beam which creates the vortex and the probe beam. As the two beams are separated in energy, a pulse-shaper which only selects the wavelengths of the probe beam would be an adequate solution.

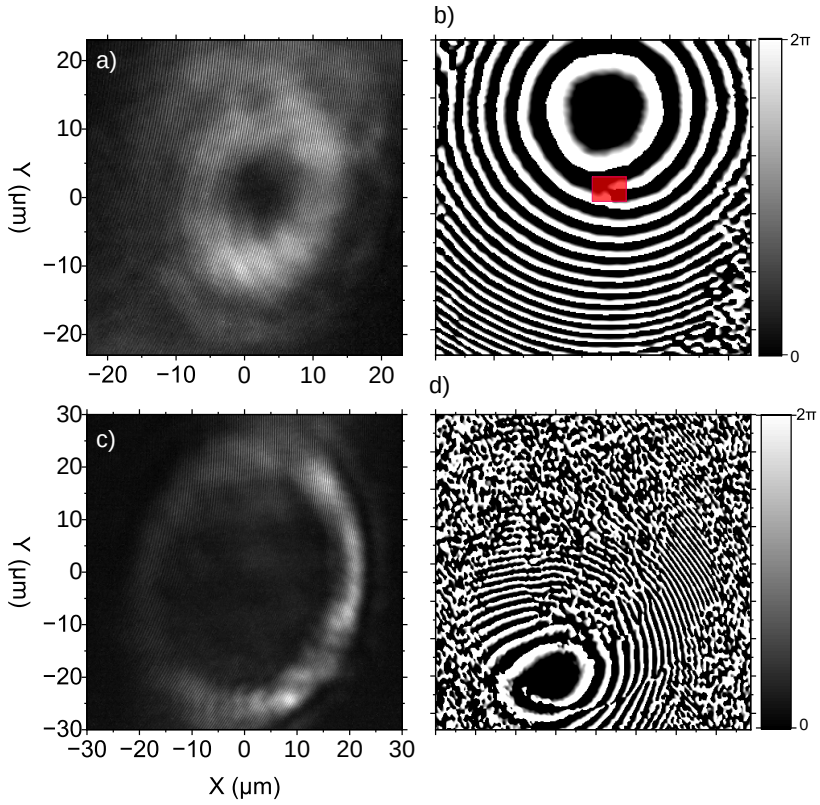

Figure 6.15: a) Interferometric measurement of the $l = 1$ ring, without being transmitted through the sample. b) Phase map as extracted using [301]. The red highlight corresponds to the dislocation identifying a $l = 1$ vortex.
a) Interferometric measurement of the $l = 10$ ring, without being transmitted through the sample. b) Phase map as extracted using [301]. The data is too noisy to identify any discernable features.

6.5.4 Conclusion

We have demonstrated a number of necessary conditions (non-linear threshold and superfluidity) to realise analogue physics on our sample using exciton-polaritons. The very large parameter space and the instability of the lasers used in this experiment are challenges. However, confirming that we have an event horizon proves to be difficult. The experimental work continues at the time of writing this thesis.

Chapter 7

Conclusion and perspectives

Exciton-polaritons are an extremely rich topic of study. In this thesis, we have tried to show the breadth of the subject with an extensive literature review and the presentation of original research.

The introduction provides a definition of the phenomenon, explaining where the idea of "hybrid light-matter particles" comes from. We define the strong coupling regime while paying attention to the limiting case of the weak coupling regime, and noting that extreme regimes such as the *deep coupling regime* can be studied. We give an introduction to the three families of materials used in the remaining chapter of this thesis. The remainder of the introduction serves as an illustration of the potential application of exciton-polaritons. We provide an introduction to the notion of "coherence" in quantum physics and Bose-Einstein condensation. Building on that, we describe exciton-polariton condensation, importantly describing how it can be distinguished form weak coupling lasing. Some applications of polariton condensates such as superfluidity are further described.

The second chapter dealt with our experimental methods. It showed how versatile exciton-polaritons are experimentally, with many techniques of quantum optics available for their study. These techniques are used in the other chapters of this thesis.

The third chapter consists of a published paper [21] which is original research. This paper demonstrated how a polariton laser can be realised in a ring resonator geometry up to room temperature. Some questions are left open with this paper, such as the reason why there is such a drastic shift in threshold at 300 K compared to 200 K. The geometry realised could also be used as a building block for more complex circuits, for example by coupling the ring to a

waveguide. This paper shows one of the greatest strengths of the III-N families of materials, which is their ability to maintain an exciton up to room temperature, and as such polaritonic effects are visible without an expensive cryogenic setup. This could be a first step towards practical, transportable on-chip polaritonic devices. Since exciton-polaritons show very strong non-linearities, there are some potentially useful applications such as frequency combs [302], or as logic gates [303] for use in a light-based computer (which can be classical [304] or quantum [305]). There are nevertheless some challenges which need to be addressed to fully realise the potential of exciton-polariton in III-N materials. Firstly, the fabrication processes in such materials is still relatively novel when compared to more established structures, such as Gallium Arsenide. In the case of our experiment, this had an impact, because we were only able to realise high quality rings with a large radial thickness. Such thick rings can support many ring resonator modes, who then couple to the excitons in the quantum wells. Having multiple modes in the ring is not desirable, since the signal is spread out with emission at different energies. A strong signal at a well-defined energy would be preferable. Improvements in the fabrication process could lead to sample fabrication that lends itself better to future applications.

Another challenge we faced when working with the Gallium Nitride ring resonators is that, while we were able to identify their photoluminescence spectra as polariton lasing both at room temperature and cryogenic temperatures, there were noticeable differences in their emission features, with high temperatures having a higher threshold of emission. A more thorough analysis of the lasing threshold with respect to temperature would provide some interesting insight in the polariton lasing process, with the aim of achieving a lower threshold at room temperature, something desirable in the case of practical applications. Finally, we should stress that the photoluminscence spectra collected are only a small fraction of the light emitted by the ring resonator during the pumping process. Indeed, due to the geometry of the ring resonators, most of the light resulting from the polariton lasing is emitted in the plane perpendicular to the ring resonator, and very little can be collected. This feature can be useful for coupling this emitted light to other structures in the sample, such as a waveguide; however in our case it just means we get a lower signal than optimal. Patterning defects around the ring, which could act as scattering centres, would be a way to increase the signal from the sample, resulting in better data.

In the fourth chapter, we presented another published paper in a very active field of study, Rydberg exciton-polaritons. We demonstrate for the first time non-linear behaviour of polaritons in this system, scaling with the principal quantum number of the exciton n. We give a tentative theoretical model showing that the exciton-polaritons display an intermediate regime, between the highly sought-after Rydberg blockade, and Pauli blockade from the fermionic nature of the electrons and holes which make up the excitons. Rydberg exciton-polaritons show how exciton-polaritons can still open up new avenues of original research, more than 60 years after their original theoretical discovery by Hop-

field and Pekar, and almost 30 years after their first realisation in microcavities. Rydberg exciton-polaritons allow experimentalists to bridge two worlds: the well-established field of Rydberg atomic physics, and the world of light-matter interaction solid-state Physics. Rydberg atoms are studied in many different areas of research: they can be used as sensors [306], in quantum computing [307], or for quantum simulation [308], in which they are used to reproduce other physical phenomena. However, Rydberg Atoms have many limitations that must be taken into account for practical experiments, such as the need to use laser cooling. Rydberg excitons are an analogue of Rydberg Atoms in the solid-state, and can be manipulated experimentally more easily, and sample fabrication is easier. Rydberg excitons also only need to be cooled down to a few Kelvins, which can be done using a liquid Helium cryostat, as opposed to a more involved setup using laser cooling. The interaction of Rydberg excitons with light can be further enhanced by placing them in a microcavity. We stress that this is a very new topic, with the first realisation of Rydberg exciton-polaritons being realised only in 2022 [132]. Our work is a stepping stone for further research and applications involving Rydberg exciton-polaritons, since knowing how the non-linearities scale with quantum number is the first step towards leveraging these non-linearities for potential applications. Our results are encouraging, since they show that the scaling does follow results expected by Rydberg blockade theory, but we would need to achieve higher quantum numbers to reach this regime. We also note that our work has motivated some new research in the study of Rydberg exciton lifetimes, since our results were in contradiction with some experiments done on bare flake, non-cavity samples. Overall, the topic of Rydberg exciton-polaritons is quite novel, and further fundamental research on their properties would be needed to develop applications. Our work contributes to that fundamental research.

Finally, in the fifth chapter, we described how exciton-polaritons can be used for studying astrophysics. We began with a layman's approach on black holes to give motivation, and showed how exciton-polaritons can make a realisation of an analogue black hole. This experiment is still ongoing, with the ultimate goal of displaying the Aharonov-Bohm effect.

This last experiment is slightly different from our previous work, as it uses a material that is quite commonly when studying polaritons, since our sample is a GaAs microcavity. The novelty here is in the application we seek from this experiment, as we are using it in a context that is far removed from traditional solid state physics, and instead as an experimental tool to study questions of cosmology and general relativity. This shows the experimental versatility of exciton-polaritons and how they can be used in a variety of different contexts, with very precise control over the experimental parameters, which are critical for this particular experiment. The "artificial black hole" created using exciton-polaritons can be used to get experimental data on phenomena which are predicted by theory, such as black hole evaporation, but have not been observed due to the nature of black holes. A more long-term goal of analogue physics ex-

periments is to use the data resulting from the experiment to critically evaluate the underlying theory. While the theory of general relativity remains one of the most successful and precise theories formulated, it is inconsistent with quantum mechanics, and cannot accurately describe some predictions such as the "Black Hole Information paradox", which predicts that the information going "into" the black hole is irreversibly destroyed during the evaporation process [309]. Being able to get experimental data showing analogue black hole evaporation could be useful to see how the paradox arises. This, however, is a task that is beyond the scope of this thesis, and perhaps beyond what a simple experimentalist in solid-state physics can achieve.

We end this thesis with a remark on how broad this research topic proved to be, going from ultra-violet all the way to infrared, from condensates to superfluidity, and with an emphasis on how all the original research presented in this thesis fuels further work.

Marco Polo describes a bridge, stone by stone. 'But which is the stone that supports the bridge?' Kublai Khan asks.
'The bridge is not supported by one stone or another,' Marco answers, 'but by the line of the arch that they form.'
Kublai Khan remains silent, reflecting. Then he adds: 'Why do you speak to me of the stones? It is only the arch that matters to me.'
Polo answers: 'Without stones there is no arch.'
— Italo Calvino, "Invisible Cities"

Images licences

IEEE

The IEEE does not require individuals working on a thesis to obtain a formal reuse license.

AIP

I have registered a free re-use RightsLink licence for copyrighted AIP images which covers up to 10 figures.

Springer Link

I have registered a free re-use RightsLink licence for copyrighted Springer Link images.

APS

I have registered a free re-use RightsLink licence for copyrighted APS images.

References

[1] S. I Pekar. "Observation of the coupled exciton-photon mode splitting in a semiconductor quantum microcavity". In: *SOVIET PHYSICS JETP* 6 (33).4 (Apr. 1958), pp. 785–796. ISSN: 1063-7761. URL: http://jetp.ras.ru/cgi-bin/e/index/e/9/2/p314.

[2] J. J. Hopfield. "Theory of the Contribution of Excitons to the Complex Dielectric Constant of Crystals". In: *Physical Review* 112.5 (Dec. 1958), pp. 1555–1567. ISSN: 0031-899X. DOI: 10.1103/physrev.112.1555. URL: http://dx.doi.org/10.1103/PhysRev.112.1555.

[3] C. H. Henry and J. J. Hopfield. "Raman Scattering by Polaritons". In: *Physical Review Letters* 15.25 (Dec. 1965), pp. 964–966. ISSN: 0031-9007. DOI: 10.1103/physrevlett.15.964. URL: http://dx.doi.org/10.1103/PhysRevLett.15.964.

[4] C. Benoit a la Guillaume, A. Bonnot, and J. M. Debever. "Luminescence from Polaritons". In: *Physical Review Letters* 24.22 (June 1970), pp. 1235–1238. ISSN: 0031-9007. DOI: 10.1103/physrevlett.24.1235. URL: http://dx.doi.org/10.1103/PhysRevLett.24.1235.

[5] J. Lagois and B. Fischer. "Experimental Observation of Surface Exciton Polaritons". In: *Physical Review Letters* 36.12 (Mar. 1976), pp. 680–683. ISSN: 0031-9007. DOI: 10.1103/physrevlett.36.680. URL: http://dx.doi.org/10.1103/PhysRevLett.36.680.

[6] Heba Megahd, Davide Comoretto, and Paola Lova. "(INVITED)Planar microcavities: Materials and processing for light control". In: *Optical Materials: X* 13 (Jan. 2022), p. 100130. ISSN: 2590-1478. DOI: 10.1016/j.omx.2021.100130. URL: http://dx.doi.org/10.1016/j.omx.2021.100130.

[7] C. Weisbuch et al. "Observation of the coupled exciton-photon mode splitting in a semiconductor quantum microcavity". In: *Physical Review Letters* 69.23 (Dec. 1992), pp. 3314–3317. DOI: 10.1103/physrevlett.69.3314. URL: https://doi.org/10.1103/physrevlett.69.3314.

[8] Dallin S. Durfee and Wolfgang Ketterle. "Experimental studies of Bose-Einstein condensation". In: *Optics Express* 2.8 (Apr. 1998), p. 299. ISSN: 1094-4087. DOI: 10.1364/oe.2.000299. URL: http://dx.doi.org/10.1364/OE.2.000299.

[9] Lasha Berezhiani and Justin Khoury. "Emergent long-range interactions in Bose-Einstein condensates". In: *Physical Review D* 99.7 (Apr. 2019). ISSN: 2470-0029. DOI: 10.1103/physrevd.99.076003. URL: http://dx.doi.org/10.1103/PhysRevD.99.076003.

[10] Bose. "Plancks Gesetz und Lichtquantenhypothese". In: *Zeitschrift fur Physik* 26.1 (Dec. 1924), pp. 178–181. ISSN: 1434-601X. DOI: 10.1007/bf01327326. URL: http://dx.doi.org/10.1007/BF01327326.

[11] A. Einstein. *Quantentheorie des einatomigen idealen Gases*. Dec. 2005. DOI: 10.1002/3527608958.ch27. URL: http://dx.doi.org/10.1002/3527608958.ch27.

[12] Iulia Georgescu. "25 years of BEC". In: *Nature Reviews Physics* 2.8 (July 2020), pp. 396–396. ISSN: 2522-5820. DOI: 10.1038/s42254-020-0211-7. URL: http://dx.doi.org/10.1038/s42254-020-0211-7.

[13] K. B. Davis et al. "Bose-Einstein Condensation in a Gas of Sodium Atoms". In: *Physical Review Letters* 75.22 (Nov. 1995), pp. 3969–3973. DOI: 10.1103/physrevlett.75.3969. URL: https://doi.org/10.1103/physrevlett.75.3969.

[14] Annesh Mukhopadhyay et al. "Observation of Momentum Space Josephson Effects in Weakly Coupled Bose-Einstein Condensates". In: *Physical Review Letters* 132.23 (June 2024). ISSN: 1079-7114. DOI: 10.1103/physrevlett.132.233403. URL: http://dx.doi.org/10.1103/PhysRevLett.132.233403.

[15] Ke Wang, Han Fu, and K. Levin. "Simulating cosmological evolution by quantum quench of an atomic Bose-Einstein condensate". In: *Physical Review A* 109.1 (Jan. 2024). ISSN: 2469-9934. DOI: 10.1103/physreva.109.013316. URL: http://dx.doi.org/10.1103/PhysRevA.109.013316.

[16] Hui Deng, Hartmut Haug, and Yoshihisa Yamamoto. "Exciton-polariton Bose-Einstein condensation". In: *Reviews of Modern Physics* 82.2 (May 2010), pp. 1489–1537. DOI: 10.1103/revmodphys.82.1489. URL: https://doi.org/10.1103/revmodphys.82.1489.

[17] P. C. Hohenberg. "Existence of Long-Range Order in One and Two Dimensions". In: *Physical Review* 158.2 (June 1967), pp. 383–386. ISSN: 0031-899X. DOI: 10.1103/physrev.158.383. URL: http://dx.doi.org/10.1103/PhysRev.158.383.

[18] J M Kosterlitz and D J Thouless. "Ordering, metastability and phase transitions in two-dimensional systems". In: *Journal of Physics C: Solid State Physics* 6.7 (Apr. 1973), pp. 1181–1203. ISSN: 0022-3719. DOI: 10.1088/0022-3719/6/7/010. URL: http://dx.doi.org/10.1088/0022-3719/6/7/010.

[19] Alberto Amo et al. "Superfluidity of polaritons in semiconductor microcavities". In: *Nature Physics* 5.11 (Sept. 2009), pp. 805–810. DOI: 10.1038/nphys1364. URL: https://doi.org/10.1038/nphys1364.

[20] Andrew A. Allocca et al. "Cavity superconductor-polaritons". In: *Physical Review B* 99.2 (Jan. 2019). ISSN: 2469-9969. DOI: 10.1103/physrevb.99.020504. URL: http://dx.doi.org/10.1103/PhysRevB.99.020504.

[21] Anthonin Delphan et al. "Polariton lasing in AlGaN microring with GaN/AlGaN quantum wells". In: *APL Photonics* 8.2 (Feb. 2023). ISSN: 2378-0967. DOI: 10.1063/5.0132170. URL: http://dx.doi.org/10.1063/5.0132170.

[22] Maxim Makhonin et al. "Nonlinear Rydberg exciton-polaritons in Cu2O microcavities". In: *Light: Science & Applications* 13.1 (Feb. 2024). ISSN: 2047-7538. DOI: 10.1038/s41377-024-01382-9. URL: http://dx.doi.org/10.1038/s41377-024-01382-9.

[23] W. G. Unruh. "Experimental Black-Hole Evaporation?" In: *Physical Review Letters* 46.21 (May 1981), pp. 1351–1353. ISSN: 0031-9007. DOI: 10.1103/physrevlett.46.1351. URL: http://dx.doi.org/10.1103/PhysRevLett.46.1351.

[24] M. Sich et al. "Observation of bright polariton solitons in a semiconductor microcavity". In: *Nature Photonics* 6.1 (Nov. 2011), pp. 50–55. ISSN: 1749-4893. DOI: 10.1038/nphoton.2011.267. URL: http://dx.doi.org/10.1038/nphoton.2011.267.

[25] Fabrice P. Laussy, Alexey V. Kavokin, and Ivan A. Shelykh. "Exciton-Polariton Mediated Superconductivity". In: *Physical Review Letters* 104.10 (Mar. 2010). ISSN: 1079-7114. DOI: 10.1103/physrevlett.104.106402. URL: http://dx.doi.org/10.1103/PhysRevLett.104.106402.

[26] A. Imamoğlu et al. "Nonequilibrium condensates and lasers without inversion: Exciton-polariton lasers". In: *Physical Review A* 53.6 (June 1996), pp. 4250–4253. DOI: 10.1103/physreva.53.4250. URL: https://doi.org/10.1103/physreva.53.4250.

[27] S. Christopoulos et al. "Room-Temperature Polariton Lasing in Semiconductor Microcavities". In: *Phys. Rev. Lett.* 98 (2007), p. 126405.

[28] Charles Kittel. *Introduction to solid state physics*. en. 8th ed. Nashville, TN: John Wiley & Sons, Oct. 2004.

[29] Neil W Ashcroft and N Mermin. *Solid State Physics*. en. Florence, KY: Brooks/Cole, Jan. 1976.

[30] Hsiao-Yi Chen et al. "Ab initiocalculations of exciton radiative lifetimes in bulk crystals, nanostructures, and molecules". In: *Physical Review B* 100.7 (Aug. 2019). ISSN: 2469-9969. DOI: 10.1103/physrevb.100.075135. URL: http://dx.doi.org/10.1103/PhysRevB.100.075135.

[31] Vatsal A Jhalani et al. "Precise radiative lifetimes in bulk crystals from first principles: the case of wurtzite gallium nitride". In: *Journal of Physics: Condensed Matter* 32.8 (Nov. 2019), p. 084001. ISSN: 1361-648X. DOI: 10.1088/1361-648x/ab5563. URL: http://dx.doi.org/10.1088/1361-648X/ab5563.

[32] Daniel Steiauf, Emmanouil Kioupakis, and Chris G. Van de Walle. "Auger Recombination in GaAs from First Principles". In: *ACS Photonics* 1.8 (July 2014), pp. 643–646. ISSN: 2330-4022. DOI: 10.1021/ph500119q. URL: http://dx.doi.org/10.1021/ph500119q.

[33] V.M. Agranovich et al. "Superradiance of 2D Frenkel exciton-polaritons: mixing of molecular configurations and resonance interaction with the substrate". In: *Chemical Physics* 203.1 (Feb. 1996), pp. 11–21. ISSN: 0301-0104. DOI: 10.1016/0301-0104(96)88026-8. URL: http://dx.doi.org/10.1016/0301-0104(96)88026-8.

[34] H. J. Bakker, S. Hunsche, and H. Kurz. "Coherent phonon polaritons as probes of anharmonic phonons in ferroelectrics". In: *Reviews of Modern Physics* 70.2 (Apr. 1998), pp. 523–536. ISSN: 1539-0756. DOI: 10.1103/revmodphys.70.523. URL: http://dx.doi.org/10.1103/RevModPhys.70.523.

[35] Francisco J. Garcia-Vidal et al. "Spoof surface plasmon photonics". In: *Reviews of Modern Physics* 94.2 (May 2022). ISSN: 1539-0756. DOI: 10.1103/revmodphys.94.025004. URL: http://dx.doi.org/10.1103/RevModPhys.94.025004.

[36] M S Skolnick, T A Fisher, and D M Whittaker. "Strong coupling phenomena in quantum microcavity structures". In: *Semiconductor Science and Technology* 13.7 (July 1998), pp. 645–669. ISSN: 1361-6641. DOI: 10.1088/0268-1242/13/7/003. URL: http://dx.doi.org/10.1088/0268-1242/13/7/003.

[37] Tintu Kuriakose et al. "Few-photon all-optical phase rotation in a quantum-well micropillar cavity". In: *Nature Photonics* 16.8 (June 2022), pp. 566–569. DOI: 10.1038/s41566-022-01019-6. URL: https://doi.org/10.1038/s41566-022-01019-6.

[38] Aymeric Delteil et al. "Towards polariton blockade of confined exciton–polaritons". In: *Nature Materials* 18.3 (Feb. 2019), pp. 219–222. DOI: 10.1038/s41563-019-0282-y. URL: https://doi.org/10.1038/s41563-019-0282-y.

[39] K. Huang. "On the interaction between the radiation field and ionic crystals". In: *Proceedings of the Royal Society of London. Series A. Mathematical and Physical Sciences* 208.1094 (Sept. 1951), pp. 352–365. ISSN: 2053-9169. DOI: 10.1098/rspa.1951.0166. URL: http://dx.doi.org/10.1098/rspa.1951.0166.

[40] Lucio Claudio Andreani. "Exciton-Polaritons in Bulk Semiconductors and in Confined Electron and Photon Systems". In: *Strong Light-Matter Coupling*. WORLD SCIENTIFIC, Jan. 2014, pp. 37–82. ISBN: 9789814460354. DOI: 10.1142/9789814460354_0002. URL: http://dx.doi.org/10.1142/9789814460354_0002.

[41] Alexey V Kavokin et al. *Microcavities*. 2nd ed. Series on Semiconductor Science and Technology. London, England: Oxford University Press, May 2017.

[42] G. Cappellini et al. "Model dielectric function for semiconductors". In: *Physical Review B* 47.15 (Apr. 1993), pp. 9892–9895. ISSN: 1095-3795. DOI: 10.1103/physrevb.47.9892. URL: http://dx.doi.org/10.1103/PhysRevB.47.9892.

[43] Eduardo B. Barros and Stephanie Reich. "Longitudinal polaritons in crystals". In: *Physical Review B* 110.16 (Oct. 2024). ISSN: 2469-9969. DOI: 10.1103/physrevb.110.165108. URL: http://dx.doi.org/10.1103/PhysRevB.110.165108.

[44] V. A. Kiselev, B. S. Razbirin, and I. N. Uraltsev. "Additional waves and Fabry-Perot interference of photoexcitons (polaritons) in thin II–VI crystals". In: *physica status solidi (b)* 72.1 (Nov. 1975), pp. 161–172. ISSN: 1521-3951. DOI: 10.1002/pssb.2220720117. URL: http://dx.doi.org/10.1002/pssb.2220720117.

[45] B. Hönerlage et al. "The dispersion of excitons, polaritons and biexcitons in direct-gap semiconductors". In: *Physics Reports* 124.3 (July 1985), pp. 161–253. ISSN: 0370-1573. DOI: 10.1016/0370-1573(85)90025-0. URL: http://dx.doi.org/10.1016/0370-1573(85)90025-0.

[46] D. D. Sell et al. "Polariton Reflectance and Photoluminescence in High-Purity GaAs". In: *Physical Review B* 7.10 (May 1973), pp. 4568–4586. ISSN: 0556-2805. DOI: 10.1103/physrevb.7.4568. URL: http://dx.doi.org/10.1103/PhysRevB.7.4568.

[47] Rainer G. Ulbrich and Claude Weisbuch. "Resonant Brillouin Scattering of Excitonic Polaritons in Gallium Arsenide". In: *Physical Review Letters* 38.15 (Apr. 1977), pp. 865–868. ISSN: 0031-9007. DOI: 10.1103/physrevlett.38.865. URL: http://dx.doi.org/10.1103/PhysRevLett.38.865.

[48] S. Suga et al. "Luminescence of exciton-polaritons in semiconductors". In: *Journal of Luminescence* 12–13 (Mar. 1976), pp. 109–117. ISSN: 0022-2313. DOI: 10.1016/0022-2313(76)90070-3. URL: http://dx.doi.org/10.1016/0022-2313(76)90070-3.

[49] R. J. Anderson. "Theory of the Interaction of Light Beams via Polariton-Polariton Scattering". In: *Physical Review B* 8.8 (Oct. 1973), pp. 3861–3864. ISSN: 0556-2805. DOI: 10.1103/physrevb.8.3861. URL: http://dx.doi.org/10.1103/PhysRevB.8.3861.

[50] F. Vallée, F. Bogani, and C. Flytzanis. "Time-resolved investigation of exciton-polariton dephasing in CuCl". In: *Physical Review Letters* 66.11 (Mar. 1991), pp. 1509–1512. ISSN: 0031-9007. DOI: 10.1103/physrevlett.66.1509. URL: http://dx.doi.org/10.1103/PhysRevLett.66.1509.

[51] Xiantong Yu et al. "Strong Coupling in Microcavity Structures: Principle, Design, and Practical Application". In: *Laser & Photonics Reviews* 13.1 (Nov. 2018). ISSN: 1863-8899. DOI: 10.1002/lpor.201800219. URL: http://dx.doi.org/10.1002/lpor.201800219.

[52] Kai Zhang et al. "Design and Fabrication Technology of Metal Mirrors Based on Additive Manufacturing: A Review". In: *Applied Sciences* 11.22 (Nov. 2021), p. 10630. ISSN: 2076-3417. DOI: 10.3390/app112210630. URL: http://dx.doi.org/10.3390/app112210630.

[53] F Avino, A Sublet, and M Taborelli. "Evidence of ion energy distribution shift in HiPIMS plasmas with positive pulse". In: *Plasma Sources Science and Technology* 28.1 (Jan. 2019), 01LT03. ISSN: 1361-6595. DOI: 10.1088/1361-6595/aaf5c9. URL: http://dx.doi.org/10.1088/1361-6595/aaf5c9.

[54] E. S. Ameh. "A review of basic crystallography and x-ray diffraction applications". In: *The International Journal of Advanced Manufacturing Technology* 105.7–8 (Nov. 2019), pp. 3289–3302. ISSN: 1433-3015. DOI: 10.1007/s00170-019-04508-1. URL: http://dx.doi.org/10.1007/s00170-019-04508-1.

[55] Charalambos C. Katsidis and Dimitrios I. Siapkas. "General transfer-matrix method for optical multilayer systems with coherent, partially coherent, and incoherent interference". In: *Applied Optics* 41.19 (July 2002), p. 3978. ISSN: 1539-4522. DOI: 10.1364/ao.41.003978. URL: http://dx.doi.org/10.1364/AO.41.003978.

[56] C. Koks and M. P. van Exter. "Microcavity resonance condition, quality factor, and mode volume are determined by different penetration depths". In: *Optics Express* 29.5 (Feb. 2021), p. 6879. ISSN: 1094-4087. DOI: 10.1364/oe.412346. URL: http://dx.doi.org/10.1364/OE.412346.

[57] C. Schneider et al. "Quantum dot micropillar cavities with quality factors exceeding 250, 000". In: *Applied Physics B* 122.1 (Jan. 2016). ISSN: 1432-0649. DOI: 10.1007/s00340-015-6283-x. URL: http://dx.doi.org/10.1007/s00340-015-6283-x.

[58] K. Winkler et al. “High quality factor GaAs microcavity with buried bullseye defects”. In: *Physical Review Materials* 2.5 (May 2018). ISSN: 2475-9953. DOI: 10.1103/physrevmaterials.2.052201. URL: http://dx.doi.org/10.1103/PhysRevMaterials.2.052201.

[59] Rajat Sharma et al. “Gallium-nitride-based microcavity light-emitting diodes with air-gap distributed Bragg reflectors”. In: *Applied Physics Letters* 91.21 (Nov. 2007). ISSN: 1077-3118. DOI: 10.1063/1.2805028. URL: http://dx.doi.org/10.1063/1.2805028.

[60] R. Butté et al. “Recent Progress in the Growth of Highly Reflective Nitride-Based Distributed Bragg Reflectors and Their Use in Microcavities”. In: *Japanese Journal of Applied Physics* 44.10R (Oct. 2005), p. 7207. ISSN: 1347-4065. DOI: 10.1143/jjap.44.7207. URL: http://dx.doi.org/10.1143/JJAP.44.7207.

[61] Tsu-Chi Chang et al. “ZnO-Based Microcavities Sculpted by Focus Ion Beam Milling”. In: *Nanoscale Research Letters* 11.1 (June 2016). ISSN: 1556-276X. DOI: 10.1186/s11671-016-1526-2. URL: http://dx.doi.org/10.1186/s11671-016-1526-2.

[62] Emilia Palo and Konstantinos S. Daskalakis. “Prospects in Broadening the Application of Planar Solution-Based Distributed Bragg Reflectors”. In: *Advanced Materials Interfaces* 10.19 (Jan. 2023). ISSN: 2196-7350. DOI: 10.1002/admi.202202206. URL: http://dx.doi.org/10.1002/admi.202202206.

[63] Michal Gryga, Dalibor Ciprian, and Petr Hlubina. “Distributed Bragg Reflectors Employed in Sensors and Filters Based on Cavity-Mode Spectral-Domain Resonances”. In: *Sensors* 22.10 (May 2022), p. 3627. ISSN: 1424-8220. DOI: 10.3390/s22103627. URL: http://dx.doi.org/10.3390/s22103627.

[64] Lord Rayleigh. “CXII. The problem of the whispering gallery”. In: *The London, Edinburgh, and Dublin Philosophical Magazine and Journal of Science* 20.120 (Dec. 1910), pp. 1001–1004. ISSN: 1941-5990. DOI: 10.1080/14786441008636993. URL: http://dx.doi.org/10.1080/14786441008636993.

[65] Lord Rayleigh. “On the Propagation of Waves through a Stratified Medium, with Special Reference to the Question of Reflection”. In: *Proceedings of the Royal Society of London. Series A, Containing Papers of a Mathematical and Physical Character* 86.586 (1912), pp. 207–226. ISSN: 09501207. URL: http://www.jstor.org/stable/93163 (visited on 08/29/2024).

[66] Guoping Lin, Aurélien Coillet, and Yanne K. Chembo. “Nonlinear photonics with high-Q whispering-gallery-mode resonators”. In: *Advances in Optics and Photonics* 9.4 (Nov. 2017), p. 828. ISSN: 1943-8206. DOI: 10.1364/aop.9.000828. URL: http://dx.doi.org/10.1364/AOP.9.000828.

[67] Shancheng Yang, Yue Wang, and Handong Sun. "Advances and Prospects for Whispering Gallery Mode Microcavities". In: *Advanced Optical Materials* 3.9 (Aug. 2015), pp. 1136–1162. ISSN: 2195-1071. DOI: 10.1002/adom.201500232. URL: http://dx.doi.org/10.1002/adom.201500232.

[68] Xuefeng Jiang et al. "Whispering-Gallery Sensors". In: *Matter* 3.2 (Aug. 2020), pp. 371–392. ISSN: 2590-2385. DOI: 10.1016/j.matt.2020.07.008. URL: http://dx.doi.org/10.1016/j.matt.2020.07.008.

[69] Shun Fujii and Takasumi Tanabe. "Dispersion engineering and measurement of whispering gallery mode microresonator for Kerr frequency comb generation". In: *Nanophotonics* 9.5 (Feb. 2020), pp. 1087–1104. ISSN: 2192-8606. DOI: 10.1515/nanoph-2019-0497. URL: http://dx.doi.org/10.1515/nanoph-2019-0497.

[70] Mark Oxborrow. "How to simulate the whispering-gallery modes of dielectric microresonators in FEMLAB/COMSOL". In: *Laser Resonators and Beam Control IX*. Ed. by Alexis V. Kudryashov, Alan H. Paxton, and Vladimir S. Ilchenko. SPIE, Feb. 2007. DOI: 10.1117/12.714954. URL: http://dx.doi.org/10.1117/12.714954.

[71] Haiyong Quan and Zhixiong Guo. "Simulation of whispering-gallery-mode resonance shifts for optical miniature biosensors". In: *Journal of Quantitative Spectroscopy and Radiative Transfer* 93.1–3 (June 2005), pp. 231–243. ISSN: 0022-4073. DOI: 10.1016/j.jqsrt.2004.08.023. URL: http://dx.doi.org/10.1016/j.jqsrt.2004.08.023.

[72] C. G. B. Garrett, W. Kaiser, and W. L. Bond. "Stimulated Emission into Optical Whispering Modes of Spheres". In: *Physical Review* 124.6 (Dec. 1961), pp. 1807–1809. ISSN: 0031-899X. DOI: 10.1103/physrev.124.1807. URL: http://dx.doi.org/10.1103/PhysRev.124.1807.

[73] S. L. McCall et al. "Whispering-gallery mode microdisk lasers". In: *Applied Physics Letters* 60.3 (Jan. 1992), pp. 289–291. ISSN: 1077-3118. DOI: 10.1063/1.106688. URL: http://dx.doi.org/10.1063/1.106688.

[74] Gangyi Zhu et al. "Whispering-Gallery Mode Lasing in a Floating GaN Microdisk with a Vertical Slit". In: *Scientific Reports* 10.1 (Jan. 2020). ISSN: 2045-2322. DOI: 10.1038/s41598-019-57118-y. URL: http://dx.doi.org/10.1038/s41598-019-57118-y.

[75] B. D. Jones et al. "Splitting and lasing of whispering gallery modes in quantum dot micropillars". In: *Optics Express* 18.21 (Oct. 2010), p. 22578. ISSN: 1094-4087. DOI: 10.1364/oe.18.022578. URL: http://dx.doi.org/10.1364/OE.18.022578.

[76] Nirmalendu Acharyya and Gregory Kozyreff. "Large Q Factor with Very Small Whispering-Gallery-Mode Resonators". In: *Physical Review Applied* 12.1 (July 2019). ISSN: 2331-7019. DOI: 10.1103/physrevapplied.12.014060. URL: http://dx.doi.org/10.1103/PhysRevApplied.12.014060.

[77] Zecen Zhang et al. “Compact microring resonators integrated with grating couplers working at 2 µm wavelength on silicon-on-insulator platform”. In: *Applied Optics* 56.19 (June 2017), p. 5444. ISSN: 1539-4522. DOI: 10.1364/ao.56.005444. URL: http://dx.doi.org/10.1364/AO.56.005444.

[78] A N Tait et al. “Microring resonator-coupled photoluminescence from silicon W centers”. In: *Journal of Physics: Photonics* 2.4 (July 2020), p. 045001. ISSN: 2515-7647. DOI: 10.1088/2515-7647/ab95f2. URL: http://dx.doi.org/10.1088/2515-7647/ab95f2.

[79] Chih-Wei Tseng et al. “Study of coupling loss on strongly-coupled, ultra compact microring resonators”. In: *Optics Express* 21.6 (Mar. 2013), p. 7250. ISSN: 1094-4087. DOI: 10.1364/oe.21.007250. URL: http://dx.doi.org/10.1364/OE.21.007250.

[80] J. Schrauwen, D. Van Thourhout, and R. Baets. “Trimming of silicon ring resonator by electron beam induced compaction and strain”. In: *Optics Express* 16.6 (Mar. 2008), p. 3738. ISSN: 1094-4087. DOI: 10.1364/oe.16.003738. URL: http://dx.doi.org/10.1364/OE.16.003738.

[81] Pankaj K. Sahoo et al. “On the reproducibility of electron-beam lithographic fabrication of photonic nanostructures”. In: *Scientific Reports* 14.1 (Apr. 2024). ISSN: 2045-2322. DOI: 10.1038/s41598-024-58842-w. URL: http://dx.doi.org/10.1038/s41598-024-58842-w.

[82] J. D. Joannopoulos, Pierre R. Villeneuve, and Shanhui Fan. “Photonic crystals: putting a new twist on light”. In: *Nature* 386.6621 (Mar. 1997), pp. 143–149. ISSN: 1476-4687. DOI: 10.1038/386143a0. URL: http://dx.doi.org/10.1038/386143a0.

[83] M.A. Butt, S.N. Khonina, and N.L. Kazanskiy. “Recent advances in photonic crystal optical devices: A review”. In: *Optics & Laser Technology* 142 (Oct. 2021), p. 107265. ISSN: 0030-3992. DOI: 10.1016/j.optlastec.2021.107265. URL: http://dx.doi.org/10.1016/j.optlastec.2021.107265.

[84] Raji Shankar et al. “Mid-infrared photonic crystal cavities in silicon”. In: *Optics Express* 19.6 (Mar. 2011), p. 5579. ISSN: 1094-4087. DOI: 10.1364/oe.19.005579. URL: http://dx.doi.org/10.1364/OE.19.005579.

[85] Mark Fox and Radu Ispasoiu. “Quantum Wells, Superlattices, and Band-Gap Engineering”. In: *Springer Handbook of Electronic and Photonic Materials*. Springer International Publishing, 2017, pp. 1–1. ISBN: 9783319489339. DOI: 10.1007/978-3-319-48933-9_40. URL: http://dx.doi.org/10.1007/978-3-319-48933-9_40.

[86] Y Yamamoto, F Tassone, and H Cao. *Semiconductor cavity quantum electrodynamics*. en. 2000th ed. Springer Tracts in Modern Physics. Berlin, Germany: Springer, Sept. 2000.

[87] Feng Liu et al. “High Purcell factor generation of indistinguishable on-chip single photons”. In: *Nature Nanotechnology* 13.9 (July 2018), pp. 835–840. ISSN: 1748-3395. DOI: 10.1038/s41565-018-0188-x. URL: http://dx.doi.org/10.1038/s41565-018-0188-x.

[88] E. M. Purcell, H. C. Torrey, and R. V. Pound. “Resonance Absorption by Nuclear Magnetic Moments in a Solid”. In: *Physical Review* 69.1–2 (Jan. 1946), pp. 37–38. ISSN: 0031-899X. DOI: 10.1103/physrev.69.37. URL: http://dx.doi.org/10.1103/PhysRev.69.37.

[89] T. H. MAIMAN. “Stimulated Optical Radiation in Ruby”. In: *Nature* 187.4736 (Aug. 1960), pp. 493–494. ISSN: 1476-4687. DOI: 10.1038/187493a0. URL: http://dx.doi.org/10.1038/187493a0.

[90] C. Chen et al. “Temperature Analysis of Threshold Current in Infrared Vertical-Cavity Surface-Emitting Lasers”. In: *IEEE Journal of Quantum Electronics* 42.10 (Oct. 2006), pp. 1078–1083. ISSN: 0018-9197. DOI: 10.1109/jqe.2006.881828. URL: http://dx.doi.org/10.1109/JQE.2006.881828.

[91] Yang Mei et al. “Optically pumped flexible GaN-based ultraviolet VCSELs”. In: *Optics Letters* 49.7 (Mar. 2024), p. 1816. ISSN: 1539-4794. DOI: 10.1364/ol.517756. URL: http://dx.doi.org/10.1364/OL.517756.

[92] Anjin Liu et al. “Vertical-cavity surface-emitting lasers for data communication and sensing”. In: *Photonics Research* 7.2 (Jan. 2019), p. 121. ISSN: 2327-9125. DOI: 10.1364/prj.7.000121. URL: http://dx.doi.org/10.1364/PRJ.7.000121.

[93] G. Khitrova et al. “Vacuum Rabi splitting in semiconductors”. In: *Nature Physics* 2.2 (Feb. 2006), pp. 81–90. ISSN: 1745-2481. DOI: 10.1038/nphys227. URL: http://dx.doi.org/10.1038/nphys227.

[94] V. Savona et al. “Quantum well excitons in semiconductor microcavities: Unified treatment of weak and strong coupling regimes”. In: *Solid State Communications* 93.9 (1995), pp. 733–739. ISSN: 0038-1098. DOI: https://doi.org/10.1016/0038-1098(94)00865-5. URL: https://www.sciencedirect.com/science/article/pii/0038109894008655.

[95] L.C. Andreani et al. “Polaritons in high reflectivity microcavities: semiclassical and full quantum treatment of optical properties”. In: *Superlattices and Microstructures* 15.4 (June 1994), pp. 453–458. ISSN: 0749-6036. DOI: 10.1006/spmi.1994.1086. URL: http://dx.doi.org/10.1006/spmi.1994.1086.

[96] Bryan Nelsen et al. “Dissipationless Flow and Sharp Threshold of a Polariton Condensate with Long Lifetime”. In: *Physical Review X* 3.4 (Nov. 2013). ISSN: 2160-3308. DOI: 10.1103/physrevx.3.041015. URL: http://dx.doi.org/10.1103/PhysRevX.3.041015.

[97] Ding Xu et al. "Ultrafast imaging of polariton propagation and interactions". In: *Nature Communications* 14.1 (June 2023). ISSN: 2041-1723. DOI: 10.1038/s41467-023-39550-x. URL: http://dx.doi.org/10.1038/s41467-023-39550-x.

[98] P. Forn-Díaz et al. "Ultrastrong coupling regimes of light-matter interaction". In: *Reviews of Modern Physics* 91.2 (June 2019). ISSN: 1539-0756. DOI: 10.1103/revmodphys.91.025005. URL: http://dx.doi.org/10.1103/RevModPhys.91.025005.

[99] Salvatore Gambino et al. "Exploring Light–Matter Interaction Phenomena under Ultrastrong Coupling Regime". In: *ACS Photonics* 1.10 (Oct. 2014), pp. 1042–1048. ISSN: 2330-4022. DOI: 10.1021/ph500266d. URL: http://dx.doi.org/10.1021/ph500266d.

[100] Johannes Koch et al. "Quantum Rabi dynamics of trapped atoms far in the deep strong coupling regime". In: *Nature Communications* 14.1 (Feb. 2023). ISSN: 2041-1723. DOI: 10.1038/s41467-023-36611-z. URL: http://dx.doi.org/10.1038/s41467-023-36611-z.

[101] Tingting Wang et al. "Magnetically-dressed CrSBr exciton-polaritons in ultrastrong coupling regime". In: *Nature Communications* 14.1 (Sept. 2023). ISSN: 2041-1723. DOI: 10.1038/s41467-023-41688-7. URL: http://dx.doi.org/10.1038/s41467-023-41688-7.

[102] Husam Aldin A. Abdul Amir, Makram A. Fakhri, and Ali Abdulkhaleq Alwahib. "Review of GaN optical device characteristics, applications, and optical analysis technology". In: *Materials Today: Proceedings* 42 (2021), pp. 2815–2821. ISSN: 2214-7853. DOI: 10.1016/j.matpr.2020.12.727. URL: http://dx.doi.org/10.1016/j.matpr.2020.12.727.

[103] G. Rossbach et al. "High-temperature Mott transition in wide-band-gap semiconductor quantum wells". In: *Physical Review B* 90.20 (Nov. 2014), 201308(R). DOI: 10.1103/physrevb.90.201308. URL: https://doi.org/10.1103/physrevb.90.201308.

[104] Herbert Paul Maruska and Walden Clark Rhines. "A modern perspective on the history of semiconductor nitride blue light sources". In: *Solid-State Electronics* 111 (Sept. 2015), pp. 32–41. ISSN: 0038-1101. DOI: 10.1016/j.sse.2015.04.010. URL: http://dx.doi.org/10.1016/j.sse.2015.04.010.

[105] A Trichet et al. "From strong to weak coupling regime in a single GaN microwire up to room temperature". In: *New Journal of Physics* 14.7 (July 2012), p. 073004. ISSN: 1367-2630. DOI: 10.1088/1367-2630/14/7/073004. URL: http://dx.doi.org/10.1088/1367-2630/14/7/073004.

[106] Michael R. Krames et al. "Status and Future of High-Power Light-Emitting Diodes for Solid-State Lighting". In: *Journal of Display Technology* 3.2 (June 2007), pp. 160–175. ISSN: 1551-319X. DOI: 10.1109/jdt.2007.895339. URL: http://dx.doi.org/10.1109/JDT.2007.895339.

[107] Takuji Sekiya, Takashi Sasaki, and Kazuhiro Hane. "Design, fabrication, and optical characteristics of freestanding GaN waveguides on silicon substrate". In: *Journal of Vacuum Science & Technology B, Nanotechnology and Microelectronics: Materials, Processing, Measurement, and Phenomena* 33.3 (Apr. 2015). ISSN: 2166-2754. DOI: 10.1116/1.4917487. URL: http://dx.doi.org/10.1116/1.4917487.

[108] Ryan Ley et al. "Strain relaxation of InGaN/GaN multi-quantum well light emitters via nanopatterning". In: *Optics Express* 27.21 (Oct. 2019), p. 30081. ISSN: 1094-4087. DOI: 10.1364/oe.27.030081. URL: http://dx.doi.org/10.1364/OE.27.030081.

[109] Joachim Ciers et al. "Near-UV narrow bandwidth optical gain in lattice-matched III–nitride waveguides". In: *Japanese Journal of Applied Physics* 57.9 (July 2018), p. 090305. ISSN: 1347-4065. DOI: 10.7567/jjap.57.090305. URL: http://dx.doi.org/10.7567/JJAP.57.090305.

[110] Raphaël Butté and Nicolas Grandjean. "III-nitride photonic cavities". In: *Nanophotonics* 9.3 (Jan. 2020), pp. 569–598. ISSN: 2192-8614. DOI: 10.1515/nanoph-2019-0442. URL: http://dx.doi.org/10.1515/nanoph-2019-0442.

[111] G. D. Chen et al. "Fundamental optical transitions in GaN". In: *Applied Physics Letters* 68.20 (May 1996), pp. 2784–2786. ISSN: 1077-3118. DOI: 10.1063/1.116606. URL: http://dx.doi.org/10.1063/1.116606.

[112] Gabriel Christmann et al. "Room temperature polariton lasing in a GaN/AlGaN multiple quantum well microcavity". In: *Applied Physics Letters* 93.5 (Aug. 2008), p. 051102. DOI: 10.1063/1.2966369. URL: https://doi.org/10.1063/1.2966369.

[113] J. Ciers et al. "Propagating Polaritons in III-Nitride Slab Waveguides". In: *Physical Review Applied* 7.3 (Mar. 2017), p. 034019. DOI: 10.1103/physrevapplied.7.034019. URL: https://doi.org/10.1103/physrevapplied.7.034019.

[114] Mohammad Soltani et al. "AlGaN/AlN integrated photonics platform for the ultraviolet and visible spectral range". In: *Optics Express* 24.22 (Oct. 2016), p. 25415. ISSN: 1094-4087. DOI: 10.1364/oe.24.025415. URL: http://dx.doi.org/10.1364/OE.24.025415.

[115] E. F. Gross. "Optical spectrum of excitons in the crystal lattice". In: *Il Nuovo Cimento* 3.S4 (Apr. 1956), pp. 672–701. DOI: 10.1007/bf02746069. URL: https://doi.org/10.1007/bf02746069.

[116] T. Kazimierczuk et al. "Giant Rydberg excitons in the copper oxide Cu_2O ". In: *Nature* 514.7522 (Oct. 2014), pp. 343–347. DOI: 10.1038/nature13832. URL: https://doi.org/10.1038/nature13832.

[117] Mitsuyoshi Takahata and Nobuko Naka. "Photoluminescence properties of the entire excitonic series in Cu_2O ". In: *Physical Review B* 98.19 (Nov. 2018). ISSN: 2469-9969. DOI: 10.1103/physrevb.98.195205. URL: http://dx.doi.org/10.1103/PhysRevB.98.195205.

[118] Hannes Busche et al. “Contactless nonlinear optics mediated by long-range Rydberg interactions”. In: *Nature Physics* 13.7 (July 2017). DOI: 10.1038/nphys4058. URL: https://doi.org/10.1038/nphys4058.

[119] J. Heckötter et al. “Scaling laws of Rydberg excitons”. In: *Physical Review B* 96.12 (Sept. 2017). DOI: 10.1103/physrevb.96.125142. URL: https://doi.org/10.1103/physrevb.96.125142.

[120] Aaron Gross et al. “Temperature dependent scaling laws of Rydberg excitons in Cu2O”. In: *Conference on Lasers and Electro-Optics*. Vol. 514. CLEO˙QELS. Optica Publishing Group, 2021, FTh4M.4. DOI: 10.1364/cleo_qels.2021.fth4m.4. URL: http://dx.doi.org/10.1364/CLEO_QELS.2021.FTh4M.4.

[121] A. Bouillon, E. Marin-Bujedo, and M. Génévriez. “Direct Laser Cooling of Rydberg Atoms with an Isolated-Core Transition”. In: *Physical Review Letters* 132.19 (May 2024). ISSN: 1079-7114. DOI: 10.1103/physrevlett.132.193402. URL: http://dx.doi.org/10.1103/PhysRevLett.132.193402.

[122] Xiaoling Wu et al. “A concise review of Rydberg atom based quantum computation and quantum simulation*”. In: *Chinese Physics B* 30.2 (Feb. 2021), p. 020305. DOI: 10.1088/1674-1056/abd76f. URL: https://dx.doi.org/10.1088/1674-1056/abd76f.

[123] Lida Zhang et al. “Photon-photon interactions in Rydberg-atom arrays”. In: *Quantum* 6 (Mar. 2022), p. 674. ISSN: 2521-327X. DOI: 10.22331/q-2022-03-30-674. URL: https://doi.org/10.22331/q-2022-03-30-674.

[124] Poulab Chakrabarti et al. *Direct measurement of the lifetime and coherence time of* Cu_2O *Rydberg excitons*. 2024. DOI: 10.48550/ARXIV.2410.07355. URL: https://arxiv.org/abs/2410.07355.

[125] Kerwan Morin et al. “Large-scale characterization of Cu_2O monocrystals via Rydberg excitons”. In: *Physical Review Materials* 8.2 (Feb. 2024). ISSN: 2475-9953. DOI: 10.1103/physrevmaterials.8.026202. URL: http://dx.doi.org/10.1103/PhysRevMaterials.8.026202.

[126] S. Mani et al. “High-quality crystals with various morphologies grown by thermal oxidation”. In: *Journal of Crystal Growth* 311.14 (July 2009), pp. 3549–3552. ISSN: 0022-0248. DOI: 10.1016/j.jcrysgro.2009.05.006. URL: http://dx.doi.org/10.1016/j.jcrysgro.2009.05.006.

[127] Changli Li, Yanbo Li, and Jean-Jacques Delaunay. “A Novel Method to Synthesize Highly Photoactive Cu2O Microcrystalline Films for Use in Photoelectrochemical Cells”. In: *ACS Applied Materials & Interfaces* 6.1 (Dec. 2013), pp. 480–486. ISSN: 1944-8252. DOI: 10.1021/am404527q. URL: http://dx.doi.org/10.1021/am404527q.

[128] Stephen A. Lynch et al. "Rydberg excitons in synthetic cuprous oxide Cu_2O ". In: *Physical Review Materials* 5.8 (Aug. 2021). ISSN: 2475-9953. DOI: 10.1103/physrevmaterials.5.084602. URL: http://dx.doi.org/10.1103/PhysRevMaterials.5.084602.

[129] E. Urban et al. "Observation of Rydberg blockade between two atoms". In: *Nature Physics* 5.2 (Feb. 2009). DOI: 10.1038/nphys1178. URL: https://doi.org/10.1038/nphys1178.

[130] Alexander Guttridge et al. "Observation of Rydberg Blockade Due to the Charge-Dipole Interaction between an Atom and a Polar Molecule". In: *Physical Review Letters* 131.1 (July 2023). ISSN: 1079-7114. DOI: 10.1103/physrevlett.131.013401. URL: http://dx.doi.org/10.1103/PhysRevLett.131.013401.

[131] Julian Heckötter et al. "Asymmetric Rydberg blockade of giant excitons in Cuprous Oxide". In: *Nature Communications* 12.1 (June 2021). DOI: 10.1038/s41467-021-23852-z. URL: https://doi.org/10.1038/s41467-021-23852-z.

[132] Konstantinos Orfanakis et al. "Rydberg exciton–polaritons in a Cu_2O microcavity". In: *Nature Materials* 21.7 (Apr. 2022), pp. 767–772. DOI: 10.1038/s41563-022-01230-4. URL: https://doi.org/10.1038/s41563-022-01230-4.

[133] J. M. Luttinger and W. Kohn. "Motion of Electrons and Holes in Perturbed Periodic Fields". In: *Physical Review* 97.4 (Feb. 1955), pp. 869–883. ISSN: 0031-899X. DOI: 10.1103/physrev.97.869. URL: http://dx.doi.org/10.1103/PhysRev.97.869.

[134] M. F. Doty et al. "Hole-spin mixing in InAs quantum dot molecules". In: *Physical Review B* 81.3 (Jan. 2010). ISSN: 1550-235X. DOI: 10.1103/physrevb.81.035308. URL: http://dx.doi.org/10.1103/PhysRevB.81.035308.

[135] R. Balili et al. "Bose-Einstein Condensation of Microcavity Polaritons in a Trap". In: *Science* 316.5827 (May 2007), pp. 1007–1010. ISSN: 1095-9203. DOI: 10.1126/science.1140990. URL: http://dx.doi.org/10.1126/science.1140990.

[136] P. M. Walker et al. "Ultra-low-power hybrid light–matter solitons". In: *Nature Communications* 6 (1 Sept. 2015). DOI: 10.1038/ncomms9317. URL: https://doi.org/10.1038/ncomms9317.

[137] S. Klembt et al. "Exciton-polariton topological insulator". In: *Nature* 562.7728 (Oct. 2018), pp. 552–556. ISSN: 1476-4687. DOI: 10.1038/s41586-018-0601-5. URL: http://dx.doi.org/10.1038/s41586-018-0601-5.

[138] Jiaqi Hu et al. "Polariton Laser in the Bardeen-Cooper-Schrieffer Regime". In: *Physical Review X* 11.1 (Jan. 2021). ISSN: 2160-3308. DOI: 10.1103/physrevx.11.011018. URL: http://dx.doi.org/10.1103/PhysRevX.11.011018.

[139] J. Kasprzak et al. “Bose–Einstein condensation of exciton polaritons”. In: *Nature* 443.7110 (Sept. 2006), pp. 409–414. DOI: 10.1038/nature05131. URL: https://doi.org/10.1038/nature05131.

[140] K. Biermann et al. “Controlled growth of exciton–polariton microcavities using in situ spectral reflectivity measurements”. In: *Journal of Crystal Growth* 323.1 (May 2011), pp. 56–59. ISSN: 0022-0248. DOI: 10.1016/j.jcrysgro.2010.10.107. URL: http://dx.doi.org/10.1016/j.jcrysgro.2010.10.107.

[141] M. Opher-Lipson et al. “Photoluminescence in GaAs/AlGaAs microcavities”. In: *Journal of Luminescence* 72–74 (June 1997), pp. 386–388. ISSN: 0022-2313. DOI: 10.1016/s0022-2313(96)00348-1. URL: http://dx.doi.org/10.1016/S0022-2313(96)00348-1.

[142] S. B. Nam et al. “Free-exciton energy spectrum in GaAs”. In: *Physical Review B* 13.2 (Jan. 1976), pp. 761–767. ISSN: 0556-2805. DOI: 10.1103/physrevb.13.761. URL: http://dx.doi.org/10.1103/PhysRevB.13.761.

[143] S. I. Tsintzos et al. “A GaAs polariton light-emitting diode operating near room temperature”. In: *Nature* 453.7193 (May 2008), pp. 372–375. ISSN: 1476-4687. DOI: 10.1038/nature06979. URL: http://dx.doi.org/10.1038/nature06979.

[144] Yongbao Sun et al. “Direct measurement of polariton–polariton interaction strength”. In: *Nature Physics* 13.9 (June 2017), pp. 870–875. ISSN: 1745-2481. DOI: 10.1038/nphys4148. URL: http://dx.doi.org/10.1038/nphys4148.

[145] Min Park et al. “Exciton reservoir-induced destabilization and reformation of polariton condensate”. In: *Optics Express* 33.8 (Apr. 2025), p. 18530. ISSN: 1094-4087. DOI: 10.1364/oe.553836. URL: http://dx.doi.org/10.1364/OE.553836.

[146] F. Tassone and Y. Yamamoto. “Exciton-exciton scattering dynamics in a semiconductor microcavity and stimulated scattering into polaritons”. In: *Physical Review B* 59.16 (Apr. 1999), pp. 10830–10842. ISSN: 1095-3795. DOI: 10.1103/physrevb.59.10830. URL: http://dx.doi.org/10.1103/PhysRevB.59.10830.

[147] Hui Hu, Hui Deng, and Xia-Ji Liu. “Polariton-polariton interaction beyond the Born approximation: A toy model study”. In: *Physical Review A* 102.6 (Dec. 2020). ISSN: 2469-9934. DOI: 10.1103/physreva.102.063305. URL: http://dx.doi.org/10.1103/PhysRevA.102.063305.

[148] Daegwang Choi et al. “Realization of exciton-polariton condensation in GaAs-based microcavity grown by metalorganic chemical vapor deposition”. In: *Physical Review Research* 4.3 (Sept. 2022). ISSN: 2643-1564. DOI: 10.1103/physrevresearch.4.033188. URL: http://dx.doi.org/10.1103/PhysRevResearch.4.033188.

[149] Jiaxin Zhao et al. "Exciton polariton interactions in Van der Waals superlattices at room temperature". In: *Nature Communications* 14.1 (Mar. 2023). ISSN: 2041-1723. DOI: 10.1038/s41467-023-36912-3. URL: http://dx.doi.org/10.1038/s41467-023-36912-3.

[150] P. G. Savvidis et al. "Angle-Resonant Stimulated Polariton Amplifier". In: *Physical Review Letters* 84.7 (Feb. 2000), pp. 1547–1550. ISSN: 1079-7114. DOI: 10.1103/physrevlett.84.1547. URL: http://dx.doi.org/10.1103/PhysRevLett.84.1547.

[151] R. M. Stevenson et al. "Continuous Wave Observation of Massive Polariton Redistribution by Stimulated Scattering in Semiconductor Microcavities". In: *Physical Review Letters* 85.17 (Oct. 2000), pp. 3680–3683. ISSN: 1079-7114. DOI: 10.1103/physrevlett.85.3680. URL: http://dx.doi.org/10.1103/PhysRevLett.85.3680.

[152] D. Sanvitto et al. "Persistent currents and quantized vortices in a polariton superfluid". In: *Nature Physics* 6.7 (May 2010), pp. 527–533. ISSN: 1745-2481. DOI: 10.1038/nphys1668. URL: http://dx.doi.org/10.1038/nphys1668.

[153] D. M. Whittaker. "Effects of polariton-energy renormalization in the microcavity optical parametric oscillator". In: *Physical Review B* 71.11 (Mar. 2005). ISSN: 1550-235X. DOI: 10.1103/physrevb.71.115301. URL: http://dx.doi.org/10.1103/PhysRevB.71.115301.

[154] P.I. Khadzhi and O.F. Vasilieva. "Exciton-Polariton Parametric Oscillator Dynamics in the Semiconductor Microcavity". In: *2018 IEEE 8th International Conference Nanomaterials: Application & Properties (NAP)*. Vol. 1. IEEE, Sept. 2018, pp. 1–5. DOI: 10.1109/nap.2018.8914824. URL: http://dx.doi.org/10.1109/NAP.2018.8914824.

[155] J. J. Baumberg et al. "Parametric oscillation in a vertical microcavity: A polariton condensate or micro-optical parametric oscillation". In: *Physical Review B* 62.24 (Dec. 2000), R16247–R16250. ISSN: 1095-3795. DOI: 10.1103/physrevb.62.r16247. URL: http://dx.doi.org/10.1103/PhysRevB.62.R16247.

[156] L. V. Butov et al. "Stimulated Scattering of Indirect Excitons in Coupled Quantum Wells: Signature of a Degenerate Bose-Gas of Excitons". In: *Physical Review Letters* 86.24 (June 2001), pp. 5608–5611. ISSN: 1079-7114. DOI: 10.1103/physrevlett.86.5608. URL: http://dx.doi.org/10.1103/PhysRevLett.86.5608.

[157] R Spano et al. "Coherence properties of exciton polariton OPO condensates in one and two dimensions". In: *New Journal of Physics* 14.7 (July 2012), p. 075018. ISSN: 1367-2630. DOI: 10.1088/1367-2630/14/7/075018. URL: http://dx.doi.org/10.1088/1367-2630/14/7/075018.

[158] J. A. Giordmaine and Robert C. Miller. "Tunable Coherent Parametric Oscillation in $LiNbO_3$ at Optical Frequencies". In: *Physical Review Letters* 14.24 (June 1965), pp. 973–976. ISSN: 0031-9007. DOI: 10.1103/physrevlett.14.973. URL: http://dx.doi.org/10.1103/PhysRevLett.14.973.

[159] K. Dunnett et al. "Properties of the signal mode in the polariton optical parametric oscillator regime". In: *Physical Review B* 98.16 (Oct. 2018). ISSN: 2469-9969. DOI: 10.1103/physrevb.98.165307. URL: http://dx.doi.org/10.1103/PhysRevB.98.165307.

[160] P. G. Drazin and R. S. Johnson. *Solitons: An Introduction*. Cambridge University Press, Feb. 1989. ISBN: 9781139172059. DOI: 10.1017/cbo9781139172059. URL: http://dx.doi.org/10.1017/CBO9781139172059.

[161] John Scott Russell. *Report on waves: Made to the meetings of the British association in 1842-43 (classic reprint)*. London, England: Forgotten Books, Feb. 2019.

[162] Y. Kodama and K. Nozaki. "Soliton interaction in optical fibers". In: *Optics Letters* 12.12 (Dec. 1987), p. 1038. ISSN: 1539-4794. DOI: 10.1364/ol.12.001038. URL: http://dx.doi.org/10.1364/OL.12.001038.

[163] Yufeng Song et al. "Recent progress of study on optical solitons in fiber lasers". In: *Applied Physics Reviews* 6.2 (May 2019). ISSN: 1931-9401. DOI: 10.1063/1.5091811. URL: http://dx.doi.org/10.1063/1.5091811.

[164] Asad Zubair and Nauman Raza. "Bright and dark solitons in (n + 1)-dimensions with spatio-temporal dispersion". In: *Journal of Optics* 48.4 (Nov. 2019), pp. 594–605. ISSN: 0974-6900. DOI: 10.1007/s12596-019-00572-8. URL: http://dx.doi.org/10.1007/s12596-019-00572-8.

[165] Alfred R. Osborne. "Internal Waves and Solitons". In: *Nonlinear Ocean Waves and the Inverse Scattering Transform*. Elsevier, 2010, pp. 597–622. DOI: 10.1016/s0074-6142(10)97025-3. URL: http://dx.doi.org/10.1016/S0074-6142(10)97025-3.

[166] L. Khaykovich et al. "Formation of a Matter-Wave Bright Soliton". In: *Science* 296.5571 (May 2002), pp. 1290–1293. ISSN: 1095-9203. DOI: 10.1126/science.1071021. URL: http://dx.doi.org/10.1126/science.1071021.

[167] P. M. Walker et al. "Exciton polaritons in semiconductor waveguides". In: *Applied Physics Letters* 102.1 (Jan. 2013), p. 012109. DOI: 10.1063/1.4773590. URL: https://doi.org/10.1063/1.4773590.

[168] Anne Maître et al. "Dark-Soliton Molecules in an Exciton-Polariton Superfluid". In: *Physical Review X* 10.4 (Nov. 2020). ISSN: 2160-3308. DOI: 10.1103/physrevx.10.041028. URL: http://dx.doi.org/10.1103/PhysRevX.10.041028.

[169] Kieran A. Fraser and Francesco Piazza. "Topological soliton-polaritons in 1D systems of light and fermionic matter". In: *Communications Physics* 2.1 (May 2019). ISSN: 2399-3650. DOI: 10.1038/s42005-019-0149-1. URL: http://dx.doi.org/10.1038/s42005-019-0149-1.

[170] R. Hivet et al. "Half-solitons in a polariton quantum fluid behave like magnetic monopoles". In: *Nature Physics* 8.10 (Aug. 2012), pp. 724–728. ISSN: 1745-2481. DOI: 10.1038/nphys2406. URL: http://dx.doi.org/10.1038/nphys2406.

[171] P A M Dirac. "Quantised singularities in the electromagnetic field". en. In: *Proc. R. Soc. Lond. A Math. Phys. Sci.* 133.821 (Sept. 1931), pp. 60–72.

[172] Bernard Diu et al. *Eléments de physique statistique*. fr. Editions Hermann, 1989.

[173] Claude Cohen-Tannoudji, Bernard Diu, and Franck Laloë. *Quantum mechanics, volume 1*. en. 2nd ed. Berlin, Germany: Blackwell Verlag, Oct. 2019.

[174] Norbert Wiener. "Generalized harmonic analysis". In: *Acta Mathematica* 55.0 (1930), pp. 117–258. ISSN: 0001-5962. DOI: 10.1007/bf02546511. URL: http://dx.doi.org/10.1007/BF02546511.

[175] R. HANBURY BROWN and R. Q. TWISS. "Correlation between Photons in two Coherent Beams of Light". In: *Nature* 177.4497 (Jan. 1956), pp. 27–29. ISSN: 1476-4687. DOI: 10.1038/177027a0. URL: http://dx.doi.org/10.1038/177027a0.

[176] H. Paul. "Photon antibunching". In: *Reviews of Modern Physics* 54.4 (Oct. 1982), pp. 1061–1102. ISSN: 0034-6861. DOI: 10.1103/revmodphys.54.1061. URL: http://dx.doi.org/10.1103/RevModPhys.54.1061.

[177] Christophe Couteau et al. "Applications of single photons to quantum communication and computing". In: *Nature Reviews Physics* 5.6 (May 2023), pp. 326–338. ISSN: 2522-5820. DOI: 10.1038/s42254-023-00583-2. URL: http://dx.doi.org/10.1038/s42254-023-00583-2.

[178] Christophe Couteau et al. "Applications of single photons in quantum metrology, biology and the foundations of quantum physics". In: *Nature Reviews Physics* 5.6 (May 2023), pp. 354–363. ISSN: 2522-5820. DOI: 10.1038/s42254-023-00589-w. URL: http://dx.doi.org/10.1038/s42254-023-00589-w.

[179] Jonathan N. Tinsley et al. "Direct detection of a single photon by humans". In: *Nature Communications* 7.1 (July 2016). ISSN: 2041-1723. DOI: 10.1038/ncomms12172. URL: http://dx.doi.org/10.1038/ncomms12172.

[180] Peter Lodahl, Sahand Mahmoodian, and Søren Stobbe. "Interfacing single photons and single quantum dots with photonic nanostructures". In: *Reviews of Modern Physics* 87.2 (May 2015), pp. 347–400. ISSN: 1539-0756. DOI: 10.1103/revmodphys.87.347. URL: http://dx.doi.org/10.1103/RevModPhys.87.347.

[181] Brahim Lounis and Michel Orrit. "Single-photon sources". In: *Reports on Progress in Physics* 68.5 (Apr. 2005), pp. 1129–1179. ISSN: 1361-6633. DOI: 10.1088/0034-4885/68/5/r04. URL: http://dx.doi.org/10.1088/0034-4885/68/5/R04.

[182] Lukasz Komza et al. "Indistinguishable photons from an artificial atom in silicon photonics". In: *Nature Communications* 15.1 (Aug. 2024). ISSN: 2041-1723. DOI: 10.1038/s41467-024-51265-1. URL: http://dx.doi.org/10.1038/s41467-024-51265-1.

[183] Johann Stachurski et al. "Single photon emission and recombination dynamics in self-assembled GaN/AlN quantum dots". In: *Light: Science & Applications* 11.1 (Apr. 2022). ISSN: 2047-7538. DOI: 10.1038/s41377-022-00799-4. URL: http://dx.doi.org/10.1038/s41377-022-00799-4.

[184] T. Greytak and D. Kleppner. "A History of Bose-Einstein Condensation of Atomic Hydrogen". In: *Universal Themes of Bose-Einstein Condensation*. Cambridge University Press, 2012, pp. 22–37. DOI: 10.1017/9781316084366.004. URL: http://dx.doi.org/10.1017/9781316084366.004.

[185] M. H. Anderson et al. "Observation of Bose-Einstein Condensation in a Dilute Atomic Vapor". In: *Science* 269.5221 (July 1995), pp. 198–201. DOI: 10.1126/science.269.5221.198. URL: https://doi.org/10.1126/science.269.5221.198.

[186] Dale G. Fried et al. "Bose-Einstein Condensation of Atomic Hydrogen". In: *Physical Review Letters* 81.18 (Nov. 1998), pp. 3811–3814. ISSN: 1079-7114. DOI: 10.1103/physrevlett.81.3811. URL: http://dx.doi.org/10.1103/PhysRevLett.81.3811.

[187] Ross C. Schofield et al. "Bose–Einstein condensation of light in a semiconductor quantum well microcavity". In: *Nature Photonics* (Aug. 2024). ISSN: 1749-4893. DOI: 10.1038/s41566-024-01491-2. URL: http://dx.doi.org/10.1038/s41566-024-01491-2.

[188] Jan Klaers et al. "Bose–Einstein condensation of photons in an optical microcavity". In: *Nature* 468.7323 (Nov. 2010), pp. 545–548. ISSN: 1476-4687. DOI: 10.1038/nature09567. URL: http://dx.doi.org/10.1038/nature09567.

[189] S. A. Moskalenko and D. W. Snoke. *Bose-Einstein Condensation of Excitons and Biexcitons: And Coherent Nonlinear Optics with Excitons*. Cambridge University Press, Feb. 2000. ISBN: 9780511721687. DOI: 10.1017/cbo9780511721687. URL: http://dx.doi.org/10.1017/CBO9780511721687.

[190] Monique Combescot, Odile Betbeder-Matibet, and Roland Combescot. "Bose-Einstein Condensation in Semiconductors: The Key Role of Dark Excitons". In: *Physical Review Letters* 99.17 (Oct. 2007). ISSN: 1079-7114. DOI: 10.1103/physrevlett.99.176403. URL: http://dx.doi.org/10.1103/PhysRevLett.99.176403.

[191] Chongyun Jiang et al. "Microsecond dark-exciton valley polarization memory in two-dimensional heterostructures". In: *Nature Communications* 9.1 (Feb. 2018). ISSN: 2041-1723. DOI: 10.1038/s41467-018-03174-3. URL: http://dx.doi.org/10.1038/s41467-018-03174-3.

[192] Julien Madéo et al. "Directly visualizing the momentum-forbidden dark excitons and their dynamics in atomically thin semiconductors". In: *Science* 370.6521 (Dec. 2020), pp. 1199–1204. ISSN: 1095-9203. DOI: 10.1126/science.aba1029. URL: http://dx.doi.org/10.1126/science.aba1029.

[193] M. R. Molas et al. "Probing and Manipulating Valley Coherence of Dark Excitons in Monolayer WSe_2". In: *Physical Review Letters* 123.9 (Aug. 2019). ISSN: 1079-7114. DOI: 10.1103/physrevlett.123.096803. URL: http://dx.doi.org/10.1103/PhysRevLett.123.096803.

[194] Monique Combescot et al. "Optical signatures of a fully dark exciton condensate". In: *EPL (Europhysics Letters)* 105.4 (Feb. 2014), p. 47011. ISSN: 1286-4854. DOI: 10.1209/0295-5075/105/47011. URL: http://dx.doi.org/10.1209/0295-5075/105/47011.

[195] Daniel Rhodes et al. "Disorder in van der Waals heterostructures of 2D materials". In: *Nature Materials* 18.6 (May 2019), pp. 541–549. ISSN: 1476-4660. DOI: 10.1038/s41563-019-0366-8. URL: http://dx.doi.org/10.1038/s41563-019-0366-8.

[196] H. M. Gibbs, G. Khitrova, and S. W. Koch. "Exciton–polariton light–semiconductor coupling effects". In: *Nature Photonics* 5.5 (Mar. 2011), pp. 273–273. ISSN: 1749-4893. DOI: 10.1038/nphoton.2011.15. URL: http://dx.doi.org/10.1038/nphoton.2011.15.

[197] Iacopo Carusotto and Cristiano Ciuti. "Quantum fluids of light". In: *Reviews of Modern Physics* 85.1 (Feb. 2013), pp. 299–366. ISSN: 1539-0756. DOI: 10.1103/revmodphys.85.299. URL: http://dx.doi.org/10.1103/RevModPhys.85.299.

[198] R. Jayaprakash et al. "Ultra-low threshold polariton lasing at room temperature in a GaN membrane microcavity with a zero-dimensional trap". In: *Scientific Reports* 7.1 (July 2017). ISSN: 2045-2322. DOI: 10.1038/s41598-017-06125-y. URL: http://dx.doi.org/10.1038/s41598-017-06125-y.

[199] Mark Steger et al. "Ultra-low threshold polariton condensation". In: *Optics Letters* 42.6 (Mar. 2017), p. 1165. ISSN: 1539-4794. DOI: 10.1364/ol.42.001165. URL: http://dx.doi.org/10.1364/OL.42.001165.

[200] Jiaxin Zhao et al. “Ultralow Threshold Polariton Condensate in a Monolayer Semiconductor Microcavity at Room Temperature”. In: *Nano Letters* 21.7 (Apr. 2021), pp. 3331–3339. ISSN: 1530-6992. DOI: 10.1021/acs.nanolett.1c01162. URL: http://dx.doi.org/10.1021/acs.nanolett.1c01162.

[201] Ying-Yu Lai et al. “Crossover from polariton lasing to exciton lasing in a strongly coupled ZnO microcavity”. In: *Scientific Reports* 6.1 (Feb. 2016). ISSN: 2045-2322. DOI: 10.1038/srep20581. URL: http://dx.doi.org/10.1038/srep20581.

[202] Hui Deng et al. “Polariton lasing vs. photon lasing in a semiconductor microcavity”. In: *Proceedings of the National Academy of Sciences* 100.26 (Dec. 2003), pp. 15318–15323. ISSN: 1091-6490. DOI: 10.1073/pnas.2634328100. URL: http://dx.doi.org/10.1073/pnas.2634328100.

[203] M. Pieczarka et al. “Crossover from exciton-polariton condensation to photon lasing in an optical trap”. In: *Optics Express* 30.10 (May 2022), p. 17070. ISSN: 1094-4087. DOI: 10.1364/oe.452918. URL: http://dx.doi.org/10.1364/OE.452918.

[204] A. L. Schawlow and C. H. Townes. “Infrared and Optical Masers”. In: *Physical Review* 112.6 (Dec. 1958), pp. 1940–1949. ISSN: 0031-899X. DOI: 10.1103/physrev.112.1940. URL: http://dx.doi.org/10.1103/PhysRev.112.1940.

[205] M. Wouters and I. Carusotto. “Excitations in a Nonequilibrium Bose-Einstein Condensate of Exciton Polaritons”. In: *Phys. Rev. Lett.* 99 (2007), p. 140402.

[206] D. N. Krizhanovskii et al. “Self-organization of multiple polariton-polariton scattering in semiconductor microcavities”. In: *Physical Review B* 77.11 (Mar. 2008). ISSN: 1550-235X. DOI: 10.1103/physrevb.77.115336. URL: http://dx.doi.org/10.1103/PhysRevB.77.115336.

[207] J. J. Baumberg et al. “Spontaneous Polarization Buildup in a Room-Temperature Polariton Laser”. In: *Physical Review Letters* 101.13 (Sept. 2008). ISSN: 1079-7114. DOI: 10.1103/physrevlett.101.136409. URL: http://dx.doi.org/10.1103/PhysRevLett.101.136409.

[208] Aron Beekman, Louk Rademaker, and Jasper van Wezel. “An introduction to spontaneous symmetry breaking”. In: *SciPost Physics Lecture Notes* (Dec. 2019). ISSN: 2590-1990. DOI: 10.21468/scipostphyslectnotes.11. URL: http://dx.doi.org/10.21468/SciPostPhysLectNotes.11.

[209] S. V. Sergeyev. “Spontaneous light-polarization symmetry breaking for an anisotropic ring-cavity dye laser”. In: *Physical Review A* 59.5 (May 1999), pp. 3909–3917. ISSN: 1094-1622. DOI: 10.1103/physreva.59.3909. URL: http://dx.doi.org/10.1103/PhysRevA.59.3909.

[210] David Snoke. "Polariton Condensation and Lasing". In: *Exciton Polaritons in Microcavities*. Springer Berlin Heidelberg, 2012, pp. 307–327. ISBN: 9783642241864. DOI: 10.1007/978-3-642-24186-4_12. URL: http://dx.doi.org/10.1007/978-3-642-24186-4_12.

[211] E. W. Hagley et al. "Measurement of the Coherence of a Bose-Einstein Condensate". In: *Physical Review Letters* 83.16 (Oct. 1999), pp. 3112–3115. ISSN: 1079-7114. DOI: 10.1103/physrevlett.83.3112. URL: http://dx.doi.org/10.1103/PhysRevLett.83.3112.

[212] Tobias Damm et al. "First-order spatial coherence measurements in a thermalized two-dimensional photonic quantum gas". In: *Nature Communications* 8.1 (July 2017). ISSN: 2041-1723. DOI: 10.1038/s41467-017-00270-8. URL: http://dx.doi.org/10.1038/s41467-017-00270-8.

[213] Hassan Alnatah et al. "Coherence measurements of polaritons in thermal equilibrium reveal a power law for two-dimensional condensates". In: *Science Advances* 10.18 (May 2024). ISSN: 2375-2548. DOI: 10.1126/sciadv.adk6960. URL: http://dx.doi.org/10.1126/sciadv.adk6960.

[214] Feng Li et al. "Fabrication and characterization of a room-temperature ZnO polariton laser." In: *Appl. Phys. Lett.* 102 (2013), p. 051102.

[215] David W. Snoke and Andrew J. Daley. *The Question of Spontaneous Symmetry Breaking in Condensates*. 2015. DOI: 10.48550/ARXIV.1507.07456. URL: https://arxiv.org/abs/1507.07456.

[216] Robert P. Smith. *Effects of Interactions on Bose-Einstein Condensation*. 2016. DOI: 10.48550/ARXIV.1609.04762. URL: https://arxiv.org/abs/1609.04762.

[217] Matthew J. Davis et al. *Formation of Bose-Einstein condensates*. 2016. DOI: 10.48550/ARXIV.1601.06197. URL: https://arxiv.org/abs/1601.06197.

[218] Oliver Penrose and Lars Onsager. "Bose-Einstein Condensation and Liquid Helium". In: *Physical Review* 104.3 (Nov. 1956), pp. 576–584. ISSN: 0031-899X. DOI: 10.1103/physrev.104.576. URL: http://dx.doi.org/10.1103/PhysRev.104.576.

[219] C. N. Yang. "Concept of Off-Diagonal Long-Range Order and the Quantum Phases of Liquid He and of Superconductors". In: *Reviews of Modern Physics* 34.4 (Oct. 1962), pp. 694–704. ISSN: 0034-6861. DOI: 10.1103/revmodphys.34.694. URL: http://dx.doi.org/10.1103/RevModPhys.34.694.

[220] J. Bloch and J. Y. Marzin. "Photoluminescence dynamics of cavity polaritons under resonant excitation in the picosecond range". In: *Physical Review B* 56.4 (July 1997), pp. 2103–2108. ISSN: 1095-3795. DOI: 10.1103/physrevb.56.2103. URL: http://dx.doi.org/10.1103/PhysRevB.56.2103.

[221] C. Piermarocchi et al. “Nonequilibrium dynamics of free quantum-well excitons in time-resolved photoluminescence”. In: *Physical Review B* 53.23 (June 1996), pp. 15834–15841. ISSN: 1095-3795. DOI: 10.1103/physrevb.53.15834. URL: http://dx.doi.org/10.1103/PhysRevB.53.15834.

[222] Takeo Matsubara and Hirotsugu Matsuda. “A Lattice Model of Liquid Helium, I”. In: *Progress of Theoretical Physics* 16.6 (Dec. 1956), pp. 569–582. ISSN: 0033-068X. DOI: 10.1143/ptp.16.569. URL: http://dx.doi.org/10.1143/PTP.16.569.

[223] Ronald Fisch. “Ferromagnetism in the XY model with random threefold anisotropy”. In: *Physical Review B* 46.1 (July 1992), pp. 242–246. ISSN: 1095-3795. DOI: 10.1103/physrevb.46.242. URL: http://dx.doi.org/10.1103/PhysRevB.46.242.

[224] Takao Ohta and David Jasnow. “**XY** model and the superfluid density in two dimensions”. In: *Physical Review B* 20.1 (July 1979), pp. 139–146. ISSN: 0163-1829. DOI: 10.1103/physrevb.20.139. URL: http://dx.doi.org/10.1103/PhysRevB.20.139.

[225] E. Babaev and H. Kleinert. “Nonperturbative **XY**-model approach to strong coupling superconductivity in two and three dimensions”. In: *Physical Review B* 59.18 (May 1999), pp. 12083–12089. ISSN: 1095-3795. DOI: 10.1103/physrevb.59.12083. URL: http://dx.doi.org/10.1103/PhysRevB.59.12083.

[226] Joel Giedt and James Flamino. “Berezinskii-Kosterlitz-Thouless phase transition from lattice sine-Gordon model”. In: *EPJ Web of Conferences* 175 (2018). Ed. by M. Della Morte et al., p. 14003. ISSN: 2100-014X. DOI: 10.1051/epjconf/201817514003. URL: http://dx.doi.org/10.1051/epjconf/201817514003.

[227] Richard J. Fletcher et al. “Connecting Berezinskii-Kosterlitz-Thouless and BEC Phase Transitions by Tuning Interactions in a Trapped Gas”. In: *Physical Review Letters* 114.25 (June 2015). ISSN: 1079-7114. DOI: 10.1103/physrevlett.114.255302. URL: http://dx.doi.org/10.1103/PhysRevLett.114.255302.

[228] G. Dagvadorj, P. Comaron, and M. H. Szymańska. “Unconventional Berezinskii-Kosterlitz-Thouless Transition in the Multicomponent Polariton System”. In: *Physical Review Letters* 130.13 (Mar. 2023). ISSN: 1079-7114. DOI: 10.1103/physrevlett.130.136001. URL: http://dx.doi.org/10.1103/PhysRevLett.130.136001.

[229] Wolfgang H. Nitsche et al. “Observation of BKT Transition in BEC of Exciton-Polaritons in a Semiconductor Microcavity”. In: *CLEO: 2013*. Vol. 69. CLEO˙QELS. OSA, 2013, QM1D.3. DOI: 10.1364/cleo_qels.2013.qm1d.3. URL: http://dx.doi.org/10.1364/CLEO_QELS.2013.QM1D.3.

[230] N. D. Mermin and H. Wagner. "Absence of Ferromagnetism or Antiferromagnetism in One- or Two-Dimensional Isotropic Heisenberg Models". In: *Physical Review Letters* 17.22 (Nov. 1966), pp. 1133–1136. ISSN: 0031-9007. DOI: 10.1103/physrevlett.17.1133. URL: http://dx.doi.org/10.1103/PhysRevLett.17.1133.

[231] Maksim Tomchenko. "Bose–Einstein Condensation in a One-Dimensional System of Interacting Bosons". In: *Journal of Low Temperature Physics* 182.5–6 (Jan. 2016), pp. 170–184. ISSN: 1573-7357. DOI: 10.1007/s10909-015-1435-2. URL: http://dx.doi.org/10.1007/s10909-015-1435-2.

[232] A.B. Acharyya and M. Acharyya. "Bose–Einstein Condensation in Arbitrary Dimensions". In: *Acta Physica Polonica B* 43.9 (2012), p. 1805. ISSN: 1509-5770. DOI: 10.5506/aphyspolb.43.1805. URL: http://dx.doi.org/10.5506/APhysPolB.43.1805.

[233] Jonathan Keeling et al. "BCS-BEC crossover in a system of microcavity polaritons". In: *Physical Review B* 72.11 (Sept. 2005). ISSN: 1550-235X. DOI: 10.1103/physrevb.72.115320. URL: http://dx.doi.org/10.1103/PhysRevB.72.115320.

[234] Dirk van Delft and Peter Kes. "The discovery of superconductivity". In: *Physics Today* 63.9 (Sept. 2010), pp. 38–43. ISSN: 1945-0699. DOI: 10.1063/1.3490499. URL: http://dx.doi.org/10.1063/1.3490499.

[235] J. Bardeen, L. N. Cooper, and J. R. Schrieffer. "Microscopic Theory of Superconductivity". In: *Physical Review* 106.1 (Apr. 1957), pp. 162–164. ISSN: 0031-899X. DOI: 10.1103/physrev.106.162. URL: http://dx.doi.org/10.1103/PhysRev.106.162.

[236] R. J. Cava et al. "Superconductivity near 30 K without copper: the Ba0.6K0.4BiO3 perovskite". In: *Nature* 332.6167 (Apr. 1988), pp. 814–816. ISSN: 1476-4687. DOI: 10.1038/332814a0. URL: http://dx.doi.org/10.1038/332814a0.

[237] Sukbae Lee, Ji-Hoon Kim, and Young-Wan Kwon. *The First Room-Temperature Ambient-Pressure Superconductor*. 2023. DOI: 10.48550/ARXIV.2307.12008. URL: https://arxiv.org/abs/2307.12008.

[238] G M Vuhicic. "Exciton and polariton mechanisms of superconductivity". In: *Journal of Physics C: Solid State Physics* 12.9 (May 1979), pp. 1699–1702. ISSN: 0022-3719. DOI: 10.1088/0022-3719/12/9/012. URL: http://dx.doi.org/10.1088/0022-3719/12/9/012.

[239] Fabrice P. Laussy. "Superconductivity with excitons and polaritons: review and extension". In: *Journal of Nanophotonics* 6.1 (May 2012), p. 064502. ISSN: 1934-2608. DOI: 10.1117/1.jnp.6.064502. URL: http://dx.doi.org/10.1117/1.JNP.6.064502.

[240] Ovidiu Cotleţ et al. “Superconductivity and other collective phenomena in a hybrid Bose-Fermi mixture formed by a polariton condensate and an electron system in two dimensions”. In: *Physical Review B* 93.5 (Feb. 2016). ISSN: 2469-9969. DOI: 10.1103/physrevb.93.054510. URL: http://dx.doi.org/10.1103/PhysRevB.93.054510.

[241] Andrey S. Plyashechnik et al. “Coupled system of electrons and exciton-polaritons: Screening, dynamical effects, and superconductivity”. In: *Physical Review B* 108.2 (July 2023). ISSN: 2469-9969. DOI: 10.1103/physrevb.108.024513. URL: http://dx.doi.org/10.1103/PhysRevB.108.024513.

[242] Ivan A. Shelykh, Thomas Taylor, and Alexey V. Kavokin. “Rotons in a Hybrid Bose-Fermi System”. In: *Physical Review Letters* 105.14 (Sept. 2010). ISSN: 1079-7114. DOI: 10.1103/physrevlett.105.140402. URL: http://dx.doi.org/10.1103/PhysRevLett.105.140402.

[243] Huaiyuan Yang, Xinqiang Wang, and Xin-Zheng Li. “Exciton-polariton properties of hexagonal BN-based microcavity and their potential applications in BEC and superconductivity”. In: *Physical Review B* 104.20 (Nov. 2021). ISSN: 2469-9969. DOI: 10.1103/physrevb.104.205307. URL: http://dx.doi.org/10.1103/PhysRevB.104.205307.

[244] P. Kapitza. “Viscosity of Liquid Helium below the λ-Point”. In: *Nature* 141.3558 (Jan. 1938), pp. 74–74. ISSN: 1476-4687. DOI: 10.1038/141074a0. URL: http://dx.doi.org/10.1038/141074a0.

[245] J. F. ALLEN and A. D. MISENER. “Flow Phenomena in Liquid Helium II”. In: *Nature* 142.3597 (Oct. 1938), pp. 643–644. ISSN: 1476-4687. DOI: 10.1038/142643a0. URL: http://dx.doi.org/10.1038/142643a0.

[246] L. Landau. “Theory of the Superfluidity of Helium II”. In: *Physical Review* 60.4 (Aug. 1941), pp. 356–358. ISSN: 0031-899X. DOI: 10.1103/physrev.60.356. URL: http://dx.doi.org/10.1103/PhysRev.60.356.

[247] A. J. Leggett. “Superfluidity”. In: *Reviews of Modern Physics* 71.2 (Mar. 1999), S318–S323. ISSN: 1539-0756. DOI: 10.1103/revmodphys.71.s318. URL: http://dx.doi.org/10.1103/RevModPhys.71.S318.

[248] R. Onofrio et al. “Observation of Superfluid Flow in a Bose-Einstein Condensed Gas”. In: *Physical Review Letters* 85.11 (Sept. 2000), pp. 2228–2231. ISSN: 1079-7114. DOI: 10.1103/physrevlett.85.2228. URL: http://dx.doi.org/10.1103/PhysRevLett.85.2228.

[249] Alexey Kavokin, Guillaume Malpuech, and Fabrice P. Laussy. “Polariton laser and polariton superfluidity in microcavities”. In: *Physics Letters A* 306.4 (Jan. 2003), pp. 187–199. ISSN: 0375-9601. DOI: 10.1016/s0375-9601(02)01579-7. URL: http://dx.doi.org/10.1016/S0375-9601(02)01579-7.

[250] A. Amo et al. “Collective fluid dynamics of a polariton condensate in a semiconductor microcavity”. In: *Nature* 457.7227 (Jan. 2009), pp. 291–295. ISSN: 1476-4687. DOI: 10.1038/nature07640. URL: http://dx.doi.org/10.1038/nature07640.

[251] S. Utsunomiya et al. “Observation of Bogoliubov excitations in exciton-polariton condensates”. In: *Nature Physics* 4.9 (Aug. 2008), pp. 700–705. ISSN: 1745-2481. DOI: 10.1038/nphys1034. URL: http://dx.doi.org/10.1038/nphys1034.

[252] M. Pieczarka et al. “Bogoliubov excitations of a polariton condensate in dynamical equilibrium with an incoherent reservoir”. In: *Physical Review B* 105.22 (June 2022). ISSN: 2469-9969. DOI: 10.1103/physrevb.105.224515. URL: http://dx.doi.org/10.1103/PhysRevB.105.224515.

[253] D. V. Skryabin et al. “Backward Cherenkov radiation emitted by polariton solitons in a microcavity wire”. In: *Nature Communications* 8.1 (Nov. 2017). ISSN: 2041-1723. DOI: 10.1038/s41467-017-01751-6. URL: http://dx.doi.org/10.1038/s41467-017-01751-6.

[254] Giovanni Lerario et al. “Room-temperature superfluidity in a polariton condensate”. In: *Nature Physics* 13.9 (June 2017), pp. 837–841. ISSN: 1745-2481. DOI: 10.1038/nphys4147. URL: http://dx.doi.org/10.1038/nphys4147.

[255] Kai Peng et al. “Room-temperature polariton quantum fluids in halide perovskites”. In: *Nature Communications* 13.1 (Nov. 2022). ISSN: 2041-1723. DOI: 10.1038/s41467-022-34987-y. URL: http://dx.doi.org/10.1038/s41467-022-34987-y.

[256] Joris Barrat et al. “Qubit analog with polariton superfluid in an annular trap”. In: *Science Advances* 10.43 (Oct. 2024). ISSN: 2375-2548. DOI: 10.1126/sciadv.ado4042. URL: http://dx.doi.org/10.1126/sciadv.ado4042.

[257] J. Ciers et al. “Polariton relaxation and polariton nonlinearities in non-resonantly cw-pumped III-nitride slab waveguides”. In: *Physical Review B* 102.15 (Oct. 2020), p. 155304. DOI: 10.1103/PhysRevB.102.155304. URL: https://doi.org/10.1103/PhysRevB.102.155304.

[258] Md. Shariful Islam and Ahmed Zubair. “Aluminium nanoparticle-based ultra-wideband high-performance polarizer”. In: *Heliyon* 10.20 (Oct. 2024), e38840. ISSN: 2405-8440. DOI: 10.1016/j.heliyon.2024.e38840. URL: http://dx.doi.org/10.1016/j.heliyon.2024.e38840.

[259] Georgios Sinatkas et al. “Electro-optic modulation in integrated photonics”. In: *Journal of Applied Physics* 130.1 (July 2021). ISSN: 1089-7550. DOI: 10.1063/5.0048712. URL: http://dx.doi.org/10.1063/5.0048712.

[260] Chen-How Huang, Yung-Hsiang Wen, and Yi-Wei Liu. "Measuring the second order correlation function and the coherence time using random phase modulation". In: *Optics Express* 24.4 (Feb. 2016), p. 4278. ISSN: 1094-4087. DOI: 10.1364/oe.24.004278. URL: http://dx.doi.org/10.1364/OE.24.004278.

[261] R. P. A. Emmanuele et al. "Highly nonlinear trion-polaritons in a monolayer semiconductor". In: *Nature Communications* 11 (1 July 2020), p. 3589. DOI: 10.1038/s41467-020-17340-z. URL: https://doi.org/10.1038/s41467-020-17340-z.

[262] Corentin Morin et al. "Self-Kerr Effect across the Yellow Rydberg Series of Excitons in Cu_2O ". In: *Physical Review Letters* 129.13 (Sept. 2022). DOI: 10.1103/physrevlett.129.137401. URL: https://doi.org/10.1103/physrevlett.129.137401.

[263] Colin Montgomery, Wayne Orchiston, and Ian Whittingham. "MICHELL, LAPLACE AND THE ORIGIN OF THE BLACK HOLE CONCEPT". In: *Journal of Astronomical History and Heritage* 12.2 (July 2009), pp. 90–96. ISSN: 1440-2807. DOI: 10.3724/sp.j.1440-2807.2009.02.01. URL: http://dx.doi.org/10.3724/SP.J.1440-2807.2009.02.01.

[264] K. Schwarzschild. *On the gravitational field of a sphere of incompressible fluid according to Einstein's theory*. 1999. DOI: 10.48550/ARXIV.PHYSICS/9912033. URL: https://arxiv.org/abs/physics/9912033.

[265] David Finkelstein. "Past-Future Asymmetry of the Gravitational Field of a Point Particle". In: *Physical Review* 110.4 (May 1958), pp. 965–967. ISSN: 0031-899X. DOI: 10.1103/physrev.110.965. URL: http://dx.doi.org/10.1103/PhysRev.110.965.

[266] E. T. Newman et al. "Metric of a Rotating, Charged Mass". In: *Journal of Mathematical Physics* 6.6 (June 1965), pp. 918–919. ISSN: 1089-7658. DOI: 10.1063/1.1704351. URL: http://dx.doi.org/10.1063/1.1704351.

[267] Piotr T. Chruściel, João Lopes Costa, and Markus Heusler. "Stationary Black Holes: Uniqueness and Beyond". In: *Living Reviews in Relativity* 15.1 (May 2012). ISSN: 1433-8351. DOI: 10.12942/lrr-2012-7. URL: http://dx.doi.org/10.12942/lrr-2012-7.

[268] HL Shipman. "The implausible history of triple star models for Cygnus X-1 Evidence for a black hole". In: *Astrophysical Letters, vol. 16, no. 1, 1975, p. 9-12. Research supported by the Research Corp.* 16 (1975), pp. 9–12.

[269] B. P. et al. Abbott. "Observation of Gravitational Waves from a Binary Black Hole Merger". In: *Physical Review Letters* 116.6 (Feb. 2016). ISSN: 1079-7114. DOI: 10.1103/physrevlett.116.061102. URL: http://dx.doi.org/10.1103/PhysRevLett.116.061102.

[270] J. M. Bardeen, B. Carter, and S. W. Hawking. "The four laws of black hole mechanics". In: *Communications in Mathematical Physics* 31.2 (June 1973), pp. 161–170. ISSN: 1432-0916. DOI: 10.1007/bf01645742. URL: http://dx.doi.org/10.1007/BF01645742.

[271] Suvrat Raju. "Lessons from the information paradox". In: *Physics Reports* 943 (Jan. 2022), pp. 1–80. ISSN: 0370-1573. DOI: 10.1016/j.physrep.2021.10.001. URL: http://dx.doi.org/10.1016/j.physrep.2021.10.001.

[272] P. et al. Panuzzo. "Discovery of a dormant 33 solar-mass black hole in pre-release Gaia astrometry". In: *Astronomy & Astrophysics* 686 (May 2024), p. L2. ISSN: 1432-0746. DOI: 10.1051/0004-6361/202449763. URL: http://dx.doi.org/10.1051/0004-6361/202449763.

[273] Mário Novello, Matt Visser, and Grigori Volovik. *Artificial Black Holes*. WORLD SCIENTIFIC, Oct. 2002. ISBN: 9789812778178. DOI: 10.1142/4861. URL: http://dx.doi.org/10.1142/4861.

[274] Carlos Barceló. "Analogue black-hole horizons". In: *Nature Physics* 15.3 (Dec. 2018), pp. 210–213. ISSN: 1745-2481. DOI: 10.1038/s41567-018-0367-6. URL: http://dx.doi.org/10.1038/s41567-018-0367-6.

[275] Carlos Barceló, Stefano Liberati, and Matt Visser. "Analogue Gravity". In: *Living Reviews in Relativity* 14.1 (May 2011). ISSN: 1433-8351. DOI: 10.12942/lrr-2011-3. URL: http://dx.doi.org/10.12942/lrr-2011-3.

[276] Ralf Schützhold and William G. Unruh. "Gravity wave analogues of black holes". In: *Physical Review D* 66.4 (Aug. 2002). ISSN: 1089-4918. DOI: 10.1103/physrevd.66.044019. URL: http://dx.doi.org/10.1103/PhysRevD.66.044019.

[277] Sam Patrick et al. "Backreaction in an Analogue Black Hole Experiment". In: *Physical Review Letters* 126.4 (Jan. 2021). ISSN: 1079-7114. DOI: 10.1103/physrevlett.126.041105. URL: http://dx.doi.org/10.1103/PhysRevLett.126.041105.

[278] Silke Weinfurtner et al. "Measurement of Stimulated Hawking Emission in an Analogue System". In: *Physical Review Letters* 106.2 (Jan. 2011). ISSN: 1079-7114. DOI: 10.1103/physrevlett.106.021302. URL: http://dx.doi.org/10.1103/PhysRevLett.106.021302.

[279] Oren Lahav et al. "Realization of a Sonic Black Hole Analog in a Bose-Einstein Condensate". In: *Physical Review Letters* 105.24 (Dec. 2010). ISSN: 1079-7114. DOI: 10.1103/physrevlett.105.240401. URL: http://dx.doi.org/10.1103/PhysRevLett.105.240401.

[280] Jeff Steinhauer. "Observation of self-amplifying Hawking radiation in an analogue black-hole laser". In: *Nature Physics* 10.11 (Oct. 2014), pp. 864–869. ISSN: 1745-2481. DOI: 10.1038/nphys3104. URL: http://dx.doi.org/10.1038/nphys3104.

[281] Yi-Hsieh Wang et al. “Mechanism of stimulated Hawking radiation in a laboratory Bose-Einstein condensate”. In: *Physical Review A* 96.2 (Aug. 2017). ISSN: 2469-9934. DOI: 10.1103/physreva.96.023616. URL: http://dx.doi.org/10.1103/PhysRevA.96.023616.

[282] Jeff Steinhauer and Juan Ramón Muñoz de Nova. “Self-amplifying Hawking radiation and its background: A numerical study”. In: *Physical Review A* 95.3 (Mar. 2017). ISSN: 2469-9934. DOI: 10.1103/physreva.95.033604. URL: http://dx.doi.org/10.1103/PhysRevA.95.033604.

[283] G E Volovik. *The universe in a helium droplet*. en. International Series of Monographs on Physics. London, England: Oxford University Press, Feb. 2009.

[284] M. Človečko et al. “Magnonic Analog of Black- and White-Hole Horizons in Superfluid ^{3}He – B”. In: *Physical Review Letters* 123.16 (Oct. 2019). ISSN: 1079-7114. DOI: 10.1103/physrevlett.123.161302. URL: http://dx.doi.org/10.1103/PhysRevLett.123.161302.

[285] Patrik Švančara et al. “Rotating curved spacetime signatures from a giant quantum vortex”. In: *Nature* 628.8006 (Mar. 2024), pp. 66–70. ISSN: 1476-4687. DOI: 10.1038/s41586-024-07176-8. URL: http://dx.doi.org/10.1038/s41586-024-07176-8.

[286] M. J. Jacquet et al. “Polariton fluids for analogue gravity physics”. In: *Philosophical Transactions of the Royal Society A: Mathematical, Physical and Engineering Sciences* 378.2177 (July 2020), p. 20190225. ISSN: 1471-2962. DOI: 10.1098/rsta.2019.0225. URL: http://dx.doi.org/10.1098/rsta.2019.0225.

[287] Anton Svetlichnyi, Andrii Chaika, and Alexander Yakimenko. “Acoustic analogs of extremal rotating black holes in exciton-polariton condensates”. In: *Physical Review B* 109.21 (June 2024). ISSN: 2469-9969. DOI: 10.1103/physrevb.109.214516. URL: http://dx.doi.org/10.1103/PhysRevB.109.214516.

[288] Dario Gerace and Iacopo Carusotto. “Analog Hawking radiation from an acoustic black hole in a flowing polariton superfluid”. In: *Physical Review B* 86.14 (Oct. 2012). ISSN: 1550-235X. DOI: 10.1103/physrevb.86.144505. URL: http://dx.doi.org/10.1103/PhysRevB.86.144505.

[289] R. PENROSE and R. M. FLOYD. “Extraction of Rotational Energy from a Black Hole”. In: *Nature Physical Science* 229.6 (Feb. 1971), pp. 177–179. ISSN: 2058-1106. DOI: 10.1038/physci229177a0. URL: http://dx.doi.org/10.1038/physci229177a0.

[290] D. D. Solnyshkov et al. “Quantum analogue of a Kerr black hole and the Penrose effect in a Bose-Einstein condensate”. In: *Physical Review B* 99.21 (June 2019). ISSN: 2469-9969. DOI: 10.1103/physrevb.99.214511. URL: http://dx.doi.org/10.1103/PhysRevB.99.214511.

[291] D. V. Freilich et al. “Real-Time Dynamics of Single Vortex Lines and Vortex Dipoles in a Bose-Einstein Condensate”. In: *Science* 329.5996 (Sept. 2010), pp. 1182–1185. ISSN: 1095-9203. DOI: 10.1126/science.1191224. URL: http://dx.doi.org/10.1126/science.1191224.

[292] W. G. Unruh. “Second quantization in the Kerr metric”. In: *Physical Review D* 10.10 (Nov. 1974), pp. 3194–3205. ISSN: 0556-2821. DOI: 10.1103/physrevd.10.3194. URL: http://dx.doi.org/10.1103/PhysRevD.10.3194.

[293] D. D. Solnyshkov, H. Flayac, and G. Malpuech. “Black holes and wormholes in spinor polariton condensates”. In: *Physical Review B* 84.23 (Dec. 2011). ISSN: 1550-235X. DOI: 10.1103/physrevb.84.233405. URL: http://dx.doi.org/10.1103/PhysRevB.84.233405.

[294] Yashuai Yang, Yongliang Li, and Chi Wang. “Generation and expansion of Laguerre–Gaussian beams”. In: *Journal of Optics* 51.4 (May 2022), pp. 910–926. ISSN: 0974-6900. DOI: 10.1007/s12596-022-00857-5. URL: http://dx.doi.org/10.1007/s12596-022-00857-5.

[295] Jonathan Pinnell, Valeria Rodríguez-Fajardo, and Andrew Forbes. “How perfect are perfect vortex beams?” In: *Optics Letters* 44.22 (Nov. 2019), p. 5614. ISSN: 1539-4794. DOI: 10.1364/ol.44.005614. URL: http://dx.doi.org/10.1364/OL.44.005614.

[296] Prabin Pradhan, Manish Sharma, and Bora Ung. “Generation of Perfect Cylindrical Vector Beams With Complete Control Over the Ring Width and Ring Diameter”. In: *IEEE Photonics Journal* 10.1 (Feb. 2018), pp. 1–10. ISSN: 1943-0647. DOI: 10.1109/jphot.2018.2790175. URL: http://dx.doi.org/10.1109/JPHOT.2018.2790175.

[297] Y. Aharonov and D. Bohm. “Significance of Electromagnetic Potentials in the Quantum Theory”. In: *Physical Review* 115.3 (Aug. 1959), pp. 485–491. ISSN: 0031-899X. DOI: 10.1103/physrev.115.485. URL: http://dx.doi.org/10.1103/PhysRev.115.485.

[298] J Audretsch and C Lammerzahl. “Neutron interference: general theory of the influence of gravity, inertia and space-time torsion”. In: *Journal of Physics A: Mathematical and General* 16.11 (Aug. 1983), pp. 2457–2477. ISSN: 1361-6447. DOI: 10.1088/0305-4470/16/11/017. URL: http://dx.doi.org/10.1088/0305-4470/16/11/017.

[299] Michael A. Hohensee et al. “Force-Free Gravitational Redshift: Proposed Gravitational Aharonov-Bohm Experiment”. In: *Physical Review Letters* 108.23 (June 2012). ISSN: 1079-7114. DOI: 10.1103/physrevlett.108.230404. URL: http://dx.doi.org/10.1103/PhysRevLett.108.230404.

[300] Chris Overstreet et al. “Observation of a gravitational Aharonov-Bohm effect”. In: *Science* 375.6577 (Jan. 2022), pp. 226–229. ISSN: 1095-9203. DOI: 10.1126/science.abl7152. URL: http://dx.doi.org/10.1126/science.abl7152.

[301] Harmeet Singh and James S. Sirkis. "Direct extraction of phase gradients from Fourier-transform and phase-step fringe patterns". In: *Applied Optics* 33.22 (Aug. 1994), p. 5016. ISSN: 1539-4522. DOI: 10.1364/ao.33.005016. URL: http://dx.doi.org/10.1364/AO.33.005016.

[302] K. Rayanov et al. "Frequency Combs with Weakly Lasing Exciton-Polariton Condensates". In: *Physical Review Letters* 114.19 (May 2015). ISSN: 1079-7114. DOI: 10.1103/physrevlett.114.193901. URL: http://dx.doi.org/10.1103/PhysRevLett.114.193901.

[303] Hui Li et al. "All-optical temporal logic gates in localized exciton polaritons". In: *Nature Photonics* 18.8 (Aug. 2024), pp. 864–869. ISSN: 1749-4893. DOI: 10.1038/s41566-024-01483-2. URL: http://dx.doi.org/10.1038/s41566-024-01483-2.

[304] Peter L. McMahon. "The physics of optical computing". In: *Nature Reviews Physics* 5.12 (Oct. 2023), pp. 717–734. ISSN: 2522-5820. DOI: 10.1038/s42254-023-00645-5. URL: http://dx.doi.org/10.1038/s42254-023-00645-5.

[305] Sanjib Ghosh and Timothy C. H. Liew. "Quantum computing with exciton-polariton condensates". In: *npj Quantum Information* 6.1 (Feb. 2020), p. 16. DOI: 10.1038/s41534-020-0244-x. URL: https://doi.org/10.1038/s41534-020-0244-x.

[306] Matthias Schmidt et al. "Rydberg-atom-based radio-frequency sensors: amplitude-regime sensing". In: *Optics Express* 32.16 (July 2024), p. 27768. ISSN: 1094-4087. DOI: 10.1364/oe.530148. URL: http://dx.doi.org/10.1364/OE.530148.

[307] Xiaoling Wu et al. "A concise review of Rydberg atom based quantum computation and quantum simulation". In: *Chinese Physics B* 30.2 (Feb. 2021), p. 020305. DOI: 10.1088/1674-1056/abd76f. URL: https://doi.org/10.1088/1674-1056/abd76f.

[308] Hendrik Weimer et al. "A Rydberg quantum simulator". In: *Nature Physics* 6.5 (Mar. 2010), pp. 382–388. DOI: 10.1038/nphys1614. URL: https://doi.org/10.1038/nphys1614.

[309] S. W. Hawking. *The Information Paradox for Black Holes*. 2015. DOI: 10.48550/ARXIV.1509.01147. URL: https://arxiv.org/abs/1509.01147.

Supplementary material from articles

Polariton lasing in AlGaN microring with GaN/AlGaN quantum wells - Supplemental Material

Anthonin Delphan[1], Maxim N. Makhonin[1], Tommi Isoniemi[1], Paul M. Walker[1], Maurice S. Skolnick [1], Dmitry N. Krizhanovskii[1], Dmitry V. Skryabin[2], Jean-François Carlin[3], Nicolas Grandjean[3], and Raphaël Butté*[3]

[1]Department of Physics and Astronomy, University of Sheffield, Sheffield, S3 7RH, UK
[2]Department of Physics, University of Bath, Claverton Down, Bath BA2 7AY, UK
[3]Institute of Physics, École Polytechnique Fédérale de Lausanne (EPFL), CH-1015 Lausanne, Switzerland

December 20, 2022

Corresponding email: raphael.butte@epfl.ch

1 Growth details and fabrication process

The sample was grown using metal organic vapour phase epitaxy on high-quality low threading dislocation density ($\sim 10^6$ cm^{-2}) *c*-plane free-standing GaN substrate. The sample structure consists of a 130-nm-thick active region with 22 embedded GaN/$Al_{0.1}Ga_{0.9}N$ (1.5 nm/3.5 nm) quantum wells (QWs) grown on top of a 400-nm-thick $Al_{0.83}In_{0.17}N$ cladding lattice-matched to GaN. It is essentially a replica of the samples in which waveguided polaritons were reported for the first time in III-nitride slab waveguides [1] and for which we subsequently demonstrated ultrafast-nonlinear ultraviolet pulse modulation in the strong coupling regime up to room temperature [2]. For electron beam lithography (EBL) a layer of the photoresist CSAR-62 [3] with the adhesion enhancer hexamethyldisilazane was spinned on the sample. The soft mask has a thickness of 1130 nm. The resist was exposed with a 50 keV electron beam using a Raith Voyager EBL system, using a base dose of 94 µC/cm^2 together with a proximity dose correction. The mask was developed in xylene for 60 s at 23 °C and rinsed in isopropanol. After development, inductively-coupled plasma reactive ion etching (ICP-RIE) was used to etch the patterns through the core and partly into the cladding. The dry etch process uses a RF power of 80 W, ICP power of 450 W and 4 mTorr pressure. The gas flows were 1.5 sccm for $SiCl_4$, 15 sccm for Cl_2 and 4 sccm for Ar. The etching time was 10.75 min with the etching rates of 67 nm/min for the resist and 30 nm/min for GaN. After etching the resist was removed with 4 min O_2 plasma ashing with 100 W power, submerging the sample in heated Microposit resist remover 1165 for 4 min and rinsing it in isopropanol for 2 min.

A scanning electron microscopy (SEM) image of a ring resonator is shown in Fig. 1 that illustrates the very good flatness of the top ring. The small droplets on the outer side of the ring are from unetched photoresist and are not believed to have any impact on the optical measurements.

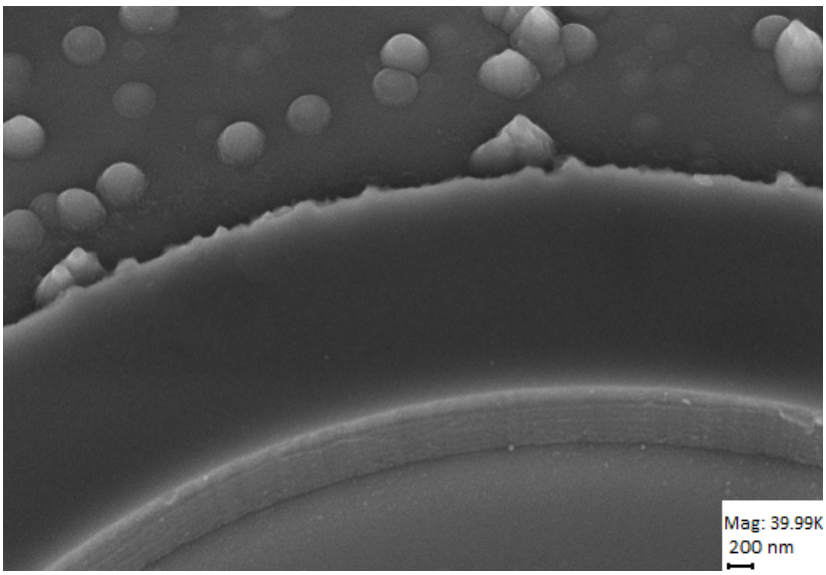

Figure 1: Close-up view of a ring resonator obtained with SEM imaging.

2 Normalisation of Photoluminescence Spectra

In the main text, we present in Fig. 1 the photoluminescence (PL) spectra of the 4 μm ring at different pulse energies. We also give PL spectra of the 8 µm ring in Fig. 3 for different pulse energies and temperatures. These spectra are normalised to the PL intensity of the QW A exciton, according to equation 1:

$$\mathrm{PL}_N(\mathcal{E}) = \frac{\mathrm{PL}(\mathcal{E})}{\mathrm{PL}(\mathcal{E}_X)}, \tag{1}$$

where $\mathcal{E}$ is the energy, PL is the raw photoluminescence data, $\mathcal{E}_X$ is the energy of the QW A exciton resonance, and PL_N is the resulting normalised spectrum. We observe that the function PL_N is almost constant for the QW peaks and the bulk GaN peaks across all pulse energies, which shows that both follow a similar pulse energy dependency (shown in section 6 to be quasi-linear), but varies significantly in the region where the modes appear. This shows that the polariton modes follow a non-linear pulse energy dependency.

The PL spectra are all shifted vertically for clarity. The value of the shifts is as follows:

- for the 4 µm ring at 4 K, the shift is equal to 0.5 for all powers;
- for the 8 µm ring at 4 K, the shift is equal to 0.7 for 0.25 nJ, then 1.5 for 0.5 nJ, 2 for 0.7 nJ, and finally 1 for 1.4 nJ;
- for the 8 µm ring at 200 K, the shift is equal to 1 for 0.3 nJ, then 2.5 for 0.7 nJ, and finally 1.5 for 1 nJ;

- for the 8 µm ring at 300 K, the shift is equal to 3 for all pulse energies.

The interest of this representation is to emphasize the evolution in relative contrast between the polariton modes and the neighbouring excitons. In Fig. 2, we show the non-shifted, non-normalised spectra, which show the evolution in absolute contrast.

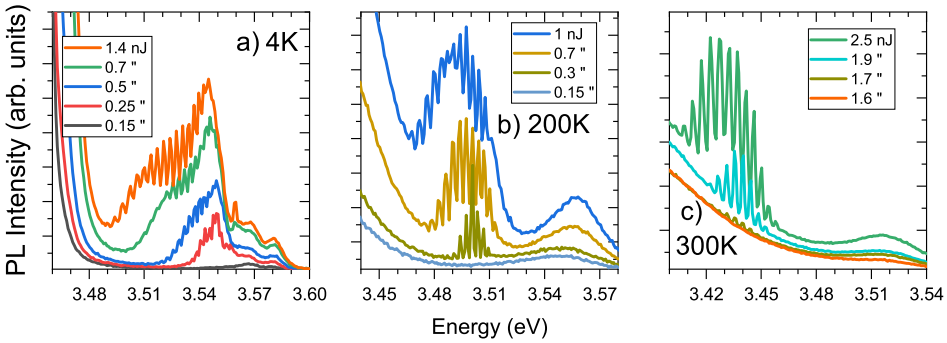

Figure 2: (a), (b), (c) PL spectra for the 8 µm radius, 2 µm wide ring at different pulse energies (in nJ) labeled in the figures for $T = 4$, 200, and 300 K, respectively. Non-normalised data.

3 Polariton mode linewidth

One of the distinctive signatures of lasing is a reduction of the linewidth of the cavity modes supporting lasing when crossing the threshold. For a single mode laser the linewidth of the lasing mode is predicted to decrease inversely proportional to the mode filling factor according to the celebrated Schawlow-Townes linewidth formula [4]. In our experiment, the scattered photoluminescence signal from the cavity modes is not observed below threshold, since it is too weak to efficiently contribute to the collected signal with our backscattering configuration as discussed in the main text. Above the polariton lasing threshold the peak intensities of the modes quickly saturate with power (see Fig. 4 of the main text) and no measurable reduction of the polariton mode linewidths is observed. The linewidth of the polariton modes is observed to be around 2-3 meV and is very likely limited by the polariton-polariton interactions, cross scattering and gain competition between the modes. Given that our system is pumped with a 1 kHz laser of very short (100 fs) pulses there is most likely a strong variation in the total exciton and polariton density (and hence in the modes peak positions) from pulse to pulse, which further leads to polariton mode broadening in the time-averaged spectra we measure.

4 Polariton dispersion and photonic loss of ring resonators

The strong reduction in free spectral range (FSR) as the energy approaches that of the exciton resonance arises due to the strong dispersion of polaritons. This is illustrated in Fig. 3 which shows the experimentally measured energy vs. wavenumber dispersion relation for the planar waveguide. The points give the experimental data while the solid curve gives the best fit of the polariton model. Panels a) and b) show the cases for two representative temperatures: 4 K and

300 K, respectively. The data and analysis are taken from Ref. [2] and are fully described in that work.

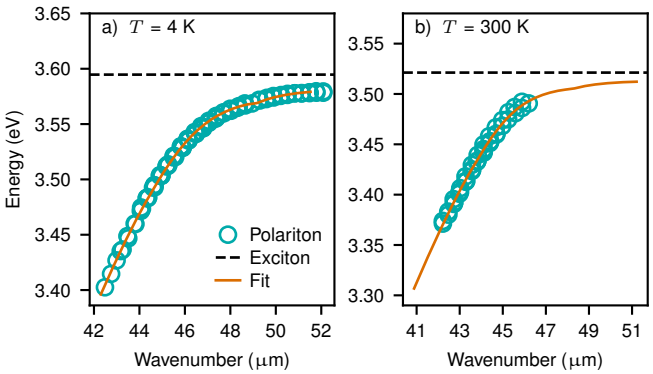

Figure 3: Dispersion of the unstructured planar waveguide. Experimental energy vs. wavenumber dispersion relation (points) and best fit of the coupled oscillator model (solid curve) for a) $T = 4$ K and b) $T = 300$ K.

Exciton-polaritons (hereafter polaritons) are formed by hybridisation of photons and excitons. The polariton dispersion is obtained by first calculating the dispersion of the purely photonic modes of the planar waveguide structure using electromagnetic simulation, and then employing a coupled oscillator model to calculate the dispersion of the polaritons. The photons and excitons hybridise to form two polariton branches, the upper polaritons (UP) and lower polaritons (LP). The UP are not observed because of strong absorption at energies above the exciton resonance [1]. The dispersion of the LP given by the conventional coupled oscillator model is

$$E_{\mathrm{LP}} = \left[E_{\mathrm{ph}} + E_{\mathrm{ex}} - \sqrt{(E_{\mathrm{ph}} - E_{\mathrm{ex}})^2 + \Omega^2} \right] /2. \tag{2}$$

Here E_{LP} is the lower polariton energy, E_{ph} and E_{ex} are the photon and exciton energies, respectively, and Ω is the coupling strength between photon and exciton, known as the vacuum Rabi splitting. The hybridisation leads to an avoided crossing, where the LP does not cross the exciton energy but strongly curves over as it approaches it. This leads to very strong dispersion and ultimately underlies the strongly reducing FSR for resonator modes at energies close to the exciton energy.

We now consider the dispersive properties of the ring resonators which we study in this work. Following a similar general method we first calculated the dispersion of purely photonic modes using electromagnetic simulation, and then calculated the dispersion of resonator polaritons using a coupled oscillator model. The photon dispersion was calculated using the finite difference eigenmode (FDE) solver of the commercial Lumerical MODE solutions package. This was used to simulate curved waveguides with transverse profile corresponding to the 2 μm wide ridge waveguides in the experiment. For a wide range of optical wavelengths the solver calculates the corresponding angular wavenumber $\hat{\beta}$ (rate of phase accumulation with angle travelled around the curved waveguide). The dashed orange curve in Fig. 4a) shows the photon energy vs. angular wavenumber. The polariton energy at each angular wavenumber is then obtained using the coupled oscillator model, as above, and is shown as the solid blue curve in Fig. 4a). The small kink in the curves around 3.64 eV for the photons and around 3.58 eV for polaritons is

due to the rapid variation of the background refractive index of the quantum wells near the band edge. It is well above the energies of the experimentally investigated polariton modes and does not affect the results.

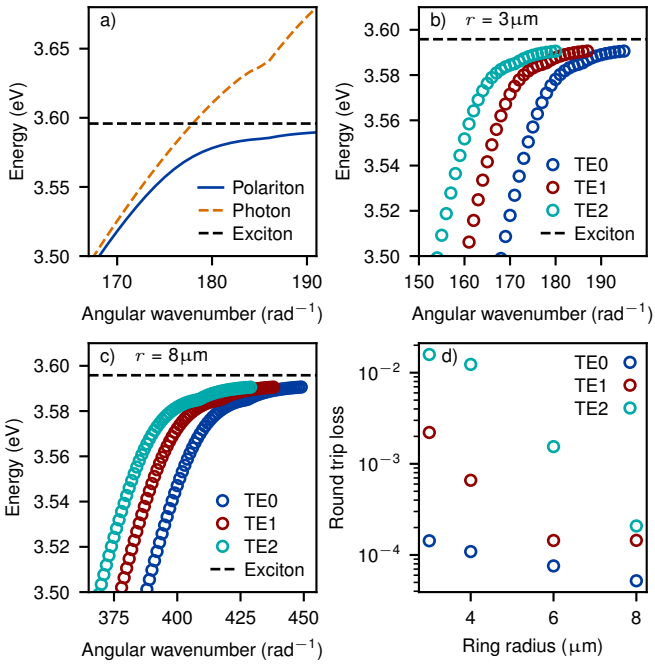

Figure 4: Dispersive properties of ring resonators computed for a system at 4 K. a) Dispersion of purely photonic (dashed orange) and polaritonic (solid blue) curved ridge waveguide with 3 µm radius of curvature. b) Modes of a 3 µm polariton ring resonator. The first three transverse modes are shown. c) Modes of an 8 µm ring resonator. d) Round trip photonic loss of ring resonators vs. ring radius for the first three transverse modes. Losses are calculated for photons at the same energy as the exciton.

Once the dispersion of curved waveguides is known the energies of ring resonator modes can be calculated. The phase accumulated in one round trip of a circular resonator is $2\pi\hat{\beta}$ and the condition for resonance is that the round trip phase should be a multiple of 2π. Thus we obtain $\hat{\beta} = m$ where m is an integer. Interpolating into the curved waveguide dispersion gives the polariton energies of the resonances. These are shown in Figs. 4b) and c) for 3 µm and 8 µm rings, respectively. A feature of relatively wide resonators such at the 2 µm devices we use is that they support several transverse modes in addition to the longitudinal modes. This leads to a set of longitudinal modes for each transverse modal index. Figs. 4b) and c) show the first three transverse-electric polarised transverse mode families, TE0, TE1 and TE2. The transverse-magnetic polarised modes have a weak coupling to the quantum wells [1] and do not play a role in these experiments. The energy difference between any given longitudinal mode and the closest mode in the next transverse family is less than the distance between longitudinal modes.

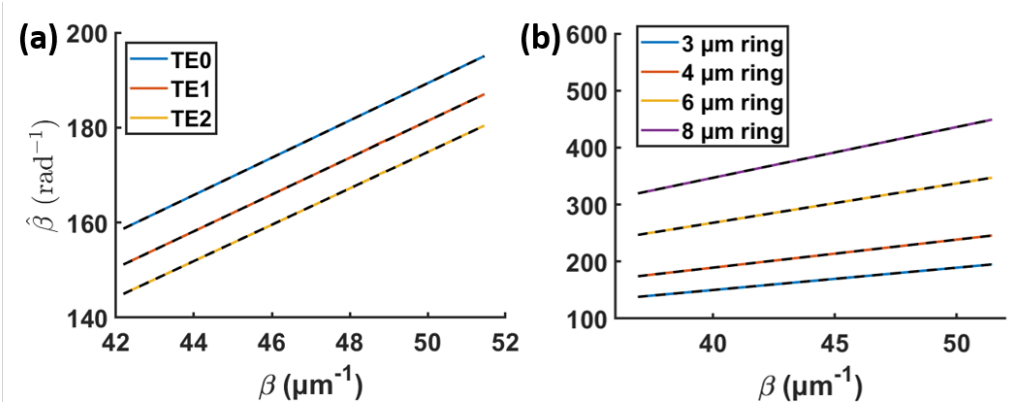

Figure 5: Computed angular wavenumber of the ring resonator modes vs. wavenumber of the planar waveguide from which the rings are etched. a) Values for the three lowest order TE modes of the 3 micron ring. b) Values for the lowest order TE mode of different rings. Coloured curves are the computed values. Dashed black lines are the best fit straight lines to each curve.

As discussed above we calculated the angular wavenumber of the pure photonic modes of the rings for a range of frequencies. At the same frequencies we also calculated the wavenumber of pure photons in the planar waveguide from which the rings were etched (also using Lumerical MODE). In Fig. 5 we plot the angular wavenumbers $\hat{\beta}$ vs. the planar waveguide wavenumber β. Fig. 5(a) shows this for the three lowest order TE modes of the 3 micron ring. The coloured curves are the simulated data. The black dashed lines are best fit straight lines. It is seen that $\hat{\beta}$ is a linear function of β to a high precision over a large range of wavenumbers, which correspond to photon wavelengths of 335 nm to 400 nm. This is true for all the different modes. Fig. 5(b) shows the same data for the lowest order TE mode of several different rings of different radii, showing the same linear relationship. Mathematically we have $\hat{\beta}_n(E) = \hat{\beta}_{n,0} + r_n\beta(E)$ where $\hat{\beta}_{n,0}$ is an offset analagous to the quantisation energy coming from the transverse confinement, and r_n is an effective radius of propagation for the mode labelled by index n. The radius comes in because we are comparing angular wavenumber (in units of rad^{-1}) and actual wavenumber (in units of m^{-1}). The offset $\hat{\beta}_{n,0}$ will disappear when taking derivatives to find, for example, the group velocity. The dispersive properties of all these modes (which have different orders and propagate in different rings) can therefore be explained entirely by the dispersion of the underlying planar waveguide. We conclude that the transverse confinement and circular propagation have negligible effect on the modal dispersive properties and that all transverse modes are equivalent to within a linear scaling factor related to the radius.

We finally consider the radiation losses in the resonators. Fig. 4d) shows the calculated round trip loss for photons in the resonator due to radiation loss and tunnelling through the cladding into the substrate. The round trip losses are obtained from the imaginary part of $\hat{\beta}$ as calculated by the FDE solver using perfectly-matched-layer boundary conditions. As expected, the losses are higher for the rings with smaller radius. The losses are also higher for higher order transverse modes TE1 and TE2 compared to the fundamental transverse mode family TE0. This suggests that either higher order transverse modes experience higher radiation losses or that their lower effective refractive index increases tunnelling loss through the substrate, or both.

5 Frequency dependence of free spectral range as evidence of strong coupling

A key signature of strong coupling is the anti-crossing of photon and exciton states which leads to a strong curvature of the lower polariton dispersion as it asymptotically approaches the exciton energy with increasing wavenumber (see section 4). A good measure of this curvature is the group velocity $v_g = (\partial E/\partial k)/\hbar$. For uncurved (linear) dispersion relations it is just a constant whereas in the strong coupling regime it is expected to vary strongly, starting from the pure-photon group velocity and tending to zero as the polariton energy approaches the exciton energy from below. In a simplified picture of a linear dispersion relation for the pure photons the polariton group velocity is proportional to the photonic fraction. In reality the pure photon dispersion relation also exhibits some curvature due to the wavelength dependence of the material refractive indexes, especially near the material band edges. As discussed in supplementary section 4, the dispersive properties (e.g. $v_g(E)$) of our ring resonator modes are determined entirely by those of the planar waveguide from which the rings are etched.

Experimentally we have direct access to the group velocity since it is directly proportional to the FSR. We have $v_g = (E_{\mathrm{FSR}} \cdot r_{\mathrm{eff}})/\hbar$ where r_{eff} is the radius around which the lasing mode propagates and E_{FSR} is the energy spacing between ring resonator modes (free spectral range). Because of this direct proportionality the variation of the FSR with energy is also a good measure of the polaritonic character of the modes. Theoretically, we can also calculate the expected free spectral range for both polaritons and also pure photons, as discussed in supplementary section 4. We note that r_{eff} can in principle be different from the geometrical ring radius R since it is the effective radius at which the lasing mode propagates. We do not have experimental access to the transverse profile of the lasing modes but they are likely to propagate near the center of the ring where the intensity of the pump spot is the largest and the losses due to scattering on the rough sidewalls (see Fig. 1 of the supplemental material (SM)) are the lowest. We therefore calculate the FSR for a radius corresponding to the center of the 2 micron wide ridge, $r_{\mathrm{eff}} = R$, for comparison with the experiment. We note that the mode propagating at this radius has the same dispersive properties as the modes propagating at any other radius up to a constant scaling factor (see SM section 4). The exciton energy, used in Eqn. 2 to calculate the polariton energies, is taken from the spectra. The Rabi splitting is treated as a fitting parameter and we obtain values between 55 and 65 meV, in good agreement with the value reported in Ref. [1].

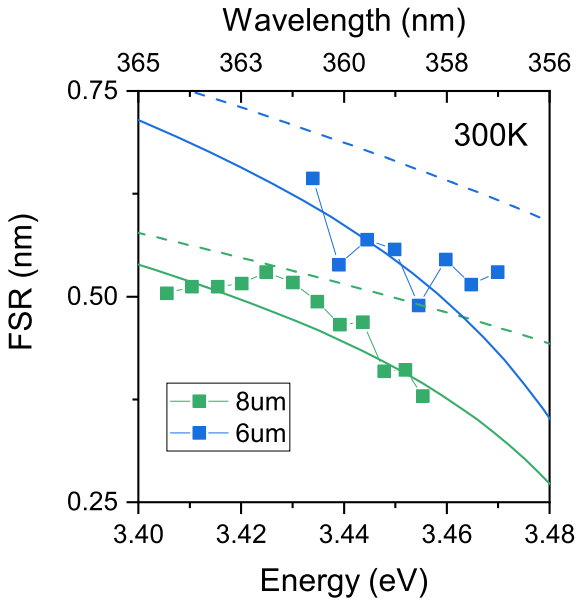

Figure 6: FSR of microring resonators measured for radii of 6 and 8 µm), with a 2 µm width, at pulse energy above the polariton lasing threshold (1.7 nJ) taken at 300 K. The solid line represents a theoretical model accounting for polariton non-linearities, whereas the dashed line represents a purely photonic model.

Figure 2b in the main text shows the experimentally measured FSR for several rings at 4 K. In the case of the 3 μm radius ring the experimental FSR (and hence the group velocity) decreases by 65% of the maximum measured value over an energy range of 41 meV. As discussed in the main text this large variation in FSR cannot be accounted for by a purely photonic model. The rings with other radii at 4 K show similar behaviour, with changes in FSR (group velocity) too large for the purely photonic model to explain. They evidence the strong coupling and its strong effect on the curvature of the dispersion relation.

In Fig. 6 we show the experimental FSR for two rings at 300 K as points. For the 8 μm radius ring the FSR varies by 25% between lowest and highest energy points over a 54 meV range of energies. This is less than the case at 4 K since the data points at 300 K are for energies further from the exciton where the polaritons are more photonic and the curvature due to strong coupling is therefore expected to be lower. The solid (dashed) curves show the theoretical FSR for polaritons (pure photons). For 8 μm radius rings the theory predicts a variation of 24% for polaritons over the same energy range as the experimental points. The purely photonic model can account for a change of only 14%. Overall at 300 K there is better agreement with the strongly coupled model than the purely photonic one, which confirms that the strong coupling is retained in the lasing regime up to room temperature. This is further supported by our observation that above threshold the luminescence peak from the exciton does not exhibit broadening or energy blueshift, which would be expected if we were beyond the Mott density where strong coupling collapses (see main text).

6 PL spectra without GaN background

At 4 K the polariton emission intensity was integrated in the region where the contribution from the QW and GaN exciton emissions is negligible.

By contrast, the polariton modes at 200 and 300 K sit on a strong, smooth, and broad incoherent PL background coming mainly from the bulk GaN excitons. This background was removed by fitting it with a Gaussian peak. In the main text, our analysis to extract the threshold-like behaviour of the modes relies on the removal of this background for enhanced contrast. In Figs. 7.a and b, we present the PL spectra measured at 200 and 300 K of the 8 µm ring with the PL background removed. These spectra show how the modes quickly grow in intensity, much faster than the linear evolution of the GaN exciton peaks themselves (cf. next SM section).

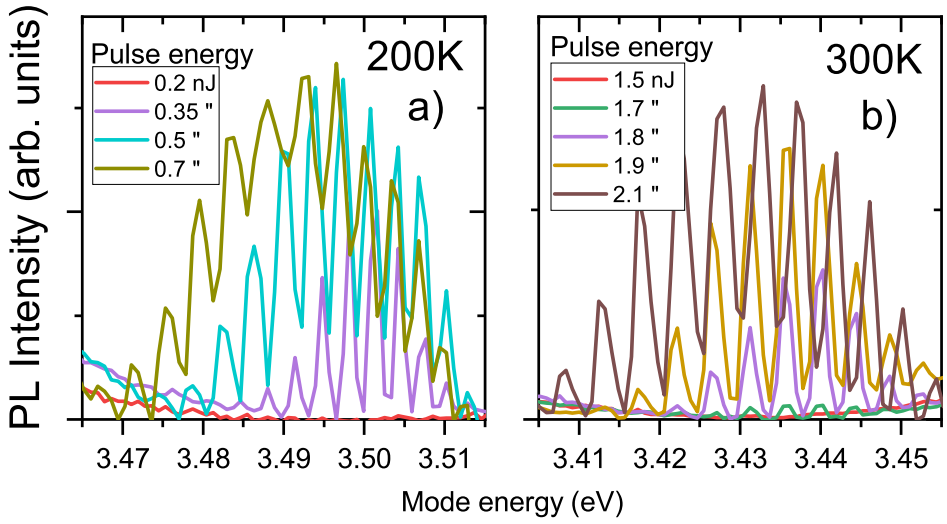

Figure 7: PL spectra of the 8 µm ring resonator recorded at $T = 200$, and 300 K, with the PL background resulting from the GaN exciton peaks removed. The bottom line of the graph is zero intensity.

7 Power dependency of the bulk GaN excitonic luminescence peaks and QW exciton luminescence peaks at different temperatures

One argument used to prove polariton lasing operation is the presence of a sharp threshold at which the PL intensity of the lasing modes rapidly increases. In this section, we give the pulse energy dependency of the integrated PL intensity of the bulk GaN exciton peaks at 4, 200, and 300 K for the 8 µm microring resonator (Fig. 8).

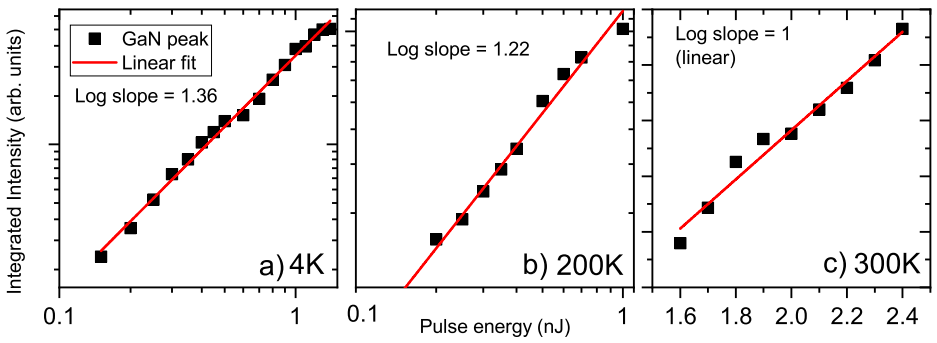

Figure 8: Integrated PL intensity of the bulk GaN exciton peaks recorded at 4, 200, and 300 K for the 8 µm ring. The red solid lines represent quasi-linear fits with the corresponding slope indicated in each figure. Log-log scale at 4 and 200 K. Linear scale at 300 K.

Note that from the log-log scale used to display the data recorded at 4 and 200 K, a slope slightly higher than unity is obtained for the power dependency of the integrated PL intensity of the bulk GaN exciton peaks, which implies a weak nonlinearity. For example, at 4 K, we have a fit leading to $y \sim x^{1.36}$. All the exponents remain reasonably close to 1 and hence the power dependence of the bulk GaN exciton peak PL intensity is found to be close to linear. We use a linear scale at 300 K due to the smaller accessible range of powers. This is in sharp contrast with the polariton modes, whose intensity follows a superlinear increase well-above a quadratic function (see the main text). The same analysis applies for the QW excitonic peaks as seen in Fig. 9. Similar results were obtained for the 4 µm microring and are shown in Fig. 1 of the main text.

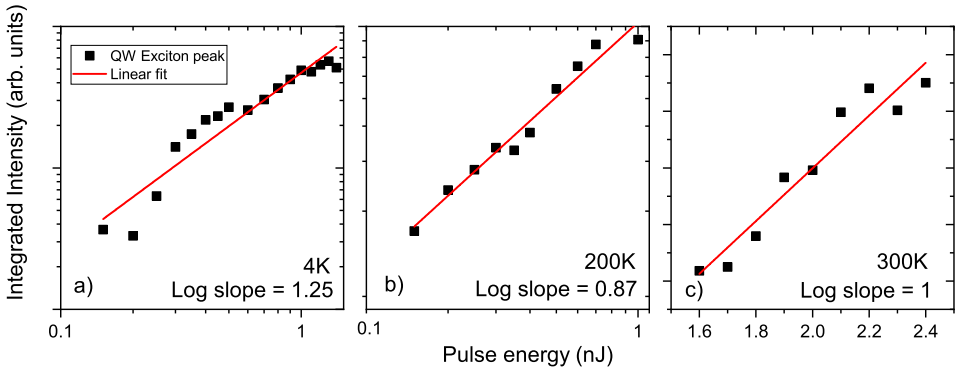

Figure 9: Integrated PL intensity of the QW excitonic peaks at 4, 200, and 300 K for the 8 µm ring. The red solid lines represent fits with the corresponding slope indicated in each figure. Doubly logarithmic scale for 4 and 200 K. Linear scale for 300 K.

8 Blueshift of the 4 µm ring

Blueshift is a defining feature of polaritons. It is a signature of their non-linearity owing to their excitonic part. In the main text, we have described strong blueshift in the 8 µm ring at all temperatures. Such blueshift is also seen in the smaller 4 µm ring, as shown in Fig. 10. The difference in the range of pulse energies is due to a slightly different excitation scheme compared to the main text, exciting a smaller part of the ring with each pulse. Under this excitation scheme, the blueshift is much clearer than in Figure 1 of the main text, but happens at higher pulse powers.

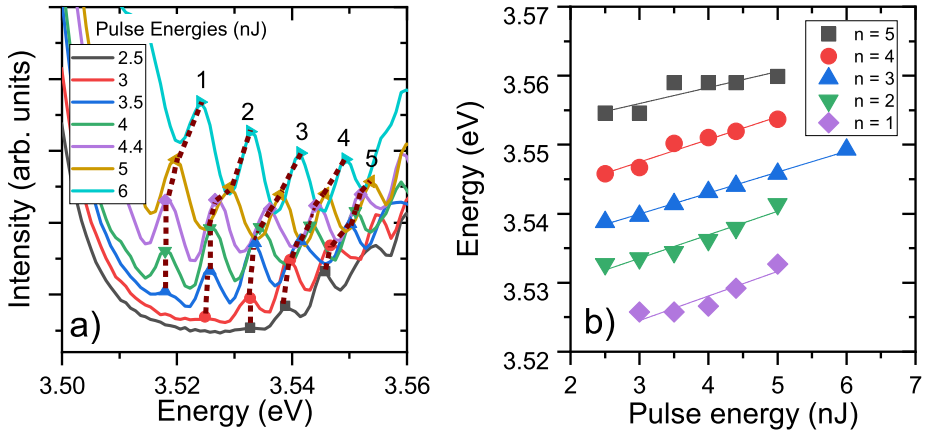

Figure 10: a) PL spectra of the 4 µm ring recorded at 4 K at different pulse energies, above threshold, showing the blueshift of the modes. The lines are guides for the eyes. b) Evolution of the peak positions as a function of pulse energy. The solid line is a linear fit.

References

[1] J. Ciers et al. "Propagating Polaritons in III-Nitride Slab Waveguides". In: *Physical Review Applied* 7.3 (Mar. 2017), p. 034019. DOI: 10.1103/physrevapplied.7.034019. URL: https://doi.org/10.1103/physrevapplied.7.034019.

[2] D. M. Di Paola et al. "Ultrafast-nonlinear ultraviolet pulse modulation in an AlInGaN polariton waveguide operating up to room temperature". In: *Nature Communications* 12.1 (June 2021), p. 3504. DOI: 10.1038/s41467-021-23635-6. URL: https://doi.org/10.1038/s41467-021-23635-6.

[3] Stephen Thoms and Douglas S. Macintyre. "Investigation of CSAR 62, a new resist for electron beam lithography". In: *Journal of Vacuum Science & Technology B* 32.6 (Nov. 2014), 06FJ01. DOI: 10.1116/1.4899239. URL: https://doi.org/10.1116/1.4899239.

[4] A. L. Schawlow and C. H. Townes. "Infrared and optical masers". In: *Physical Review* 112.6 (Dec. 1958), pp. 1940–1949.

Nonlinear Rydberg exciton-polaritons in Cu_2O microcavities

Maxim Makhonin[1], Anthonin Delphan[1], Kok Wee Song[2], Paul Walker[1], Tommi Isoniemi[1], Peter Claronino[1], Konstantinos Orfanakis[3], Sai Kiran Rajendran[3], Hamid Ohadi[3], Julian Heckötter[4], Marc Assmann[4], Manfred Bayer[4], Alexander Tartakovskii[1], Maurice Skolnick[1], Oleksandr Kyriienko[2] and Dmitry Krizhanovskii[1]

[1]Department of Physics and Astronomy, University of Sheffield, Sheffield, S3 7RH, United Kingdom.
[2]Department of Physics and Astronomy, University of Exeter, Stocker Rd, Exeter, EX4 4PY, United Kingdom.
[3]School of Physics & Astronomy, University of St Andrews, St Andrews, KY16 9AJ, United Kingdom.
[4]Fakultät Physik, TU Dortmund, August-Schmidt-Straße 4, Dortmund, 44227, Germany.

Supplementary Information

1 Transmission spectra fitting procedure

To fit the transmission spectra we used the model of cavity transmission from Ref. [1], multiplied by a Gaussian function which accounts for the spectrum of the pulse incident on the cavity. This reads

$$T_n \approx \frac{A \exp\left(-2\left(\frac{\Delta_n}{\sigma}\right)^2\right)}{(\frac{\kappa}{2} + G_n^2 \frac{\gamma_n/2 + 2Q_n\Delta_n}{\gamma_n^2/4+\Delta_n^2})^2 + (\Delta_n - G_n^2 \frac{\Delta_n - Q_n\gamma_n}{\gamma_n^2/4+\Delta_n^2})^2}, \tag{S1}$$

where A is the peak amplitude, Δ_n is the laser frequency detuning from the excitonic resonance with principal quantum number n, γ_n is the excitonic linewidth for corresponding n, κ is the cavity linewidth, G_n is the coupling strength, Q_n is the Fano asymmetry parameter, and σ is the pulse spectral width. In all cases the subscript n refers to the exciton with index n. We use Eq. (S1) to fit the transmission spectra at each n by fixing the parameters γ_n, κ and Q_n corresponding to each excitonic resonance taken from separate measurements (see Section 2 below). For each excitonic resonance we perform a global fit over all excitation powers, with only the coupling strength G_n and the amplitude A varying as a function of power. Thus we obtain power dependence of G_n.

2 Measurement of excitonic and cavity linewidths

In Fig. **S1**, we extract the photonic cavity linewidth κ of several modes at different energies. The data are taken from angle-resolved transmission (also called Fourier imaging or $\boldsymbol{k}$-space imaging) of a broadband super-continuum laser. A section of the angle-resolved data at zero incidence angle to the sample normal ($k = 0$) is presented in the figure. As we want to extract an uncoupled and unperturbed "purely photonic" cavity mode, the spectra are taken from a spatial region of the sample where the cavity modes are detuned far away from the excitonic resonances. This occurs due to a small wedge in the thickness of the sample.

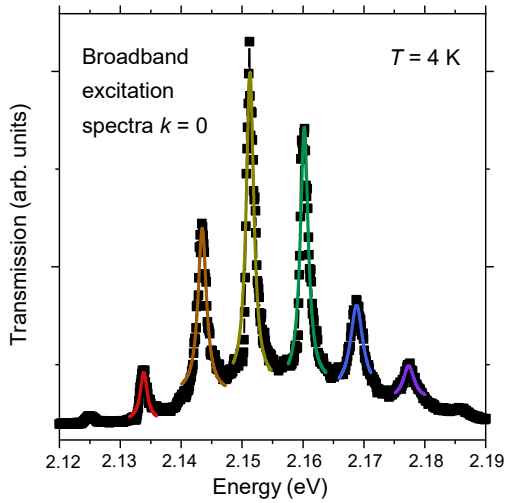

Fig. S1: Normal incidence transmission spectrum of a Cu_2O microcavity under broadband excitation, showing uncoupled Fabry–Pérot cavity modes. Points are experimental data. Solid curves show Lorentzian lineshape fits to the modes.

From the Lorentzian fits in Fig. S1, we can extract the cavity linewidth as a function of energy, which we plot in Fig. S2. The trend can then be extrapolated to find appropriate κ values for energy levels matching exciton resonances.

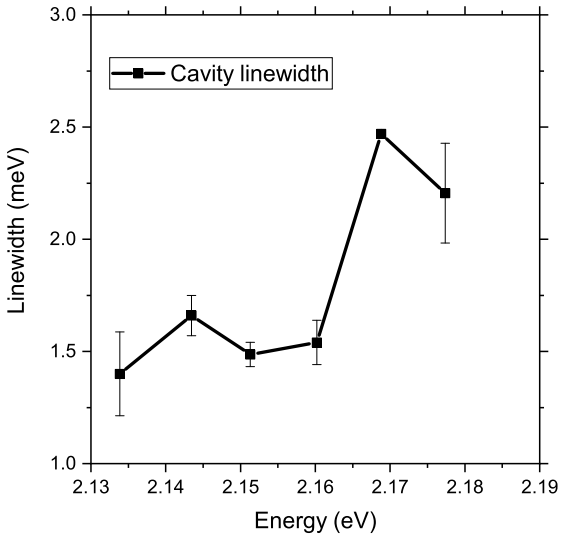

Fig. S2: Cavity linewidth extracted from Fig. S1 as a function of energy.

From white light transmission spectra of a bare Cu_2O flake with excitonic resonances fitted as an asymmetrical Fano resonances we extract exciton linewidth γ_n and Fano asymmetry parameter Q_n (see Fig. **S3**).

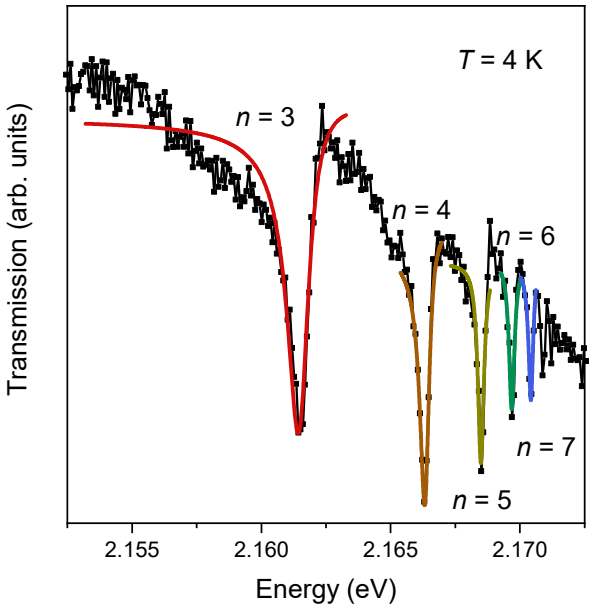

Fig. S3: Transmission spectra of a bare Cu_2O flake. Points are experimental data. Solid curves are Fano lineshape fits for each resonance.

3 The effect of temperature on the exciton resonances

We believe the laser induced heating effects are negligible in our experiment. To verify this we performed an additional measurement where the exciton resonances were monitored in transmission in a bare Cu_2O crystal using white light for different temperatures. With the increase of temperature of the sample from 4 to 20 K we observed a significant red shift of the exciton resonances by about 0.6 meV as shown in the Fig. **S4**, whereas the exciton linewidth and the dip of the exciton resonance stay almost the same, indicating no reduction of the exciton oscillator strength with temperature. By contrast, our measurements of the polariton resonances for different powers in Fig. 2 of the main text do not show any red shift of the bare exciton resonances within the spectrometer resolution ~ 0.1 meV: the energy positions of the dip between the polariton resonances corresponding to the exciton levels do not change. This indicates that the sample temperature does not change with increase of pump power and the reduction of the exciton-photon coupling can not be explained by heating.

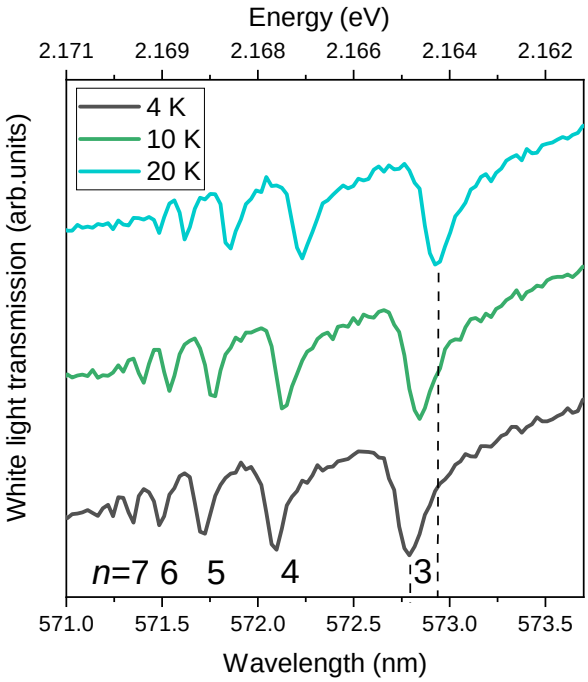

Fig. S4: White light transmission spectra of a bare Cu_2O flake at different temperatures.

4 Strong coupling in broadband excitation regime up to $n = 7$

In Fig. 1 of the main text we demonstrated strong coupling in the broadband excitation regime using angle-resolved transmission spectra, by showing the anti-crossing of the cavity modes around the excitonic lines for $n = 3$, $n = 4$, and $n = 5$. In this section, we show that such anti-crossing can be observed for up to $n = 7$ in the broadband excitation regime, similarly to the narrowband excitation scheme demonstrated in the main text of the article.

While Fig. 1 of the main text was obtained using $\boldsymbol{k}$-space imaging, it was not possible to use this technique for higher n. Indeed, the cavity modes become noisy and harder to resolve at higher energy, which makes the identification of such modes challenging. Instead, the anti-crossing is obtained by scanning the excitation position on the sample, which results in the cavity modes shifting due to the slight wedge in sample thickness and thus changing their detuning with respect to the excitons. This is similar to the technique used in Ref. [1]. When the modes cross the exciton resonance, a doublet and splitting characteristic of strong coupling are observed. This scan across different positions on the sample is shown in Fig. **S5**.

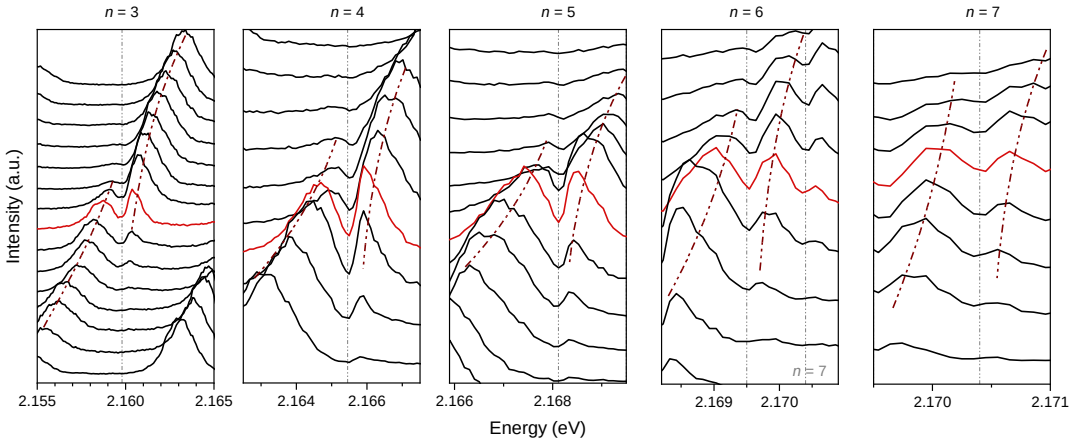

Fig. S5: Broadband excitation and position scan across the sample showing anticrossing for excitonic resonances from $n = 3$ to $n = 7$. Brown dash-dot lines are a guide to the eye showing positions of upper and lower polariton modes. Grey lines are showing positions of exciton resonances.

5 Calculation of the density

The density of photons inside a cavity can be calculated from the power emitted by the cavity together with the rate of escape through the mirrors, which have a finite transmission coefficient. A detailed explanation of the principle can be found in the supplementary information of Ref. [2]. In the present work, the power emitted by the cavity was measured directly, while the transmission of the mirrors was calculated using a transfer matrix model of the sample with calibrated parameters. Transfer matrix modelling is a standard technique which exactly solves Maxwell's equations for planar layer structures of the type we use in this work. In our work we deduce the size of the nonlinearity at the lowest powers, in the limit where the interaction energy compared to the the other energy scales in the system, such as losses, are tending towards zero. We therefore use the reasonable approximation that in this limit the density of particles in the cavity can be deduced using a linear model of the cavity electromagnetic response.

The first step in the model was to calibrate the reflection, transmission and absorption of the silver mirrors. In the same deposition runs in which the mirrors were deposited onto the Cu_2O to form the cavity the same silver films were also deposited onto a glass substrate. We then measured the transmission and reflection of these silver films using the same laser as in the main experiments, and a commercial laser power meter. We measured reflection of $R = 92 \pm 3\%$ and transmission of $T = 2.0 \pm 0.3\%$. The silver thickness of 51.5 nm was known from the deposition rate and time. We then used the transfer matrix method to model the reflection and transmission of the structure and found the silver refractive index that gave the measured transmission and reflection. We find real and imaginary parts of the refractive index $\mathrm{n} = 0.24 \pm 0.11$ and $k = 3.78 \pm 0.10$ respectively. Here the errors were

obtained by propagating the errors in R and T using the numerically calculated gradients $\partial \mathrm{n}/\partial T$, $\partial \mathrm{n}/\partial R$, $\partial k/\partial T$, and $\partial k/\partial R$. For the error $\Delta \mathrm{n}$ in n we used the formula $\Delta \mathrm{n} = |\partial \mathrm{n}/\partial T|\Delta T + |\partial \mathrm{n}/\partial R|\Delta R$, and similar for the error Δk in k. We note that our refractive index is also consistent with values from the literature [3]. We checked that our deduced values of density do not vary by more than a few percent with the real part of the refractive index of the silver mirrors.

Next we calibrated the Cu_2O layer properties. The background refractive index 2.7386 was taken from the literature [4]. We then modelled transmission through the cavity using the transfer matrix method and varied the thickness of the Cu_2O until the free spectral range between adjacent photonic modes matched that in the experiment. In this manner we found a cuprous oxide thickness of 26.0 micrometers. The imaginary part of the cuprous oxide refractive index, 0.000483, was then found so that the quality factor of the calculated modes was 2000 away from the excitonic resonances, in agreement with the experimental results. We checked that our deduced values of density do not depend (by more than a few percent) on the refractive index of the cuprous oxide provided that the free spectral range matched the experimental value.

Having calibrated both mirror and cavity properties we then used the transfer matrix model to calculate both the energy density inside the cavity and the Poynting flux (power per unit area) outside the cavity for a monochromatic incident laser, as in Ref. [2]. Integrating the energy density over the cavity length and dividing by the flux gives τ', the inverse of the rate of tunnelling of photons through the mirror. We then have $P_{\mathrm{out}} = E_{\mathrm{cav}}/\tau'$ where P_{out} is the measured power coming out of the cavity and E_{cav} is the energy stored as photons inside the cavity.

We calculated τ' as a function of photon wavelength and found variation of only 0.4% over the 1.75 meV (0.467 nm) energy range corresponding to the bandwidth of the spectra shown in the experiments. Since in the linear regime the time-varying fields inside the cavity may be viewed as a superposition of different frequency waves (by the Fourier transform) we can therefore assume that the ratio of stored energy to output power is the same for the pulsed case as for the monochromatic case. We arrive at $\tau' = 14 \pm 2$ ps. Here the uncertainty $\Delta\tau'$ in τ' was obtained by propagating the errors $\Delta \mathrm{n}$ and Δk in the silver mirror real and imaginary refractive indices respectively using $\Delta\tau' = |\partial\tau'/\partial \mathrm{n}|\Delta \mathrm{n} + |\partial\tau'/\partial k|\Delta k$. The gradients $\partial\tau'/\partial \mathrm{n} = 3.27$ ps and $\partial\tau'/\partial k = 19.48$ ps were obtained numerically by running the transfer matrix simulation over a range of different refractive indices.

The number of particles in the cavity is related to the energy by $N = E_{\mathrm{cav}}/(\hbar\omega)$ where ω is the central angular frequency of the pulses. The areal density of photons $\rho_{\mathrm{photons}} = N/A$ can then be obtained using the effective area A for the nonlinear interaction. This is given by [5] $1/A = \int\int_{-\infty}^{\infty} I^2(x,y)dxdy$ where $I(x,y)$ is the normalised spatial intensity distribution inside the cavity, which in our case has a Gaussian shape. This takes account of the fact that the

density varies over the Gaussian spot and so we measure a weighted average of more and less strongly interacting regions.

In a similar way our time-averaged measurement of the $\sim$ 1 ps pulses coming from the cavity is an average over the time-varying interaction energy in the cavity weighted by the occupancy of the cavity. Both the interaction energy and occupancy are proportional to the temporal shape of the cavity occupancy $I(t)$. Taking this weighted average gives the effective pulse length τ_{p} using $1/\tau_p = \int_{-\infty}^{\infty} I^2(t)dt$. Transform limited Gaussian pulses with 1.75 meV spectral width have a temporal width of 1.0 ps. This is then a lower bound for the possible temporal width of the density in the cavity, which provides an upper bound for the density and hence a lower bound for the nonlinearity. However, the real temporal width is likely to be longer due to partial cavity filtering of the incident spectrum and/or chirp in the incident pulses. Using the lower bound of a 1 ps Gaussian we obtain $\tau_{\mathrm{p}} = 1.57$ ps.

We then use $E_{\mathrm{cav}} = P_{\mathrm{out}}\tau'$ from above and insert the effective output pulse power $P_{\mathrm{out}} = P_{\mathrm{avg,T}}/\left(f\tau_{\mathrm{p}}\right)$. Here $P_{\mathrm{avg,T}}$ is the average power of the *transmitted* beam, $f = 1$ kHz is the laser repetition rate and τ_{p} is the effective pulse length defined above. We finally make the substitution $P_{\mathrm{avg,T}} = TP_{\mathrm{avg}}$ where P_{avg} is the average *incident* beam power and $T = 1/180$ is the measured transmission through the cavity. This accounts for the reflection of spectral components of the incident pulse which are not resonant with the cavity modes. Recalling that $\rho_{\mathrm{photons}} = N/A = E_{\mathrm{cav}}/\left(A\hbar\omega\right)$ finally leads to an expression for the photon density in cavity:

$$\rho_{\mathrm{photons}} = \frac{TP_{\mathrm{avg}}\tau'}{f\tau_{\mathrm{p}}A\hbar\omega}. \tag{S2}$$

So far our discussion has concerned a purely photonic cavity with no strong exciton-photon coupling. When strong coupling is included the fundamental eigenstates of the system, the polaritons, are part photon and part exciton. The fractions of photon and exciton content are $|C|^2$ and $|X|^2$ respectively with $|C|^2 + |X|^2 = 1$. Since our measurements of nonlinearity are made at zero exciton-photon detuning we have $|C|^2 = |X|^2 = 0.5$. Only the photonic component of the polaritons leads to tunnelling through the mirror into free space modes outside the cavity. Thus Eqn. S2 still holds and the output power from the cavity gives the density of photons inside the cavity, where we are careful to remember that this is really the density of the photonic component of the polaritons. The density of the photonic component is related to the density of polaritons by $\rho_{\mathrm{photons}} = \rho_{\mathrm{polaritons}}|C|^2$. We can then write the density of polaritons as

$$\rho_{\mathrm{polariton}} = \frac{TP_{\mathrm{avg}}\tau'}{f\tau_{\mathrm{p}}A\hbar\omega|C|^2}. \tag{S3}$$

Finally, to obtain the density of excitons (the excitonic component of the polaritons) we multiply the polariton density by the excitonic fraction,

$$\rho = \frac{TP_{\mathrm{avg}}\tau'|X|^2}{f\tau_{\mathrm{p}}A\hbar\omega|C|^2}. \tag{S4}$$

6 Comparison of nonlinearities

We find that in our system the nonlinearity coefficient β, relevant for applications, ranges between 0.01 μeV μm^3 for $n = 3$, to 0.4 μeV μm^3 for $n = 7$ Rydberg exciton-polaritons (see Fig. 3 in the main text). It is important to note that in a Cu_2O cavity the excitons are delocalised within the cavity thickness of 26 μm, and so the exciton density is expressed per unit volume of the cavity region and the appropriate units for the nonlinear parameter are energy shift divided by number of particles per unit volume, that is μeV μm^3.

In other highly nonlinear polariton systems, such as for example microcavities with embedded (In)GaAs quantum wells, the excitons are confined within the thickness of the quantum wells (typically $\sim$ 10 nm per quantum well in the device). A single quantum well thickness is comparable to the exciton Bohr radius and hence the density is usually expressed per unit area of a single quantum well. For GaAs polaritonic systems the reported strengths of exciton-polariton nonlinearity (either β-values or g-values characterising the collapse of strong exciton-photon coupling or the exciton energy shifts, respectively) are in the range from 2 to 10 μeV μm^2 [2, 6–9]. In order to compare these to β-values of the bulk excitons we study, one has to transform the 2D density to effective 3D density by dividing it by the thickness of the quantum wells. This enables a unified characterisation of the strength of interactions between two excitons separated by a certain distance irrespective of how they are positioned within the cavity region, whether they are bulk or confined to a single or multiple 2D layers.

Following this procedure the 2D values of 2–10 μeV μm^2 in GaAs-based systems are equivalent to 0.02–0.1 μeV μm^3. These values are exceeded by the β values in Cu_2O microcavity already for $n = 5$ exciton-polaritons. Qualitatively, this is expected since the exciton Bohr radius for $n = 5$ is already of the order of 30 nm, being three times larger than that in GaAs, leading to stronger dipole-dipole interactions or Pauli blockade mechanism. Similarly, nonlinearities in hybrid perovskites containing order 3000 layers have been studied [10]. Each layer is of order 1.7 nm thick. The per-layer nonlinearity of 3 μeV μm^2 is equivalent to a bulk-like nonlinearity of 0.005 μeV μm^3. This 3D value is then convenient to deduce the effective 2D nonlinearity of perovskite structures with different numbers of layers.

7 Theoretical analysis

In this section we present the theoretical analysis of Rydberg excitons coupled to photons in a microcavity. In the first part, we focus on the relation of the Rabi splitting (Ω_n) and the light-matter coupling constant (G_n). In particular, we derive $\Omega_n \approx \Omega_n^{(0)} - \beta_n \rho$, where ρ is the exciton density, and $\Omega_n^{(0)}$ is the Rabi splitting at vanishing density, $\rho = 0$. This gives the theoretical beta factor β_n used to characterise the strength of nonlinearity. In general, $\beta_n \sim V_B/V$ is mostly determined by the ratio between blockade (V_B) and the total volume (V). In the next part, we discuss the blockade V_B due to Rydberg and Pauli

blockade. These two different mechanisms lead to distinct scaling behavior. Also, we discuss the estimates for β_n in Cu_2O (Fig. 3**b** in the main text). In the final part, we deduce the nonlinear refractive index n_2 for Cu_2O using the nonlinear polaritonic response.

7.1 Rabi splitting and light-matter coupling

Transmission of the Cu_2O microcavity system around n-th excitonic state can be modeled as [1]

$$T_n \approx \frac{1}{(\frac{\kappa}{2} + G_n^2 \frac{\gamma_n/2 + 2Q_n\Delta_n}{\gamma_n^2/4+\Delta_n^2})^2 + (\Delta_n - G_n^2 \frac{\Delta_n - Q_n\gamma_n}{\gamma_n^2/4+\Delta_n^2})^2}, \tag{S5}$$

where κ is the cavity line-width, G_n is the exciton-photon coupling constant, Δ_n is the detuning, γ_n is the excitonic linewidth, and Q_n is the Fano asymmetry parameter. In the weak light-matter coupling regime ($G_n \ll \gamma_n$), the system only responds to light with frequency near the exciton resonance ($\Delta_n = 0$). One can see from Eq. (S5) that in the strong coupling regime ($G_n \gg \gamma_n$) the optical response changes qualitatively [11]. Namely, in this regime the resonance changes from $\Delta_n = 0$ to two resonances at $\Delta_n = \pm\frac{1}{2}\Omega_n$. This comes from the hybridisation of photonic and excitonic modes. The resulting states – polaritons – are quasiparticles which energies are characterised by the Rabi splitting Ω_n.

The Rabi splitting can be analytically calculated from Eq. (S5) by identifying the separation between points of maximum response in the transmission spectrum. For instance, in the absence of asymmetry ($Q_n = 0$), Rabi splitting can be obtained from Eq. (S5) as [12]

$$\Omega_n = 2\sqrt{G_n\sqrt{\tfrac{1}{2}\gamma_n(\kappa+\gamma_n) + G_n^2} - \tfrac{1}{4}\gamma_n^2}. \tag{S6}$$

We can see that the Rabi splitting explicitly depends on the coupling constants G_n and the linewidth γ_n. These quantities can be exciton density-dependent. For instance, the exciton blockade can lead to the reduction of G_n, and the scattering between excitons broadens the linewidth γ_n. These effects will eventually renormalise the Rabi splitting or the shift of polariton energy which directly translates into optical nonlinearity. To see these effects, we expand Eq. (S6) at low exciton density ρ as

$$\Omega_n = \Omega_n^{(0)} - \beta_n\rho + \mathcal{O}(\rho^2), \tag{S7}$$

where the Rabi splitting in low density is

$$\Omega_n^{(0)} = 2\sqrt{G_n^{(0)}\Lambda_n - \tfrac{1}{4}(\gamma_n^{(0)})^2}, \tag{S8}$$

with $G_n^{(0)} := G_n|_{\rho=0}$, $\gamma_n^{(0)} := \gamma_n|_{\rho=0}$, and $\Lambda_n := \sqrt{\frac{1}{2}\gamma_n^{(0)}(\kappa+\gamma_n^{(0)})+(G_n^{(0)})^2}$. Here, the β-factor then reads

$$\beta_n = -\frac{2}{\Omega_n^{(0)}\Lambda_n}\Big[(\Lambda_n^2+(G_n^{(0)})^2)\frac{dG_n}{d\rho}+G_n^{(0)}(\tfrac{1}{2}\kappa+\gamma_n^{(0)})\frac{d\gamma_n}{d\rho}\Big]. \tag{S9}$$

This factor quantifies the rate of the Rabi splitting reduction. In the above, the exciton blockade and the linewidth broadening effects are present in the first and second terms. However, no strong inhomogeneous broadening has been resolved in the measurement within the low-density regime. Therefore, in our analysis, we focus on the blockade effect in the first term.

7.2 Rydberg and Pauli blockade

In this subsection, we discuss the possible blockade mechanism that leads to reduction of G_n, and present the details for derivations. First, let us comment on the case of Rydberg excitons outside of optical cavities. In the presence of N Rydberg excitons, the absorption (α) of Cu_2O follows the scaling relation $\alpha \propto V/V_B - N$, where V is the total volume of the system and V_B is the Rydberg blockade volume [13]. The N-dependent behavior in α can be well explained by Rydberg blockade physics [14]. When placed inside an optical cavity, the absorption is related to the light-matter coupling constant as $\alpha \propto G_n^2$ [1]. In the low-density limit, the coupling constant may be written as

$$G_n \approx G_n^{(0)}(1-\tfrac{1}{2}B_nN), \tag{S10}$$

where $B_n = V_B/V$ is the blockade coefficient for a single Rydberg exciton. In the case of Rydberg blockade it is given by

$$B_n = \frac{4\pi}{3}\frac{r_C^3}{V}. \quad \text{(Rydberg)} \tag{S11}$$

The Rydberg exciton blockade radius is modeled by $r_C = (C_k/\gamma_n)^{1/k}$ with C_k being the dipole-dipole interacting constant [14, 15]. Here, $k=3$ is the Förster-type interaction and $k=6$ is the van der Waals interaction. This parameter plays a crucial role in determining blockade physics which has been estimated theoretically in Ref. [15]. To calculate the β-factor, we substitute Eq. (S10) into Eq. (S9), and get

$$\beta_n = \frac{\Lambda_n^2+(G_n^{(0)})^2}{\Omega_n^{(0)}\Lambda_n}G_n^{(0)}B_nV. \tag{S12}$$

We then extract the light-matter coupling constant $G_n^{(0)}$ from the measurement in Fig. 3**a** of the main text by using Eq. (S8). This gives the best fit $G_n^{(0)} = 2.29(\frac{n^2-1}{n^5})^{1/2}$meV in the main text, see Fig. **S6a**. We obtain the β-factor

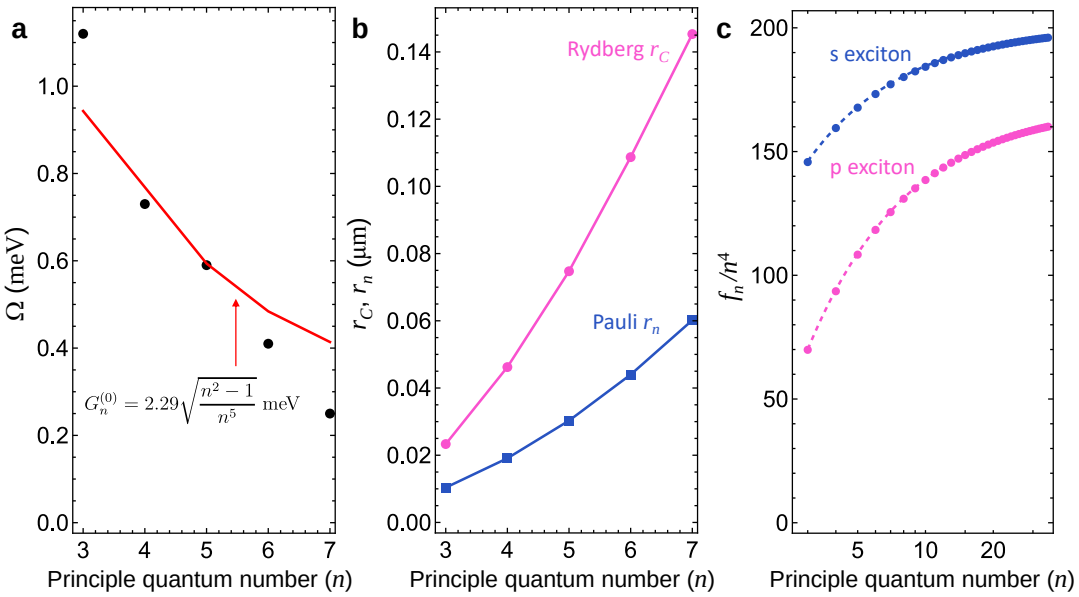

Fig. S6: Scaling of Rydberg exciton. (a) Rabi splitting in low density. Closed black circles are the point taking from Fig. 3**a** of the main text at $\rho = 0$. Dashed curved is the fitted result by using $G_n^{(0)} \propto \sqrt{(n^2-1)/n^5}$ and Eq. (S6). (b) Comparison between Rydberg (r_C magenta) and Pauli (r_n, light blue) blockade radius. (c) Scaling of Pauli blockade coefficient. The factor f_n in Eq. (S18) gives the asymptotic scaling behavior for the blockade coefficient $B_n \sim n^4$ [Eq. (S17)]. Dashed curves are the fits by using $f_n = n^4(b_0 + b_1 n^{-1} + b_2 n^{-2})$.

plotted as the purple solid curve in Fig. 3**b**. In the large n-limit, the blockade coefficient shows a power-law scaling with $B_n \sim n^7$[14]. Hence, Eq. (S12) gives the asymptotic scaling for $\beta_n \sim n^{5.5}$.

However, this scaling property which is very often used for identifying the Rydberg blockade has only been established in the large quantum number regimes ($n \geq 12$) [14]. In our case, the exciton quantum number are in the range from $n = 3$ to $n = 7$, where the scaling behavior may not be evident. Therefore, the power-law scaling may not be a single argument supporting the observation of the Rydberg blockade in our low-n measurement. Next, we consider another potential contribution to the reduction of Rabi frequency.

As the exciton radius $r_n = \frac{1}{2}a_0(3n^2 - 2)$ [14] is comparable to the Rydberg blockade radius r_C (see Fig. **S6**b), we consider the effects of Pauli blockade. This comes from the composite nature of excitons and fermionic statistics of the electrons and holes. In order to identify the Rydberg physics in this low-n regime, we analyse the Pauli blockade and investigate its contribution.

For the Pauli blockade, the coefficient in Eq. (S10) can be evaluated exactly as

$$B_n = \sum_{\boldsymbol{k}} |\psi_n(\boldsymbol{k})|^4, \quad \text{(Pauli)}, \tag{S13}$$

where $\psi_n(\boldsymbol{k})$ is the exciton wavefunction with quantum number n and wavevector $\boldsymbol{k}$ [16]. The p-wave hydrogen-like wavefunction [17] ($l = 1, m = 0$)

is

$$\psi_n(\boldsymbol{k}) = \sqrt{\frac{(na_0)^3}{V}\frac{n(n-l-1)!}{(n+l)!}}\left[C_{n-l-1}^{(l+1)}\left(\tfrac{\xi^2-1}{\xi^2+1}\right)\frac{2^{2l+3}2\pi l!\xi^l}{(\xi^2+1)^{l+2}}\right]\Upsilon_{lm}(\theta,\phi), \quad \text{(S14)}$$

where $\xi = nka_0$. Here, $C_n^{(\alpha)}(x)$ is the Gegenbauer functions and $\Upsilon_{lm}(\theta,\phi)$ is the spherical harmonic function. We note that the momentum $\boldsymbol{k}$ is discrete, defined by a finite sample size with volume V. The normalisation condition is $\sum_{\boldsymbol{k}} |\psi_n(\boldsymbol{k})|^2 = 1$. In contrast to the Rydberg blockade, the shape of the exciton wavefunction $\psi_n(\boldsymbol{k})$ completely determines B_n or the Bohr radius a_0. The Bohr radius can be determined by the experiment's Rydberg exciton energies, $\omega_n = E_{\rm g} + E_n^{\rm b}$ in Fig. **S3** with bandgap energy $E_{\rm g}$ and the exciton binding energy

$$E_n^{\rm b} = -\frac{\mathrm{Ry}^*}{n^2}. \quad \text{(S15)}$$

The Rydberg constant $\mathrm{Ry}^* = \frac{e^2}{4\pi\epsilon_0\epsilon_r}\frac{1}{2a_0}$, which allows us to estimate a_0. Using the Cu_2O dielectric constant $\epsilon_r = 7.5$ [18], and

$$\mathrm{Ry}^* = -\frac{\omega_{n-1}-\omega_n}{(n-1)^{-2}-n^{-2}}, \quad \text{(S16)}$$

we can deduce the Bohr radius $a_0 \approx 0.83$ nm. Therefore, in the Pauli blockade, the experiment leaves no free adjustable parameter for the β-factor. We plot β_n from the contribution due to the Pauli blockade in Fig. 3 of the main text (blue dashed curve). It is an order of magnitude smaller than the measured values.

In terms of power-law scaling, we let

$$B_n = f_n\frac{a_0^3}{V}. \quad \text{(Pauli)} \quad \text{(S17)}$$

The prefactor is

$$f_n = \frac{9\times 2^{20}n^3}{10(n^2-1)^2}\int_0^\infty d\xi \frac{\xi^6[C_{n-2}^{(2)}(\frac{\xi^2-1}{\xi^2+1})]^4}{(1+\xi^2)^{12}}, \quad \text{(S18)}$$

where we used $\sum_{\boldsymbol{k}}\frac{(2\pi)^3}{V} \to \int d^3k$ for wavevector $\boldsymbol{k}$ in large V. This f_n prefactor determines the scaling behavior of B_n and we plot in Fig. **S6**c. As we can see, the Pauli blockade coefficient (B_n) scales with a power law weaker than n^4 for low n, and approaches an $\sim n^{3.5}$ scaling in the high-n range. Overall, it is lower than the Rydberg blockade scaling with n^7. Using Eq. (S12), this yields a a scaling trend of $\beta_n \sim n^{2.5}$ for small n, significantly different as compared to experiment.

7.3 n_2 parameter from Rabi frequency measurement

To estimate the n_2 nonlinear parameter, we begin with the definition of the total refractive index and the optical susceptibility as follows [4]

$$n_T{}^2 = \epsilon_b + \chi(\omega). \tag{S19}$$

The optical susceptibility in a cavity for each excitonic mode near the resonance can be modeled by [1, 11]

$$\chi(\omega) \approx \frac{h_n G_n^2}{\omega - \omega_n + \frac{1}{2} i\gamma_n}, \quad (\omega \simeq \omega_n), \tag{S20}$$

where ω_n is the Rydberg exciton energy. We note that the constant of proportionality h_n can be determined from the Rabi splitting measurement.

The coupling constant G_n changes due to the Rydberg blockade as the laser power increases [Eq. (S10)]. This leads to the nonlinear response in the susceptibility

$$\chi(\omega) = \chi^{(1)}(\omega) + \chi^{(3)}(\omega) E^2. \tag{S21}$$

In the vicinity of $\omega \simeq \omega_n$, the linear response of the above is $\chi^{(1)}(\omega) \approx h_n (G_n^{(0)})^2 (\omega - \omega_n + \frac{1}{2} i\gamma_n)^{-1}$, and the Kerr nonlinear response is

$$\chi^{(3)}(\omega) \approx \frac{h_n (G_n^{(0)})^2 (-B_n)(\frac{1}{2}\epsilon_0 V/\omega)}{\omega - \omega_n + \frac{1}{2} i\gamma_n}, \tag{S22}$$

where we have converted the exciton number N into the electric field E by using $\omega N/V \approx \frac{1}{2}\epsilon_0 E^2$ with V being the volume of the nonlinear medium. Also, the blockade coefficient is given by Eq. (S11). The nonlinear refractive index n_2 is defined as

$$n_2(\omega) = \frac{\mathrm{Re}[\chi^{(3)}(\omega)]}{\epsilon_0 c n_0^2}, \tag{S23}$$

where $n_0^2 = \epsilon_b + \mathrm{Re}[\chi^{(1)}(\omega)]$. Therefore, the n_2-parameter (near $\omega \simeq \omega_n$) from the quench of Rabi frequency is

$$n_2(\omega) \approx -\frac{h_n \beta_n}{2 c n_0^2 \omega} \frac{G_n^{(0)}(\omega - \omega_n)}{(\omega - \omega_n)^2 + \frac{1}{4}\gamma_n^2}, \tag{S24}$$

where we have used Eq. (S12) by taking the strong-coupling limit ($G_n^{(0)} \gg \gamma_n^{(0)}$).

At the polaritonic peaks ($\omega = \omega_n \pm \frac{1}{2}\Omega_n^{(0)}$), the total refractive index satisfies [11]

$$n_T(\omega_n \pm \tfrac{1}{2}\Omega_n^{(0)}) = n_b \frac{\omega_n}{\omega_n \pm \frac{1}{2}\Omega_n^{(0)}} \tag{S25}$$

where $n_b = n_T(\omega_n) = \sqrt{\epsilon_b}$ is the background refractive index ($n_b = 1$ for the device is vacuum). The condition in Eq. (S25) determines the constant of proportionality h_n. Therefore, we can deduce the nonlinear refractive index n_2 from our Rabi splitting measurements.

Alternatively, we can also deduce the constant of proportionality h_n from the absorption data by following the method in Ref. [11]. First, the Rabi splitting of a nonlinear medium with susceptibility in Eq. (S20) can also be estimated as

$$\Omega_n^{(0)} = \sqrt{2\omega_n h_n (G_n^{(0)})^2 / {n_b}^2 - (\gamma_n^{(0)})^2} \tag{S26}$$

Substituting the experimental measurements into the above, we get h_n which has the same orders of magnitude as the h_n obtained from Eq. (S25). Furthermore, in Ref.[11], we have $h_n (G_n^{(0)})^2 \approx (n_b c \alpha_0 \gamma_n)/(\omega_n/\hbar)$ where α_0 is the absorption. Using the absorption data in Ref. [13], we again obtain the h_n with the same order of magnitude.

8 Non-resonant pumping and quenching of Rabi Splitting

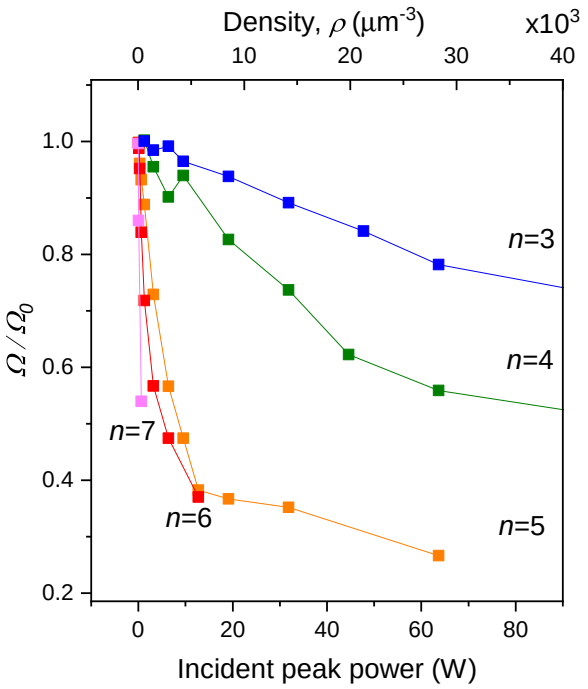

Fig. S7: Normalized Rabi splitting as a function of resonant peak laser power (bottom axis) and/or photon density in the cavity (top axis). Normalization is based on the case where smallest value of laser power is used.

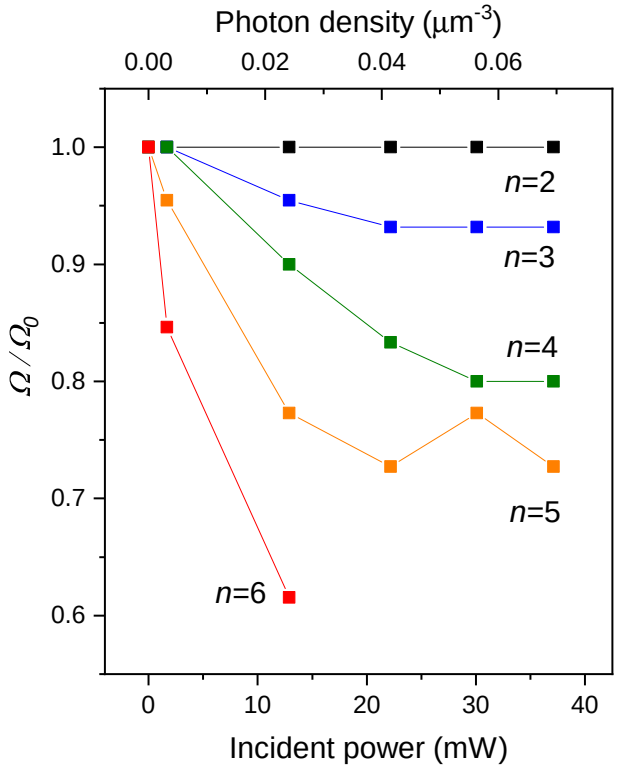

Fig. S8: Normalized Rabi splitting as a function of non-resonant CW laser power (bottom axis) and/or photon density inside the cavity (top axis). Rabi splitting values are normalized based on the case where no non-resonant laser is used.

In this section we compare two regimes of quenching of Rabi splitting. One case is the resonant pulsed excitation presented in the main paper in Fig. 3. Here we show these data as normalised Rabi splitting plotted as a function of incident peak power and/or photon density created by the pulse in the active cavity region (Fig. S7). The second case is non-resonant continuous wave (CW) excitation with above band gap green laser at wavelength 520 nm (Fig. S8). Varying the power of non-resonant laser and probing with weak broadband super-continuum laser filtered from 568 to 582 nm in transmission geometry the transmission spectra are recorded and then fitted to extract Rabi splitting. Normalised Rabi splitting for this experiment is plotted as a function of CW power of green laser or photon density in the cavity for excitons from $n = 2$ to 6 (see Fig. S8).The photon density in pulsed case is calculated using Eq. S2 whereas photon density in CW case is calculated using the following equation:

$$\rho^{\mathrm{CW}} = \frac{TP_{inc}}{3A\hbar\omega(c_0/n_0)}, \tag{S27}$$

where T is the transmission through the mirror(2%), P_{inc} is the incident power, A is the illuminated area (95 μm^2), $\hbar\omega$ is the photon energy, c_0 is the speed of light in vacuum, n_0 is Cu_2O background refractive index, 1/3 is from the

fact that propagation length of the excitation laser ≈ 10 μm in Cu_2O with thickness of ≈ 30 μm. The data for CW case are obtained on microcavity Cu_2O sample with distributed Bragg reflector mirrors reported in Ref. [1], which is very similar in optical characteristics to the sample presented in the main paper — cavity with silver mirrors. Note that the incident powers used in CW excitation case are in tens of mW range for quenching of Rabi splitting whereas in resonant experiment with pulsed excitation quenching of Rabi splitting is achieved at peak powers of tens of Watts. Even higher difference can be noted in the photon density required for quenching the Rabi between CW and pulsed regime (6 orders of magnitude). Such big difference of 6 orders of magnitude in photon densities can be explained by population of free electrons and holes and long lived states in the case of CW excitation contributing to nonlinear behaviour and quenching of Rabi splitting. We also note that in our experiments the photon densities in case of non-resonant CW pumping are only 6 orders of magnitude less than in the case of pulsed excitation. So our experiment with CW nonresonant pumping alone cannot explain why there is 8 orders of magnitude difference in the n_2 parameters measured in the case of resonant pulsed and CW pumping in Ref. [4]. It is possible that such a difference is sample dependent (for example, the density of long-lived localised states, which could be associated with metallic impurities may vary from sample to sample).

9 Pump-probe zero delay point

The interference between residual pump and probe pulses results in modulation of the spectra at small delays between pulses (see Fig. **S9**a). The modulation frequency depends on separation of the pulses whereas its visibility depends on the relative intensities of the two pulses. The analysis of modulation at small delay times allow us to define the zero delay between pulses with accuracy of ±0.25 ps (see Fig. **S9**). Fig. **S9**a shows pump-probe transmission spectra on glass substrate without the Cu_2O at different delay times where pump signal after rejection with a polariser was ≈ 3 times bigger than the probe signal. We extract free spectral range (FSR) of the modulated signal and plot it as a function delay stage position in Fig. **S9**b. Fitting the FSR data allow us to define the zero delay position for the probe delay stage.

Although we have used much smaller pump powers in the experiment with Cu_2O in Fig. 5 and rejected the unwanted pump signal with polarisers on detection small amount of pump still provides enough modulation for the probe signal to interfere with polariton resonance. So we not plot data points in Fig. 5 of the main text for the range of -30 to 37 ps apart from exact time 0 where the frequency of modulation is bigger than the polariton resonance and it doesn't influence the transmitted probe polariton spectrum.

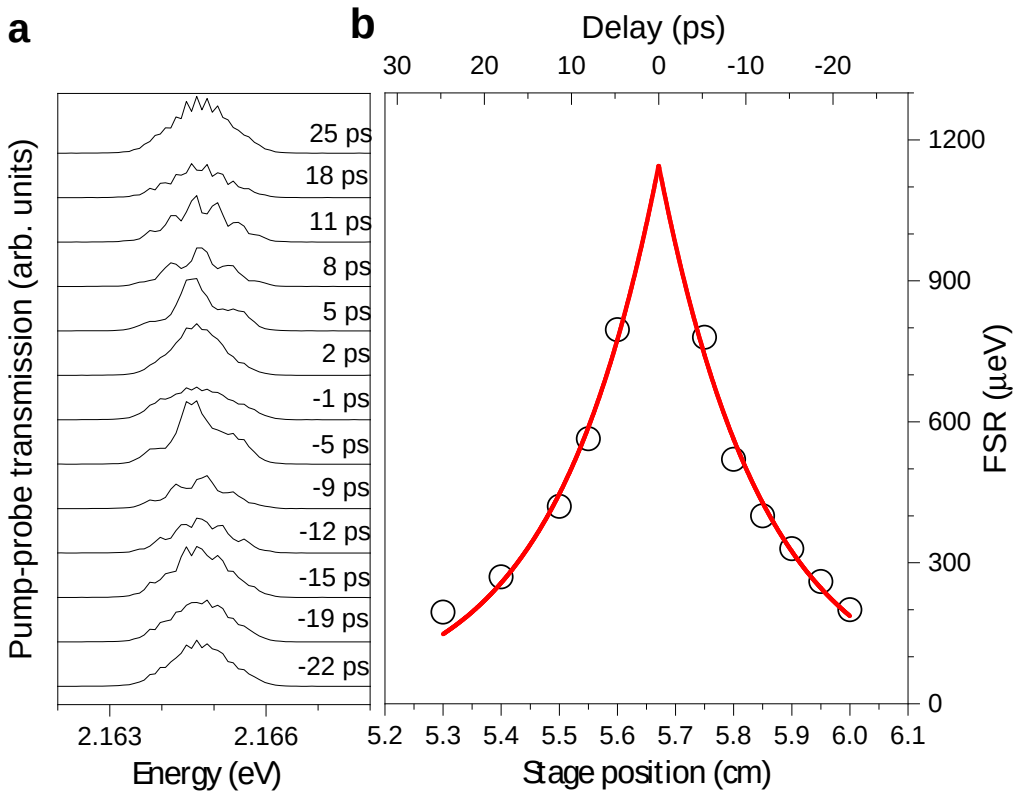

Fig. S9: **Pump-probe signal on substrate without the sample. a** transmitted probe spectra for different delays displays interference with residual pump beam not fully rejected by polarisers. Intensity of probe (pump) beam is 20 μJ cm^{-2} (20 mJ cm^{-2}). Period of modulation in energy or free spectral range (FSR) increases closer to zero delay. **b** FSR plot (extracted from spectra in **a**) as a function of probe delay stage position (bottom axis) and/or time delay (top axis). Time zero between arrival of two pulses is defined from the fit of FSR with exponential function with accuracy of ±0.25 ps.

References

[1] Orfanakis, K., Rajendran, S.K., Walther, V., Volz, T., Pohl, T., Ohadi, H.: Rydberg exciton–polaritons in a Cu_2O microcavity. Nature Materials **21**(7), 767–772 (2022). https://doi.org/10.1038/s41563-022-01230-4

[2] Kuriakose, T., Walker, P.M., Dowling, T., Kyriienko, O., Shelykh, I.A., St-Jean, P., Zambon, N.C., Lemaître, A., Sagnes, I., Legratiet, L., Harouri, A., Ravets, S., Skolnick, M.S., Amo, A., Bloch, J., Krizhanovskii, D.N.: Few-photon all-optical phase rotation in a quantum-well micropillar cavity. Nature Photonics **16**(8), 566–569 (2022). https://doi.org/10.1038/s41566-022-01019-6

[3] Ferrera, M., Magnozzi, M., Bisio, F., Canepa, M.: Temperature-dependent permittivity of silver and implications for thermoplasmonics. Phys. Rev.

Mater. **3**, 105201 (2019). https://doi.org/10.1103/PhysRevMaterials.3.105201

[4] Morin, C., Tignon, J., Mangeney, J., Dhillon, S., Czajkowski, G., Karpiński, K., Zielińska-Raczyńska, S., Ziemkiewicz, D., Boulier, T.: Self-kerr effect across the yellow rydberg series of excitons in Cu_2O . Physical Review Letters **129**(13) (2022). https://doi.org/10.1103/physrevlett.129.137401

[5] Carusotto, I., Volz, T., Imamoğlu, A.: Feshbach blockade: Single-photon nonlinear optics using resonantly enhanced cavity polariton scattering from biexciton states. EPL (Europhysics Letters) **90**(3), 37001 (2010). https://doi.org/10.1209/0295-5075/90/37001

[6] Walker, P.M., Tinkler, L., Skryabin, D.V., Yulin, A., Royall, B., Farrer, I., Ritchie, D.A., Skolnick, M.S., Krizhanovskii, D.N.: Ultra-low-power hybrid light–matter solitons. Nature Communications **6** (2015). https://doi.org/10.1038/ncomms9317

[7] Ferrier, L., Wertz, E., Johne, R., Solnyshkov, D.D., Senellart, P., Sagnes, I., Lemaître, A., Malpuech, G., Bloch, J.: Interactions in confined polariton condensates. Phys. Rev. Lett. **106**, 126401 (2011). https://doi.org/10.1103/PhysRevLett.106.126401

[8] Estrecho, E., Gao, T., Bobrovska, N., Comber-Todd, D., Fraser, M.D., Steger, M., West, K., Pfeiffer, L.N., Levinsen, J., Parish, M.M., Liew, T.C.H., Matuszewski, M., Snoke, D.W., Truscott, A.G., Ostrovskaya, E.A.: Direct measurement of polariton-polariton interaction strength in the thomas-fermi regime of exciton-polariton condensation. Phys. Rev. B **100**, 035306 (2019). https://doi.org/10.1103/PhysRevB.100.035306

[9] Brichkin, A.S., Novikov, S.I., Larionov, A.V., Kulakovskii, V.D., Glazov, M.M., Schneider, C., Höfling, S., Kamp, M., Forchel, A.: Effect of coulomb interaction on exciton-polariton condensates in gaas pillar microcavities. Phys. Rev. B **84**, 195301 (2011). https://doi.org/10.1103/PhysRevB.84.195301

[10] Fieramosca, A., Polimeno, L., Ardizzone, V., Marco, L.D., Pugliese, M., Maiorano, V., Giorgi, M.D., Dominici, L., Gigli, G., Gerace, D., Ballarini, D., Sanvitto, D.: Two-dimensional hybrid perovskites sustaining strong polariton interactions at room temperature. Science Advances **5**(5) (2019). https://doi.org/10.1126/sciadv.aav9967

[11] Khitrova, G., Gibbs, H.M., Jahnke, F., Kira, M., Koch, S.W.: Nonlinear optics of normal-mode-coupling semiconductor microcavities. Rev. Mod. Phys. **71**, 1591–1639 (1999). https://doi.org/10.1103/RevModPhys.71.1591

[12] Savona, V., Andreani, L.C., Schwendimann, P., Quattropani, A.: Quantum well excitons in semiconductor microcavities: Unified treatment of weak and strong coupling regimes. Solid State Communications **93**(9), 733–739 (1995). https://doi.org/10.1016/0038-1098(94)00865-5

[13] Kazimierczuk, T., Fröhlich, D., Scheel, S., Stolz, H., Bayer, M.: Giant rydberg excitons in the copper oxide Cu_2O. Nature **514**(7522), 343–347 (2014). https://doi.org/10.1038/nature13832

[14] Aßmann, M., Bayer, M.: Semiconductor rydberg physics. Advanced Quantum Technologies **3**(11), 1900134 (2020). https://doi.org/10.1002/qute.201900134

[15] Walther, V., Krüger, S.O., Scheel, S., Pohl, T.: Interactions between rydberg excitons in Cu_2O. Phys. Rev. B **98**, 165201 (2018). https://doi.org/10.1103/PhysRevB.98.165201

[16] Combescot, M., Betbeder-Matibet, O., Dubin, F.: The many-body physics of composite bosons. Physics Reports **463**(5-6), 215–320 (2008)

[17] Podolsky, B., Pauling, L.: The momentum distribution in hydrogen-like atoms. Phys. Rev. **34**, 109–116 (1929). https://doi.org/10.1103/PhysRev.34.109

[18] Kavoulakis, G.M., Chang, Y.-C., Baym, G.: Fine structure of excitons in Cu_2O. Phys. Rev. B **55**, 7593–7599 (1997). https://doi.org/10.1103/PhysRevB.55.7593